DEVELOPMENT OF A NOVEL CELL TRACTION FORCE TRANSDUCER BASED ON CHOLESTERYL ESTER LIQUID CRYSTALS

CHIN FHONG SOON

PhD

University of Bradford

2011

DEVELOPMENT OF A NOVEL CELL TRACTION FORCE TRANSDUCER BASED ON CHOLESTERYL ESTER LIQUID CRYSTALS

Characterisation, quantification and evaluation of a cholesteryl ester liquid crystal based single cell force transducer system

Chin Fhong SOON

Submitted for the degree
of Doctor of Philosophy

School of Life Sciences

University of Bradford

2011

ABSTRACT

Development of a novel cell traction force transducer based on cholesteryl ester liquid crystals

CHIN FHONG SOON

Keywords: cholesteryl ester liquid crystals, cell force transducer, cell traction force mapping, lyotropic liquid crystals.

Abstract:

In biomechano-transducing, cellular generated tension can be measured by soft substrates based on polymers but these techniques are limited either by spatial resolution or ability to detect localised cell traction forces (CTF) due to their non-linear viscous behaviour under shear rates. A newly developed cell traction force transducer system based on cholesteryl ester lyotropic liquid crystals (LCTFT) was developed to sense localised traction forces of human keratinocyte cell lines (HaCaTs), in which the length of the deformation line induced represents the intensity of the CTF exerted. The physical properties of the cholesteryl ester based lyotropic liquid crystals (LLC) were characterised by using polarising microscopy, rheology, atomic force microscopy (AFM) based nano-indentation, spherical indentation, and micro-tensile tests. The interactions of LLC with cells were studied by using cell viability studies, cytochemical treatments, widefield surface plasmon resonance (WSPR) microscopy and various immuno-staining techniques. The results show that LLC is thermally stable (0 - 50 ^{o}C) and linearly viscoelastic below 10 % shear strain at shear rates of < 1 s^{-1}. AFM nano and spherical indentations show a good agreement on the Young's modulus of both determined at ~110 kPa which is close to the elastic modulus of the epidermis. The Poisson's ratio of LLC was determined at ~0.58 by using micro tensile tests. The biophysical interaction studies indicated that LLC is biocompatible and allowed cell attachment. Cell relaxation technique by cytochalasin-B treatment suggested that the attachment and contraction of cells on LLC was due to the contractile activity of actin cytoskeletons that are mediated by focal adhesions. The staining experiments showed that cells consistently expressed the same suites of integrins (α2, α3, α5 and β1) and ECM proteins (collagen type IV, laminin and fibronectin) on both glass and LLC coated substrates. Interfacial interaction of cells with LLC observed via the staining of actin and vinculin, and WSPR imaging suggest the association of marginal actin filaments and focal adhesions in attaching HaCaT cells to the LLC. Linear static analysis applied in the Finite Element model of focal adhesion-LC confirmed the compressive force patterns induced by cells. By applying cell relaxation techniques and Hooke's theorem, the force-deformation relationships of the LLC were derived and used for direct quantification of CTF in culture. The sensitivity of the LCTFT was implied by a wide range of CTF (10 - 140 nN) measured at high resolutions (~2 μm). Nonetheless, a custom-built cell traction force measurement and mapping software (CTFM) was developed to map CTF of single cells. Reliability of the LCTFT was evaluated by using a known pharmacological active cytokine, TGF-β1, in inducing contraction of human keratinocytes. This study inferred internal consistency and repeatability of the LCTFT in sensing contraction responses of HaCaT cells in a concentration dependent manner of TGF-β1. The overall LCTFT and CTFM software had shown good potential for use in the study of contraction and migration of keratinocytes.

ACKNOWLDEGEMENTS

First of all, I would like to praise the name of almighty God who has made things possible for me. I am deeply thankful to Malaysia Ministry of Higher Education for a scholarship to pursue PhD in University of Bradford, United Kingdom. I am also grateful and indebted to my supervisors Dr. Morgan Denyer, Dr. Mansour Youseffi, Dr. Nick Blagden. During my PhD research, they have played different roles and are highly committed in helping me to achieve my aims and objectives for this work. Their constant support, belief, guidance and encouragement have kept me motivated during the project. I would like to thank Dr. Peter Twigg and Dr. Samira Batista Lobo for providing useful technical help, Professor Des Tobin for his kind permission to use the fluorescence microscope in his laboratory. I am also grateful to Dr. Steve Britland for the use of his micrometer and micropipette puller. I would like to extent special thanks to Dr. Tim Gough, Emtiaz Abdul Aziz, Darren Brown, Dr. Salydani Khagani, Rebecca Berends, Angela Tucny, Alan Lindley, Noshin Sheikh for creating a supportive research environment. I appreciate and would like to thank Rachel Denyer for her help in proof reading one of the published manuscripts. Thanks to the anonymous reviewers for their criticism and helpful inputs to improve this work. Thanks to Dr. Muhammad Mahadi Abdul Jamil for introducing widefield surface plasmon microscopy to me and the British Liquid Crystal Society for organising a winter workshop on liquid crystals at the University of Hull in 2008. Last but not least, my special thanks to Kian Sek Tee for many thoughtful discussions, technical advice and exchange of views during the research.

This thesis is especially dedicated to my beloved late father, my mother, Kian Sek Tee (Husband) and Chloe Tee (Daughter). Thanks to my parents who have nurtured me with many sacrifices and their unconditional love to me. I am also very grateful to my brother and sister who have been taking care of my mother during my absenteeism from home.

STATEMENT OF ORIGINALITY

To the best of my knowledge, material or the contents presented in this thesis are original except where otherwise noted within the text. None of this research has been submitted in whole or in part for a degree at this or any other university.

Chin Fhong Soon

LIST OF ASSOCIATED PUBLICATION

Journal papers

1. Rheological characterization of the time-dependent cholesteric based lyotropic liquid crystals
   C. F. Soon, M. Youseffi, T. Gough, N. Blagden, M.C.T. Denyer
   Materials Science and Engineering C (2011), doi:10.1016/j.msec.2011.05.006 [Accepted]

2. Influence of time dependent factor to the phases and Poisson's ratio of cholesteryl ester liquid crystals
   C. F. Soon, M. Youseffi, N. Blagden, M.C.T Denyer
   Journal of Science and Technology, Volume 3, No. 1, 2011. ISSN No. : 2229-8460.

3. Liquid crystal based cell traction force microscopy
   C. F. Soon, M. Youseffi, N. Blagden, M.C.T. Denyer
   [In preparation]

Book Chapters

1. Finite element quantification of compressive forces induced by keratinocyte on a liquid crystal substrate.
   C. F. Soon, M. Youseffi, P. Twigg, N. Blagden, M.C.T. Denyer
   BOOK CHAPTER in a research monograph "Analysis and Design of Biological Materials and Structures" by Springer in Germany 2011. [In Press]

2. Investigation of Physical Restructuring of cells on the shear sensitive liquid crystals.
   C. F. Soon, M. Youseffi, P. Twigg, N. Blagden, M.C.T Denyer.
   'Electrical Engineering and Applied Computing, Lecture Notes in Electrical Engineering, Vol. 90, 623-635, DOI:10.1007/978-94-007-1192-1_49, Springer 2011.

Conference Papers

1. Characterisation and biocompatibility study of nematic and cholesteric liquid crystals.
   C. F. Soon, M. Youseffi, N. Blagden, S.B. Lobo, F. A. Javid and M. C. T. Denyer
   WCE2009, London, U.K., 1-3 July 2009. Proceedings of the World Congress on Engineering. Volume II, Page: 1872-1875. ISBN: 978-988-18210-1-0. [Peer reviewed]

2. Interaction of cells with elastic cholesteryl liquid crystal
   Chin Fhong Soon, Mansour Youseffi, Nick Blagden, Rebecca Berends, Samira Batista Lobo, Farideh A. Javid and Morgan Denyer.
   World Congress Medical Physics and Biomedical Engineering 2009, Munich, Germany, 7-12 September 2009. IFBME Proceedings 25/10, Volume 25/10, Page: 9-12. DOI: 10.1007/978-3-642-03900-3_4. [Peer reviewed]

3. Effects of an enzyme, depolymerization and polymerization drugs to cells Adhesion and Contraction on Lyotropic Liquid Crystals.
   Chin Fhong Soon, Mansour Youseffi, Nick Blagden and Morgan Denyer
   Proceedings World Congress on Engineering (WCE2010), London, U.K., 30 June-2 July 2010, Volume I, Page: 556-561. ISBN: 978-988-17012-9-9. ISSN: 2078-0958. [Peer reviewed]

4. Measurement and mapping of cell traction forces on the cholesteryl ester liquid crystal force transducer
   Chin Fhong Soon, Mansour Youseffi, Nick Blagden and Morgan Denyer
   Proceedings of International Association of Science and Technology for Development Conference (IASTED). The 2nd IASTED conference on Computational Biosciences (CompBio2011), Cambridge, U.K., 11-13 July 2011. Doi: 10.2316/P.2011.742-013.

Abstracts

1. Development of a novel cell force transducing assay based on shear sensitive cholesteric liquid crystals
   C. F. Soon, M.C.T. Denyer, P. Twigg, M. Youseffi, N. Blagden, F.A. Javid, S. B. Lobo.
   Abstract book, School of Life Sciences Research Open Day, University of Bradford, Bradford, U.K., 2 April 2009, page: 4.19.

2. Rheology of cholesteryl liquid crystals for use as cells adhesion substrate
   C. F. Soon, M. Youseffi, N. Blagden, M.C.T. Denyer
   Abstract book, 11th conference of Surface Science and Biological Important Interfaces-: From fundamental surface science to clinical application. Keele University 28 October 2009, page: 5.

3. Effects of cytochalasin-B and trypsin-EDTA solution on cells adhesion to Lyotropic Liquid Crystals
   C. F. Soon, M. Youseffi, N. Blagden, M.C.T. Denyer
   Abstract book, Surface Science and Biological Important Interfaces-11th annual conference: From fundamental surface science to clinical application. Keele University, 28 October 2009, page: 6. [Best student poster award]

4. Physical interactions of cells with lyotropic liquid crystals
   Chin Fhong Soon, M. Youseffi, N. Blagden, M.C.T. Denyer
   Abstract book, Malaysia Glasgow Doctoral Colloquium (MGDC), 20-21 January 2010, Glasgow Conference Centre, Glasgow, Scotland, page: EA60-EA62.

5. Soft liquid crystals induced organised focal adhesions: a study with WSPR and immunofluorescence imaging
   C. F. Soon, M. Youseffi, N. Blagden, M.C.T. Denyer
   Abstract Book, School of Life Sciences Research Open Day, University of Bradford, Bradford, U.K., 23 March 2010, page: 6.17.

6. Finite element analysis of traction force induced by cell on the liquid crystals
   C. F. Soon, M. Youseffi, N. Blagden, M.C.T Denyer
   Abstract book, 4th International Conference on Advanced Computational Engineering and Experimenting (ACEX-2010), 8-9 July 2010, Paris, France, page: 174.

7. Determination of Young's modulus of cholesteryl ester liquid crystals using nano-indentation and spherical indentation techniques
   Chin Fhong Soon, Mansour Youseffi, Nick Blagden, Morgan Denyer
   Abstract book, 12th annual conference of Surface Science and Biological Important Interfaces, University of Ulster, Belfast, 27 October 2010, page: 17-18. [Invited talk]

LIST OF CONTENTS

ABSTRACT……i

ACKNOWLEDGEMENT……ii

DEDICATION PAGE……iii

LIST OF ASSOCIATED PUBLICATION……iv

LIST OF CONTENTS……v

LIST OF FIGURES……ix

LIST OF TABLES……xxiv

LIST OF ABBREVIATIONS AND SYMBOLS……xxv

1 INTRODUCTION……1

1.1 Research Background……2

1.2 Cellular Adhesion, Contraction and the Measurements of Cell Traction Force……6

1.2.1 Epidermal Tissue……6

1.2.2 Cellular Adhesion……8

1.2.3 Integrin Receptors and Focal Adhesion……14

1.2.4 Polymerisation of Actin Filaments and Generation of Traction Force……16

1.2.5 Force Sensor Based on Silicon Sheet……24

1.2.6 Force Sensor Based on a Collagen Lattice……26

1.2.7 Force Sensor Based on Displacements of Markers in Soft Substrates……27

1.2.8 Force Sensor Based on Micro-Pillars and Micro-Patterns……28

1.3 Introduction to Liquid Crystals……34

1.3.1 Types of Liquid Crystals……35

1.3.2 Classification of Mesophases and Associated Birefringence Texture……39

1.3.3 Elasticity Theory of Chiral Nematic Liquid Crystals 44

1.3.4 Application of Liquid Crystals in Bio-Sensing 47

1.3.5 Viscoelasticity of Lyotropic Liquid Crystals 49

1.4 Selection of Cell Type and Requirements of Cell Traction Force Sensor 50

1.5 Hypothesis of the Research 52

1.6 Aim and Objectives of the Research 53

1.7 Thesis Organisation 54

2 PHYSICAL PROPERTIES: CHARACTERISATION OF CHOLESTERYL ESTER BASED LYOTROPIC LIQUID CRYSTALS 56

2.1 Introduction 57

2.2 Material and Methods 58

2.2.1 Preparation of Cholesteric and Nematic Liquid Crystals 58

2.2.2 Thermal and Liquid Crystalline Phase Analysis 60

2.2.3 Preparation of Liquid Crystal Substrate for Liquid Crystalline Study 61

2.2.4 Preparation of Liquid Crystal Gel for Rheological Test 62

2.2.5 Amplitude and Frequency Sweep Tests 62

2.2.6 Preparation of Human Keratinocyte Cell Lines 63

2.2.7 Culturing Cells on the Liquid Crystal Substrates 64

2.2.8 Characterising the Time-Dependent Viscoelasticity and Viscosity of the Liquid Crystal In-Situ 64

2.2.9 Determining Young's modulus of the Liquid Crystals 67

2.2.10 Measurements of Poisson's Ratio of the Liquid Crystals 73

2.2.11 Statistical Analysis 76

2.3 Results and Discussion 77

2.3.1 Temperature Stability of the Liquid Crystals 77

2.3.2 Identification of the Liquid Crystalline Phase 81

2.3.3 Stabilisation of Shear Modulus at Low Shear Strain 86

2.3.4 Shear Rate Dependent Shear Modulus of the Lyotropic Liquid Crystals ..91

2.3.5 Analysis on the Structural Changes of the Liquid Crystal Substrates Cultured with Cells 96

2.3.6 Viscoelasticity and Viscosity of the Time-Dependent Liquid crystals In-Situ 102

2.3.7 The Young's Modulus of Liquid Crystals Determined by Using AFM Nano-Indentation 107

2.3.8 The Young's Modulus of the Liquid Crystals Determined by Spherical Indentation 109

2.3.9 Effects of Incubation Time to the Young's Modulus of the Liquid Crystals 113

2.3.10 Poisson's Ratio of the Liquid Crystals 114

2.4 Summary 121

3 BIOPHYSICAL INTERACTIONS OF CELLS AND LIQUID CRYSTALS 122

3.1 Introduction 123

3.2 Material and Methods 124

3.2.1 The Cell Viability Studies 124

3.2.2 Treatment with Cytochalasin B and EDTA-Trypsin 125

3.2.3 Fluorescence Staining of Cytoskeleton, Vinculin and Integrins 127

3.2.4 Immunoperoxidase Staining of Laminin 128

3.2.5 Immunoperoxidase Staining of Collagen Type IV 129
3.2.6 Immunofluorescence Staining of Fibronectin 130
3.2.7 Fluorescence Microscopy 130
3.2.8 Widefield Surface Plasmon Imaging of Cell-Liquid Crystals Interface 131
3.2.9 Statistical Analysis 133
3.3 Results and Discussion 134
3.3.1 Affinity of Liquid Crystals to Cells 134
3.3.2 Effects of Cytochalasin-B, Trypsin and Ethanol to the Cells Adhesion on the Liquid Crystal Substrate 136
3.3.3 Structure of F-actin and Vinculins 139
3.3.4 Expressions of Integrin α2, α3, α5, β1 and the Associated Extracellular Matrix Proteins 144
3.3.5 Interface Patterns of Cell Adhesion 150
3.4 Summary 152
4 QUANTIFICATION, MODELLING, MEASUREMENT AND MAPPING OF CELL TRACTION FORCES ON THE LIQUID CRYSTAL BASED CELL TRACTION FORCE TRANSDUCER 154
4.1 Introduction 155
4.2 Material and Methods 156
4.2.1 Quantification of Cell Traction Force (CTF) 156
4.2.2 Implementation of a 3D Finite Element Model for Focal Adhesion-Liquid Crystal 159
4.2.3 Development of a Cell Traction Force Measurement and Mapping (CTFM) Software 162

4.2.4 Determining the Spatial Resolution of CTFM Software 167
4.2.5 Statistical Analysis 167
4.3 Results and Discussion 168
4.3.1 Cell Relaxation and Calculation of Cell Traction Force 168
4.3.2 Determining the Cell Force-Deformation Relationship of the Liquid Crystals 170
4.3.3 Comparison with Previous Cell Traction Force Measurement Techniques 172
4.3.4 Finite Element Simulations of Focal Adhesion-Liquid Crystal Model 174
4.3.5 The Cell Traction Force Measurement and Mapping Software 180
4.3.6 Spatial Resolution of the Cell Force Measurement and Mapping Software 187
4.3.7 Analysis of the Traction Force Distribution of Quiescent Keratinocytes. 190
4.3.8 A Study on the Traction Force Distribution of a Migrating Keratinocyte 193
4.3.9 Comparison with Previous Cell Force Sensors Developed for the Study of Cell Migration 201
4.3.10 Advantages of Liquid Crystal Based Cell Traction Force Transducer 202
4.4 Summary 204
5 EVALUATION OF LIQUID CRYSTAL BASED CELL TRACTION FORCE TRANSDUCER . 206
5.1 Introduction 207
5.2 Material and Methods 208
5.2.1 Treatment of Cells with Different Concentrations of TGF-β1 208
5.2.2 Quantifying Contraction Responses of Cells to TGF-β1 209
5.2.3 Statistical Analysis 209

5.3 Results and Discussion 210

5.3.1 Differential Traction Forces of Cells Treated with Various Doses of TGF- β1 210

5.3.2 Reliability of the Liquid Crystal Based Cell Traction Force Transducer ... 217

5.4 Summary 220

6 GENERAL CONCLUSIONS, THESIS CONTRIBUTION AND FUTURE WORK 221

6.1 Conclusions 222

6.2 Thesis Contribution 229

6.3 Suggestions for Future Work 232

6.3.1 Physical Property Enhancement and Software Development 232

6.3.2 Cell Biological Applications 233

7 REFERENCES 234

8 APPENDIX A: MATLAB CODES FOR THE CTFM SOFTWARE 252

LIST OF FIGURES

Figure 1.1. (a) A schematic diagram of epidermis and dermis (Alberts et al., 2002). (b) A photomicrograph of histological section for an epidermis. (Source: courtesy of School of Life Sciences, University of Bradford). 7

Figure 1.2. A schematic diagram of cellular adhesion. 9

Figure 1.3. Structure of basal lamina and connective tissue 13

Figure 1.4. The structure of actin cytoskeleton, focal adhesion complexes, integrin receptors, and adhesion proteins. 15

Figure 1.5. Assembly of globular proteins into long chain of actin filaments in helical structure 16

Figure 1.6. The mechanism of actin filaments contraction in bi-directions. 18

Figure 1.7. Sarcomeric appearance of the actin filament (Peterson et al., 2004). (Scale bar: 2 μm) 18

Figure 1.8. A schematic showing the sub-components of the lamellipodia and filopodia: (a) tip of lamellipodium, (b) actin meshwork, (c) region of major disassembly, (d) tip of filopodium, (e) bundle, and (f) undegraded filament which contributes to the cytoplasmic network (Small et al., 2002). 19

Figure 1.9. Activation of actin filaments by Rho, Rac and Cdc42 20

Figure 1.10. The intracellular signaling pathway of TGF-β. 21

Figure 1.11. Seven experimental techniques used in probing mechanical response of a cell. (a) Atomic force microscopy (b) magnetic twisting cytometry, (c) micropipette aspiration, (d) optical trapping, (e) shear flow, (f) soft substrate stretching (Bao and Suresh, 2003) and quartz crystal (Marx et al., 2005). 23

Figure 1.12. Cells force sensor based on silicon rubber. Wrinkling patterns produced by (a) a chicken heart fibroblast (Harris et al., 1980). (Scale bar: 50 μm), and (b) fish Keratocyte on improved silicon rubber sheet (Burton et al., 1999). (Scale bar: 10 μm) 25

Figure 1.13. The structure of a typical polymer with macromolecules that are cross-linked by covalent chemical bonds. 26

Figure 1.14. Embedded marker based method. (a) A fish keratocyte cultured on the silicon sheet with embedded latex beads (Oliver and Pharr, 1992), and (b) a fibroblast migrating on the polyacrylamide (PAA) gel with fluorescence beads (Munevar et al., 2001). The arrows show the direction of the migration. 28

Figure 1.15. Patterned PDMS and silicon nano wires used for measurements of cell traction force. (a) A mouse 3T3 (Tan et al., 2003), and (b) a Madin-Darby Canine Kidney (MDCK) epithelial cell shearing the micro-pillars of PDMS (Roure et al., 2005). (c) A mechanocyte bending silicon nanowires, and (d) a close up view of the cell-wire contacts (Li et al., 2009). 29

Figure 1.16. Distortion created by a rat cardiac fibroblast on a micro-patterned silicon elastomer. (a) A cardiac fibroblast contracting on the surface of the elastomer substrate and (b) after relaxation with 2,3-butanedione monoxime (BDM). BDM is an inhibitor of the cytoskeleton (Balaban et al., 2001). (Scale bar: 10 μm) 30

Figure 1.17. G' and G'' of (a) cured PDMS and (b) PDMS solution published in (Lin et al., 2009) and (Ghannam and Esmail, 1998a) respectively. 33

Figure 1.18. A liquid crystal molecule of 5CB 35

Figure 1.19. A lyotropic liquid crystal molecule (Priestley et al., 1974) 37

Figure 1.20. The typical phases of lyotropic liquid crystals. The figure illustrates the relationship between the amphiphile compositions at various temperatures producing a very dilute surfactant solution (W), aqueous surfactant solution (L_1), micellar cubic phase (I_1), hexagonal phase (H_1), bi-continuous cubic phase (V_1) and Lamellar phase (L_α). (Fairhurst et al., 1998) 38

Figure 1.21. Melting points of MBBA 40

Figure 1.22. Three main mesophases of liquid crystals 40

Figure 1.23. (a) Uniform and (b) Schlieren patterns of a nematic liquid crystal. (Scale bar: 50 μm) 41

Figure 1.24. The orientation and distribution (order S) of mesogens. 42

Figure 1.25. A photomicrograph of Cholesteric 'oily-streaks' or Grandjean texture at room temperature. (Scale bar: 50 μm) 43

Figure 1.26. Smectic A phase of the smectic liquid crystals (Dierking, 2003). 44

Figure 1.27. Components of liquid crystal curvature. (a) Splay (b) Twist and (c) Bend (Frank, 1958). 46

Figure 1.28. Process of developing a hybrid Liquid Crystal based Cell Traction.....55

Figure 2.1. Chemical structure of the (a) cholesteryl chloride, (b) cholesteryl oleyl carbonate and (c) cholesteryl perlagonate.....59

Figure 2.2. (a) The solid mixtures of cholesteryl ester liquid crystals in vials, (b) the mixtures melted at melting temperature (112 ^{o}C), and (c) Cholesteryl ester liquid crystals gel at room temperature (25 ^{o}C). Labels of P1, P2 and P2 on the vials represent CELCP1, CECLP2 and CELCP3, respectively. 59

Figure 2.3. (a) A Zeiss AxioPlan2 digital microscope, and (b) Thermal analysis under a DSC Q2000 system. 60

Figure 2.4. Liquid crystal substrates in the (a) absence (CELCP2) and (b) presence of RPMI-1640 cell culture media (LLC). 61

Figure 2.5. Samples of CELCP2, LLC24hours, LLC48hours, and LLC72hours (a) before, and (b) after incubation in cell culture media for 24, 48 and 72 hours at 37 ^{o}C. 62

Figure 2.6. (a) A MCR501 rheometer and (b) LC sample under test. 63

Figure 2.7. Deposition of cell suspension on a liquid crystal substrate before an addition of RPMI-1640 media. 65

Figure 2.8. A bath of 2 % Formaldehyde in HBSS containing cell cultured on the liquid crystal substrate. 66

Figure 2.9. (a) AFM nano-indentation of cholesteryl ester liquid crystal after incubation in cell culture media at 37 ^{o}C for 24 hours. (b) Schematic diagrams depicting the loading and unloading of an indenter and the associated displacement parameters. The parameter, r denotes the radius of a tip. 68

Figure 2.10. A typical load-displacement curve with the associated indentation depth and load parameters. 69

Figure 2.11. (a) A steel ball of 500 µm diameter loaded to the liquid crystal surface in the cell culture media captured with a digital camera (Scale bar: 1 mm); Insert: The phase contrast image of a steel ball. (b) A schematic describing the spherical indentation to surface of the liquid crystal substrate in the cell culture media and the measurement parameters. 71

Figure 2.12. Uni-axial tensile strain of a gel sample at (a) initial state and (b) after strain in traverse direction, x. 74

Figure 2.13. A schematic diagram of a custom-built uni-axial micro-tensile stretch system. 75

Figure 2.14. (a) The actual setup of a micro-tensile system for measuring Poisson's ratio of cholesteryl ester liquid crystals, and (b) an image showing the temperature of a sample maintained at ~37 ^{o}C. 75

Figure 2.15. (a) Cross-polarising micrographs of nematic liquid crystals TL205 and CELCP1-P3 examined at (a-d) 20 ^{o}C and (e-h) 37 ^{o}C, respectively. (Scale bar: 50 μm) 80

Figure 2.16. (a) Cross-polarising micrographs of CELCP1-P3 sandwiched between a two cover slips examined at 20 ^{o}C. (b) CELCP1-P3 sandwiched between two cover slips. This image was taken with a black background. (Scale bar: 50 μm) 80

Figure 2.17. DSC profiles for the three compositions of cholesteryl liquid crystals CELCP1, CELCP2 and CELCP3. No exothermic or endothermic activities were observed at 37 ^{o}C. T_g denotes glass transition temperature. T_m denotes melting temperature. 81

Figure 2.18. The texture of cholesteryl ester liquid crystals CELCP2. (Scale bar: 50 μm) 82

Figure 2.19. (a-b) Cross-polarised micrograph show a similar liquid crystal membrane drifting off the bulk cholesteric liquid crystal or the defective lyotropic liquid crystals. (c) A DIC and (d) a cross-polarised micrographs of the same defect-free liquid crystal film examined in isolation. (Scale bar: 25 μm) . 83

Figure 2.20. A cross-polarising micrograph of cholesteric based lyotropic liquid crystals shows the wide band streaks and focal conic textures. 84

Figure 2.21. The proposed structure for the cholesteryl ester based lyotropic liquid crystals. 85

Figure 2.22. A schematic describing the effect of shear stress to the uni-axially aligned smectic lyotropic liquid crystals. 85

Figure 2.23. Amplitude sweep data showing strain dependent storage modulus (G') and loss modulus (G'') at angular frequencies: (a) $\omega = 10\ s^{-1}$, (b) $\omega = 1\ s^{-1}$, and (c) $\omega = 0.1\ s^{-1}$ for LLC24hours, LLC48hours and LLC72hours, respectively. 87

Figure 2.24. Stress-strain curves of CELCP2, LLC24hours, LLC48hours and LLC72hours from 0.1 % up to a strain of (a) 100 % and (b) 10 % at $\omega = 0.1\ s^{-1}$. The linear regression lines were used to approximate the linear viscoelastic range of the liquid crystals. 90

Figure 2.25. Simple shear of the liquid crystals. Left: Top view, Right: Cross-section. . 91

Figure 2.26. The frequency sweep results. (a) Shear rate dependent storage modulus (G', square), loss modulus (G'', triangle) and complex viscosity (η*, circle) of the CELCP2 (Yellow), LLC24hours (Green), LLC48hours (Red) and LLC72hours (Blue) obtained for angular frequencies from 0.01 s^{-1} to 100 s^{-1} at 5 % strain. (b) The bar charges of storage and loss moduli obtained at ω = 0.01 s^{-1}. The scatter plot shows the complex viscosity (η*) of CELCP2, LLC24hours, LLC48hours and LLC72hours. The asterisks (*) indicate that the storage modulus, loss modulus and complex viscosity for LLC72hours are significantly different from the CELCP2 (significant for $p < 0.05$, Tukey HSD test, N = 3). 93

Figure 2.27. (a-d) Phase contrast micrographs of the cells cultured on the liquid crystal substrates, and (e-f) cells adhering to a membrane drifting off the bulk liquid crystals. Enlarge exert of (a) shows the short deformation lines radiating out of the periphery of a cell. (Scale bar: 20 μm) 98

Figure 2.28. HaCaT cells cultured on LC surface in response to 30 μM cytochalasin-B treatment and direction of LC deformation lines shrinkage at (a) 0 minute, (b) 30 minutes, and (c) 60 minutes. Solid line arrows show the direction of the cell contraction and relaxation after treated with cytochalasin-B. Dotted line arrows show the repelling directions of the deformation line. (d) A depiction showing the correlation of the deformation line formed on the liquid crystal film with transverse shear forces induced by the contractions of cell circumferential actin filaments that are anchored at the focal adhesions. Treatment with cytochalasin-B caused F-actin depolymerisation, force degeneration and diminishing deformation lines of the liquid crystal surface. (Scale bar: 25μm) 99

Figure 2.29. (a) Phase contrast and (b) cross-polarising micrographs of deformation lines induced by HaCaT cells in the LC surface. The profile plots for the cross-section of a deformation line as shown and marked in (a) and (b). (Scale bar: 25 μm) 100

Figure 2.30. Phase contrast micrographs showing the effect of 30 μM cytochalasin B on HaCaT cells cultured over the lyotropic liquid crystals after 24, 48 and 72 hours of incubation taken every 5 minutes over a period of 60 minutes. The time shown is the period of treatment of cells in cytochalasin-B. (Scale bar: 25 μm) 103

Figure 2.31. (a) Time series images taken every 24 hours up to 96 hours for HaCaT cells treated in 2 % formaldehyde. The arrows in (a) show the deformation lines that were monitored for their changes of length; (b) Length of deformation lines measured (mean ± SD, N = 28, 3 repeats) after cells treated in formaldehyde for 24, 48, 72 and 96 hours. The arrows show the example of deformation lines used for quantification. (Scale bar: 25μm) 105

Figure 2.32. A load-displacement curve of the liquid crystals surface and the relations to the loading and unloading of an indenter. 108

Figure 2.33. (a) Cross-polarised micrographs show the elastic recovery of deformed liquid crystals (0 - 15 seconds) after a steel ball was being unloaded. The inset shows the steel ball with a diameter of 500 μm before unloading. (Scale bar: 50μm) (b) A graph of vertical displacement (δ) versus loading time for N = 3 shows the creep deformation of the liquid crystals. 110

Figure 2.34. Phase contrast micrographs show the behaviors of the lyotropic liquid crystals after a steel ball was unloaded. They were incubated at 37^{o}C for (a) 24, (b) 48 and 72 hours, respectively 113

Figure 2.35. (a) Uni-axial deformation of a solid PDMS. The bi-headed arrows show the deformation in longitudinal direction (y) of PDMS at 380 μm, 276 μm, 220 μm, 192 μm and 178 μm that are corresponding to the deformation in transverse direction (x) at 10, 20, 30, 40 and 50 μm, respectively (image from left to right). The first image from the left shows the measurement for x_o and y_o. (Scale bar: 50 μm) (b) Plots of logarithmic longitudinal strain (ε_2) versus transverse strain (ε_1) or the Poisson's ratio of PDMS at room temperature (25 ^{o}C) in three repeat of experiments (N = 10 per experiment). 116

Figure 2.36. Uni-axial deformation of CELC. The bi-headed arrows show deformation in longitudinal direction (y) of LLC at 490 μm, 260 μm, 190 μm and 90 μm that are corresponding to the transverse deformation (x) at 50, 100, 150 and 200 μm, respectively (image from left to right). The first image from the left shows the measurement for x_o and y_o. (Scale bar: 200 μm) 117

Figure 2.37. Plots of logarithmic longitudinal strain (ε_2) versus transverse strain (ε_1) or the Poisson's ratios for CELC and LLC up to (a) log ε_1 = 0.2 (60 % of strain) and (b) log ε_1 = 0.8 (600 % of strain) determined at 25 ^{o}C. The data are expressed as means ± SD. 118

Figure 2.38. (a) Plots of logarithmic longitudinal strain (ε_2) versus transverse strain (ε_1) or CELC and LLC incubated at 37 ^{o}C for 24, 48 and 72 hours. The data are expressed as means ± SD. (b) A comparison of Poisson's ratio (mean ± SD) for CELC and LLC at room (25 ^{o}C) and incubation temperature (37 ^{o}C). . 119

Figure 3.1. Preparation of liquid crystal samples in 15 wells (left, middle). Cell suspensions cultured in the presence of four liquid crystals (CELCP1, CELCP2, CELCP3 and TL205) and controls in 15 well cultures (right). 125

Figure 3.2. A cell relaxation technique implemented by applying Cytochalasin-B and trypsin to cells cultured on liquid crystal substrates (LCS) in petri dishes. Ethanol was used as a control. 126

Figure 3.3. A Nikon Eclipse 80i immunofluorescence microscope system. 131

Figure 3.4. Cell culture in the absence (left) and presence (right) of liquid crystals on gold substrate. 132

Figure 3.5. (a) A Wide Field Surface Plasmon microscope and (b) the setup for imaging fixed cells. The red circle in the image shows the location of the gold substrate holder and the oil immersion lens in the setup. 133

Figure 3.6. HaCaT cells cultured on (a) CELCP1, (b) CELCP2, (c) CELCP3, and (d) TL205 at a cell density of approximately 1200 cells/cm^2 (Scale bar: 25 μm).....135

Figure 3.7. Percentage of HaCaT cell viability (mean ± SE) in cholesteric and nematic liquid crystals relative to control. 136

Figure 3.8. Phase contrast micrographs for the treatment effects of (a) 0.0042 % (v/v) ethanol (control), (b) 30 μM cytochalasin B, and (c) 0.25 % trypsin to the cells taken every 5 minutes over a period of 60 minutes. The area of cell attachment in μm^2 are as outlined in the micrographs. (Scale bar: 25 μm) 137

Figure 3.9. Phase contrast micrographs show the interface of HaCaT cells attached to (a) a plain glass and (b) a liquid crystal substrates. Immunofluorescence micrographs of the staining against (c, d) F-actin, and (e, f) vinculin, respectively. (Scale bar: 25 μm) (Enlarge exert, scale bar: 1 μm) 141

Figure 3.10. A comparison of (a) vinculin width ($p = 0.383$), length ($p = 0$), and (b) cell surface area ($p = 0$) of HaCaT cells attached to plain glass cover slips and liquid crystal substrates. The area of cells, length and width of vinculin are expressed as mean ± standard error which is significant for $P < 0.001$, $N = 258$ (cell surface area) and $N = 525$ (vinculin). 142

Figure 3.11. Micrographs of immunocytochemical staining against α2, α3, α5 and β1 for (a, d, g, j) negative controls, HaCaT cells cultured on (b, e, h, k) glass cover slips and (c, f, i, l) liquid crystal substrates, respectively. (Scale bar: 25 μm).....145

Figure 3.12. Micrographs of immuno-staining against collagen type IV, laminin and fibronectin for (a, d, g) negative controls, HaCaT cells cultured on (b, e, f), controls and (c, f, i) liquid crystal substrates, respectively. (Scale bar: 20 μm). (Enlarged exert, scale bar: 25 μm). 146

Figure 3.13. Immunoperoxidase staining of laminin for HaCaT cells cultured on a negative control (left), control (middle) and liquid crystal substrate (right). 147

Figure 3.14. A propose model for the interaction of cell membrane and cholesteryl ester based lyotropic liquid crystals. 149

Figure 3.15. WSPR micrographs show the patterns of cells adhesion on the (a) hard cover slip, (b) soft liquid crystals and (c-d) their associated 3D structures displayed in ImageJ software, respectively. (Scale bar: 10 μm).....152

Figure 4.1. (a) Schematic diagram showing lateral view of a cell inducing deformations in the liquid crystal surface due to the contractions of circumferential actin filaments exerting traction force via the focal adhesions. (b) The dimensions of a stress site in LC surface which was loaded (dotted line) and unloaded (solid line) by compressive force (F) applied to the focal adhesion area or stress plane (A). 157

Figure 4.2. (a) Parametrical geometry of the focal adhesion-liquid crystal model. L_{fa}, H_{fa}, W_{fa}, L_{lc}, H_{lc}, and W_{lc} are the length, height and width of the focal adhesion (denoted as fa) and the liquid crystal substrate (denoted as lc), respectively. (b) Schematic diagram of a stress site in the LC surface which is under uni-axial compressive force (F) loaded by two clusters of focal adhesion to the two stress planes. Bottom: the associated tensor diagram in three dimensions. The plane stresses, σ_{xx} cause shear stress of τ_{xz} and τ_{xy} in the y and z directions. 160

Figure 4.3. Flow chart of the cell traction force measurement algorithm 164

Figure 4.4. Flow chart of the cell traction force mapping and rendering algorithm. .166

Figure 4.5. (a) The treatment effects of 30 μM cytochalasin-B in phase contrast micrographs taken at 0 and 30 minutes for a cell cultured on the surface of the liquid crystals. (Scale bar: 10 μm) (b) Enlarge exerts for the deformation lines are as shown and labelled in the boxes of (a). The inward and outward arrows show the directions of force application and degeneration, respectively. (Scale bar: 5 μm).....169

Figure 4.6. (a) The relationship of longitudinal deformation length (y_o) to the transverse displacement. (b) The relationship of traction force (F) to the transverse displacement (Δx). (c) The relationship of traction force (F) to the longitudinal deformation (y_o). The traction force was calculated for ten non-motile keratinocytes (N = 55). 171

Figure 4.7. Normally distributed traction forces ($p = 0.187$, significant for $p > 0.05$) for ten non-motile keratinocytes. N = number of deformation line.....173

Figure 4.8. A mesh containing 10842 triangular elements at a size of 5.7 μm was used in generating the solid mesh for the focal adhesion-liquid crystal model. 175

Figure 4.9. (a) Transverse displacement and stress plotted simulated by Finite Element analysis for the keratinocyte in Figure 4.5. 176

Figure 4.10 The calculation and simulation for the (a) compressive force versus transverse displacement, and (b) stress versus transverse displacement for the cell in Figure 4.5. 177

Figure 4.11. (a) A 3-D topography of a deformation with displacements in the liquid crystals induced by the loads via the contact planes. Inset: The dimensions of the focal adhesions used in the finite element model. (b) Von-mises stresses computed for the compressive loads. 178

Figure 4.12. The distribution of stresses and transverse displacements across a deformation site. 179

Figure 4.13. The GUI of the cell force measurement and mapping software. 180

Figure 4.14. Defining the start and points for calibrating the scale of the image. 181

Figure 4.15. Entering the image scale (20 μm) in the pop-up window.....181

Figure 4.16. Use of mouse to define a deformation line and displays of the calculated force values. 183

Figure 4.17. The display of traction forces and the average traction force of a cell. ..183

Figure 4.18. A display of force data points (z) over the x and y Euclidean coordinate system. 184

Figure 4.19. The fitting of force data curves by using (a) linear and (b) cubic interpolations. 185

Figure 4.20. 2D cell traction force maps which were fitted with (a) linear and (b) cubic interpolations. 186

Figure 4.21. Spatial resolution of a liquid crystal based cell traction force transducer. (Enlarged exert, scale bar: 5 μm) 187

Figure 4.22. Phase contrast micrographs of PDMS calibration gauges consisting of line patterns with an interval of (a) 3 μm and (b) 5 μm. 188

Figure 4.23. The resolution of CTFM software in resolving forces separated by a distance of (a) 3 μm and (b) 5 μm. x and y are the Euclidean coordinates and z is the axis for the traction force in the unit of nano-Newton. The scale bar in pseudo colours represents the magnitude of forces. 189

Figure 4.24. (a) A single HaCaT cell contracting on the LC traction force transducer and (b) the force distribution rendered by CTFM system. The arrows indicate the region of protrusion. 190

Figure 4.25. (a) Two adjacent HaCaT cells contracting on the LC force transducer, and (b) the force distribution generated by CTFM software. 191

Figure 4.26. (a) A polarised HaCaT contracting on the LC traction force transducer, and (b) the force distribution generated by CTFM software. 191

Figure 4.27. Time base tractions of a keratinocyte on a LCTFT shown in (a) phase contrast micrographs taken at 0, 5, 10 and 15 minutes of monitoring. The broken line arrow indicates the direction of movement and the dotted lines are the position of reference for the cell. (b) The associated distribution of traction forces. (c) The directions of forces as shown with thick arrows and the thin arrows represent the direction of the actin bundles, respectively. The scale bar in pseudo color represents the magnitude of forces. (Scale bar: 20 μm) 195

Figure 4.28. Time response curves of the traction force measured at different regions of a single keratinocyte as shown in Figure 4.27. 196

Figure 4.29. (a) Circumferential actin filaments and (b) vinculins located at the lamella of the keratinocytes cultured on LC substrate. The arrow heads indicate the short actin bundles and focal adhesions located at the circumference of the keratinocytes in (a) and (b), respectively. (Scale bar: 25 μm) 198

Figure 4.30. A new model proposed for the contraction of circumferential and straight actin bundles of a migrating keratinocyte in relation to the deformation lines form in the liquid crystals. 198

Figure 5.1. Phase contrast micrographs of HaCaT cells contracting on the surface of the liquid crystals in (a) a control and in the treatments with single dose TGF-β1 at (b) 5 ng/ml, (c) 10 ng/ml, and 20 ng/ml at 37 ^{o}C for 24 hours. (Scale bar: 20 μm) 211

Figure 5.2. Average traction forces (mean ± SE) of HaCaT cells in a control (0 ng/ml) and after treated with of single dose TGF-β1 at 5 ng/ml, 10 ng/ml and 20 ng/ml at 37 ^{o}C for 24 hours in three repeats of experiments (N = 100 cells per experiment). 212

Figure 5.3 The distribution of traction forces for HaCaT cells in the (a) control and after treated with different concentrations of single dose TGF-β1 at (b) 5 ng/ml, (c) 10 ng/ml, and 20 ng/ml for 24 hours at 37 ^{o}C in three repeats of experiment (N = 100 per experiment). 213

Figure 5.4. Percentage (Mean ± SD) of HaCaT cells responded in contractions to various concentration of single dose exogenous TGF-β1 at 37 ^{o}C in three repeats of experiment (N = 100 cells per experiment). 215

Figure 5.5. Traction forces (means ± SE) of HaCaT cells cultured on three isolated liquid crystal substrates (LCS) that were treated with TGF-β1 at 0, 5, 10 and 20 ng/ml in three repeats of experiment (N = 100 cells per experiment), respectively. Mann-Whitney post hoc tests indicate that the treatments between 0 and 5 ng/ml ($p = 0$), 5 and 10 ng/ml ($p = 0$), 10 and 20 ng/ml ($p = 0.008$) are significantly different for $p < 0.05$ in One-way ANOVA analysis. The asterisk * indicates that there is a significant difference in between treatments. 219

LIST OF TABLES

Table 1.1. Associated ligands receptor identified for human keratinocytes migration. 16

Table 1.2. Comparison of cell force measurement techniques 31

Table 1.3. Applications of the liquid crystals as biosensors.....48

Table 2.1. Shear Sensitive Liquid Crystals in different formulations. 58

Table 2.2. Test of normality for storage modulus and loss modulus of the CELCP2 which is significant for $p > 0.05$. Each sample of CELCP2 was tested 3 times. 92

Table 2.3. Comparison of Young's modulus of cholesteryl ester based lyotropic liquid crystals (after 24 hours of incubation) determine by using AFM based nano-indentation and spherical indentation.....111

Table 4.1. Properties of liquid crystals and dimension of vinculin 160

Table 4.2. Comparison of other epithelial cell force measurement techniques 174

Table 5.1. Mean ranks for traction forces of HaCaT cells treated with HBSS (control) and with different doses of TGF-β1 obtained from Kruskal-wallis test. N represents the number of cells. 218

LIST OF ABBREVIATIONS AND SYMBOLS

η^*	Complex viscosity
2D	Two dimensional
3D	Three dimensional
5CB	4’-n-pentyl-4-cyanobiphenyl
AEC	3-Amino-9-ethylcarbazole
AFM	Atomic force microscopy
ANOVA	Analysis of variance
ATP	Adenosine triphosphate
CdS	Cadmium selenide
CELC	Cholesteryl ester liquid crystals
CLC	Cholesteric liquid crystal
CMC	Critical micelle concentration
CTF	Cell traction force
CTFM	Cell traction force measurement and mapping software
DAPI	4'6-diamidino-2-phenylindole-2HCl
DIC	Differential Interference contrast microscopy
DMSO	Dimethyl sulfoxide
DSC	Differential scanning calorimeter
E	Elastic modulus
ECM	Extracellular matrix
EDTA	Ethylene diamine tetra acetic acid
F	Force

FA	Focal adhesions
FC	Focal contacts
FCS	Fetal calf serum
FDA	Food and drug administration
FEM	Finite element method
FITC	Fluorescence isothiocyanate
G’	Storage modulus
G”	Loss modulus
GAG	Glycosaminoglycan
GPa	Giga pascal
GTP	Guanosine triphosphate
GUI	Graphical user interface
HaCaT	Human keratinocyte cell line
HBSS	Hank’s balanced salt solution
HCEC	Human colonic epithelial cell line
IgG	Immunoglobulin
IND	Investigational new drug
kPa	Kilo pascal
LCs	Liquid crystals
LCS	Liquid crystal substrate
LCTFT	Liquid crystal cell traction force transducer
LLC	Cholesteryl based lyotropic liquid crystals
MBBA	N-(4-Methoxybenzylidene)-4-butylaniline
MDCK	Madin darby canine kidney

MPa	Mega pascal
n	Director
η^*	Complex viscosity
nN	Nano newton
PAA	Polyacrylamide
PDLC	Polymer dispersed liquid crystals
PDMS	Polydimethylsiloxane
PEGA	A thermolysinpolyethylene glycol acrylamide
pN	Pico newton
POM	Polarising optical microscope
RPMI	Roswell park memorial institute medium
R-Smads	Receptor activated-drosophila gene mothers against dpp
SD	Standard deviation
SE	Standard error
SPSS	Statistical package for social sciences
SSLC	Shear sensitive liquid crystal
TGF-β	Transforming growth factor beta
TGFβRI	Type I receptor of transforming growth factor beta
TGFβRII	Type II receptor of transforming growth factor beta
v	Poisson's ratio
v/v	Volume/volume
WSPR	Widefield surface plasmon resonance

CHAPTER 1

INTRODUCTION

"This journey of a thousand miles begins with a single step"-Lao Tzu

1.1 Research Background

Pharmacology is an experimental science which involves studying the effects of chemically active molecules on physiological activity. As one of the cornerstones in new drug development, pharmacology investigates the effects of new drugs through screening for desired activity, determining the mode of actions and defining the drug therapeutic function. Pharmacological studies involving animals in biological assays started as early as the 19th century (Fastier and Reid, 1949). Mammals such as rats, guinea pigs, rabbits and dogs are the most commonly used experimental subjects. In pre-clinical testing, organs or tissues are excised surgically and prepared for pharmacological study in oxygenated physiological solution within an organ bath. The organ bath technique was first applied by Henrick Magnus in 1904 on a strip of small intestine (Fastier and Reid, 1949). Today, the organ bath is still being used extensively to investigate the physiology and pharmacology of various tissues such as muscle, arterial rings, uterine tissue, ileum, colon arterial and diaphragm. In an organ bath, a section of tissue is suspended between a fixed point and an isotonic or isometric force transducer in a pre-warmed Krebs solution (Bennett and Pettigrew, 1974). Rhythmic contraction and relaxation of the tissue creates variable load forces which the force transducer converts into electrical signals (Bennett and Pettigrew, 1974). In modern systems, the electrical signals are digitised and displayed on a computer monitor as traces of contractility. Stimulation of the tissue can be induced by chemical, electrical or physical means. The range of sensitivity in terms of force transduction of commercial systems is from 50 µN to 250 mN (ADINSTRUMENT Incorporation and DMT Incorporation).

New developments in the agricultural and pharmaceutical industries require stringent evaluation and assessment of compounds before clinical trials. Prudent pre-

clinical trials usually involve large numbers of rodent and non-rodent mammalian species (Ganter et al., 2005, Jacobson-Kram and Mills, 2008). Recently, the United States Food and Drug Administration (FDA) issued a guide on Exploratory Investigational New Drug (IND) to reduce animal exploitation and simultaneously to accelerate the development of new pharmaceutical agents (Jacobson-Kram and Mills, 2008). Similarly, a new directive concerning cosmetic products (2000/0077(COD)) aims at reducing animal testing by promoting the design of in-vitro toxicological assays. Thus, cell line based culture assays are attracting interest as an alternative for drug and cosmetic testing. However, to enable this highly sensitive and high throughput screening, accurate analytical techniques for sensing cellular activities are required. During pre-clinical testing, application of an agonist and an antagonist to a tissue in an organ bath induces contraction and relaxation of a tissue, which is measured in terms of force. The question is how did the drug trigger the action of the tissue? This analysis in a tissue constructed from many different cells types is difficult (for example, the same section of tissue may contain neurons, smooth muscle cells and fibroblasts), thus, the characterisation of cell physiological responses may provide more insights if determined by examining the contractile properties of the individual cells (Bitar and Makhlouf, 1985, Li et al., 2009, Ma et al., 2002).

Motivated by the need to assess single cell contraction induced by chemical stimuli, contractility assays measuring the change in average cell length of a large population of smooth muscle cells were developed to study the responses of smooth muscle to agonists such as endothelin-1, interleukin, C-terminal octapeptide of cholecystokinin, acetylcholine and methoionine-enkephalin (Bitar and Makhlouf, 1985, Moummi and Woodford, 1992, Dallot et al., 2003, Akiho et al., 2002). These studies identified a number of advantages of single cell based biological assays for the

pharmaceutical industry such as: (a) the easy characterisation of surface receptors as a consequent of drug action, and (b) highly repeatable screening (Dallot et al., 2003, Akiho et al., 2002).

Thereafter, many single cell based biosensors have been developed for use in pharmacological screening (Stenger et al., 2001, Park and Shuler, 2003). In a cell based biosensor system, the cell is the primary detector which converts the molecular signals into electrophysiological or mechanical signals; these signals are then transduced by a secondary transducer in the form of electrode, magnetic or optical detector. Overall, the techniques in measuring physiological responses of single living cells to analytes can be classified into two broad categories: electrophysiology and mechanobiological measurement systems. Each category has its own advantages and disadvantages.

Electrophysiological techniques originated from neuroscience, in which, systems were developed to study the electrical activity of nerves cells (Hodgkin and Keynes, 1955, Hodgkin, 1937, Gross et al., 1972). These systems have since been employed to study other electrogenic cells such as smooth muscle and cardiac myocytes (Thomas, 1972, Hara et al., 1986, Cranefield and Hoffman, 1958). These techniques involve the use of electrodes to sense the depolarisation or hyperpolarisation of action potential of cells attaching to the electrodes (Gross et al., 1972). Patch clamp (Kraft and Patt, 2006, Betz. W. J. and Sakmann, 1971), potassium chloride filled glass electrode (Dole, 1941) and planar patch clamp (Behrends and Fertig, 2007) technique are among the classical electrophysiology techniques developed to monitor the activities of individual ionic channels in the cell membrane. In these systems, the recording can be intracellular or extracellular in a cell culture. Unfortunately, these techniques are time consuming and because of their invasive nature, they often result in cell death. One of the alternatives is monitoring cell electrophysiology using micro-fabricated

extracellular electrode recording or microelectrode array systems (Kovacs, 2003, Fromherz, 2003). These systems rely on culturing electrogenic cells over miniaturised recording sites made of gold or indium-tin-oxide, or arrays of field effect transistor electrodes to monitor signals from those cells directly position over the recording sites (Fromherz, 2003, Kovacs, 2003, Thomas et al., 1972, Gross et al., 1977, Offenhausser et al., 1997). These systems have been used to generate dose response curves for known pharmacological agents (Yu et al., 2006) but are subject to limitations associated with sensitivity and reliability (Muthuswamy et al., 2005, Shoham et al., 2006)

In the measurement systems using microelectrode, the electrodes allow recording of electrical activity at single point of the cell membrane or tissue but this does not provide information about the spatial distribution of bioelectric activity over the cell membrane (Loew, 1996). To circumvent this issue, an optical electrophysiology technique has been developed which involves the use of potential-sensitive dyes or fluorescing proteins that are capable of changing the fluorescence intensity when these probes detected sub-millisecond membrane potential changes or intrinsic birefringence (Obaid et al., 2004, Cohen and Salzeberg, 1978, Loew, 1996). The potential-dependent characteristic is able to shift the excitation spectra, and thus allowing the quantification of membrane potential (Waggnoner, 1979, Cohen and Salzeberg, 1978). After the tissue or cell is perfused or injected with the potential sensitive dye, two-dimensional (2D) distribution of colour intensity along the cell membrane corresponding to the field potential can be visualised and recorded. Some dyes developed earlier such as cyanine dyes are believed to inhibit the metabolic activity or inducing photodynamic damage due to the strong illumination of these dyes (Waggnoner, 1979, Obaid et al., 2004). Therefore, the potentiometric dyes developed later (Potential-sensitive ANEP dyes, Invitrogen) aim to overcome these problems.

These dyes improved the signal to noise ratio and reducing dye internalisation (absorption into the nucleus). However, these dyes still needed to be solubilised in dimethyl sulfoxide (DMSO) and are limited by moderate phototoxicity (Obaid et al., 2004). Phototoxicity increases oxygen radicals in cell cultures and can be cytotoxic in the long term (Obaid et al., 2004).

Electrophysiological measurements are more suitable for electrogenic cells that fire large action potentials. Monitoring the physiological changes of epithelial cells is more related to the measurement of cell mechanical activity in terms of forces (for example, contraction or traction forces). Traction forces are defined as forces that a cell exerts tangentially on a substrate (Oliver et al., 1998). They are the indications of the contractile forces generated within the cell cytoskeletons. Studies on how the contraction forces are generated and transmitted by a single cell as traction forces to the adjacent cell and extracellular matrix (ECM) set the foundation for the development of cell traction force (CTF) measurement technique.

1.2 Cellular Adhesion, Contraction and the Measurements of Cell Traction Force

1.2.1 Epidermal Tissue

The skin is made up of three major layers, the epidermis, dermis and hypodermis (Gawkrodger, 2003). The epidermis forms the outermost layer of skin and is constructed from four layers known as the basal, spinous, granular and cornified layer (Figure 1.1). The epidermis protects the underlying tissues of skin from abrasion and contains four major cell types (keratinocytes, melanocytes, langerhans cells and

merkels cells) (Gawkrodger, 2003). Of these cells, the keratinocytes make up about 90 % of the epidermis (Rocchad and Barrodon, 2009).

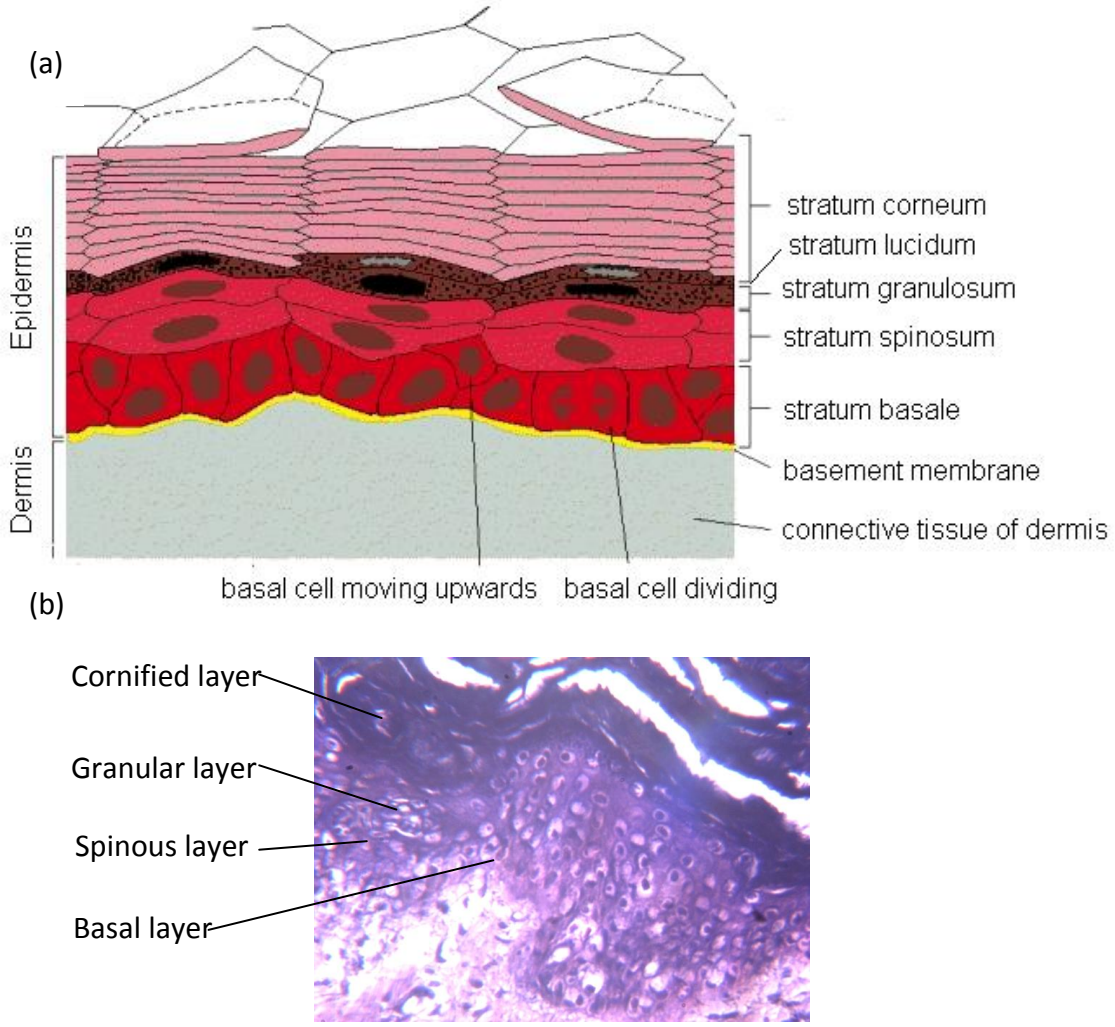

Figure 1.1. (a) A schematic diagram of epidermis and dermis (Alberts et al., 2002). (b) A photomicrograph of histological section for an epidermis. (Source: courtesy of School of Life Sciences, University of Bradford).

By division of keratinocyte stem cells at the basal layer, new epidermal cells (keratinocytes) are formed at the spinous layer (stratum spinosum) and further division continues to form the granular layer (stratum granulosum) (Hendriks, 2005). The presence of lipids in the stratum granulosum creates a hydrophobic barrier between the stratum granulosum and the stratum lucidum that prevents dehydration (Feingold, 2007). As the keratinocytes translocate superficially, the cells increase their

keratin content to protect the skin and underlying tissue from environmental damage such as ultra violet light and dehydration. Newly produced keratinocytes gradually differentiate and move upwards to replenish the overlying cells of the stratum lucidum (Gawkrodger, 2003). This process of terminal differentiation and migration continues until the cells die and become enucleated cells in the protective stratum corneum or cornified layer (Feingold, 2007).

Even though protected by the stratum corneum, the skin is delicate and can be wounded when being exposed to abrasion of sharp objects. However, under small levels of compression or shear on the skin surface, the tissue is elastic and can return to its original state upon release of applied stress. The elasticity and integrity of the skin is due to the structural organisation and strong traction forces between cells, and also, between cells and the extracellular matrix (Silver et al., 2003).

1.2.2 Cellular Adhesion

The contact which leads to the binding of a cell to a surface, another cell or the extracellular matrix is known as cellular adhesion (Dzamba et al., 2001). Cell adhesion is mediated by cell junctions (Vasioukhin et al., 2000). Cell junctions are divided into two broad classes, the intercellular junctions and the extracellular junctions. Intercellular junctions (Figure 1.2) are those that link cells to other cells such as the tight, gap, adherens and desmosomal junctions (Vasioukhin et al., 2000, Farquhar and Palade, 1963). Multiple adhesion molecules (for example, hemidesmosome and focal adhesions) are found in extracellular junctions and they function to attach cells to the extracellular matrix (ECM) (Farquhar and Palade, 1963).

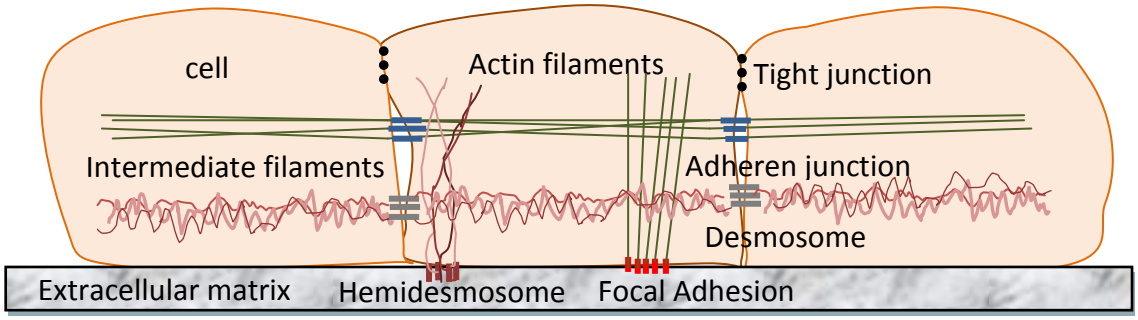

Figure 1.2. A schematic diagram of cellular adhesion.

Tight junctions (Figure 1.2) are formed from membrane proteins such as the claudins, occludins and e-cadherin that strongly couple the adjacent cell membranes (Schneeberger and Lynch, 1992, Furuse et al., 1998, Farquhar and Palade, 1963). As their names implies, molecules cannot pass through the sealed junctions, thus, allowing them to form a selective barrier. For example, it is this selective barrier in the endothelial cells that gives rise to the blood brain barrier (Wolburg et al., 1994).

Gap junctions are formed from membrane spanning proteins called the connexions. Gap junctions are continuous channels between two plasma membranes. These channels allow intercellular cytoplasmic communication and provide for cell-to-cell diffusion of small molecules, including ions, amino acids, nucleotides, and second messengers (Lampea and Laub, 2004). Gap junctions allow the propagations of action potential between cells (Rohr, 2004). Each gap junctions consists of 6 connexins subunits. These subunits are associated with the connexins of a neighbouring cell membrane, thus, forming channels that passes through the membrane of both cells (Lampea and Laub, 2004). Gap junctions are like valves and can be controlled locally. They are found between cardiac myocytes and smooth muscle cells that enable a coordinated contraction mediated by direct cell-cell impulse transmission (Lampea and Laub, 2004, Rohr, 2004).

Desmosome and hemidesmosome (Figure 1.2) are directly connected to the intermediate filaments at the extracellular junctions (Vasioukhin et al., 2000). Desmosomes link the intermediate filaments of a cell to the adjacent cell via calcium-dependent adhesion molecules or specialised cadherins called desmogleins and desmocollins (Gumbiner, 1996, Farquhar and Palade, 1963, Vasioukhin et al., 2000). Desmosomes are patch like junctions that are randomly distributed and fill the 30 nm gap between the attachment membranes (Green and Jones, 1996). Hemidesmosomes have a different function which is to connect the intermediate filaments of a cell to the ECM (Dzamba et al., 2001). They can be found in muscle cells or in stratified epithelial cells.

As shown in Figure 1.2, two extracellular junctions that are closely associated with the actin cytoskeleton are the adherens junctions and focal adhesions (Farquhar and Palade, 1963). Adherens junctions or Zonula adherens are complex proteins found at the sites of cell-cell adhesion (Farquhar and Palade, 1963). At the adherens junctions, the calcium dependent transmembrane proteins (E-cadherin) mediate cell to cell attachment (Vasioukhin et al., 2000). E-cadherins binds β-catenin which in turn binds α-catenin that link the actin cytoskeleton to the adherens junctions (Krendel et al., 1999). Focal adhesions are large macromolecules, comprise of a sub-membrane plaque which is made up of at least 50 different proteins and they mechanically bind the cell membrane to the ECM via specific transmembrane receptors (Matthews et al., 2006). Both the adheren junctions and focal adhesions connect to the actin filaments of the cytoskeleton and it is these actin filaments that exert traction forces on neighbouring cells and ECM (Burridge et al., 1986, Geiger and Ginsber, 1991).

In the epidermal layer, the ECM forms a complex meshwork which is produced and secreted by cells into their surrounding medium (filling between cells) (Buck and

Horwitz, 1987). In the connective tissue, fibroblasts mainly produce macromolecules in the ECM matrix. These macromolecules are formed from heavily glycosylated proteins giving rise to hydrogel like materials (such as, glycosaminoglycan (GAG) and proteolycans) which contain various fibrous proteins (O'Toole, 2001). Fibrous proteins embedded in the polysaccharides gel (Hay, 1981) are made up of two functional groups, the structural (collagen and elastin) and adhesive proteins (fibronectin and laminin) (O'Toole, 2001, Gray et al., 2000). Structural proteins help to organise the matrix and provide resilience (Hay, 1981, Hook et al., 1984). For example, the GAG and proteolycan gels withstand compressive forces or tension applied to the ECM while allowing the diffusion of nutrients and hormones between the blood and the cells (Hook et al., 1984). The adhesive proteins including collagen facilitate cell attachment to the ECM (Geiger et al., 2001). For example, laminin is associated with the attachment of epithelial cells to basal lamina, and fibronectin enables the attachment of fibroblasts and mast cells in the connective tissue (Kirfel and Herzog, 2004, O'Toole, 2001).

In the connective tissue of the dermis (Figure 1.3), collagen is the most abundant fibrous protein. This protein is characterised by long, stiff and triple-stranded helical structure of three single-polypeptide chains (or α chain) (Rich and Crick, 1955, Rest and Garrone, 1991). The single α-chain is constructed from many proline and glycine molecules (amino acids) (Rich and Crick, 1955, Rest and Garrone, 1991). About 28 types of α-chain molecules have been identified, including type I, II, III, V and XI collagen (Rest and Garrone, 1991, Heino, 2007). Type I is the principal collagen molecules that constituted the collagen fibres in tissue (Rest and Garrone, 1991). Type IV collagen molecules are network-forming collagen fibres that made up the meshwork

of the basal lamina, while type VII collagen binds the basal lamina to the underlying connective tissue (Heino, 2007).

Elastin is another structural protein and like collagen fibres are embedded in the ECM of skin, blood vessels and lungs (Hay, 1981). The network of elastin fibres exhibit elastic behaviour and they give tissues their elastic properties (Gotte and Serafini-Fracassini, 1963). The collagen fibrils are interwoven with the elastin fibres in order to prevent the tissue from over-stretching and tearing (Cleary and Gibson, 1983). The collagen fibres provide tensile strength while elastin fibres support tissue elasticity (Rosenbloom et al., 1993, Hay, 1981).

Fibronectin is an adhesive fibrous protein found in the connective tissue. This protein is a dimer composed of two very large subunits connected by disulfide bonds near the carboxyl terminal (Hynes and Yamada, 1982). Each subunit in the dimer has repeated sequences of what are referred to as type III fibronectin repeats (Hynes and Yamada, 1982). Along the repeating unit, there are binding sites for the heparin, collagen and specific transmembrane receptors found on the surface of the cells membrane (Hynes and Yamada, 1982). Some studies suggest that isoforms of fibronectin produced during wound healing specifically help in guiding cell migration and proliferations for new tissue development (Singer et al., 1999, Bartkova et al., 2003). Therefore, the adhesive function of fibronectin in attaching cells needs to be balanced with the needs of cell migration during wound healing (Larjava et al., 1993).

The basal lamina or basement membrane is formed from ECM proteins and it is especially rich in adhesion proteins (collagen, fibronectin and laminin) that are organised as a thin sheet underlying the epithelial cells. Hence, the basement membrane separates the cells from the connective tissue (Lillie et al., 1988, Larjava et al., 1993). In the epidermis, the basal lamina produced by the epithelial cells is divided

into two layers: lamina lucida overlying the lamina densa (Figure 1.3) (Laurie et al., 1982, Stanley et al., 1982b). The lamina lucida forms a boundary with the epithelial cells overlying the lamina densa (Laurie et al., 1982), whilst the lamina densa is connected to the underlying connective tissue by collagen fibrils (mainly made of type VII collagen molecules) (Laurie et al., 1982, Stanley et al., 1982b). The basal lamina containing the adhesion proteins can influence cells polarity, regulate cell metabolism and induce cells differentiation (Stanley et al., 1982b).

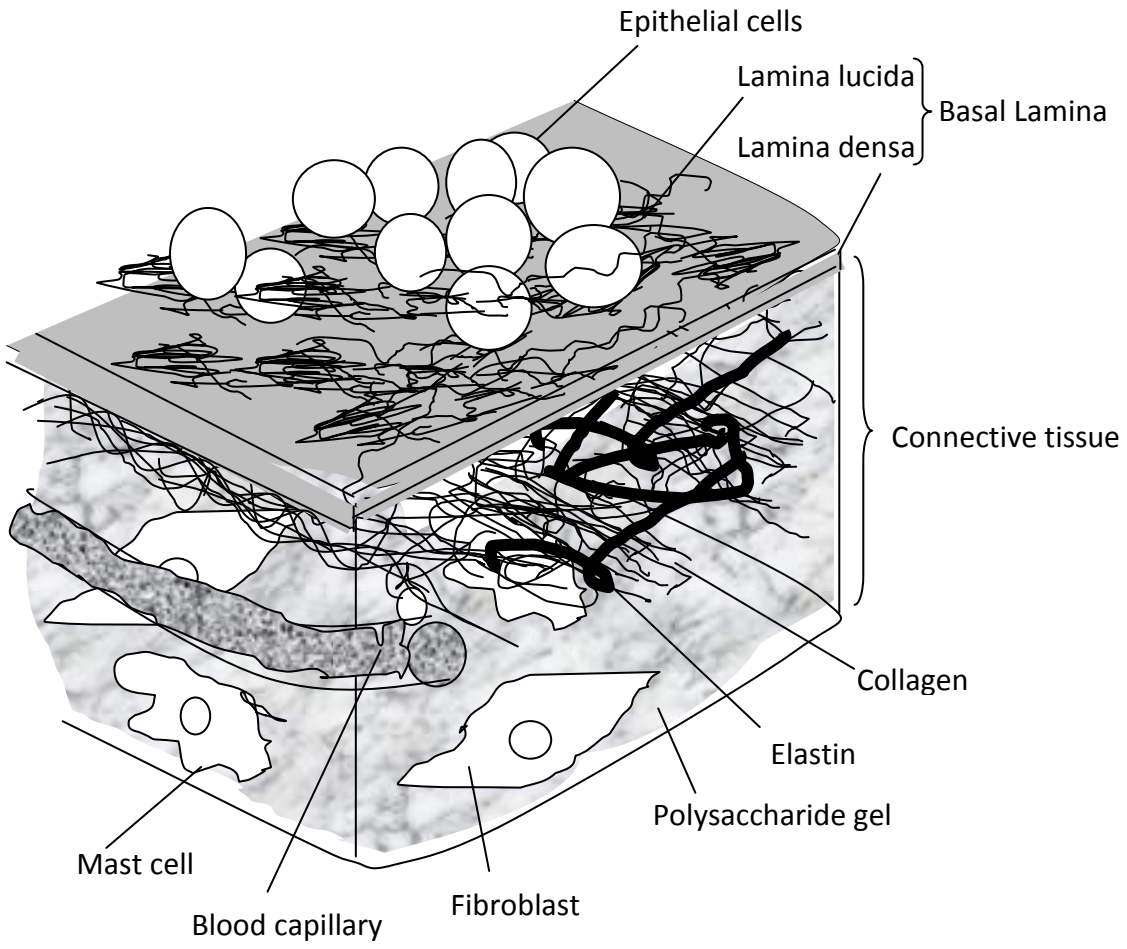

Figure 1.3. Structure of basal lamina and connective tissue

The exact composition of basal lamina varies from tissues to tissue (Pruniéras et al., 1983). A majority of the mature basal lamina consisted of type IV collage, laminin, perlecan, and entactin (Stanley et al., 1982b). During the early synthesis of basal lamina in the development of embryo, the basal lamina does not consist of collagen

type IV molecules but instead consists of a large laminin network (Turkesen et al., 1985, Pöschl et al., 2004). In the absence of collagen, laminin molecules are capable of self-assembling into a sheet in an in-vitro culture (Kirfel and Herzog, 2004, Pruniéras et al., 1983, O'Toole, 2001). Laminin has three polypeptide network that are disulfide bonded and this networks contains binding domains for collagen type IV molecules, entactin, perlecan and cell surface receptors (Beck et al., 1990). In large networks of basal lamina, laminin can directly bridge to the type IV collagen molecules which in turn, associated with type IV collagen, perlecan and entactin (Beck et al., 1990). In terms of the binding domains of laminin to the cells, fragment 1 and 8 of laminin are exposed as the adhesion sites for cell surface receptors (Aumailley et al., 1987).

1.2.3 Integrin Receptors and Focal Adhesion

The function of various types of receptors found on the surface of the cell membrane is to provide adhesion to the ECM proteins (Dzamba et al., 2001). These receptors are transmembrane proteins of a large family known as integrins. Integrins are classified as the heterodimers which are composed of two distinct chains, the α (alpha) and β (beta) subunits (Burridge et al., 1997). In cell-ECM attachment, the specific ligands in the ECM determine the type of α and β subunits of the integrins being expressed by a cell (Geiger and Bershadsky, 2001). Some examples of integrins are as given in Table 1.1. Multiple integrins exist on the cell membrane and they work co-operatively with the cell adhesion proteins in cell-cell and cell-ECM interaction (Hynes, 2002).

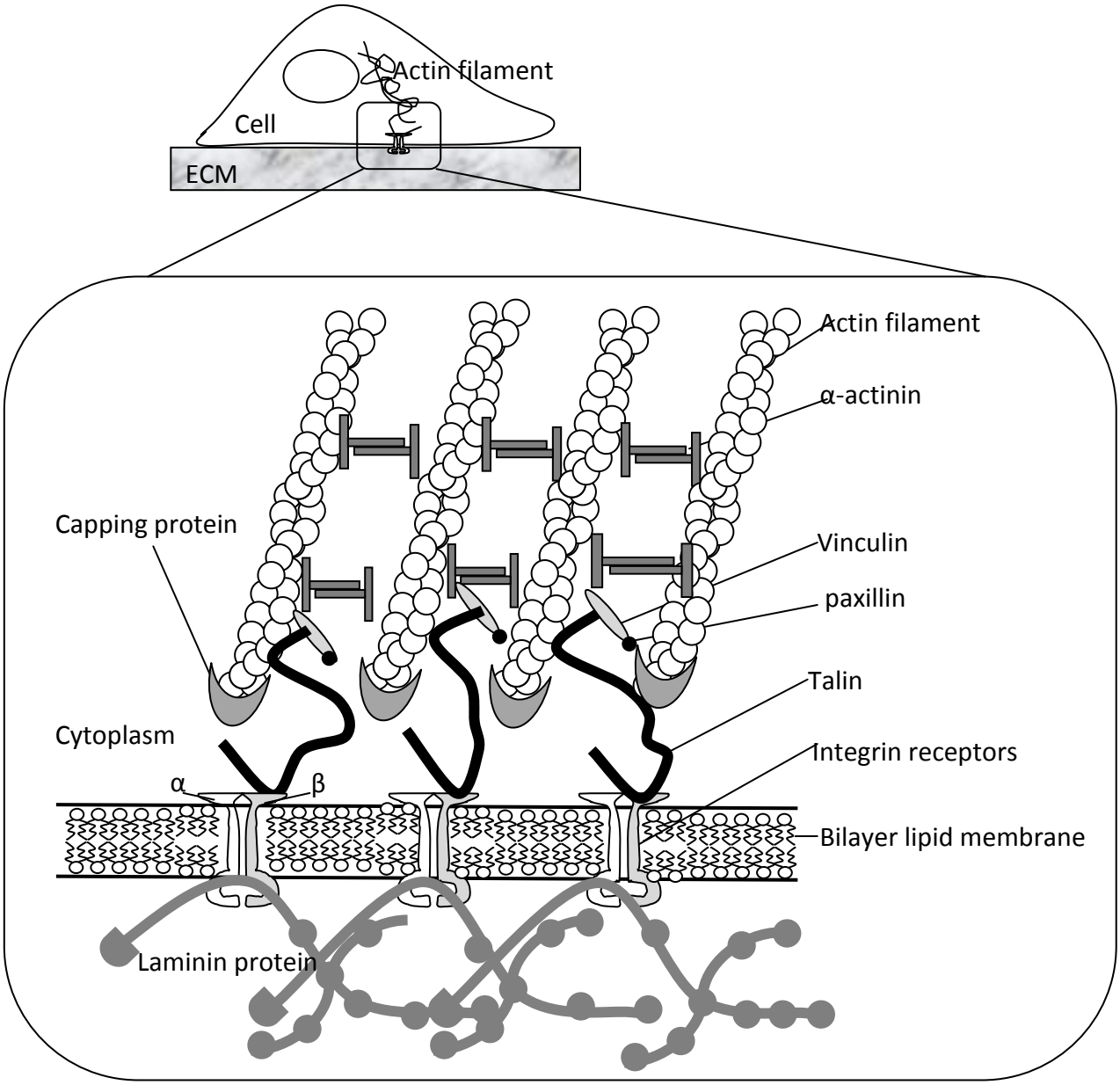

Figure 1.4. The structures of actin cytoskeleton, focal adhesion complexes, integrin receptors, and adhesion proteins.

Integrins have a dual function, that of transducing signals (either biochemical or physical) from the ECM to the cell and also the function of mediating the transmission of forces generated within the cell to the ECM (Geiger and Bershadsky, 2001, Hynes, 2002). Hence, they work as mechanosensors in sensing the stiffness of the ECM (Bershadsky et al., 2003, Rivelinea et al., 2001) whilst functioning as transmembrane messenger which trigger signals in regulating cellular attachment, migration and differentiation (Dzamba et al., 2001, Geiger et al., 2001).

Table 1.1. Associated ligands receptor identified for human keratinocytes migration.

Integrins	Ligands	Reference
α2β1	Type I Collagen	(O'Toole, 2001, Kim et al., 1992)
α2β1, α3β1	Laminin 5	(Decline and Rousselle, 2001, Kainulainen et al., 1998)
α5β1, α3β1	Fibronectin	(O'Toole, 2001, Kirfel and Herzog, 2004)

Focal adhesions (FA) or focal contacts (FC) located within the cell (Figure 1.2) are adhesion plaques which assist the actin cytoskeleton to anchor to the ECM *via* the integrin receptors (Figure 1.4). Focal adhesions consist of a number of proteins such as α-actinin, talin, paxillin and vinculin (Burridge et al., 1997, Geiger and Bershadsky, 2001, Wong, 1999) as seen in Figure 1.4. Among these protein molecules, vinculin is the major protein molecule at the sub-membrane plaque (Schwartz and DeSimone, 2008).

1.2.4 Polymerisation of Actin Filaments and Generation of Traction Force

Actin filaments of the actin cytoskeleton are the main machinery in regulating the contractility of a cell. Actin is a globular protein (Boron and Boulpaep, 2004), however, they can assemble and polymerise in a helical fashion to form filamentous actin double helix (Figure 1.5).

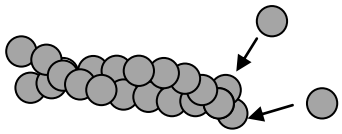

Figure 1.5. Assembly of globular proteins into long chain of actin filaments in helical structure.

The contractility of the non-muscle cells is dependent on the translational interactions between myosin-II and the filamentous actin (F-actin or sub unit of actin filament) (Langanger et al., 1986). Upon stimulation of cell contraction, the

phosphorylation of the F-actin allows the myosin II head to bind and sliding along the adjacent F-actin fibres in opposite directions (Peterson et al., 2004) as shown in Figure 1.6 (a-b). The mechanical actuation and phosphorylation of myosin II heads are driven by harnessing the energy released from adenosine triphosphate (ATP) when it is hydrolysed to ADP, this is regulated by myosin light chain kinase (Tan et al., 1992). This mechanism regulates the stretching and contraction of actin filaments in the longitudinal direction. To gain movements in transverse direction, α-actinin reduces the spacing between the two filaments by drawing bundles of actin filaments closer to each other (Figure 1.6c) (Pellegrin and Mellor, 2007). The collective actions of both myosin II and α-actinin in the actin filaments trigger the formation of stress fibres and cell contractility. With the binding of the actin filaments, FA and integrins receptor to the ECM, this creates a shear force exerted on the ECM, consequently, inducing cell surface traction (Lazarides and Weber, 1974, Pellegrin and Mellor, 2007).

Under 100x magnification of immunofluorescence microscopy, the stress fibres appear in a periodic “sarcomeric” organisation (Figure 1.7) are similar to the myofibrils of muscle (Peterson et al., 2004), in which the sarcomeres observed in non-muscle cells are the repeatable patterns of α-actinin (Pellegrin and Mellor, 2007).

The contractility of actin filaments bundles allows cells to actively re-structure their cell body to accommodate to the stiffness of the surrounding environment. When cells are grown on a glass cover slip, a broadly spread morphology is acquired by cells to sustain their bodies on the stiff substrate. For cells attached to a hard surface, isometric contraction and the parallel arrangement of aligned stress fibres are the dominant features of the cytoskeleton as shown in Figure 1.7 (Peterson et al., 2004).

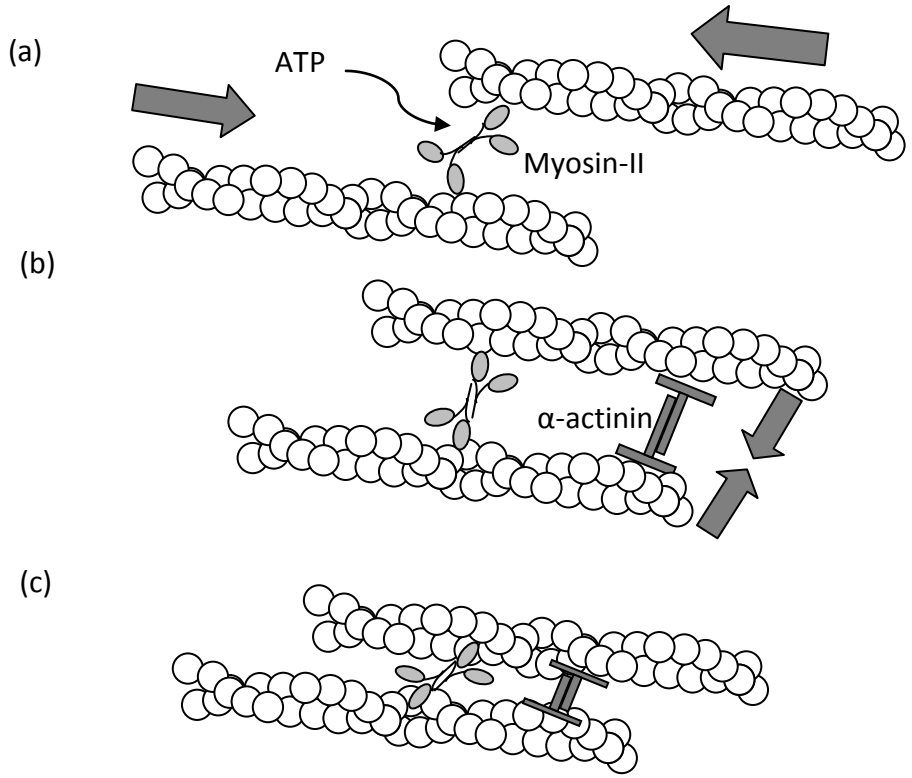

Figure 1.6. The mechanism of actin filaments contraction in bi-directions.

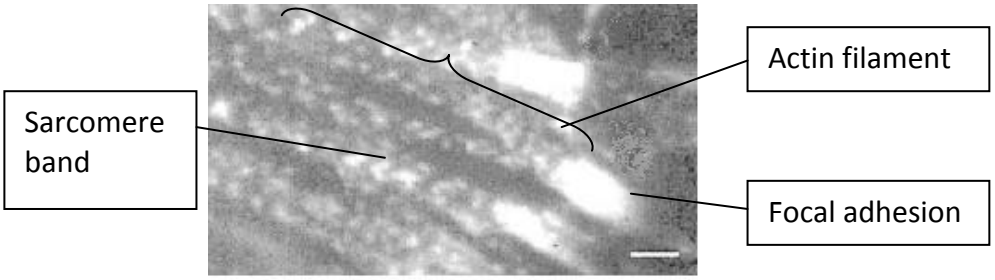

Figure 1.7. Sarcomeric appearance of the actin filament (Peterson et al., 2004). (Scale bar: 2 μm)

Some studies (Sagvolden et al., 1999, Rivelinea et al., 2001) show that cells are very sensitive to their interface tension and this can be seen when tension is applied to a cell membrane (for example, indenting the cell membrane with a microneedle). In this example, the cell rapidly generates stress fibres at that localised region (Rivelinea et al., 2001). In resisting tension, the cell reorganises the network of filaments to adapt to the stress. Consequently, focal adhesions are stimulated and assemble into clusters

in response to the onset of the contractility (Peterson et al., 2004). A higher recruitment of stress fibres increases the size of the focal adhesions, and hence induces higher contractile forces (Goffin et al., 2006). Reversible disassembly of the focal adhesions results in a disruption in the contractility of cells (Burridge and Chrzanowska-Wodnicka, 1996).

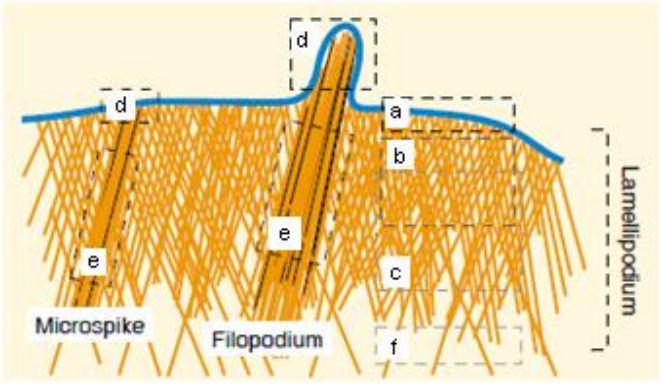

Figure 1.8. A schematic showing the sub-components of the lamellipodia and filopodia: (a) tip of lamellipodium, (b) actin meshwork, (c) region of major disassembly, (d) tip of filopodium, (e) bundle, and (f) undegraded filament which contributes to the cytoplasmic network (Small et al., 2002).

In addition to the functions of contraction, these filament networks are able to protrude and pressurise intracellularly against the cell membrane in the form of lamellipodia and filopodia. Lamellipodia contains quasi two-dimensional actin meshes that extends across and to the edge of the cell membrane (Figure 1.8a-c, f) to make contact with a surface (Small et al., 2002). Beyond the frontier of the lamellipodia, further microscopic protrusion of the membrane exists as microspikes, otherwise known as the filopodia (Figure 1.8d-e).

The assembly and disassembly of the actin filaments and associated integrin receptors are regulated by the GTPase family members (Figure 1.9) such as Rho, Rac, and cdc42 (Hall, 2005, Mackay and Hall, 1998). GTPase is an enzyme which hydrolyses guanosine triphosphate (GTP) that consists of monomeric GTP-binding proteins. These

are specialised molecular proteins that control the transduction pathways within the cell (Hall, 2005, Burridge et al., 1997). Rho triggers the bundling of actin filaments into stress fibres (Figure 1.9) (Mackay and Hall, 1998, Hall, 2005). Activation of Rac leads to the assembly of actin filaments in a meshwork at the periphery of a cell to form lamellipodia and membrane ruffles (Mackay and Hall, 1998). The third member, Cdc42 activates the actin filaments to form filopodia (Figure 1.9) (Mackay and Hall, 1998). There is also cross-talk between the monomeric G-proteins, for example, Rac can activate Rho in fibroblasts (Hall, 1998, Mackay and Hall, 1998). Hence, these signaling pathways control the structural changes that in turn are responsible for cell attachment and migration on the underlying substrate.

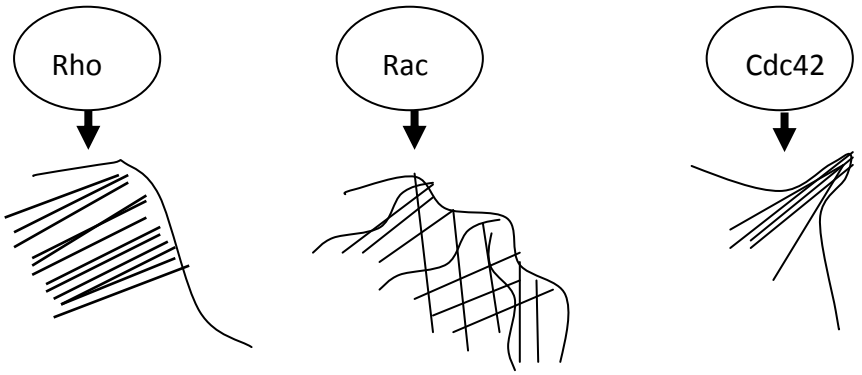

Figure 1.9. Activation of actin filaments by Rho, Rac and Cdc42

During cell migration, G-protein activates the down-stream signaling in order to elicit the formation of stress fibres, which then leads to the regulation of cell contractility. In triggering epithelial cells to change from a static to a migratory phenotype, the messaging could be regulated by cytokines such as Transforming Growth Factor Beta (TGFβ). TGFβ is a multifunctional cytokine which regulates many cellular process in keratinocytes such as the cell differentiation, proliferation and migration (Cross and Mustoe, 2003, Massague and Wotton, 2000). Over the cell membrane surface, TGFβ binds to type II receptor (TGFβRII) which then

phosphorylates type I receptor (TGFβRI) as shown in Figure 1.10. TGFβRI and TGFβRII are both obligate heteromeric transmembrane receptors (Wrana, 1998). The phosphorylation of TGFβRI leads to phosphorylation of Receptor activated-Drosophila gene Mothers against dpp (R-Smads) (as seen in Figure 1.10) with members termed Smad2 and Smad3 that continue to form complexes with Smad4 (Massague and Wotton, 2000). The complex of R-Smad and co-Smads translocates to the nucleus where these transcription factors regulate the target gene and activations of subsequent cellular processes (Massague and Wotton, 2000, O'kane and Ferguson, 1996).

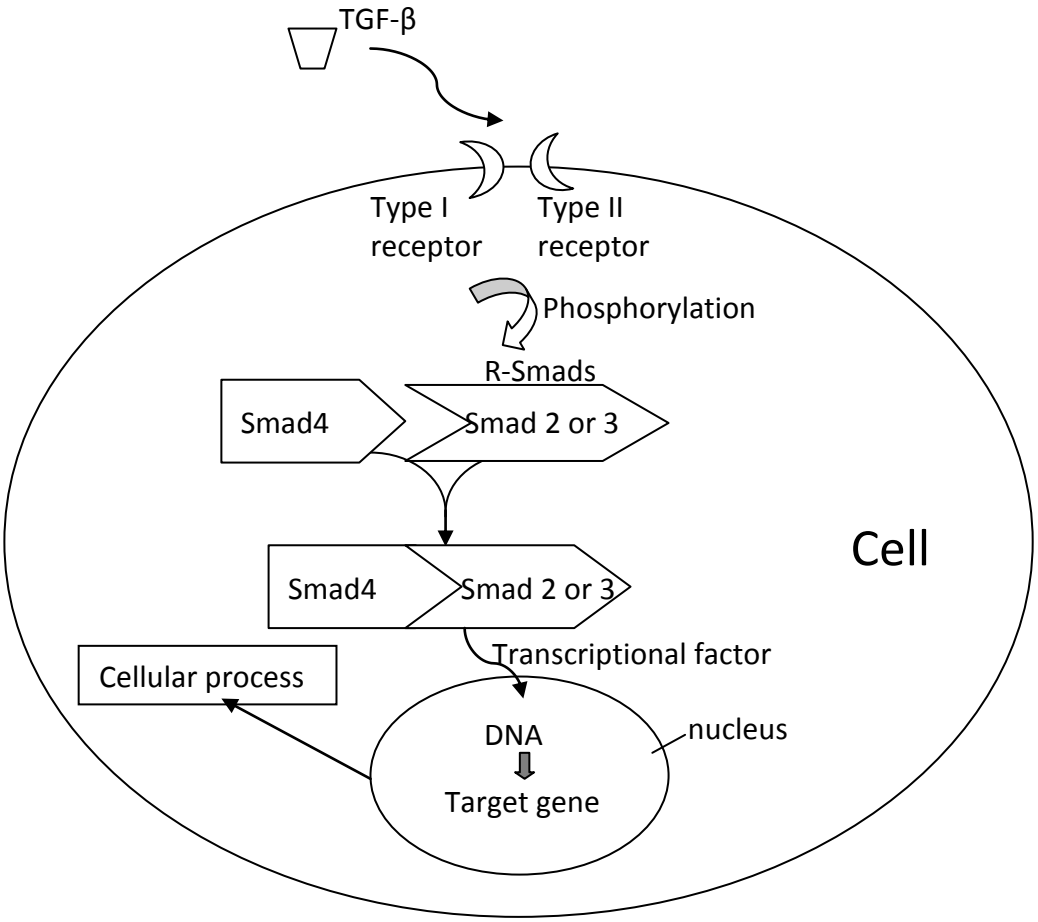

Figure 1.10. The intracellular signaling pathway of TGF-β.

The family of cytokine such as TGF-β1, TGF-β2 and TGF-β3. Particularly, TGF-β1 which is isolated from human platelets, human placenta and bovine kidney is an

attractive cytokine because of the contradicting role of the cytokine in wound therapy and abnormal epidermis formation (for example, scar formation and psoriasis) (Li et al., 2004a, Zhang et al., 2003, Gailit et al., 1994) which is still not clearly understood. However, treatment of keratinocyte in in-vitro cultures with TGF-β1 > 10 ng/ml was reported to promote cell motility, and rapidly increase the Rho activity and β-actin formation (Decline et al., 2003, Coffey et al., 1988, Bhowmick et al., 2001, Shen et al., 2001).

Contractility of cells is the basic causal event which regulates the integrity of tissue (Deugnier et al., 2002, Heida et al., 1996), cytokinesis and morphogenesis (Singer et al., 1999, Horwitz and Parsons, 1999, Kirfel and Herzog, 2004). Due to the importance of the cellular contractility, many polymer based cell traction force measurement techniques have been developed to probe the mechanics and physiological changes that occur in contracting cells (mainly fibroblasts).

Research in mechanobiological measurement systems is expanding fast. Seven methods of probing cells mechanically have been developed as shown in Figure 1.11. These methods are classified as the atomic force microscopy (AFM) nano-indentation, magnetic twisting cytometry, micropipette aspiration, optical trapping, shear flow, soft substrate stretching (Bao and Suresh, 2003) and quartz crystal microbalance systems (Pax et al., 2005, Kang and Muramatsu, 2008). Except for the use of soft substrate techniques, the majority of techniques is either very time consuming or requires considerable investment in expensive equipment, and thus these techniques are not suitable for high throughput drug screening. In comparison, the systems based around soft substrates seem to be the most promising tool for pharmacology application because of their low development cost and potential in high throughput screening.

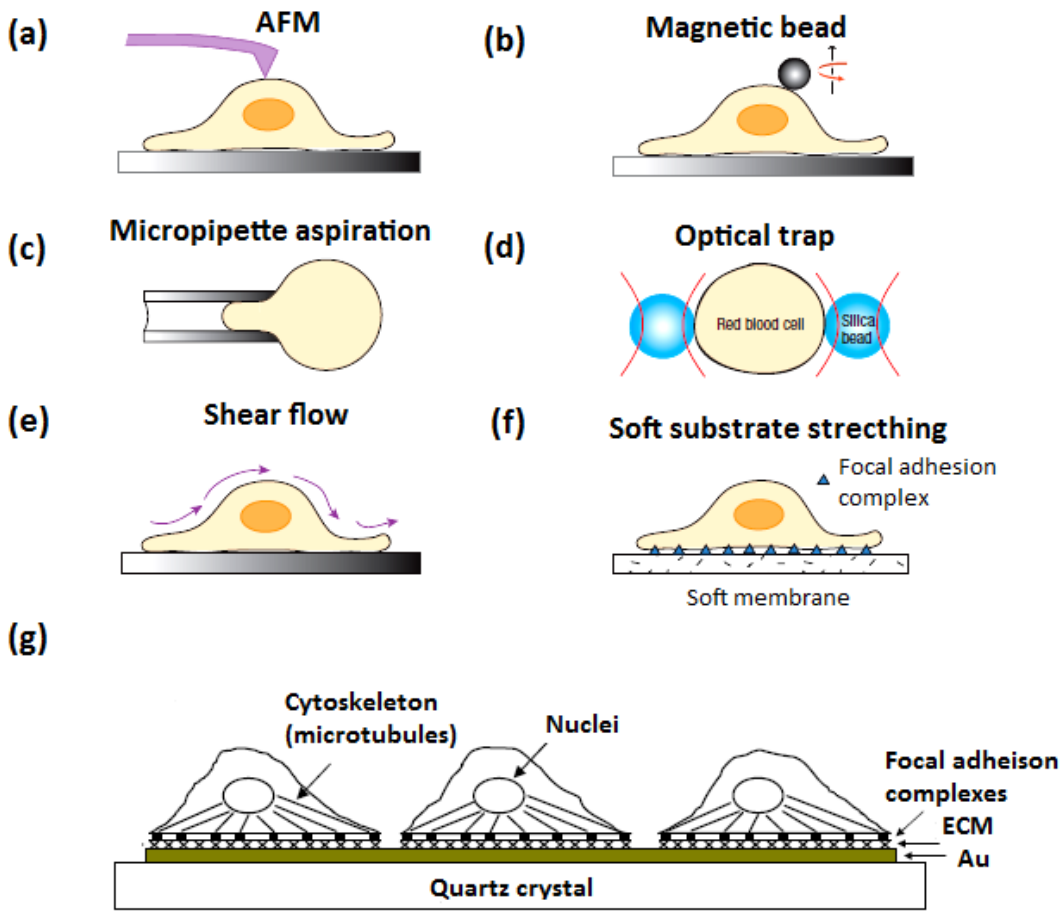

Figure 1.11. Seven experimental techniques used in probing mechanical response of a cell. (a) Atomic force microscopy (b) magnetic twisting cytometry, (c) micropipette aspiration, (d) optical trapping, (e) shear flow, (f) soft substrate stretching (Bao and Suresh, 2003) and quartz crystal (Marx et al., 2005).

The most commonly used soft materials to monitor cell forces are silicone rubber, collagen sheets, polyacrylamide (PAA) and polydimethylsiloxane (PDMS). For example, measuring the shrinkage of a collagen sheet caused by adherent contracting cells is a widely used technique. This type of soft substrate system was applied to assess the effect of Endothelin-1 on smooth muscle cells (Dallot et al., 2003) but it does not provide any information about the contractility characteristic of cells such as morphology changes, force distribution, cell mechanics and traction pattern for single cells. Therefore, more sensitive methods are required to probe the biomechanics of a single cell.

1.2.5 Force Sensor Based on Silicon Sheet

The first use of a thin flexible silicon sheet in monitoring cell traction force can be traced back to the work of (Harris et al., 1980). Buckling effects were observed on a thin sheet of silicon rubber seeded with chicken heart fibroblasts as shown in Figure 1.12a. Although fibroblast induced long lasting wrinkles on the silicone substrate, the most intense indentations did not correlate with the focal contact points (Hinz and Gabbiani, 2003). In order to measure the traction force correlated with the contraction activity of the α-smooth muscle actin, the indentation should be formed at the focal contacts where the anchoring of actin filament heads produce the most abundant stress. Numerous efforts have been made to improve the sensitivity and resolution of this material by increasing the flexibility of the silicon sheet by ultraviolet light treatment (Burton and Taylor, 1997). However, the enhancement on the flexibility of the silicon sheet did not significantly improve the efficiency in measurement (for example, isolation of localised stress) (Figure 1.12b) (Beningo, 2002).

The silicon sheet used for detection of cell forces is based on a continuum. This technique does not limit the cell spreading but allows dispersal of cells focal contacts and distribution of cell traction force in arbitrary directions (Beningo, 2002). However, there are two problems arising from this technique. Firstly, the quantification of forces involves the direct use of a longitudinal deformation line in which, the force was calculated by multiplying the length of the longitudinal deformation line (wrinkle) by the stiffness of the material (Oliver et al., 1995). The stiffness of the silicon substrate used in previous work was determined by measuring the lengths of the wrinkles induced by a calibrated deflection force (Burton et al., 1999).

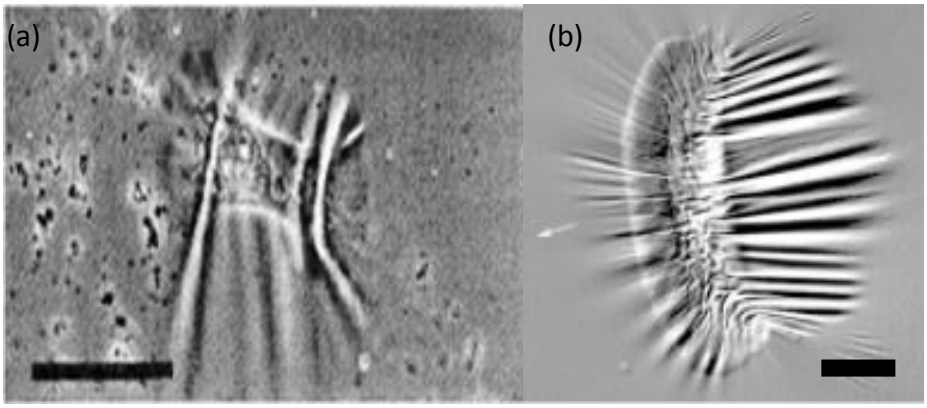

Figure 1.12. Cells force sensor based on silicon rubber. Wrinkling patterns produced by (a) a chicken heart fibroblast (Harris et al., 1980). (Scale bar: 50 μm), and (b) fish Keratocyte on improved silicon rubber sheet (Burton et al., 1999). (Scale bar: 10 μm)

However, it is important to note that, the deformation line in the longitudinal direction is a secondary effect resulted from the transverse strain. The transverse strain was due to the trajectory of transverse shear forces induced via the focal contacts as a result of actin filaments contraction. In this case, the actual strain of the material is not directly related to the longitudinal deformation lines or the wrinkles as seen but it was due to the transverse strain in the perpendicular direction (Beningo, 2002, Oliver et al., 1995). Secondly, the uncorrelated wrinkles formed were related to the molecular structure of a polymer which is highly crossed linked (Figure 1.13). In this context, a polymer is a high-molecular-weight organic compound with many repeating chains of monomers (Boyd, 1993, Ward and Sweeney, 2004). The linking topology of the monomers is not linear as shown in Figure 1.13 (Boyd, 1993, Ferry, 1948). Therefore, any force imposed on a local region of the polymer at low shear rates (slow) will cause the molecules to extend easily (fluid-flow) due to the free-form of the cross linkers. This is a typical viscous behaviour of viscoelastic polymer which is non-recoverable (Ward and Sweeney, 2004). Thus, the surrounding macromolecules of the polymer will flow and pull other molecules in adjacent chains. As a result, the chain-pulling reactions were

observed as propagations of stress or continuous deformation patterns across the surface of the polymer (Lin et al., 2008, Im and Huang, 2005). This explains why it was very difficult to identify isolated regions of compression induced by cells on the surface of a silicon rubber substrate.

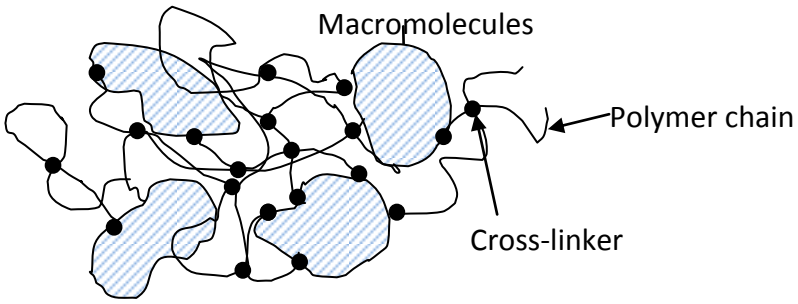

Figure 1.13. The structure of a typical polymer with macromolecules that are cross-linked by covalent chemical bonds.

1.2.6 Force Sensor Based on a Collagen Lattice

Along with the development of silicon rubber based measurement techniques, a technique to measure forces generated by the shrinkage of a cell populated collagen lattice was developed (Eastwood et al., 1996, Delvoye et al., 1991, Roy et al., 1997, Campbell et al., 2003, Freyman et al., 2001, Harley et al., 2007, Karamichos et al., 2006). This in-vitro technique enables the measurement of force induced by large groups of cells especially fibroblasts. The common principle of this technique is the acquisition of collective forces resulting from the contraction of fibroblasts seeded on a thin sheet, in which the deformed thin sheet was connected to an electronic force transducer system (Souren et al., 1989, Campbell et al., 2003). The saturated force measured was then used to estimate the force generated by a single cell. The collagen matrix method has been used to measure the forces generated by a population of fibroblasts up to a maximum force of approximately 350 μN for 2 x 10^6 cells. This enabled a coarse estimate of force generated per cell at about 0.2 nN/cell (Campbell et

al., 2003). Several factors can affect the overall measurement accuracy of this method. A tightly control environment with minimal noise disturbance is required to avoid artifacts especially when the system involves a floating collagen matrix. Also, a very delicate cantilever and strain gauge system are required. As the thickness of the gel affects the sensitivity, the elastic modulus or stiffness of the measurement transducer can be critical and the thickness of the collagen sheet must be well controlled in these systems during the polymerisation process. The density of cells cultured on a matrix must be relatively high in order to exert a force that is great enough to reach the minimum force measurement range of the strain gauge system. Previous studies (Freyman et al., 2001, Campbell et al., 2003) have not been able to show that contraction forces can be measured below a cell count of less than 2×10^6.

1.2.7 Force Sensor Based on Displacements of Markers in Soft Substrates

Polyacrylamide (PAA) sheets provide another soft substrate alternative which is very similar to the silicone sheet. The stiffness of the substrate is controlled by the relative proportions of polyacrylamide and bis-acrylamide mixtures. The material does not support cell adhesion directly and must be functionalised with ECM proteins (Beningo et al., 2002). The advantage of this material is the flexibility can be driven down to a compliance of 500 Pa (Solon et al., 2007, Engler et al., 2004a). Both silicon with embedded latex beads (Figure 1.14a) and PAA with embedded fluorescence markers (Figure 1.14b) were used to trace the changes of strain correlating with the cell movement. However, the primary flaw of this method is having low signal to noise ratio due to the randomly distributed markers and interdependence of bead displacement data due to the propagation of energy throughout the entire surface of the substrates (Addae-Mensah and Wikswo, 2008, Beningo, 2002) (Table 1.2).

Therefore, complicated mathematical functions based on Bayesian, Maximum Likelihood and Monte Carlo methods were used to estimate the source of the energy propagated throughout the substrate (Dembo et al., 1996)

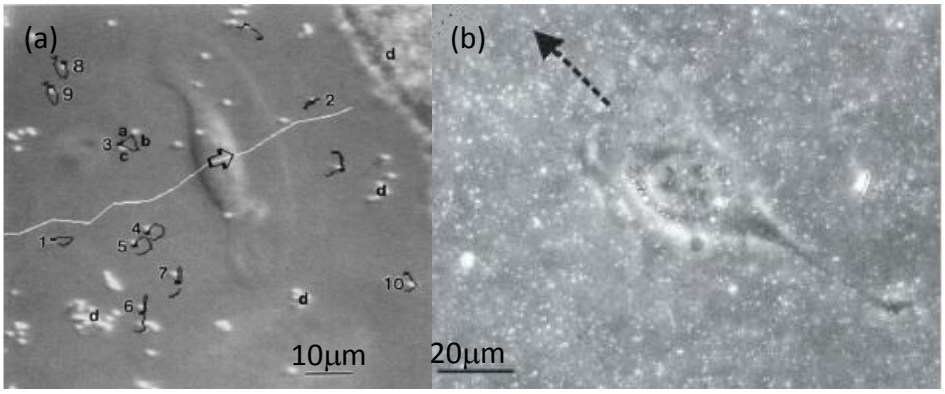

Figure 1.14. Embedded marker based method. (a) A fish keratocyte cultured on the silicon sheet with embedded latex beads (Oliver and Pharr, 1992), and (b) a fibroblast migrating on the polyacrylamide (PAA) gel with fluorescence beads (Munevar et al., 2001). The arrows show the direction of the migration.

1.2.8 Force Sensor Based on Micro-Pillars and Micro-Patterns

With the advent of micro fabrication technology, micro-fabricated polydimethylsiloxane (PDMS) micropillars (Tan et al., 2003, Roure et al., 2005), PDMS micro-patterns (Balaban et al., 2006) and silicon nano wire (Li et al., 2009) as shown in Figure 1.15 were used to measure single cell forces from approximately 50 pN to 150 nN (Roure et al., 2005, Tan et al., 2003). PDMS has the advantages of being flexible, optically transparent, chemically stable and easy for rapid prototyping (Thorslund, 2006). By characterising the physical properties of the micropillars and by the application of non-linear elastic theory, the local forces exerted by cells were calculated from the deflection of pillars in pillar arrays (Tan et al., 2003). In order to overcome the limitation of the spatial resolution in Tan et al.'s work (Tan et al., 2003) which was at 9 μm, the spacing between the pillars was reduced to 2 μm (Roure et al., 2005) (Figure 1.15). However, when the density of the PDMS pillars increase, the PDMS

pillars could easily stuck together or collapse (Hillner and Stefanou, 2004). As observed in (Roure et al., 2005), cells lying on these pillar arrays had limited space to optimally deflect a post. The bending pillars interacted with the neighbouring pillars before reaching the maximum deflection. This problem was corrected by the fabrication of shorter pillars (Ganz et al., 2006) but the cell forces measured by this technique was believed to be associated more with the restructuring of a cell's cytoskeleton to adapt to the high stiffness of PDMS pillars (~ 2 MPa) and hollow space underlying it. Obviously, stress fibres are transiently formed in response to the underlying tension (Hinz and Gabbiani, 2003).

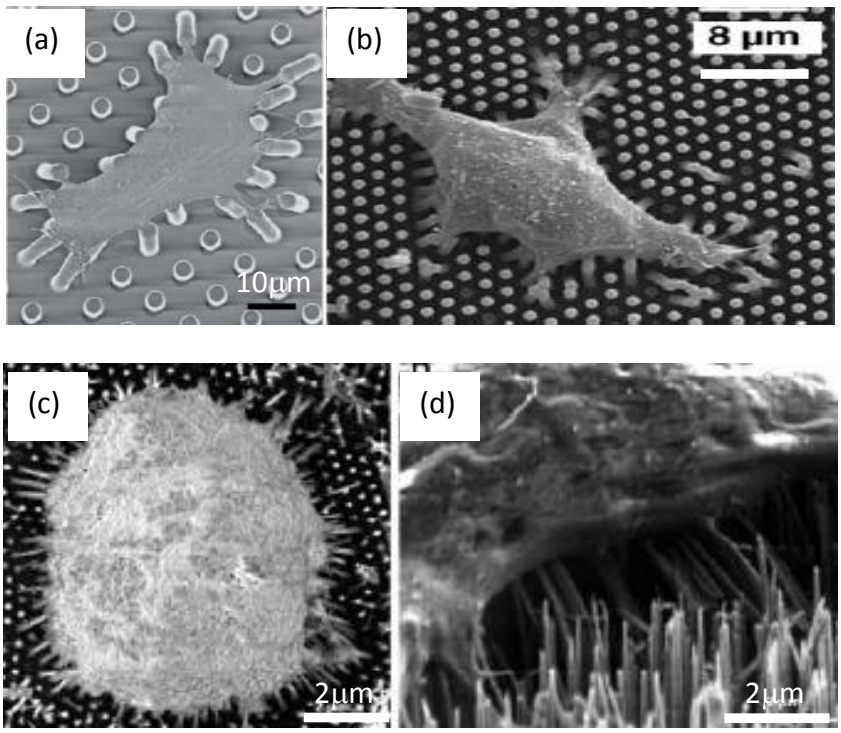

Figure 1.15. Patterned PDMS and silicon nano wires used for measurements of cell traction force. (a) A mouse 3T3 (Tan et al., 2003), and (b) a Madin-Darby Canine Kidney (MDCK) epithelial cell shearing the micro-pillars of PDMS (Roure et al., 2005). (c) A mechanocyte bending silicon nanowires, and (d) a close up view of the cell-wire contacts (Li et al., 2009).

Furthermore, the stiffness of the PDMS used is not close to the in-vivo stiffness. The Young's modulus of cells and soft tissue is between a few Pa to a few hundred kPa

(Levental et al., 2007, Solon et al., 2007), while the Young's modulus of PDMS substrates are in the range of mega Pascal (MPa) to giga Pascal (GPa). These relatively inflexible substrates may be perceived by the cells as pathological tissue (Engler et al., 2004b, Levental et al., 2007). Although one may argue that the Young's modulus of these micropillars can be tuned down, this can then cause difficulty in terms of microfabrication (for example, stickiness) (Hillner and Stefanou, 2004). This is also why PDMS micro-pillars with elastic modulus at kilo Pascal (kPa) range have not been implemented for cell force measurement.

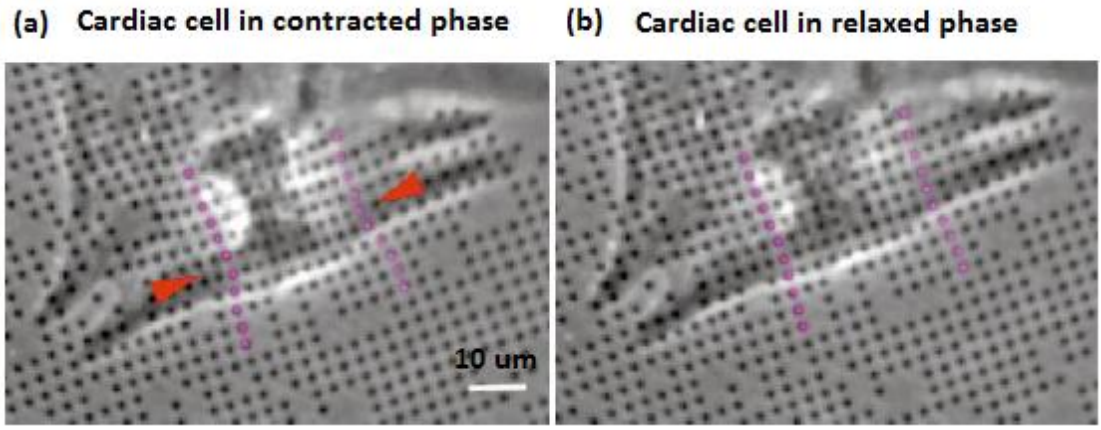

Figure 1.16. Distortion created by a rat cardiac fibroblast on a micro-patterned silicon elastomer. (a) A cardiac fibroblast contracting on the surface of the elastomer substrate and (b) after relaxation with 2,3-butanedione monoxime (BDM). BDM is an inhibitor of the cytoskeleton (Balaban et al., 2001). (Scale bar: 10 μm)

Table 1.2. Comparison of cell force measurement techniques

Method of detection	Method of force quantification	Weakness	Strength	Cell type	Reference
Silicon rubber	• Measure the length of the wrinkles • Magnitude of forces calculated by multiplying the substratum stiffness, 10-30 nN/µm with the length of wrinkles. • Detected force range: 10 - 1200 nN	• Difficult to convert the pattern of wrinkles into a map of traction forces • Complex in isolated regions of compressions.	Simple, effective means for studying compressive forces.	Fibroblast and Fish Keratocytes	(Munevar et al., 2001, Harris et al., 1980, Burton and Taylor, 1997)
Standard silicone film embedded with particles as markers	• Using physical equations (strain) for estimating the direction and magnitude of traction forces for migrating cells. • Compliance 20 nN/µm. • Traction force microscopy using optical flow algorithm. • Detected force range: 19.8 - 46.2 nN.	• Complexity in preparation procedures has limited its development. • Markers are difficult to be discerned at low magnification.	Reliable estimate of traction force.	3T3 Fibroblast	(Oliver et al., 1995)
Micro-patterned silicon substrata in dots or line pattern.	• Measure the deflection of pattern or posts to determine the strain of material in relation to Hooke's law. • Stiffness: 20-50 nN/µm. • Young's modulus: 12kPa-100kPa. • Detected force range: ~20 nN (Fibroblasts), ~70 nN (myocytes).	• Chemically or physically textured surface that might affect cell adhesion and migration through contact guidance mechanism (Britland et al., 1996). • Self-elongation over time.	Allow direct visualisation of strain.	Fibroblast and myocytes	(Balaban et al., 2001)

Cont' Table 1.2 Comparison of cell force measurement techniques

Polyacrylamide sheet	• Embedded with randomly distributed fluorescent beads as markers. • Displacement of marker taken as strain of material. • Young's modulus: ~500 Pa-28 kPa. • Detected cell stress: 3.03 x 10^3± 2.13 x 10^3 Pa.	• Cells do not show affinity for polyacrylamide and required a coating of ECM proteins. • Dependent on depth of surface, image need to be carefully focused for in-plane drift. • Require comparison with a null-force image to obtain full extend of deformation.	• Superior mechanical and optical properties. • Flexibility can be controlled by the concentration of acrylamide and bis-acrylamide.	Fibroblast	(Pelham and Wang, 1997, Beningo, 2002, Munevar et al., 2001)
Patterned PDMS	• Young modulus = 1.7-2.5 MPa. • Detected force range: a few nN - 90 nN.	• Hallow interface that might affect cell adhesion through contact guidance mechanism.	• High spatial resolution. • Extended application to smaller size or weaker contractile forces than smooth muscle cell.	Fibroblast, Madin-Darby canine kidney epithelial, C2 myogenic cells	(Saez et al., 2007, Ganz et al., 2006, Tan et al., 2003, Roure et al., 2005)
Silicon nanowire arrays	• Force derived from the degree of nanowire bending. • Young's modulus = 151 ± 38.3 GPa. • Detect force per cell: 2.25 μN (mechanocyte), 2.75 μN (Hela cell), and 3.5 μN (L929).	• A stiff material as a force transducer. • Limitation in deflection	Allow direct visualisation of strain.	Mechano-cyte, Hela, Benign cell (L929)	(Li, Song et al. 2009)

The micro-patterned PDMS method (Figure 1.16), in which the force is measured based on the strain of the patterns induced by the cell seemed to be the alternative to micro-pillars methods and markers based techniques but the rheological properties of PDMS itself generates some fundamental limitations for use as a cell force sensor. Similar to the silicon rubber or PAA, PDMS is also a viscoelastic polymer which has a structure comparable to the molecular arrangements shown in Figure 1.13. PDMS exhibits a viscous behavior at low shear rates which means that the deformation is non-reversible (non-elastic) under the influence of a slow stress (for example, the deformation induced by a cell). This view is supported by the rheology of PDMS (as shown in Figure 1.17) which shows that PDMS exhibits a viscous behaviour (G" < G') when being sheared at a low shear rate (ω < 10 rad/s) and acquires an elastic behaviour (G' > G") at high shear rates (ω > 10 rad/s) (Boutelier et al., 2008, Ghannam and Esmail, 1998b, Lin et al., 2009). G' and G" are the storage and loss moduli of the material, respectively.

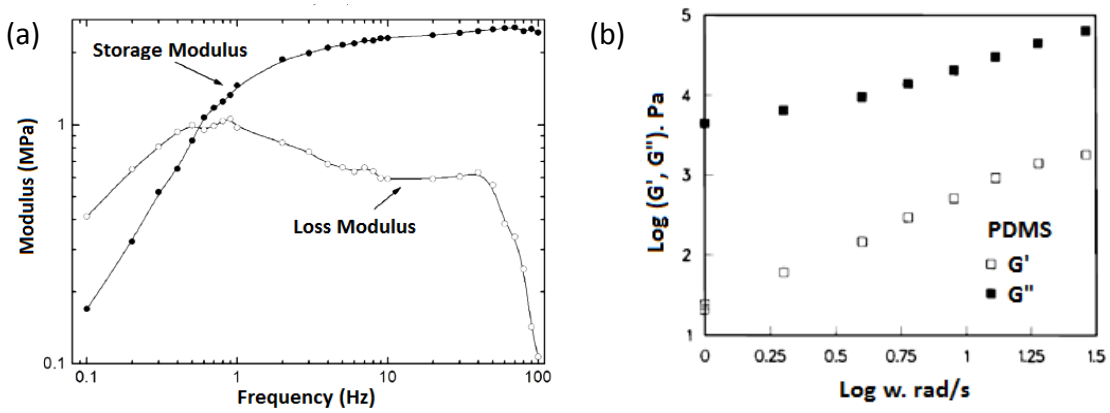

Figure 1.17. G' and G'' of (a) cured PDMS and (b) PDMS solution published in (Lin et al., 2009) and (Ghannam and Esmail, 1998a) respectively.

Similar to PAA sheets, PDMS soft substrates used in the measurement of cell force are also limited by the necessity of pre-coating these substrates with an ECM protein in order to enable cell attachment. There is a possibility that forces generated

by cells on these surfaces may be dependent on a combination of the density of the proteins on the surface or to the substrate stiffness (Engler et al., 2004a). Hence, it is difficult to determine if the forces induced are associated with the substrate stiffness, types of ECM proteins or the concentration of ECM proteins being applied (Engler et al., 2004a). It is important to note that the micro-patterned soft substrates which were used to promote contact guidance for cells strongly alter the behaviour of the cells, and the patterns may limit cell spreading and dispersal of cell surface contacts (Pathak et al., 2008, Britland et al., 1996, Curtis, 2004, Lehnert et al., 2003), and thus may impact on cell force generation. A detail comparison of the polymer based techniques applied in cell force measurements is as shown in Table 1.2. In understanding the limitation of polymer based method, this research proposes the use of liquid crystals (LCs) which is a semi-solid consisting of highly packed molecules with the absence of cross-linkages.

1.3 Introduction to Liquid Crystals

Liquid crystals were first discovered in 1888. An Austrian botanical physiologist Fredrich Reinitzer (1865 - 1927) accidentally observed a phenomenon, in which cholesteryl benzoate changed into a cloudy liquid at 145.5 ^{o}C and melted again into a clear liquid at 178.5 ^{o}C. This is an unusual phenomenon because this material has two melting points and it is quite different from the three states of matter (solid, liquid and gas) recognised at that time. Unsure of the discovery, Reinitzer brought the sample to a physicist known as Otto Lehmann for further investigation. Lehmann named the new substance as 'liquid crystal' (LC). The name reflects the fact that the substance has mesophases; in which the material has both liquid and solid properties within a single phase. Liquid crystals are ordered fluid mesophases in which the elongated molecules

possess some degree of orientational order (Collings and Patel, 1997). Liquid crystal molecules are often made of phenyl rings (aromatic group) that are attached to two substituent groups. A typical example of 4'-n-pentyl-4-cyanobiphenyl (5CB) is as shown in Figure 1.18. Some liquid crystals have linkage groups between the phenyl rings. The structure of the molecules determines the thermal stability of a liquid crystal (Collings, 2002). Liquid crystals are generally considered by physical scientists as large molecules taking the form of rod-like structures or disc-like calamitic cores.

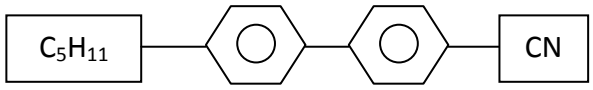

Substituent Aromatic group Substituent

Figure 1.18. A liquid crystal molecule of 5CB

1.3.1 Types of Liquid Crystals

There are two types of liquid crystals, the thermotropic and lyotropic liquid crystals. The former are temperature and potential sensitive, whilst the latter function as surfactants whose properties depend on the solute concentration (Fairhurst et al., 1998). These two types of liquid crystals have different physical properties and thus different applications. One of the examples of thermotropic liquid crystals is the cholesteric liquid crystals that have been long used in the older generation of liquid crystal displays (LCDs) (Yang et al., 1994). Discussion on the newer type of thermotropic liquid crystals such as ferroelectric and polymer dispersed liquid crystals (PDLC) that are mainly applied in electronic display system will not be included as they are beyond the scope of this work.

(a) Thermotropic Liquid Crystals

As the name implies, a thermotropic liquid crystal changes its orientation and positional order when the applied temperature increases. As a result, the material gradually turns from anisotropic crystal phase into an isotropic liquid phase. In an isotropic phase, the physical properties (for example, refractive index, elastic constant, viscosity and permittivity) are the same in all directions, whilst the physical properties of the anisotropic phase are different between one direction and another. Anisotropy by definition means that the physical properties of the phases are different and depending on the direction and orientation of the component molecules. In thermotropic liquid crystals, each molecule is oriented in a long range order (Collings and Patel, 1997). The thermotropic liquid crystals that have been used in LCDs include the N-(4-Methoxybenzylidene)-4-butylaniline (MBBA) and 4'-n-pentyl-4-cyanobiphenyl (5CB). Besides their applications in the electronic industry, thermotropic liquid crystals are also being used in thermography (for example, temperature sensors) (Stasieka et al., 2006) and optical imaging (for example, shear flow sensing and skin friction) (Reda and Muratore, 1994, Klein and Margozzi, 1969).

(b) Lyotropic Liquid Crystals

Lyo is a Greek word meaning dispersion or dissolution. Hence, Lyotropic liquid crystals have a connection with the dispersion of liquid crystal molecules in a fluidic solution (Hyde, 2001). The phases of lyotropic liquid crystals are determined by the concentration of solute molecules and these liquid crystals consist of rod like entities, all of which participate in a long range order. Lyotropic liquid crystals are generally made up of molecules larger than the thermotropic liquid crystals and have an axial ratio of less than 15 (Priestley et al., 1974). Lyotropic liquid crystals are amphiphilic,

hence, each molecule (or mesogen) consists of a polar (hydrophilic) head and a non-polar (hydrophobic with saturated hydrocarbons chains) tail group (see Figure 1.19). With the fatty acids in their hydrophobic chain, they often work as a surfactants (Surface Active Agents) and are normally categorised as lipids (Fairhurst et al., 1998). Lyotropic liquid crystals are mostly found in soap, food and in living things such as cell membranes and serum lipoproteins (Gennes, 1974, Small, 1977).

When lyotropic liquid crystals mix with a solvent such as water, self-assembling aggregates will be formed by a process driven by the effects of hydrophobic chain (or water repelling). Above a certain concentration of solvent, the aggregates or surfactants transform into micelles. The threshold of concentration in which the aggregation of micelles appears is termed as the 'critical micelle concentration' (CMC) and occurs at a very narrow range of solvent concentration.

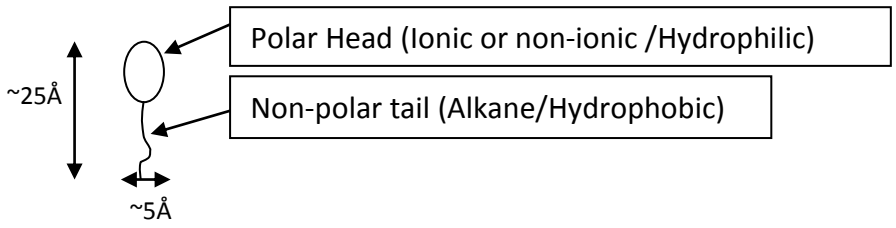

Figure 1.19. A lyotropic liquid crystal molecule (Priestley et al., 1974)

Below CMC, the surfactants dissolve as monomers. When there is a gradual increase in concentration above CMC, this result in dispersion of surfactant into micelles at the isotropic phase. The liquid crystalline phase forms only when the concentration of lyotropic liquid crystal is high enough to force the micelles to arrange into a regular structure.

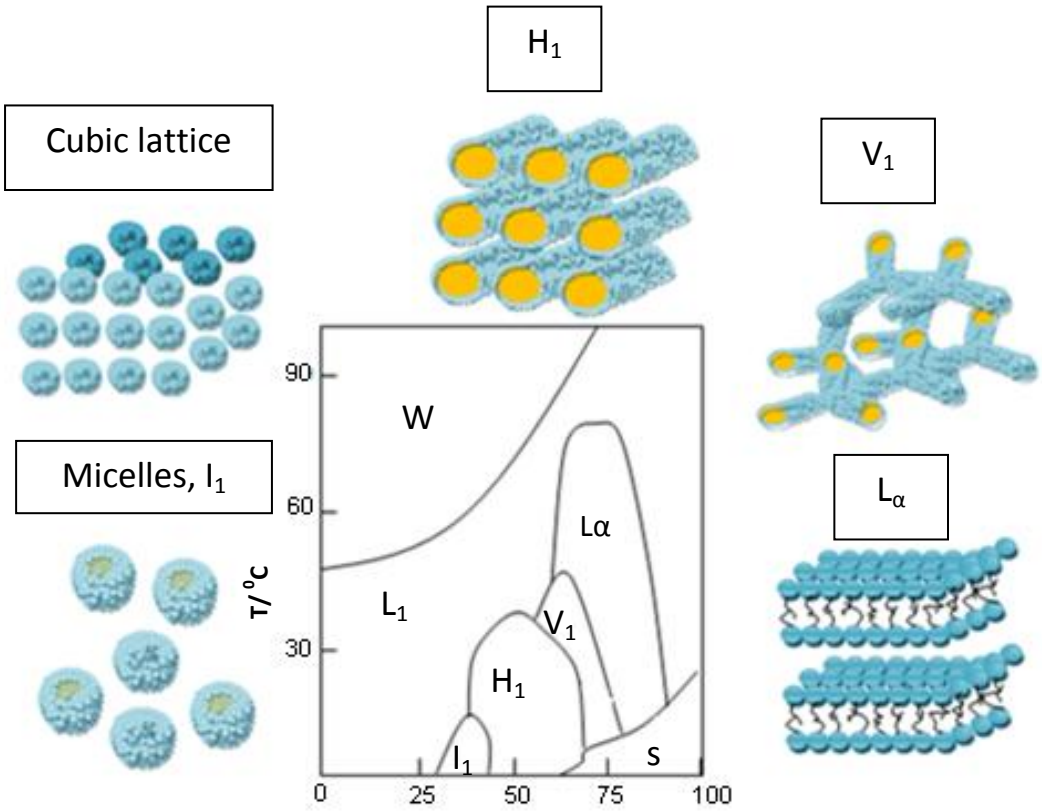

Figure 1.20. The typical phases of lyotropic liquid crystals. The figure illustrates the relationship between the amphiphile compositions at various temperatures producing a very dilute surfactant solution (W), aqueous surfactant solution (L_1), micellar cubic phase (I_1), hexagonal phase (H_1), bi-continuous cubic phase (V_1), Lamellar phase (L_α), and solid surfactant (S) (Fairhurst et al., 1998)

The relationship between the liquid crystalline phases of a surfactant and its composition concentration is expressed in a phase diagram as a function of temperature (Figure 1.20). At a typical 30 – 40 wt% of amphiphile concentration, the micellar cubic phase (I_1) will be formed while remaining in the isotropic phase but turns into a cubic lattice as the amphiphiles reach a concentration of 60 %. When the amphiphile concentration increases further, the micelles in the cubic lattice fuse to form cylindrical shaped aggregates termed as the normal hexagonal phase (H_1). Before leading to the lamellar phase, at a very narrow range of concentrations, a complex bi-

continuous cubic phase (V_1) is formed. This is follow by a very high concentration of amphiphiles, the lamellar phase (L_α) in which the amphiphile molecules are arranged in bilayers and each bilayer is separated by water molecules. If the surfactant concentration is very low and the temperature is greater than approximately 40 ^oC, the composition is then in the form of aqueous surfactant solution (L_1) or very dilute surfactant solution (W).

1.3.2 Classification of Mesophases and Associated Birefringence Texture

The structure of a solid crystal has the molecules in anisotropic state and they are arranged in long range order. Heat can destroy the solid state of a crystal. When the temperature of a crystal molecule increases to its melting point, the energy causes the molecules to vibrate so they eventually disperse with a loss of the original orientation and positional order, and into a random isotropic liquid (Priestley et al., 1974). Liquid crystals have a phase which is intermediate between an ordered solid and an amorphous liquid phase. Most of the liquid crystals have more than one phase. An example in Figure 1.21 shows the melting points of the liquid crystal MBBA and the associated phases.

The anisotropy of the liquid crystals gives rise to the birefringence property. Birefringence is an optical characteristic resultant from changes in orientation and alignment of the mesogens. The appearance of their textures is not just fascinating but provides information about the symmetrical structure and orientation of the underlying molecules. A sample of a liquid crystal gel put under a 90^o crossed polarising microscope, portrays different patterns and colour reflections due to its birefringence property.

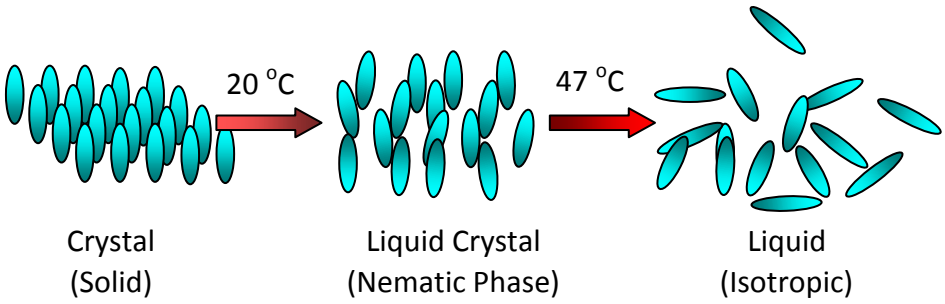

Figure 1.21. Melting points of MBBA

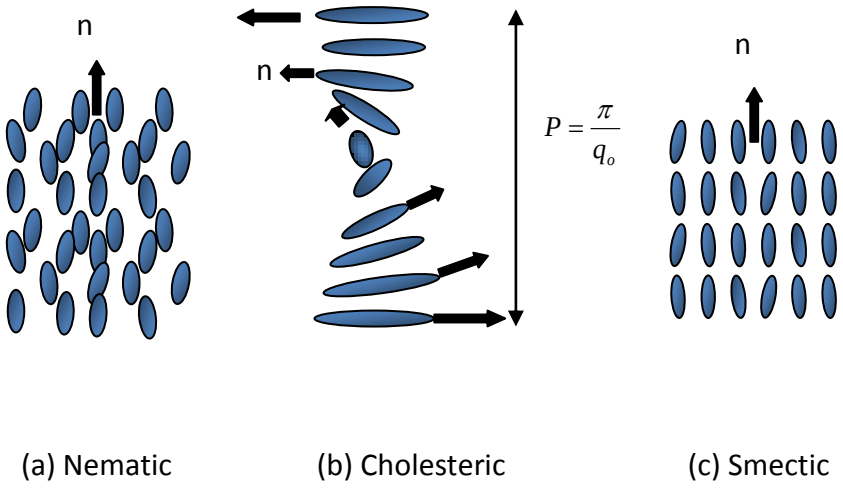

Figure 1.22. Three main mesophases of liquid crystals

Therefore, the classifications of the liquid crystal mesophases are based on the ordering present in the liquid crystal. The molecules can be arranged in short range or long-range order, and the arrangement is subjected to alteration by external stimuli. The three main liquid crystal phases are the: nematic, cubic, columnar, cholesteric and smectic phases (Figure 1.22). Only nematic, cholesteric and smectic phases that are related to this work will be discussed.

(a) Nematic Phase

The word nematic came from the Greek word “Nema” which means thread-like. As its name implies, nematic phase composed of thread-like liquid crystals that point in different directions. Under the influence of an external force (for example, force from the magnetic field), these calamatic liquid crystals align themselves to a common axis,

so called the director, “n”. Director, n, is the reference to any angle of deviation (θ) of the calamatic liquid crystal from n which indicates the orientational order of a liquid crystal. The molecules in the nematic phase are arranged parallel to each other and slide past each other. Such a systematic alignment gives rise to uniform reflectivity when being viewed under a cross-polariser at room temperature (Figure 1.23a). The schlieren pattern is a typical pattern of nematic phase near the melting point of a nematic liquid crystal (for example, TL205 at 88.6 ^{o}C in Figure 1.23b). These patterns may have different disclination (as shown in Figure 1.23b) which shows the orientation order of their molecules. A detail description of the inclination related to the molecular structure can be acquired from (Chandrasekhar, 1992).

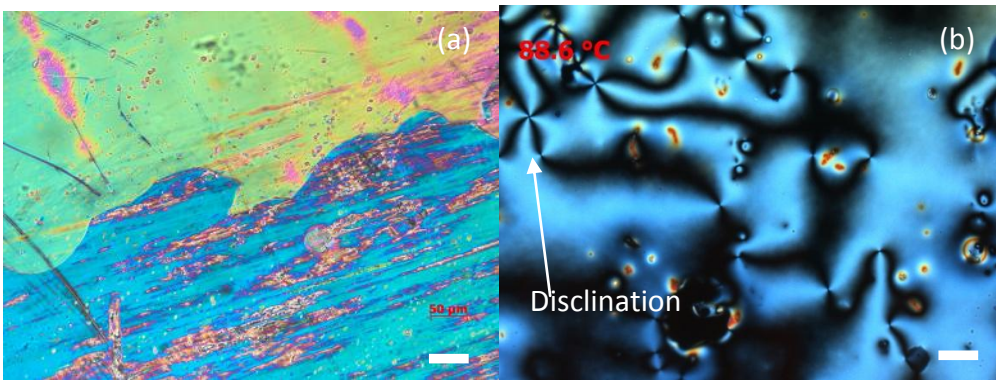

Figure 1.23. (a) Uniform and (b) Schlieren patterns of a nematic liquid crystal. (Scale bar: 50 µm)

Liquid crystals in the nematic phase have a long range orientational order but without translational order (having same direction in the same layer) (Gennes, 1974) and every molecule can be characterised by the order parameter:

$$S = \frac{1}{2}\left\langle 3\cos^2\theta - 1 \right\rangle \qquad (1.1)$$

In this equation, θ is the angle with respect to direction (n). When θ = 0^{o}, S = 1, it indicates that the molecule is homeotropic or perfectly aligned. In the isotropic phase, molecules are aligned randomly; that is when S = 0 at θ = 83.62^{o}. When θ = 90^{o}, S = -

1/2, the molecule will be lying in a plane perpendicular to the director, n (Figure 1.24). A typical liquid crystal sample has S ranging between 0.3 and 0.8, and S decreases when the temperature increases. The overall distribution function of parameter, S is as shown in Figure 1.24.

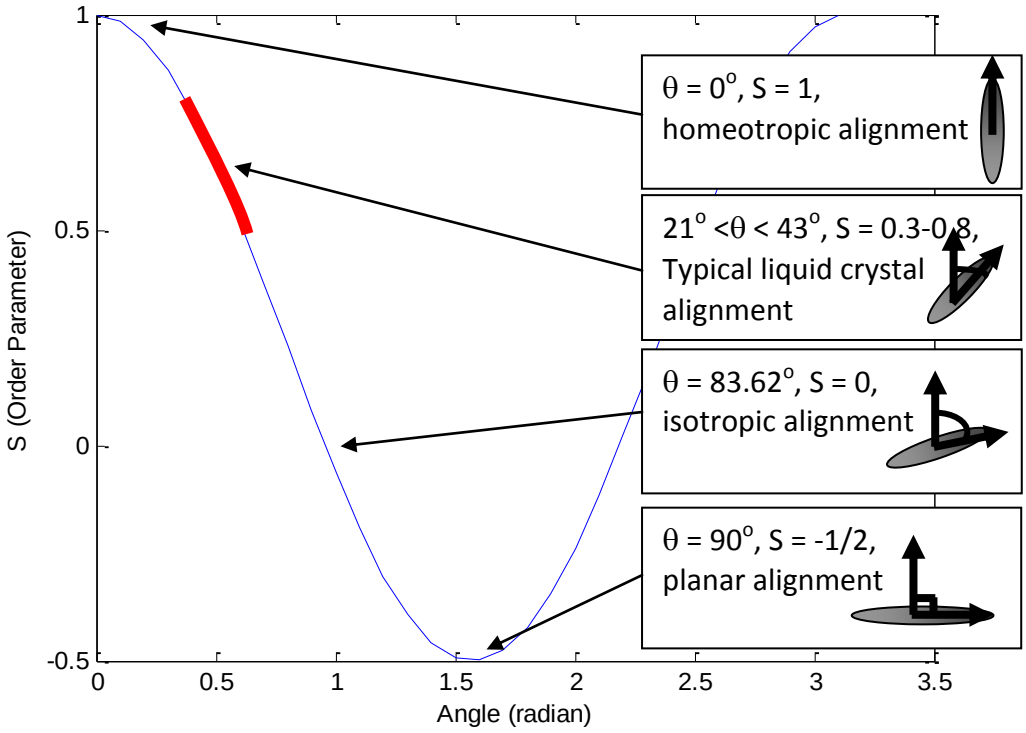

Figure 1.24. The orientation and distribution (order S) of mesogens.

(b) Cholesteric Phase

Also known as chiral nematic phase, cholesteric phase has a helical structure in which the director is twisted along the z-axis (helical axis) normal to the x-axis. The molecules are organised in layers with long range order but no positional order. The directions of the molecules are n with subscripts, x, y and z which represent the orientations:-

$$\begin{aligned} n_x &= \cos(q_0 z + \varphi) \\ n_y &= \sin(q_0 z + \varphi) \\ n_z &= 0 \end{aligned} \qquad (1.2)$$

where the phase angle φ is arbitrary and wavevector, q_0 is found by the repetition period or pitch of $P = \pi / q_o$ (Chandrasekhar, 1992, Gennes, 1974). Half of a pitch, P has a typical value of 300 nm for cholesteric liquid crystals (Collings and Patel, 1997). Normally, colourful textures are observed due to the selective colour reflection from the mesogens that are lying in planes of helical structures with different pitch length. The planar and homeotropic orientations of the cholesteric liquid crystal mesogens portray different textures. When the mesogens orientate close to the homeotropic alighment, the colour of the texture often appears dark with very low light reflectivity in the crossed-polarisers. The cholesteric phase is similar to the nematic phase but chiral molecules cause a twist in the nematic structure which is normal to the long axis. The optical property of the cholesteric phase is very different from nematic phase because of the strong twist in the molecules. The irregularities of helical pitches in different regions form defect network lines known as the Grandjean-cano lines or oil streak lines (Figure 1.25). The cholesteric phase is significant to this work and their elastic property will be discussed further.

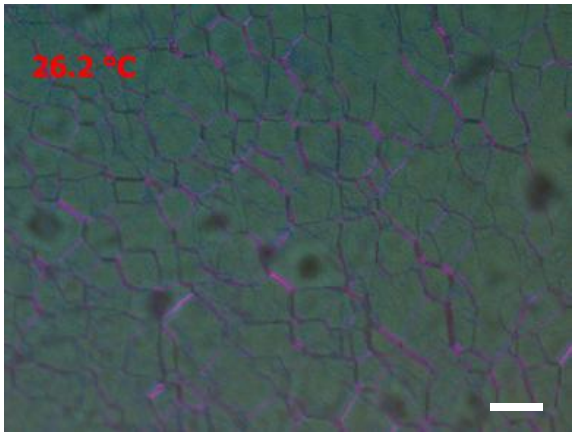

Figure 1.25. A photomicrograph of Cholesteric 'oily-streaks' or Grandjean texture at room temperature. (Scale bar: 50 μm)

(c) Smectic Phase

There are three best understood smectic orders in the smectic phase: smectic A (Figure 1.26), smectic B and smectic C. The common structure among these three orders is having one degree of translational order and the molecules are arranged in well-defined layers. Comparatively, they are more ordered than nematic phase and occur at a lower temperature than the nematic phase (Fairhurst et al., 1998).

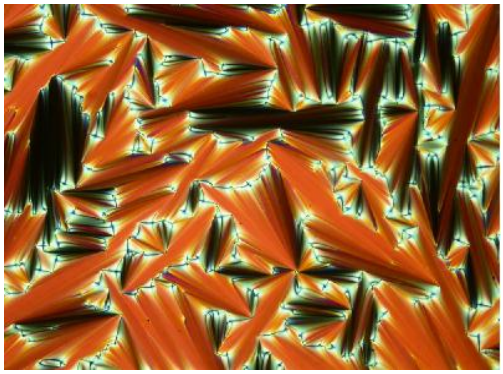

Figure 1.26. Smectic A phase of the smectic liquid crystals (Dierking, 2003).

1.3.3 Elasticity Theory of Chiral Nematic Liquid Crystals

Similar to the nematic liquid crystal, the molecules in cholesteric or chiral nematic liquid crystals have no positional order but have an orientational order and their nematic phases are arranged in twisted layers that gave rise to what is also referred as a chiral nematic order (Chandrasekhar, 1992). Without being stressed by any external force, liquid crystals are ordered in the relaxation state and orient to their default director, n. The source of the external force could be in the form of elastic, thermal or electric energy. The deformation of the liquid crystal occurs when an external force overcomes the threshold or initial torque of the liquid crystal molecule, which is known as Freedericksz Transition. In 1927, Freedericksz first discovered that the optical properties of liquid crystal can be disrupted by applications of an electric field (Fairhurst et al., 1998). It was found that liquid crystal molecules are polarisable

by the direction of electric field but the order of distortion is dependent on the elastic constant of the mesogens.

The elastic constant of the liquid crystal is defined by the ability of the molecules to support torsional strain (Dunmur et al., 2001). The terms, elastic constant or elastic moduli are normally used interchangeably (Dunmur et al., 2001). The orientation and organisation of the molecules determine the physical properties, macroscopic anisotropy, torsional and curvature elasticity of the liquid crystals (Dunmur et al., 2001). A torsional energy can disrupt the directors of uniformly aligned molecules and they generate free energy. The free energy forces the mesogen to align with the applied field (Dunmur et al., 2001). Consequently, the disruption changes the orientation of the mesogen away from the equilibrium state which is known as curvature strain. In return, the curvature strain generates an opposing force which is the curvature stress or torque. By referring to the director axes, n (in x, y and z planes) with n parallel to z in right handed system (Figure 1.27), six components (S_1, S_2, t_1, t_2, b_1 and b_2) of the curvature equation (2.3-2.5) were defined by Frederick Frank (Frank, 1958) as:-

Splay:
$$S_1 = \frac{\partial n_x}{\partial x}, S_2 = \frac{\partial n_y}{\partial y} \tag{1.3}$$

Twist:
$$t_1 = -\frac{\partial n_y}{\partial x}, t_2 = \frac{\partial n_x}{\partial y} \tag{1.4}$$

Bend:
$$b_1 = -\frac{\partial n_y}{\partial z}, b_2 = \frac{\partial n_x}{\partial z} \tag{1.5}$$

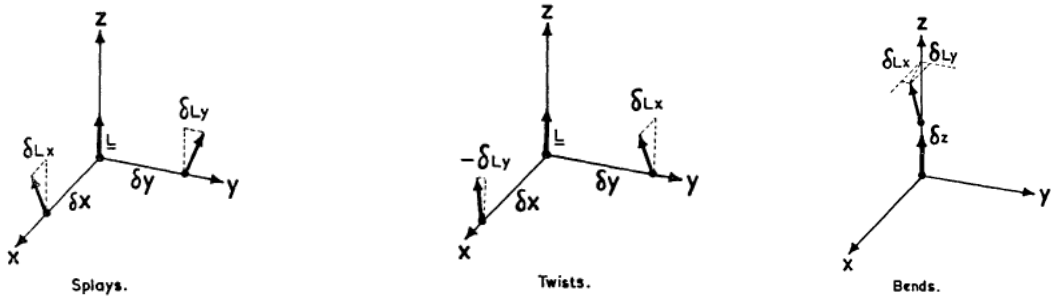

(a) (b) (c)

Figure 1.27. Components of liquid crystal curvature. (a) Splay (b) Twist and (c) Bend (Frank, 1958).

To induce the curvature strain in the cholesteric phase, the free energy density or Frank-Oseen free energy, f is needed to govern the cholesteric phase. This is written as (Chandrasekhar, 1992),

$$f = k_2(n\cdot\nabla\times n)+\frac{1}{2}K_1(\nabla\cdot n)^2+\frac{1}{2}K_2(\nabla\cdot n\times n)^2+\frac{1}{2}K_3(n\times\nabla\times n)^2 \qquad (1.6)$$

where K_1, K_2 and K_3, are the Frank elastic constants in which K_1 is the splay elastic constant, K_2 is the twist elastic constant and K_3 is the bend elastic constant. As the term chiral nematic implies, equation (1.6) describing the chiral nematic liquid crystals is very similar to the equation describing the free energy of nematic liquid crystal but with an addition of chirality which is denoted by k_2 in equation (1.6). In the cholesteric liquid crystal, the right handed ($k_2 > 0$) or left handed ($k_2 < 0$) twist is determined by chirality k_2. The twisting effect in cholesteric liquid crystal reaches equilibrium when k_2 counter-reacts with K_2. Typically, the elastic constants of cholesteric liquid crystals are $K_1 = 8$ pN (Kuball et al., 2000), $K_2 = 5.7$ pN (Miller and Gleeson, 1993) and $K_3 = 10$ pN (Kuball et al., 2000 , Dunmur et al., 2001). The intermolecular forces are angle dependent and contribute to the elastic strain energy or curvature elastic moduli

(Dunmur et al. 2001). The sources of energy that can disrupt liquid crystal directors include electric field, magnetic field, changes in temperature, and shear forces.

1.3.4 Application of Liquid Crystals in Bio-Sensing

One of the objectives in this work is to identify non-toxic liquid crystals that may be used as a force transducer in a single cell based pharmacological assay. Biocompatibility of the liquid crystals is the main concern when deciding the type of liquid crystal to be used. If liquid crystals are to be applied in tissue engineering or bio-sensing in the presence of living organism, then, the viability of cells cultured on liquid crystals has to be studied carefully. All drug and chemicals are poisons if the applied dosage exceeds a limit. The challenge of this work is to identify non-toxic liquid crystals with properties that mimic the in-vivo physical environment. Previous toxicological investigations of liquid crystals (Becker et al., 2001, Abbott et al., 2005, Woolverton et al., 2005) suggested that some liquid crystals could be toxic or non-toxic to cells, and that depends on the functional groups of the liquid crystals. Biocompatible materials are defined as non-toxic materials that support cell proliferation. Liquid crystals with cyano, imine and ether functional groups (such as, 5CB, E7, “A”, “B” series liquid crystals) have been identified as cytotoxic to 3T3 fibroblasts and SV-40 Human Colonic Epithelial Cell Line (HCEC) (Abbott et al., 2005, Luk et al., 2004). In the same studies, it was found that cells remain viable on a mixture of difluorophenyl and bicylohexyl groups such as “C” series and TL205 liquid crystals commonly used in fabricating LCDs in the electronic industry. In biosensor application, matrigel/TL205 substrates were used to detect the reorganisation of a matrigel by HCEC cells (Lockwood et al., 2006).

Table 1.3. Applications of the liquid crystals as biosensors

Type of liquid crystal	Generic name	Chemical Compound	Application	Reference
Nematic liquid crystal	5CB	4'n-pentyl-4-cyanobiphenyl	Detect optical changes due to ligand-receptor binding	(Gupta et al., 1998)
Smectic phase	-	Cholesteryl oligo(L-lactic acid)	Interaction with 3T6 Fibroblasts	(Hwang et al., 2002)
Nematic liquid crystal	5CB		Liquid crystal phase changed when Phospholipids reorganised	(Brake et al., 2003)
Nematic liquid crystal	5CB		Imaging of myofibroblast and optical amplification	(Fang et al., 2003)
Nematic liquid crystal	5CB		Imaging molecular order of lipid tubule	(Zhao et al., 2005)
Lyotropic liquid crystal phase	-	Tetra-decyldimethylamine oxide ($C_{14}AO$) and decanol (D), or disodium cromoglycate (DSCG; $C_{23}H_{14}O_1Na_2$)	LLC support replication of viruses	(Cheng et al., 2005)
Nematic Liquid crystal	TL205		Imaging reorganisation of matrigel by human embryonic stem cells	(Lockwood et al., 2006)
Nematic liquid crystal	5CB		Rapid screening of proteases	(Birchall et al., 2008)

Besides thermotropic (nematic, ferroelectric and polymer dispersed nematic) liquid crystals used for LCD, synthetic liquid crystals especially cholesteryl based liquid crystal are attracting increasing interest because of their biocompatibility. Some of the examples includes Cholesteryl oligo (L-lactic acid), which was found to be

biocompatible with 3T3 fibroblasts (Hwang et al., 2002); cadmium selenide (CdS), a semiconductor was coated with organic material such as the Cholesteryl-oligo (Ethylene Oxide) in lamellar order that may be used as implants (Rabatic et al., 2003); and, lyotropic liquid crystal in supporting the replication of viruses (Cheng et al., 2005).

Liquid crystals have been applied as biosensors which provide label free observation of biological phenomenon (Woltman et al., 2007). Examples in bio-transducing include the use of nematic liquid crystals in transforming ligand-receptor binding into an optical output (Gupta et al., 1998), detection of nematic liquid crystal reorientation as a result of phospholipids reorganisation (Brake et al., 2003), enhancement in the imaging of cell physical appearance with nematic liquid crystals (Zhao et al., 2005, Fang et al., 2003, Lockwood et al., 2006) and the LCD based detection of a protease (for example, trypsin, elastase and thermolysin) that cleaved off the Fluorenylmethyloxycarbonyl (Fmoc) peptide backing by a thermolysinpolyethylene glycol acrylamide (PEGA) hydrogel support and specific detection of protease function (Birchall et al., 2008). The application of the liquid crystals as bio-imaging sensors is in its infancy and research has not yet investigated how liquid crystals interface with a fluidic environment (Table 1.3). The understanding on how amphiphilic molecules of a liquid crystal based biosensor interact with the water molecules is critical if liquid crystals are to be used for cell culture or in a fluidic environment.

1.3.5 Viscoelasticity of Lyotropic Liquid Crystals

In liquid crystal based biosensor development, an exposure to cell culture media is inevitable and this may alter the viscoelasticity of the liquid crystals over time. Even though it is well documented structurally that liquid crystals consisting of amphiphilic

molecules, these molecules may reorient and self-organise into uni-lamellar or multi-lamellar lyotropic layers when exposed to a solvent (Helfrich, 1994, Porcar et al., 2005, Fairhurst et al., 1998). Unfortunately, the time-dependant rheological behaviour of lyotropic liquid crystals is not fully understood. However, previous literature indicates that immersion in a solvent may reduce the strength of these semi-solid materials (Small, 1977, Fairhurst et al., 1998). Besides the factor of solvent, the physical properties of the liquid crystals may also be influenced by the temperature as a function of time. Only a few studies have examined the rheology of cholesteric and lyotropic lamellar phase liquid crystals, mostly with the focus of interest on the determination of the yield stress and defects of the mesophases (Ramos et al., 2002, Zapotocky et al., 1999, Basappa et al., 1999). Some investigated the mesophases or structural changes of the lamellar system in response to flow (Munoz and Alfaro, 2000, Alcantara and Fernades Jr., 2002, Zipfel et al., 1999, Berghausen et al., 2000). Positively, an independent study conducted by (Ramos et al., 2002) and (Zapotocky et al., 1999) showed that cholesteric liquid crystals undergoing shear at low angular frequencies exhibit a linear viscoelastic behaviour. These studies attempted to further enhance the viscoelasticity of the cholesteric liquid crystals via the inclusion of micron sized particles. This suggests that the elastic behaviour of cholesteric liquid crystals at low shear rates may have elastic response to traction forces of cells.

1.4 Selection of Cell Type and Requirements of Cell Traction Force Sensor

As seen in Table 1.2, most of the soft substrate based cell force sensing techniques were used to examine forces generated by highly motile and contractile cells such as fibroblasts and smooth muscle cells that are able to induce high traction forces (up to ~2000 nN). As suggested in (Balaban et al., 2006), the micro-patterned

elastomeric technique developed may not be sensitive to poorly contractile epithelial cells. In conjunction with this suggestion, only one study has looked at measuring forces exerted at the focal adhesions by the keratinocyte type cells recently (Mohl et al., 2009). The significance of measuring the traction forces of the keratinocytes can be seen from the crucial role of keratinocytes play in wound healing (Souren et al., 1989, Deneflea et al., 1987, Schafer et al., 1989). For example, there is steadily growing evidence that keratinocyte type cells affects the shrinkage of constructed skin grafts before application in wound repair (Chakrabarty et al., 2001, Harrison et al., 2005).

Besides being biocompatible and supportive to cell proliferation, what is required to measure the contraction forces of a single skin keratinocyte or epithelial cell is a biomimetic material with an elastic modulus that gets close to mimicking the in-vivo physical properties of the epidermis layer (Engler et al., 2004a, Yeung et al., 2005, Lo et al., 2000, Levental et al., 2007). The Young's modulus of the epidermis as determined by different methods (suction and uniaxial method) was found to be between 60 kPa to 200 kPa (Barel et al., 1995, Diridollou et al., 2000, Takeo, 2007, Hendriks, 2005).

In addition to having high sensitivity, a cell traction force measurement technique should allow direct determination of the displacement on the soft substrate (not based on a reference image) which in turn, increases the signal to noise ratio. In such a system, the soft substrate shows preferable sensitivity to a wide range of cell traction forces (from a few nN to a few hundred nN), be able to detect randomly dispersed stress on a substrate, be able to distinguish isolated regions of traction, and hence reduce the effects of chaotic wrinkling when a local shear force is applied to the substrate.

If the substrate does not require pre-treatment with exogenous ECM proteins, then the controversy about the response of cell to the substrate stiffness or type of ECM proteins can be reduced (Engler et al., 2004a, Lehnert et al., 2003, Yeung et al., 2005). It is important to note that cells on a surface will secrete their own ECM proteins (O'Toole, 2001, Kirfel and Herzog, 2004). Therefore, this issue of "ECM proteins induced modifications in substrate stiffness" cannot be wholly disregarded (Discher et al., 2005, Yeung et al., 2005). The reports on the mechanism of the contraction or traction of keratinocytes are scarce and present an opportunity for investigation in this research.

1.5 Hypothesis of the Research

Generally, the liquid crystal molecules are high flexibility and possess many degrees of freedom in order to orientate (Frank, 1958). The elastic constant for the liquid crystals are about 1 pN in nematic liquid crystals (Lockwood et al., 2006) and 8 pN for K_2 in chiral nematic liquid crystals (Dunmur et al., 2001). These values indicate that the molecules can be easily tilted by a very low level of distortion forces. Since the reorientation of the liquid crystal molecules or mesogens is versatile and elastic, it might endure external distortion and recover to its original state once the stress is released. The versatility and flexibility of liquid crystals can be seen in liquid crystal displays that are switched on and off for immeasurable times. A rigid mesogen has a length of about 20 Å and a width of 5 Å (Gennes, 1974), and these mesogens are compactly packed together to form a liquid crystal system. Physically, cholesteric liquid crystals are organized in nematic layers that are twisted along the z axis (Gennes, 1974). It is hypothesised that surface perturbations may change the pitch length or organisation of the cholesteric helical structure, and thus induce physical and optical

distortions (reflectivity changes) in the liquid crystal substrate which may be observed and quantified.

Thus, shear sensitive liquid crystal (SSLC) based on cholesteric liquid crystals may meet the requirements for measuring the contractile forces of cells because cholesteric liquid crystals contain weakly-ordered mesogens that change colour in response to a shear (Reda and Muratore, 1994, Klein and Margozzi, 1969). SSLCs have very few applications, but they have been used to monitor changes of shear vector in aerodynamics (Reda and Muratore, 1994, Klein and Margozzi, 1969). In this application, the colour changes of the SSLC are continuous and reversible with a response time in milliseconds (Reda and Muratore, 1994). In observing the potential of cholesteric liquid crystals in shear sensing, this work proposes to apply shear sensitive cholesteryl ester liquid crystals (CELC) for use in cell traction force sensing.

1.6 Aim and Objectives of the Research

The primary aim of this research is to develop a novel liquid crystal based cell traction force transducer (LCTFT) system that can be used to determine the effects of pharmacological agents on the forces exerted by single cells on a liquid crystal substrate. In order to achieve this aim, this thesis will:-

(a) Examine the biocompatibility of cholesteryl ester liquid crystals.

(b) Characterise the physical and optical properties of cholesteryl ester liquid crystals in air and in aqueous media.

(c) Determine the biophysical interactions of keratinocytes and liquid crystals.

(d) Quantify cell derived traction forces using cytochemical intervened technique and Hooke's theorem followed by modelling the deformation of liquid crystals using Finite Element Method (FEM).

(e) Develop a cell force measurement graphical user interface (GUI) which enables analysis of cell traction force distributions in computer visualisation.

(f) Evaluate and validate the functionality of the liquid crystal based cell force transducer system by studying the dose response of HaCaT cells to TGF-β1. There is evidence that TGF-β1 increases stress fibre formation and affects the cell contractility (Boland et al., 1996, Zhang et al., 2003, Decline et al., 2003).

1.7 Thesis Organisation

The flow of the thesis is systematically organised according to the progressive development process of the liquid crystal based cell force transducer (Figure 1.28).

This work begins in Chapter 2 which focuses on the characterisation of the physical and optical properties of cholesteryl ester liquid crystals, and determines the limitation of the physical properties in cell culture media.

Chapter 3 will describe the biophysical interactions between cells and the liquid crystals in the context of cell viability, cell/liquid crystal interactions, interface reactions, extracellular matrix depositions, integrins, and actin cytoskeleton expression.

To develop a novel liquid crystal based cell force transducer system, it is of importance to determine how forces generated by single cells can be measured. Thus, chapter 4 will describe new quantification procedures for determining the traction forces generated by cells cultured on the LCTFT based on Hooke's theorem or stress-strain relationship. Finite Element Method (FEM) will be used to model the focal adhesions and liquid crystal interactions, and thus provides information about the compression effects to the liquid crystal substrate.

Chapter 5 will focus on the development of a cell force measurement and mapping software with a graphical user interface (GUI). This software will be applied to study the patterns of cell traction and migration.

The usefulness of the LCTFT system will be evaluated and validated in chapter 6, in which, various doses of TGF-β1 will be applied to cells cultured on the LCTFT to induce a dose response in terms of contraction forces.

Chapter 2, 3, 4, 5 and 6 will each include a brief introduction, materials and methods, results, discussions and summaries. Chapter 2 to 6 will examine the biocompatibility (affinity to cells attachment), the sensitivity (linear responsiveness of LC to force stimuli), the accuracy (compatible with measurement result shown by previous methods), and the reliability (repeatable and consistent measurements) of the LCTFT system.

Chapter 7 will overview the findings of this research in relation to the literature and this chapter will also highlight future works.

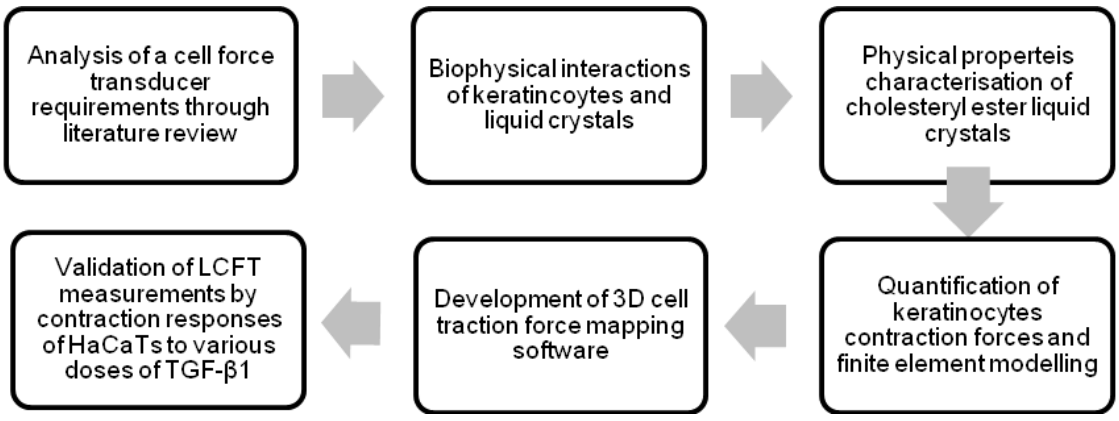

Figure 1.28. Process of developing a hybrid Liquid Crystal based Cell Traction Force Transducer (LCTFT)

CHAPTER 2

PHYSICAL PROPERTIES: CHARACTERISATION OF CHOLESTERYL ESTER BASED LYOTROPIC LIQUID CRYSTALS

2.1 Introduction

In the context of using liquid crystals (LC) as a cell force transducer, it is essential to determine their physical properties that pertain to this research. Culturing cells on liquid crystal substrates raise a critical issue associated with the exposure of LC to cell culture media, which may alter the viscoelasticity profile of the liquid crystals over time. Even though it is well documented that the polar heads and non-polar tails of the LC molecules reorient and self-organise into uni-lamellar or multi-lamellar lyotropic layer when they are expose to a solvent, the time-dependent rheological properties is less understood (Helfrich, 1994, Porcar et al., 2005, Fairhurst et al., 1998). Other than the factor of solvent, the physical properties of the liquid crystals may also be influenced by the temperature as a function of time.

Therefore, this chapter aims at first examining the thermal stability, and then the physical properties of the cholesteryl ester liquid crystals after being exposed to aqueous media over periods of time by cross-polarising microscopy, rheological characterisation, atomic force microscopy (AFM) based nano-indentation, spherical indentation, and uni-axial micro-tensile testing in order to obtain the thermal stability range, mesophases, viscoelastic range, Young's modulus, and Poisson's ratio of the liquid crystals, respectively. Examining the physical properties of the liquid crystals is crucial and critical in understanding the mechanical stability and durability of the cholesteryl ester liquid crystals in an aqueous environment. This in turn will inform on the suitability of cholesteryl ester liquid crystals for use in the development of a liquid crystal based cell force transducer.

2.2 Material and Methods

2.2.1 Preparation of Cholesteric and Nematic Liquid Crystals

Shear sensitive cholesteric liquid crystals with different compositional formulations were prepared according to the modified procedure as given by Klein et al. and Johnathan Griffths (Klein and Margozzi, 1969, Griffths, 1988). All modified formulations of the cholesteryl ester liquid crystals (CELC) were termed as CELCP1, CELCP2 and CELCP3 are as shown in Table 2.1. The chemical structures of cholesteryl chloride $C_{27}H_{45}Cl$, cholesteryl perlargonate $C_{36}H_{62}O_2$ and cholesteryl oleyl carbonate $C_{46}H_{80}O_3$ (Sigma Aldrich, UK) are as shown in Figure 2.1 and each has melting points in the range of 70 - 85 ^{o}C, 94 - 96 ^{o}C and 113 - 118 ^{o}C, respectively.

Table 2.1. Shear Sensitive Liquid Crystals in different formulations.

	Weight of samples (gram)		
Liquid Crystals	CELCP1	CELCP2	CELCP3
Cholesteryl Oleyl Carbonate	0.44	0.38	0.25
Cholesteryl Perlargonate	0.44	0.38	0.25
Cholesteryl Chloride	0.12	0.25	0.50

The crystalline or solid mixtures of CELCP1, CELCP2, and CELCP3 (Figure 2.2a) in vials were heated up to their highest clearing point, 118 ^{o}C on a hot stage. The solid mixtures turned into a turbid fluidic media at about 70 ^{o}C and then became isotropic (clear yellowish liquid) at the highest melting temperature (Figure 2.2b). At that point, 5 µl of each LC sample was transferred with a micropipette onto three glass slides and covered with glass cover slips. Subsequently, the three samples of CELC substrates were left to cool down to room temperature before examination in a Zeiss AxioPlan2 cross-polarising microscope (Figure 2.3a). The density of the three liquid crystals in the

cholesteric phase was determined at 0.849 g/cm^3. The CELC exist in gel form at room temperature (Figure 2.2c) and was stored in a vial for future use.

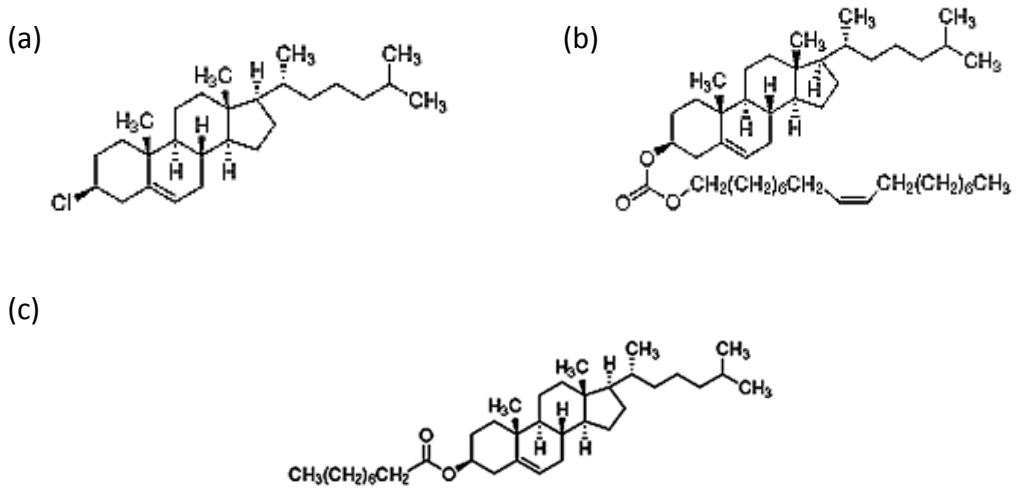

Figure 2.1. Chemical structure of the (a) cholesteryl chloride, (b) cholesteryl oleyl carbonate and (c) cholesteryl perlagonate.

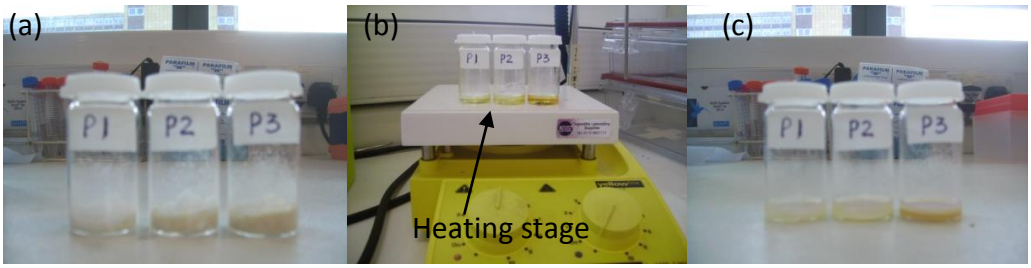

Figure 2.2. (a) The solid mixtures of cholesteryl ester liquid crystals in vials, (b) the mixtures melted at melting temperature (112 ^{o}C), and (c) Cholesteryl ester liquid crystals gel at room temperature (25 ^{o}C). Labels of P1, P2 and P2 on the vials represent CELCP1, CECLP2 and CELCP3, respectively.

Other than the cholesteric liquid crystals, this work investigated the suitability of TL205 (Merck, Germany) as a cell adhesion substrate in the preliminary study. TL205 was supplied in an aqueous solution which has a clearing point at 80 ^{o}C and was used directly as supplied without any purification. The exact composition of TL205 is proprietary and unknown.

2.2.2 Thermal and Liquid Crystalline Phase Analysis

A temperature stability study was conducted for CELCP1, CELCP2, CELCP3 and TL205 by using cross-polarising optical microscopy (POM). Before studying the phase of the LCs in the microscopy, each LC sample were spread over a glass cover slip using a scraper and re-melted on a heating stage. This is to make sure that the shear sensitive cholesteryl ester liquid crystals return to the cholesteric phase before being studied in the microscopy. Under the illumination of an AxioPlan2 polarising optical microscope (POM) at 20x magnification, each liquid crystal substrate was placed on a Linkam THM600 hot stage. This Linkam hot stage was controlled by a Linkam control plug-in software. Subsequently, the temperature was increased at a rate of 1 ^{o}C/min and a sequence of the LC transition images starting from 20 ^{o}C was captured at 1 frame/sec. The heating temperature was terminated at 37 ^{o}C. Photomicrographs were captured using AxioVision version 4.6 software bundled to a Zeiss Axiocam MRc5 digital camera mounted on the Zeiss AxioPlan2 microscope (Figure 2.3a).

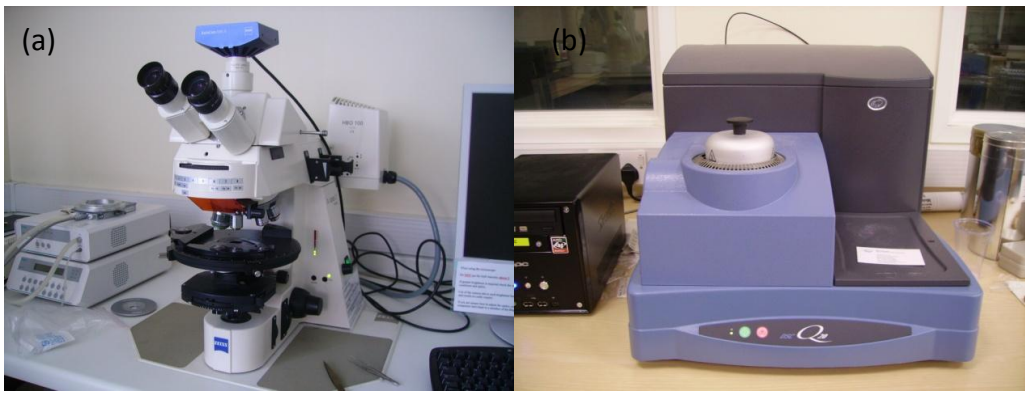

Figure 2.3. (a) A Zeiss AxioPlan2 digital microscope, and (b) Thermal analysis under a DSC Q2000 system.

Further thermal analysis on the CELCP1-P3 samples was performed by using a DSC Q2000 Differential Scanning Calorimeter (DSC). TL205 was not examined using DSC because of availability issues. For the DSC analysis, 2 – 3 mg of each CELCP1-P3

was analysed (Figure 2.3b). A ramp temperature of 1 ^{o}C/sec was applied to the samples from -50 ^{o}C to 120 ^{o}C, and the relationship between heat flow and heating temperature was obtained.

2.2.3 Preparation of Liquid Crystal Substrates for Liquid Crystalline Study

CELCP2 gel will be mainly used in this research and the preparation of the liquid crystal substrates coated with CELCP2 will be described. The CELCP2 gel was prepared as described in section 2.2.1. When CELCP2 gel was re-melted in a vial on a heating stage, 5 µl of the fluid mixtures was spread at a thickness of approximately 100 – 200 µm on two glass cover slips using a cell scraper (Corning Incorporation) and then, each of the LC substrates was immediately transferred to a cooling fan to be spin coated at 1000 rpm for 30 seconds. The thickness of the liquid crystal coating was controlled by using thin gold grids with a thickness of 100 µm (Agar Scientific, UK) and confirmed by using a microscopy focusing technique.

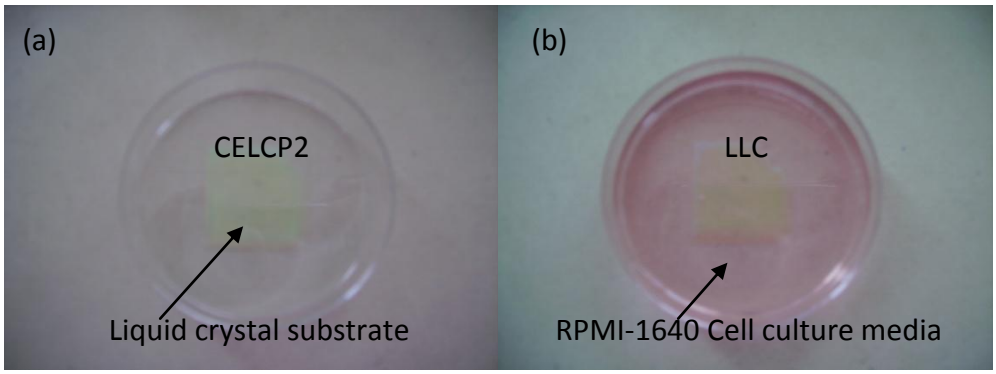

Figure 2.4. Liquid crystal substrates in the (a) absence (CELCP2) and (b) presence (LLC) of RPMI-1640 cell culture media.

Subsequently, one of the LC substrates was placed in an empty petri dish (Figure 2.4a) and another in a petri dish containing 6 ml of Roswell Park Memorial Institute (RPMI)-1640 culture media (Figure 2.4b). When maintained in 6 ml of cell culture media, the liquid crystals (CELCP2) transformed to cholesteryl ester based lyotropic

liquid crystals (LLC). Both were incubated in an incubator at 37°C for 24 hours. After incubation, they were removed from the petri dishes and examined in the AxioPlan2 cross-polarising microscope mounted with a digital camera.

2.2.4 Preparation of Liquid Crystal Gel for Rheological Test

A total of four vials containing 1 g of CELCP2 were prepared (Figure 2.5a). One control vial containing CELCP2 was incubated without RPMI-1640 media and three vials containing CELCP2 were incubated with 6 ml of RPMI-1640 media (Figure 2.5b) at 37 °C for 24 hours (LLC24hours), 48 hours (LLC48hours), and 72 hours (LLC72hours).

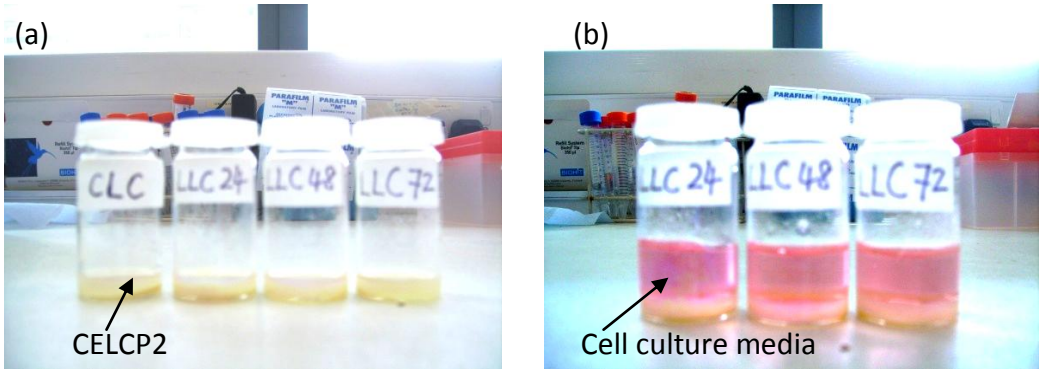

Figure 2.5. Samples of CELCP2, LLC24hours, LLC48hours, and LLC72hours (a) before, and (b) after incubation in cell culture media for 24, 48 and 72 hours at 37 °C.

2.2.5 Amplitude and Frequency Sweep Tests

For the rheological characterisation, amplitude and frequency sweep tests were applied to CELCP2, LLC24hours, LLC48hours and LLC72hours, respectively. The liquid crystal gel was transferred to the stationary disc of an Anton Paar Rheoplus MCR501 strain-controlled rheometer (Figure 2.6a) using a spatula. The liquid crystals were then sheared in the rheometer at a gap of 0.5 mm between a rotating disc of 25 mm diameter and the stationary disc, both of which were heated to 37 °C (Figure 2.6b). The region of linear viscoelasticity was determined by oscillatory measurements for which the maximum strain amplitude (γ) was increased from 0.001 to 1 (0.1 - 100 %

shear strain) over a frequency range of 0.1 - 10 s^{-1}. Frequency sweep experiments were performed at a constant strain amplitude of 5 % (within the linear viscoelastic regime) over a frequency range of 0.01 - 100 s^{-1}, in which the storage modulus (G') and loss modulus (G'') were determined. The complex viscosity (η*) of the cholesteric liquid crystals was determined from the shear stress, σ and shear rate, $\dot{\gamma}$ using steady rate frequency sweeps in the range of 0.01 – 100 s^{-1}. In order to reduce solvent vaporisation, a collar was installed to cover the test platform.

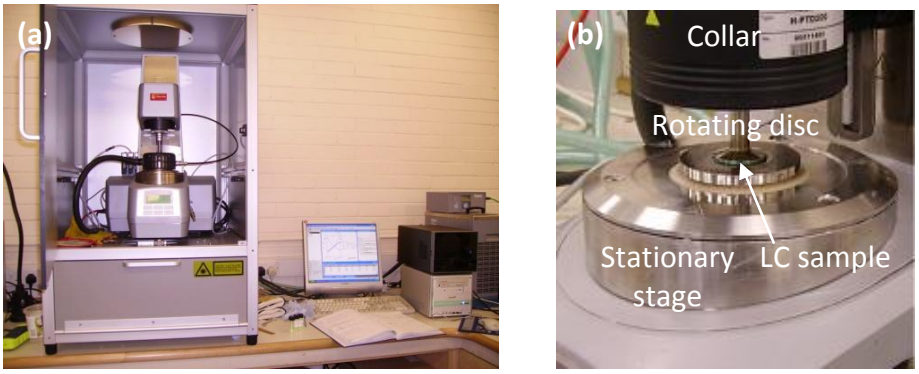

Figure 2.6. (a) A MCR501 rheometer and (b) LC sample under test.

2.2.6 Preparation of Human Keratinocyte Cell Lines

Human keratinocyte cell lines (HaCaT) were kindly provided by Dr. Steve Britland (University of Bradford). These cells were used to examine cell/liquid crystal interactions. Sub-cultures of HaCaT cells were maintained in a 25 cm^2 cell culture flask of tissue-culture (TC) graded. When reaching confluency, they were split using the following procedures. The old media of the culture flask with confluent cells was removed from the cell culture flask and the flask was washed three times with 5 ml Hank's Balanced Salt Solution (HBSS). After washing, the cells were detached from the culture flask surface with trypsin (0.5 mg/ml) in an incubator at 37 ^{o}C for 4 minutes. 5 ml of RPMI-1640 media supplemented with L-Glutamine (2 mM, Sigma Aldrich, UK), penicillin (100 units/ml, Sigma Aldrich, UK), streptomycin (100 mg/ml, Sigma Aldrich,

UK), Fungizone (2.5 mg/l, Sigma Aldrich, UK) and 10 % Foetal Calf Serum (Promocell, UK) was then added into the culture flask to halt the trypsinisation process. Subsequently, the cell suspension was centrifuged for 5 minutes at 1600 rpm. After centrifugation, the supernatant was discarded and the pellet of cells was re-suspended with 5 ml of RPMI-1640 media. Cells were either replated in a $25cm^2$ TC graded culture flask at a cell density of 1.5×10^4 cells/cm^2 or used for further experiments.

2.2.7 Culturing Cells on the Liquid Crystal Substrates

Liquid crystal substrates and HaCaT cells were prepared as described in section 2.2.3 and 2.3.6, respectively. A liquid crystal substrate was placed in a petri dish and cells were seeded in the petri dish at a density of 500 cells/cm^2 (Figure 2.7). Subsequently, the petri dish containing the liquid crystal substrate and cells was added with 6 ml of supplemented RPMI-1640 cell culture media and incubated at 37 ^oC for 24 hours. After 24 hours of incubation, the responses of the LC to cell adhesion were studied in a phase contrast microscope mounted with a digital camera at 25x magnification and linked to the Scion Imaging Software.

2.2.8 Characterising the Time-Dependent Viscoelasticity and Viscosity of the Liquid Crystal In-Situ

The in-situ viscoelasticity and viscosity of the time-dependent liquid crystals were examined via a cell relaxation and cell fixation experiment, respectively. In an in-situ rheological method used by Stoodley et al. (Stoodley et al., 1999), fluctuations in fluid shear were applied to observe the in-situ rheological behaviour of biofilms. This method is not suitable for our in-vitro cell culture on liquid crystal surfaces that were not subjected to fluid flow. Therefore, this work has developed new in-situ methods using cells as a source of stress generators to characterize the time-dependent

rheological behaviour of the LLC. To achieve this, the cells were relaxed or fixed by cytochemical treatment methods in order to control the stresses of cells exerted on the liquid crystal surface. In our in-situ cell relaxation and fixation methods, cytochalasin-B and formaldehyde were used to disrupt the actin cytoskeleton and fix the morphology of cells, respectively. Consequently, the stresses generated by cells can be either released or sustained constantly due to the responses of cells to the treatments of cytochalasin-B and formaldehyde, respectively (Paljarvi et al., 1979, Stournaras et al., 1996). Therefore, the cell induced structural changes in the LC surface can be monitored while maintaining the structural integrity of the lyotropic liquid crystals. Corresponding to the controlled stresses, recovery of a flat LC surface from deformations represents the ability of the liquid crystals to display elastic recovery while creep of the deformation represents a decrease in the viscosity of the liquid crystals. The elasticity is a reversible stress-strain behaviour while viscosity is a measure of resistance to deformation (Barnes et al., 1989, Whorlow, 1992).

Prior to cell plating, four liquid crystal coated substrates (LCS) were prepared as previously described and each was placed in a petri dish. HaCaT cells were seeded in the petri dishes at a density of 500 cells/cm^2. The cells cultured on the liquid crystal substrate were maintained in 6 ml of RPMI-1640 cell culture media in an incubator at 37 ^{o}C (Figure 2.7).

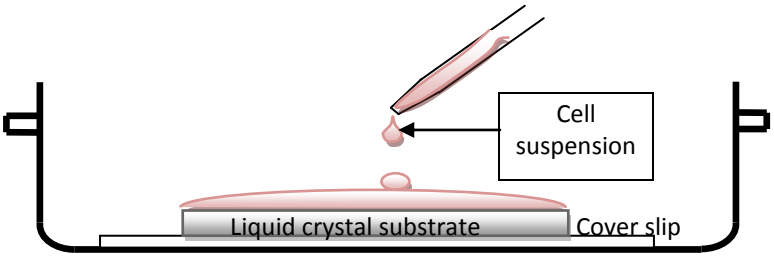

Figure 2.7. Deposition of cell suspension on a liquid crystal substrate before an addition of RPMI-1640 media.

After 24 hours of incubation, one of the petri dishes was removed from the incubator and treated with 5 µl of 30 µM cytochalasin-B for an hour at 37 ^{o}C. Cytochalasin-B (35 mg/ml, Sigma Aldrich, UK) was solubilised in 0.042 % (v/v) ethanol (in distilled water). The sample treated with cytochalasin-B was used to study the structural changes of the liquid crystal surface induced by cells. The cytochalasin-B treatment was repeated for the second and third LC substrates after 48 and 72 hours of incubations, respectively. For all the three treatments, the petri dishes were placed on a hot stage maintained at 37 ^{o}C while time lapse images were captured every 5 minutes over an hour via a phase contrast microscope mounted with a digital camera. This was performed to monitor the changes in the surface of the liquid crystals with respect to the changes of viscoelasticity in-situ over time.

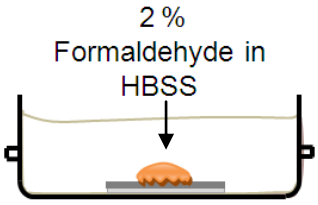

Figure 2.8. A bath of 2 % Formaldehyde in HBSS containing cell cultured on the liquid crystal substrate.

For monitoring the viscosity of the liquid crystals using in-situ cell fixation technique, the last petri dish containing cells cultured on a liquid crystal substrate was treated with 2 % formaldehyde (Sigma Aldrich, UK) to preserve the morphology of the cells or fix the cell stresses after 24 hours of incubation. The culture media in the petri dish was replaced with a bath of 2 % formaldehyde and then incubated at 37 ^{o}C (Figure 2.8). After the addition of formaldehyde, cells induced structural changes to the surface of the lyotropic liquid crystals and they were monitored every 24 hours during a period of 96 hours by using a phase contrast microscope. To monitor the

viscosity of the lyotropic liquid crystals under constant stress in this context, it was necessary to monitor the LCs at least 16 hours after fixation because cells shrink within this period of treatment in formaldehyde (Paljarvi et al., 1979, Leong and Gilham, 1989). After 16 hours, one could assume forces exerted by the cells would be constant and any changes after that would be due to a change in the strain of material. The ImageJ software was used to measure any time related structural changes in the LCs appeared in the phase contrast micrographs.

2.2.9 Determining Young's modulus of the Liquid Crystals

2.2.9.1 Atomic Force Microscopy Nano-Indentation Method

Liquid crystal coated substrates were prepared as described in section 2.2.3 and cultured in petri dishes containing cell culture media in an incubator at 37 ^{o}C. The objective of this experiment was to determine the Young's modulus (E) of the LC surface in fluid using an AFM based nano-indentation technique. After 24 hours of incubation, the petri dish containing a liquid crystal coated substrate was placed in a Hysitron Triboscope nano-mechanical testing system bundled with Hysitron Triboscope 3.5 software to obtain the force-displacement curve for the LC substrate maintained in the culture media (Figure 2.9a). A Berkovich pyramidal indenter with a tip of 200 nm in radii was immersed in the fluid (Figure 2.9b). A loading rate of 750 µN/s and a hold period of 3 seconds were applied to indent the substrate. After the hold period, the indenter was unloaded to complete a cycle of measurement. The hold time compensated for any creep of the material.

During the measurement using AFM based nano-indentation, careful considerations were made to take into account the fluid buoyancy, hold time and re-

cycling indentations in the measurements. An average of twenty measurements per substrate was taken at various sites of indentation.

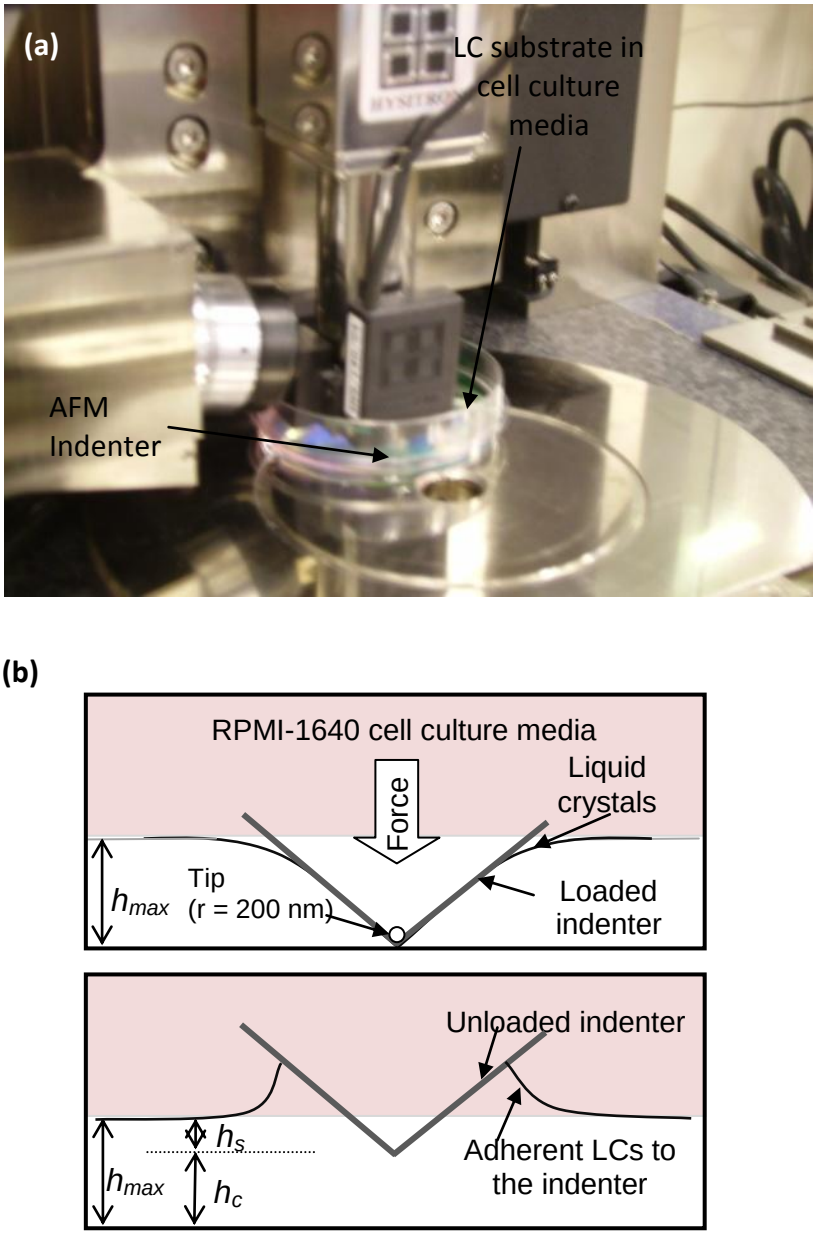

Figure 2.9. (a) AFM nano-indentation of cholesteryl ester liquid crystal after incubation in cell culture media at 37 ^{o}C for 24 hours. (b) Schematic diagrams depicting the loading and unloading of an indenter and the associated displacement parameters. The parameter, r denotes the radius of a tip.

The data from the force-displacement for each indentation was collected and plotted using Statistical Package for Social Sciences (SPSS) software. The contact

stiffness, *S*, of the liquid crystals was then determined from the unloading curve using the power law fits (Pharr, 1998, Doerner and Nix, 1986, Oliver and Pharr, 1992),

$$S = \frac{dp}{dh}(h = h_{\max}) = Am \cdot \left(h_{\max} - h_f\right)^{m-1} \tag{2.1}$$

where *p* is the loading force in μN, and h is the displacement with h_{max} and h_f being the maximum displacement and final unloading depth in nm, respectively. *A* and *m* are the curve fitting parameters determined empirically by the Triboscope software.

The contact depth, h_c was calculated from the load-displacement data by including the geometric constant, $\varepsilon = 0.75$ (Oliver and Pharr, 1992) in the following equations,

$$h_c = h_{\max} - h_s \tag{2.2}$$

$$h_s = \varepsilon \frac{P_{\max}}{S} \tag{2.3}$$

where, h_s is defined as the perimeter contact depth and maximum loading force, P_{max} was determined from the peak of the load-displacement curve.

The contact area for an ideal Berkovich indenter was then established using the following equation (Oliver and Pharr, 1992),

$$Area = 24.5 h_c^{\,2} \tag{2.4}$$

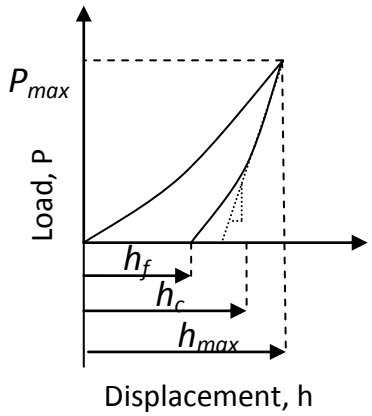

Figure 2.10. A typical load-displacement curve with the associated indentation depth and load parameters.

Once the contact area was estimated, the reduced modulus, E_r can be determined,

$$E_r = \frac{S\sqrt{\pi}}{2\sqrt{Area}} \tag{2.5}$$

Where reduced modulus, E_r is a measurement with contributions from both the specimen and the indenter, therefore, the following relationship (Doerner and Nix, 1986) was used to determine the Young's modulus of the liquid crystal:-

$$\frac{1}{E_r} = \frac{1-v^2}{E} + \frac{1-v_i^2}{E_i} \tag{2.6}$$

where *E* and *v* are the elastic modulus and Poisson's ratio of the test specimen. *E* and *v* with subscript *i,* are the same parameter definitions for the indenter. The Poisson's ratio for liquid crystals was set to 0.5, close to that of the rubber. The E_i and v_i for the diamond Berkovich pyramidal indenter are 1141 GPa and 0.07 (Pharr, 1998), respectively. The Young's modulus determined for all the measurements were averaged.

2.2.9.2 Spherical Indentation Method

Spherical indentation is becoming a commonly use method to determine the Young's modulus of soft gels because this technique provides small strain deformation in a bi-axial direction and it is applicable to permeable or semi permeable membrane (Munevar et al., 2001, Dimitriadis et al., 2002, Ahearne et al., 2005). In our experiment, the Young's modulus of the liquid crystals bonded to a rigid glass substrate in cell culture media was determined by using the theory of Hertz's contact mechanics. Three LC substrates with a thickness, h of approximately 100 µm were prepared as described in section 2.2.3 and incubated at 37 ^{o}C for 24, 48, and 72 hours, respectively.

After incubation, the petri dish containing the liquid crystal substrate was placed on a heating peltier maintained at 37 ^{o}C. Subsequently, a chrome steel ball (Radius, *R* of 250 µm and density of 7.849 g/cm^{3}, simplebearings co., UK) was loaded on the surface of the liquid crystals (Figure 2.11). The mass of the steel ball is 0.5 mg or a weight (gram-force) of 5 µN. The buoyancy corrected weight of the steel ball, *F* was ~ 4.6 µN.

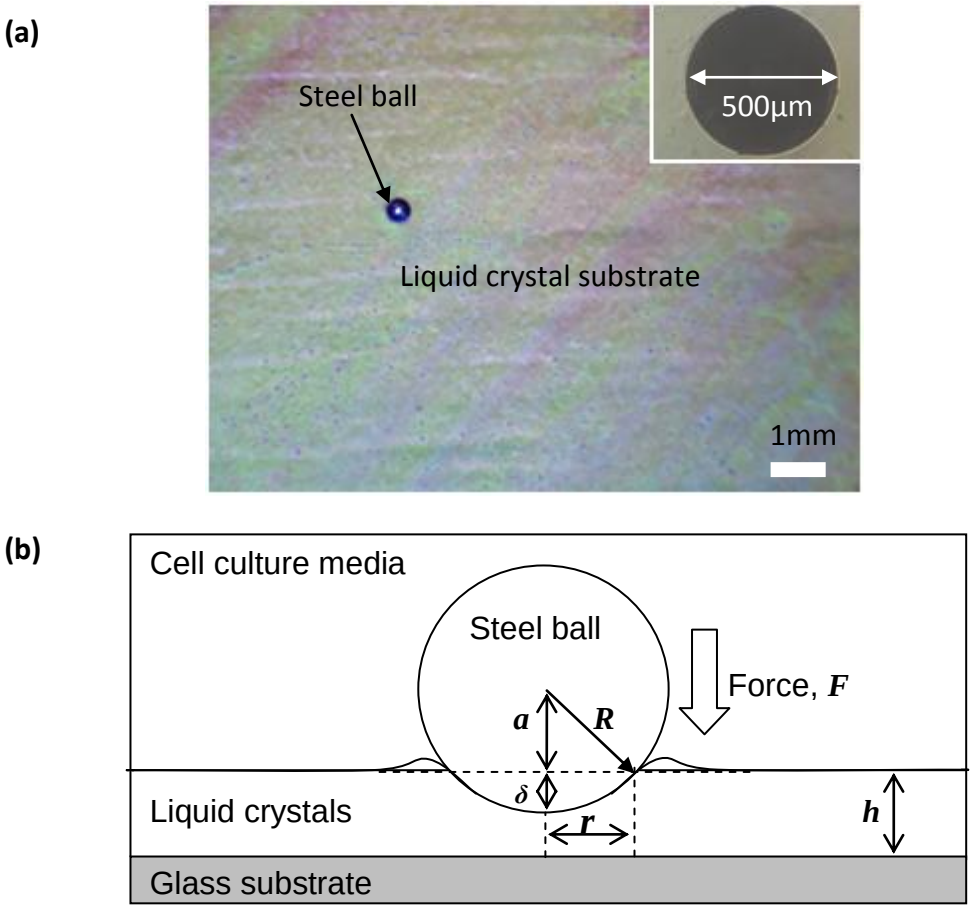

Figure 2.11. (a) A steel ball of 500 µm diameter loaded to the liquid crystal surface in the cell culture media captured with a digital camera (Scale bar: 1 mm); Insert: The phase contrast image of a steel ball. (b) A schematic describing the spherical indentation to surface of the liquid crystal substrate in the cell culture media and the measurement parameters.

In order to determine an appropriate loading period, measurements of creep deformation was performed. During the experiment, a load period at an interval of 10

seconds up to 60 seconds was applied to indent the LC surface. The Young's modulus was determined at the time when the creep deformation was saturated. After the steel ball was unloaded vertically using tweezers, a series of photomicrographs at an interval of 5 seconds were captured by using a digital camera mounted to a cross-polarising microscope and a phase contrast microscope.

The diameter of the contact circle was measured using ImageJ software upon removal of the steel ball. The spherical indentation was repeated randomly at twenty sites for three independent samples of liquid crystals. The indentation by the steel ball of radius, R formed a circular contact area with a radius of *r* (Figure 2.11b). The displacement (δ) of the liquid crystal surface formed vertically under the centre of the steel ball (Figure 2.11b) was calculated by using $\delta = R - a$ where $a = \sqrt{R^2 - r^2}$.

The Young's modulus, *E*, of the liquid crystals was calculated based on equation of the Hertz contact theory as given in equation (2.7),

$$E = \frac{3\left(1-v^2\right)F}{4R^{1/2}\delta^{3/2}} \tag{2.7}$$

where F is the force in terms of weight of a micro sphere, δ is the vertical displacement due to the indentation, R is the radius of the sphere and *v* is the Poisson's ratio of the material. At this point, the Poisson's ratio, v was assumed to be incompressible at 0.5 due to the high water content in the lyotropic liquid crystals. However, the Poisson's ratio will be investigated using a tensile stretch method which will be discussed in the following section.

2.2.10 Measurements of Poisson's Ratio of the Liquid Crystals

To measure the Poisson's ratio of the liquid crystals at a micrometre scale, the mechanical tensile tester for a solid material lacks sensitivity. Therefore, a custom-built microscopy based micro-tensile test system was developed to measure the uni-axial strain of the liquid crystals. The measurement system was developed (See Figure 2.12-2.14) according to the method reported by Stannarius et al. 2004 (Stannarius et al., 2004). In this system, one fixed glass and movable glass displacer was placed on a gridded glass slide (25 μm grids spacing), the movable displacer was attached to a three-axis micrometer and the temperature of the sandwiched glass slides was maintained by a Proportional Integral Derivative (PID) feedback temperature controller system (Figure 2.13). This temperature controller consists of a thermistor attached to the top of the fixed plate at a position adjacent to the measurement site plate and a heating pad was placed under the glass slides as shown in Figure 2.13.

Calibration of the system was first achieved by measuring the Poisson's ratio of Polydimethylsiloxane (PDMS). The PDMS was prepared at 1 : 10 (curing agent : elastometric gel, Sylgard 184, Corning Corp.) mixing ratio. Before the PDMS was cured, 10 nl of the PDMS gel was put in between the edge of the fixed glass slide and movable displacer by using a microneedle. The gel contacting the two plates at an initial distance of 10 μm was left to cure over night before the measurements. With the gridded glass slide as a guide, the separation distance between the fixed plate and displacer was finely tuned by a 3-axis micrometer. Subsequently, the uni-axial deformation in longitudinal direction (y) of the sample was measured by displacing the movable plate in x direction at a speed of 25 μm/min, and the deformations was captured by using a digital camera mounted on a phase-contrast microscope. The deformation of viscoelastic material is a time-dependent quantity, and hence a

relaxation time of 1 minute was considered before each measurement was taken. As shown in Figure 2.12, x_o and y_o are the initial transverse and longitudinal lengths of the sample under test, while x and y are the same defined parameters after the uni-axial stretching, respectively. Similar procedures were used to determine the Poisson' ratio for the liquid crystals except that the Poisson's ratio of the solid PDMS was determined at room temperature.

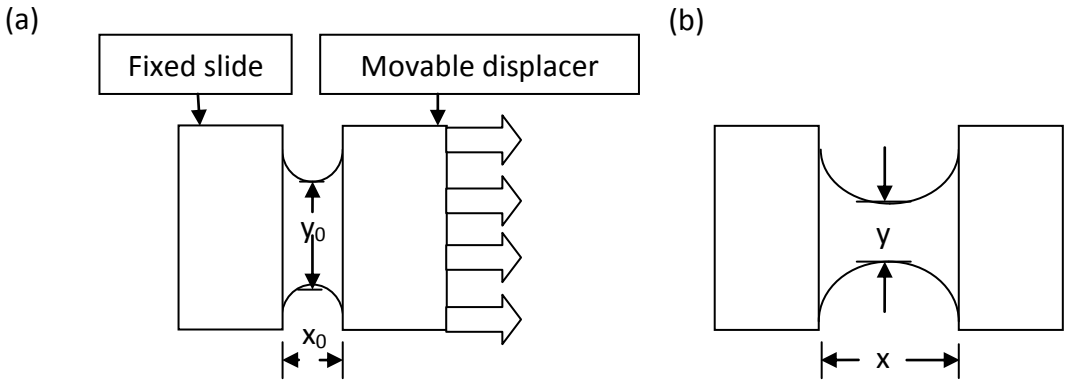

Figure 2.12. Uni-axial tensile strain of a gel sample at (a) initial state and (b) after strain in traverse direction.

The preparation of the LLC samples was as described in section 2.2.3. A LLC substrate was prepared and incubated at 25 ^{o}C for 24 hours. In another group, a CELCP2 substrate was incubated at 37 ^{o}C for 24 hours, and three LLC substrates in cell culture media were incubated at 37 ^{o}C for 24, 48, and 72 hours, respectively. The measurements of the Poisson's ratio for CELCP2 was performed by first putting approximately 10 nl of LC gel at the edge of a fixed glass slide by using a microneedle and steadily bringing the sample gel into close contact with the edge of another piece of movable glass slide as shown in Figure 2.12-2.14. The temperature of the test samples was constantly checked with an infrared thermometer at close proximity (Figure 2.14b). The initial slides separation, x_o for LC gel was set at 50 μm and Δx was increased at a speed of 25 μm/step. These procedures were repeated for LLC24hours,

LLC48hours and LLC72hours. Extraction of LLC gel was performed by scraping the transparent membrane residue on top of the liquid crystal substrate in cell culture media.

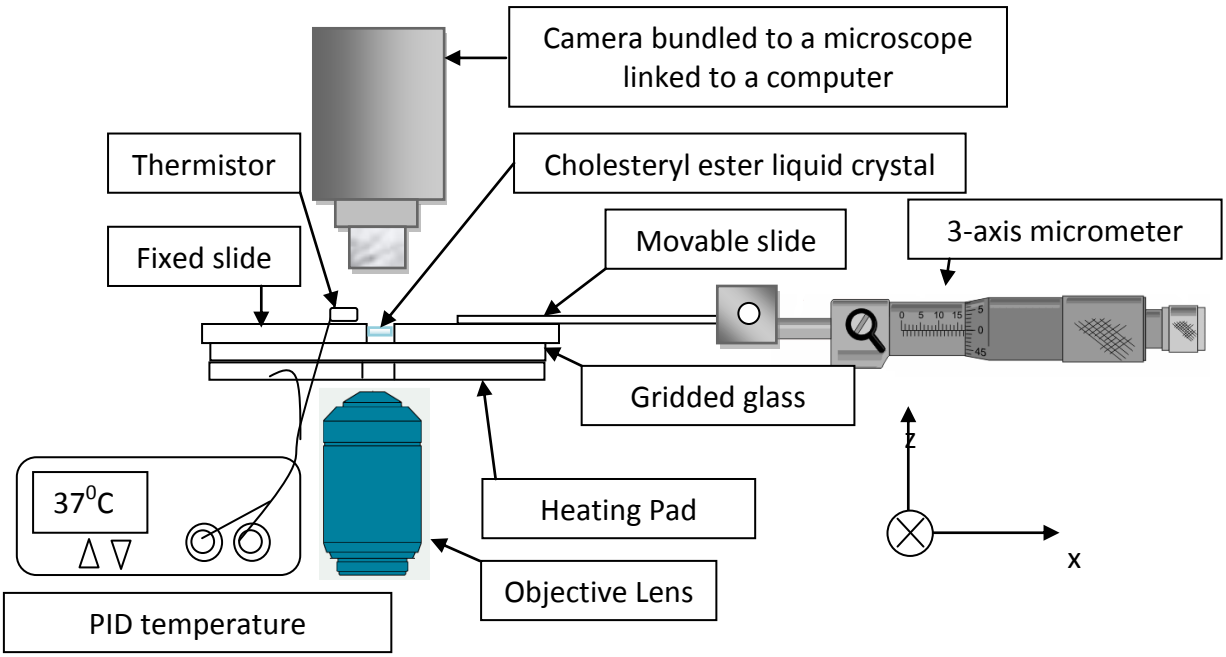

Figure 2.13. A schematic diagram of a custom-built uni-axial micro-tensile stretch system.

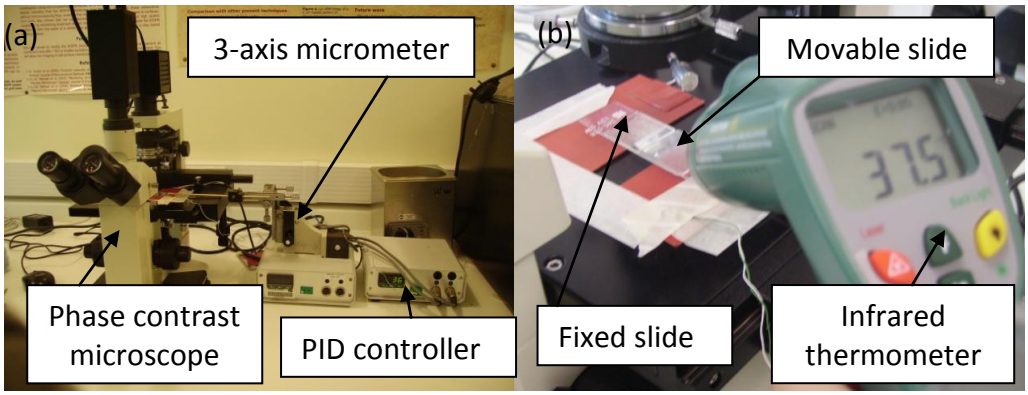

Figure 2.14. (a) The actual setup of a micro-tensile system for measuring Poisson's ratio of cholesteryl ester liquid crystals, and (b) an image showing the temperature of a sample maintained at ~37 ^{o}C.

For each of the LC substrates, ten randomly selected samples were picked and the measurements were performed in isolation. The temperature set for the test samples is according to their incubation temperature, respectively.

Subsequently, equations (2.8-2.9) were used to determine the deformation in a plane and then, Poisson's ratio was calculated (Urayama et al., 1993). The strain of the material in uni-axial direction is determined by,

$$\varepsilon_1 = \frac{x}{x_0} \tag{2.8}$$

and $\varepsilon_2 = \frac{y}{y_0}$ (2.9)

where x_o and y_o are initial dimensions. Variables x and y, are the dimensions after deformation in each direction (Figure 2.12a-b). Deformation in the z direction was not considered in this work. For a viscoelastic material which exhibits non-linear strain such as the PDMS (Takigawa et al., 1996), the generalised solution for Poisson's ratio, ν was given by (Urayama et al., 1993).

$$\varepsilon_2 = \varepsilon_1^{-\nu} \tag{2.10}$$

$$\nu = -\frac{\log \varepsilon_2}{\log \varepsilon_1} \tag{2.11}$$

2.2.11 Statistical Analysis

All the experiments were performed in triplicate unless stated. The storage modulus, loss modulus and complex viscosity of the frequency sweeps were expressed as means ± standard errors (SE) while the length of deformation lines was expressed as means ± standard deviations (SD). For the comparison of the storage modulus, loss modulus, and complex viscosity, statistical analyses were performed by using a one way Analysis of Variance (ANOVA) followed by Tukey's honest significance test (HSD) multiple comparisons post-test available in the Statistical Package for Social Sciences (SPSS) software. Differences in the means were considered significant for $p < 0.05$. The Young's modulus of the liquid crystals was expressed as means ± standard deviation

(SD). The Poisson's ratio of the LLC was obtained from the gradient of a linear regression line plotted in a graph of log ε_2 versus long ε_1. The error of the data points to the approximated line was calculated by using the least square error method, which also gives the standard error (SE) of the slope. The Poisson's ratio was expressed as means ± SE. Tukey HSD test was performed to test the significant differences ($p < 0.05$) in the time-dependent deformation length (means ± SD) measured in the in-situ cell fixation experiment.

2.3 Results and Discussion

2.3.1 Temperature Stability of the Liquid Crystals

The phase transition of the nematic and cholesteric liquid crystals was studied by using cross-polarising microscopy. Under the illumination of the polarising microscope, TL205 was observed with multi-color reflectivity. Heat ramp from room temperature (20 ^{o}C) to incubation temperature (37 ^{o}C) changed the physical structure and colorful optical reflections of TL205 into monochromatic reflections as shown in Figure 2.15a and Figure 2.15e, indicating the temperature instability of TL205.

The birefringence properties of the CELCP1-P3 at room temperature were displayed with bright cholesteric patterns Figure 2.15b-d. This is because the helically arranged liquid crystal molecules have undergone a change in pitch length. After heating to 37 ^{o}C, the major structure and optical reflections of CELCP1, CELCP2 and CELCP3 remained constant indicating that cholesteryl ester liquid crystals are not sensitive to room or incubation temperature.

However, these birefringence properties turned into uniformed color reflectivity when cover slips were placed over the samples which indicate their shear sensitivity characteristics under compression (Figure 2.16). Under the compression of the cover

slips, CECP1, CELCP2 and CELCP3 changed from reddish cholesteric phase into purple, green and yellowish black cholesteric phases under the illumination of cross-polarising microscopy, respectively (CELCP3 appeared in pale purple colour in the AxioVision software was due to the camera exposure problem). Among the three liquid crystal samples, the reflectivity of CELCP3 changed most dramatically in the cross-polarising microscope after a cover slip was placed over it (Figure 2.16). This indicates that CELCP3 gel is highly sensitive and the black colour illumination was correlated with the dispersion of molecules under compression. Therefore, it may not be able to withstand the hydrostatic pressure of culture media which will be deposited in the cell culture. This required further investigation.

Further thermal analysis was performed by using Differential Scanning Calorimeter (DSC) which has a great sensitivity in detecting energy or heat capacity changes for CELCP1, CELCP2 and CELCP3. Figure 2.17 shows a graph of heat flow as a function of temperature. The glass transition temperatures (T_g) of the three liquid crystal samples appeared as steps in the baseline due to an exothermic reaction and that T_g occurs at ~ -38.67 ^{o}C, -34.26 ^{o}C and -28.75 ^{o}C for CELCP1, CELCP2 and CELCP3, respectively. As the temperature increased, each sample reached its first melting temperature (T_m) which can be seen as endothermic peaks at temperatures ~ 51.43 °C, 54.83 °C and 58.33 °C for CELCP1, CELCP2 and CELCP3, respectively (see Figure 2.17). All three samples remained chemically stable between T_g and up to first T_m, in which there was no sign of endothermic or exothermic activity in the range -20 °C to +50 °C. The three liquid crystal compositions, therefore, have a unique formulation that allows stability over a wide range of temperature. This would enable their use in cell culture at normal incubation temperature (37 °C).

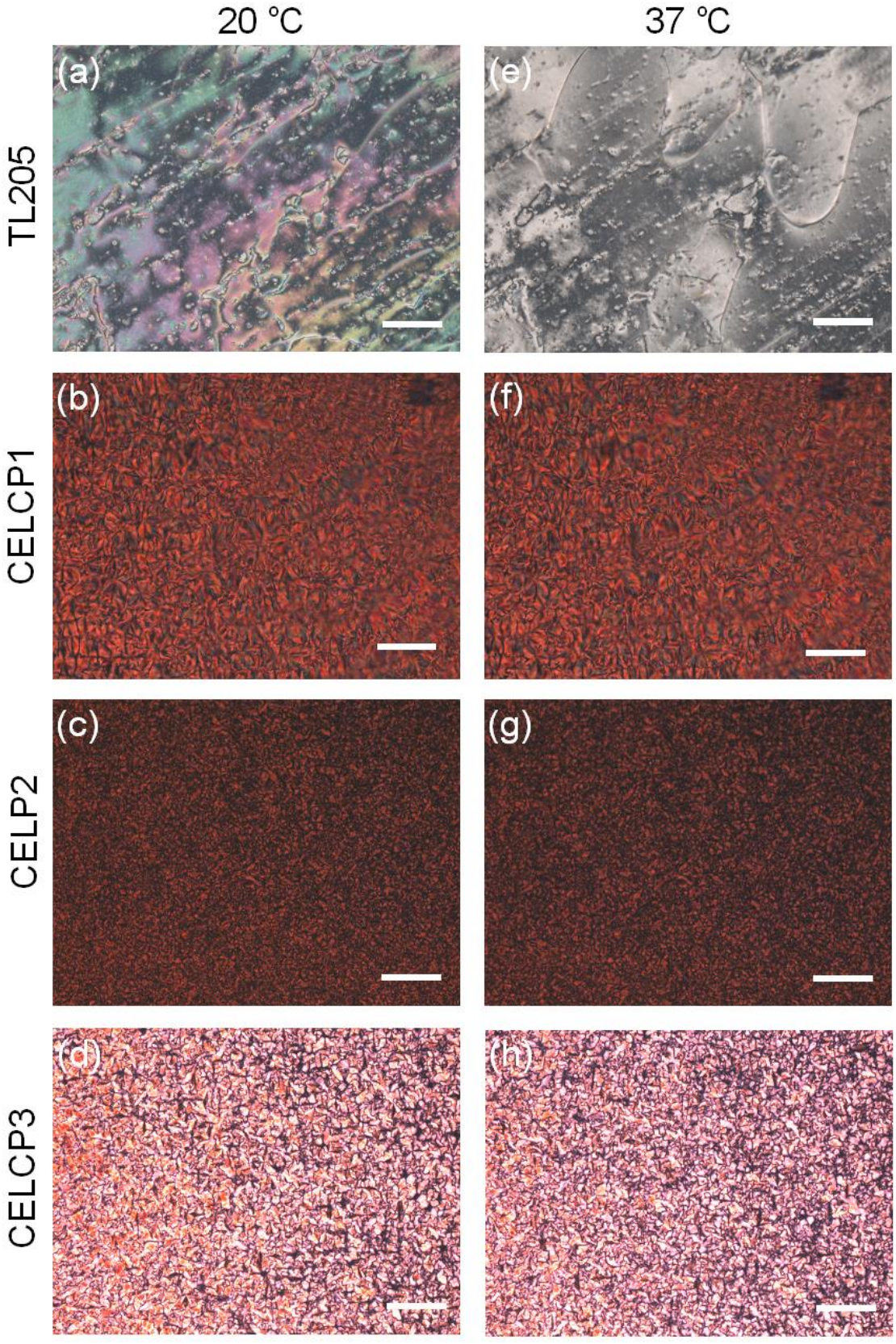

Figure 2.15. (a) Cross-polarising micrographs of nematic liquid crystals TL205 and CELCP1-P3 examined at (a-d) 20 °C and (e-h) 37 °C, respectively. (Scale bar: 50 µm)

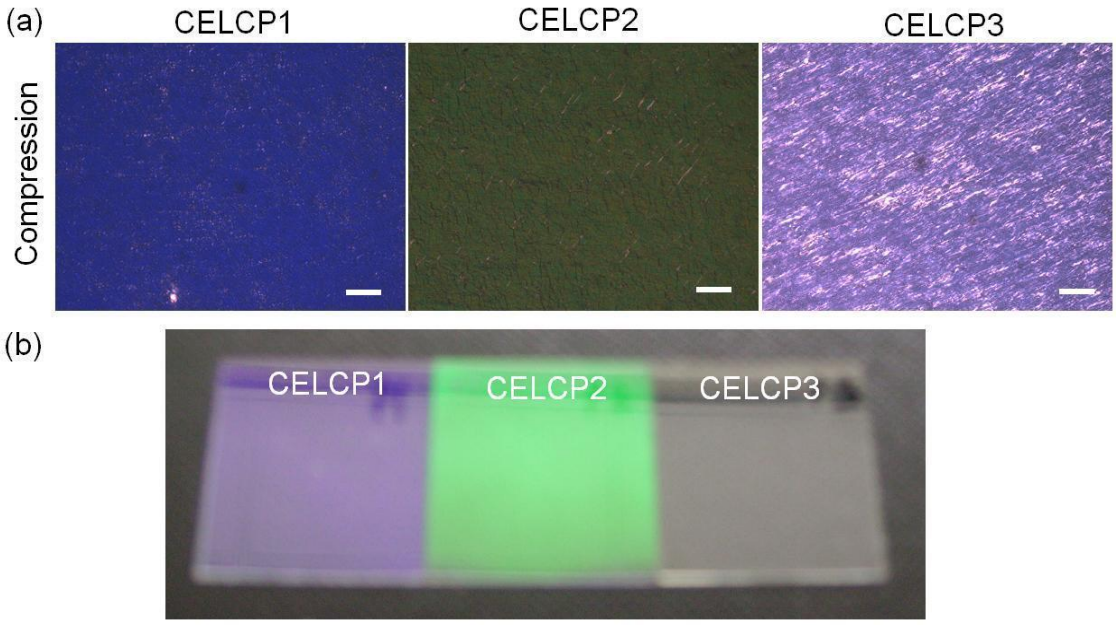

Figure 2.16. (a) Cross-polarising micrographs of CELCP1-P3 sandwiched between a two cover slips examined at 20 °C. (b) CELCP1-P3 sandwiched between two cover slips. This image was taken with a black background. (Scale bar: 50 µm)

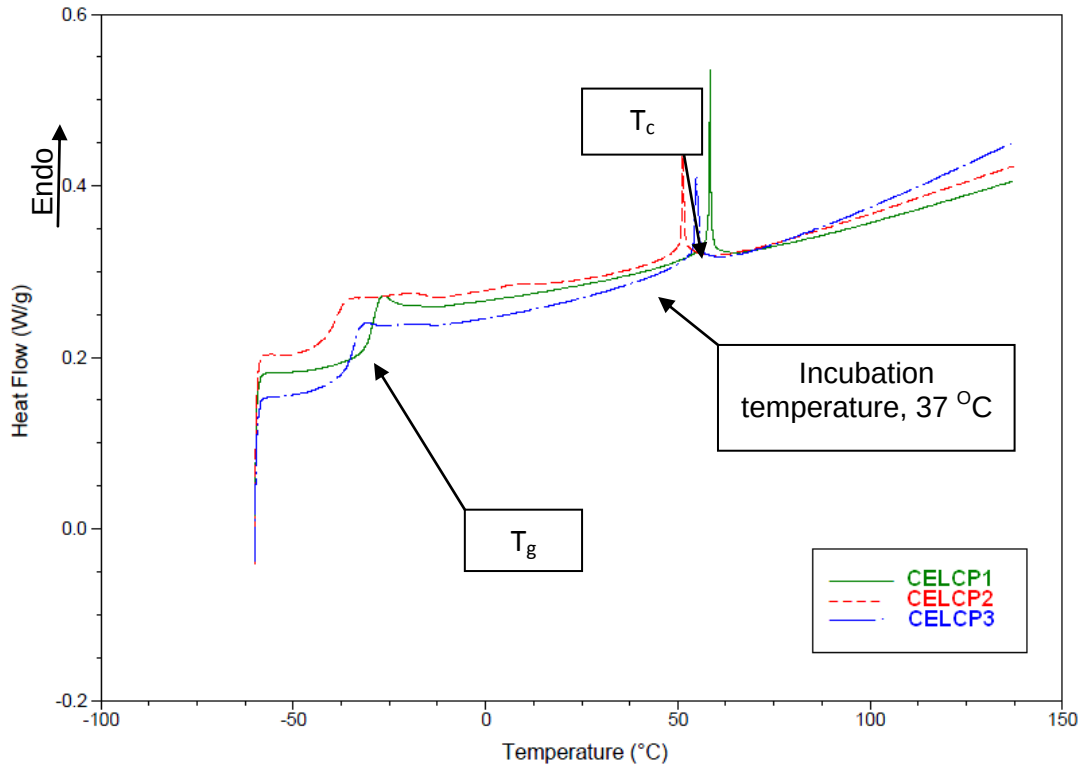

Figure 2.17. DSC profiles for the three compositions of cholesteryl liquid crystals CELCP1, CELCP2 and CELCP3. No exothermic or endothermic activities were observed at 37 °C. T_g denotes glass transition temperature. T_c denotes clearing temperature.

The thermal reactivity of the three cholesteryl ester liquid crystals is similar for the temperature range tested (Figure 2.16). In the liquid crystal mixtures, cholesteryl perlagonate and cholesteryl chloride together play a role in reducing sensitivity to a wide temperature range while demonstrating outstanding shear sensitivity (Fergason et al., 1965). However, with just these two compounds, they form crystals easily in minutes. To rectify this problem, cholesteryl oleyl carbonate was used to reduce the melting point of the mixture and maintain the mixture in cholesteric phase for more than 24 hours (Klein and Margozzi, 1969). In this experiment, the compositions of cholesteryl perlagonate and cholesteryl oleyl carbonate were maintained at the same percentage but the content of cholesteryl chloride was increased in stepwise double for CELCP2 and CELCP3 from the compositions of CELCP1, respectively. This was done to determine the effect of cholesteryl chloride to the shear sensitivity. In correlation with the percentage of cholesteryl chloride, CELCP2 was found with moderate shear sensitivity among the three samples. Despite having similarity in the thermal activity, CELCP2 showed higher stability from room to incubation temperature in the cholesteric phase compared with CELCP1 and CELCP3. From these results, a decision was made to use CELCP2 for the development of a cell force transducer.

2.3.2 Identification of the Liquid Crystalline Phase

In the cross-polarising microscopy, the cholesteric liquid crystal substrate before the addition of cell culture media showed uniform reflectivity which is an indication of a uniform cholesteric layer rotating around the helical axis (Figure 2.18). However, some network structures of oily streaks were seen in the cholesteric phase of the CELCP2.

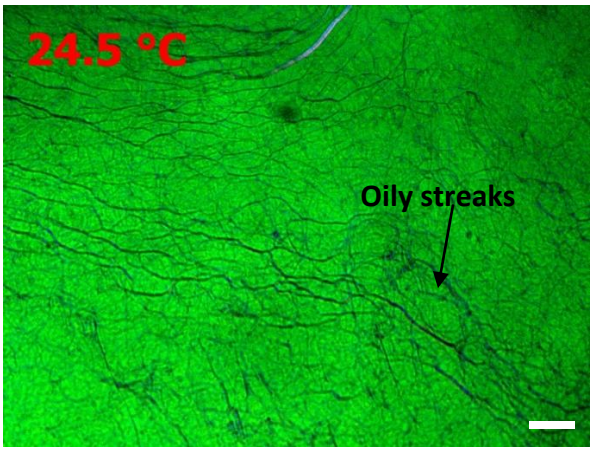

Figure 2.18. The texture of cholesteryl ester liquid crystals CELCP2. (Scale bar: 50 μm)

After cholesteryl ester liquid crystals were immersed in the cell culture media, translucent films were seen overlying the surface of the cholesteryl ester liquid crystals (Figure 2.19a-b). When another similar liquid crystal substrate incubated in cell culture media was removed from the petri dish and examined in a cross-polarising microscope, focal conic textures were seen overlying the cholesteric liquid crystals (Figure 2.20). A focal conic texture is a unique optical microstructure which is usually found in the lyotropic smectic or lyotropic lamellar mesophases under a condition of defects (Choi et al., 2004, Asher and Pershan, 1979, Helfrich, 1994). To investigate the phase of the liquid crystal film in isolation, the film which is approximately 10 - 20 μm thick was carefully transferred to a glass cover slip and examined in a Differential Interference Contrast (DIC) and cross-polarising microscope. The film appeared fluidic in DIC microscopy (Figure 2.19c) but dark in cross-polarising microscopy (Figure 2.19d). Some white streak like bands and some dark focal conic structures were observed in cross-polarising microscopy which indicates the formation of a lyotropic phase for the lipid liquid crystals (Figure 2.19 and Figure 2.20). This result indicates that uniform and homeotropically aligned lipids (smectic phase) in lyotropic phase have their directors normal to the glass surfaces.

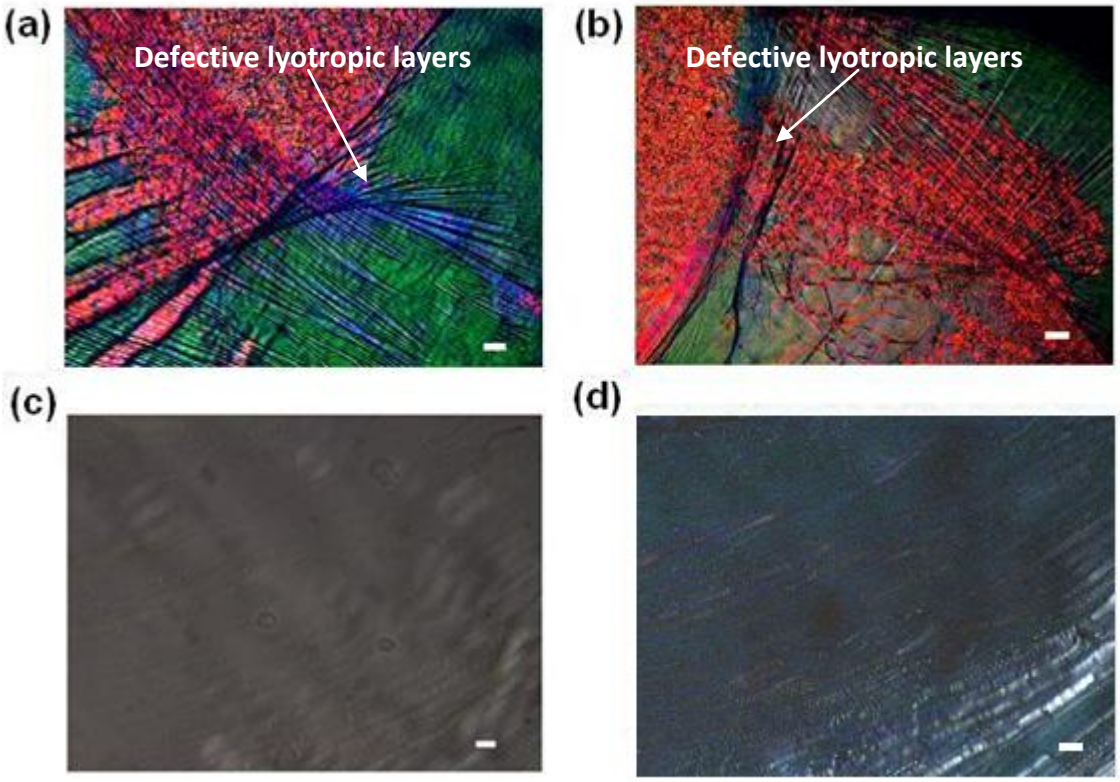

Figure 2.19. (a-b) Cross-polarised micrographs show a similar liquid crystal membrane drifting off the bulk cholesteric liquid crystal or the defective lyotropic liquid crystals. (c) A DIC and (d) cross-polarised micrographs of the same defect-free liquid crystal film examined in isolation. (Scale bar: 25 µm)

These well-aligned molecules appear uniformly dark when viewed through the cross-polariser because their alignments do not polarise the incident light but allows light to penetrate through the first polarizer, and then blocked by the second polariser (Asher and Pershan, 1979). This leads to observation of dark fields when viewed down the optical axis.

However, the defects in LC alignments create a plane of polarisation to the incident light which is neither parallel nor perpendicular to the tilt direction, in which, the light will be elliptically polarised through the pair of crossed polarisers (Hyde, 2001, Asher and Pershan, 1979) and creates bright view in the optical axis. Therefore, an unaligned lipid-water layer appears to be non-uniform and highly coloured in high

variations of tilt layers (Figure 2.19a-b and Figure 2.20). When the uni-axial lipid layer was drifted away and rolled up in defects, they form the concentric ringed defect structures or focal conic structures (Asher and Pershan, 1979).

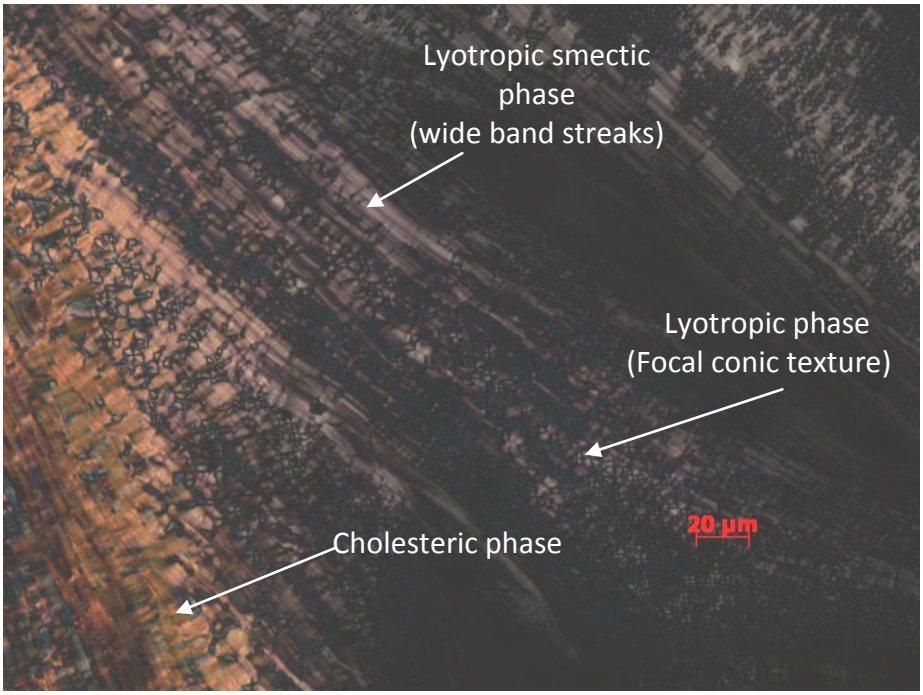

Figure 2.20. A cross-polarising micrograph of cholesteric based lyotropic liquid crystals shows the wide band streaks and focal conic textures.

This study shows that cholesteryl ester liquid crystals when immersed in a solvent formed lyotropic smectic layers associated with the amphiphilic molecules re-orientation, such that the hydrophilic heads (ester bonds) orientate towards the water and hydrophobic hydrocarbon tails (fatty acids) orientate towards the bulk layer of cholesteric liquid crystals (Figure 2.21).

In cell culture media, any distortion to the uni-axial lyotropic liquid crystals (Figure 2.21) could induce birefringence changes as seen in Figure 2.19. A shear originated from the flow of culture media forces the lyotropic layer to deform (Figure 2.22), as a result, the lyotropic liquid crystals appeared with stratification of dark and bright fields which was observed as band-like structure (Figure 2.20). Multiple optical

structures can exist in the lyotropic liquid crystals when the liquid crystals are severely distorted (Figure 2.20).

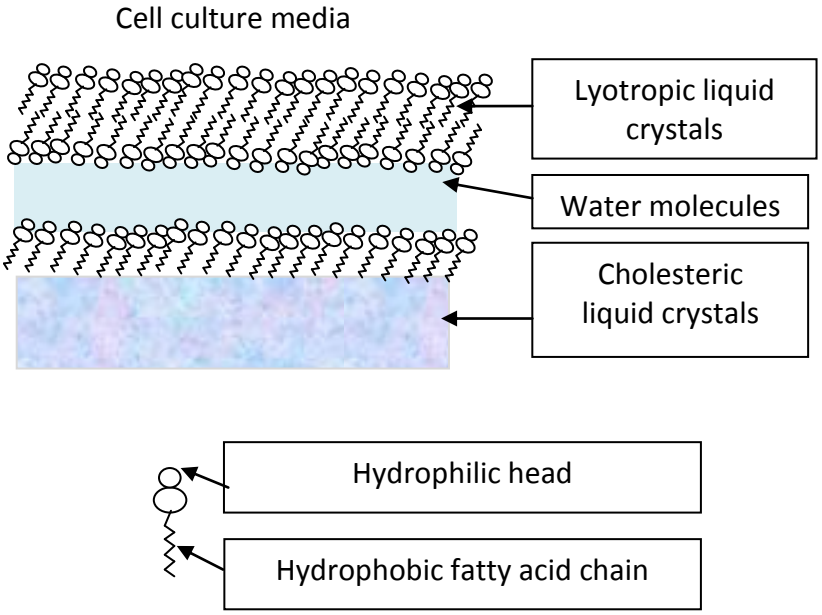

Figure 2.21. The proposed structure for the cholesteryl ester based lyotropic liquid crystals.

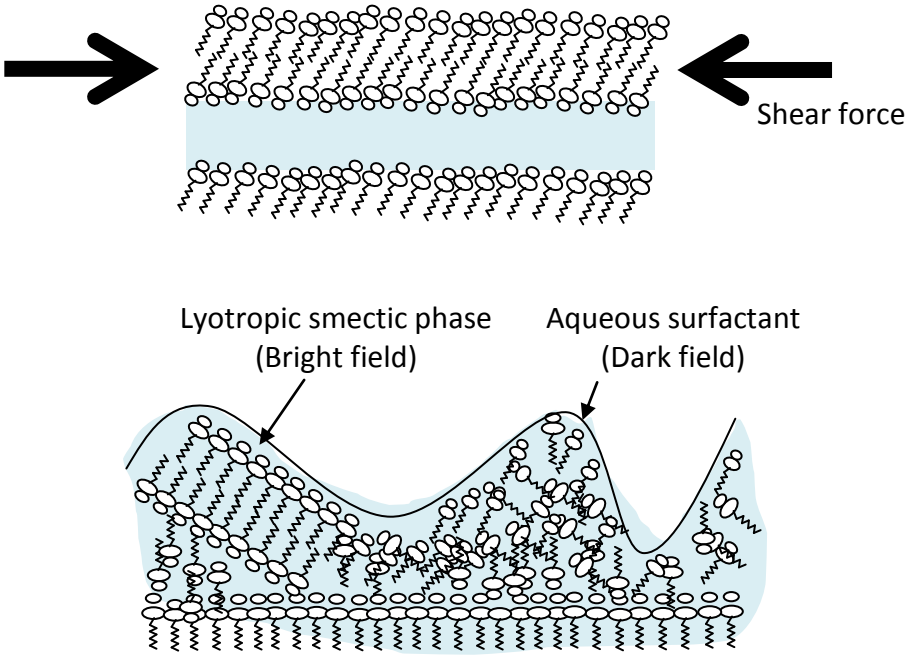

Figure 2.22. A schematic describing the effect of shear stress to the lyotropic smectic liquid crystals.

Clearly, the cell culture media has altered the physical properties and structure of the cholesteric liquid crystals, in which the amphiphilic liquid crystal molecules had

self-assembled into bilayers of lipid molecules that are interlaced by water molecules in a lyotropic or lamellar system (Asher and Pershan, 1979). The binary system (water-lipid interface) has been described as a translucent layer, basically showing fluid-like properties (Munoz and Alfaro, 2000) and this is consistent with the observations found in this work (Figure 2.19).

After an interaction with the cell culture media, the co-existent of cholesteric and multi-lamellar phases suggest that the rheological properties of the cholesteric liquid crystals probably had been altered (Helfrich, 1994). Therefore, an investigation on the effects of immersion in cell culture media to the cholesteric liquid crystals by using rheology is needed.

2.3.3 Stabilisation of Shear Modulus at Low Shear Strain

The strain dependent shear modulus (0.1 – 100 %) was investigated at various shear rates (0.1 - 10 s^{-1}) for the liquid crystals incubated in cell culture media for 24, 48 and 72 hours (Figure 2.23). For ω = 10 s^{-1}, both G' and G" remained constant for LLC24hours (G' = 8.23Pa, G" = 13.8Pa), LLC48hours (G' = 8.97 Pa, G" = 11.7 Pa) and LLC72hours (G' = 5.44 Pa, G" = 10.2 Pa) up to ~ 5 % strain and decreased thereafter (Figure 2,22a). All three LLC samples presented G" greater than G' throughout the shear strains indicating a viscous behaviour.

For ω = 1 s^{-1}, both G' and G" for LLC24hours (G' = 2.85 Pa, G" = 2.77 Pa), LLC48hours (G' = 2.42 Pa, G'' = 2.36 Pa) and LLC72 hours (G' = 1.79 Pa, G" = 1.67 Pa) remained constant but with G' > G" up to ~ 5 % strain (Figure 2.22b). During this constant phase, G' and G" were not a function of the strain and the liquid crystals presented an elastic behaviour. At approximately 5 % strain, all three LLC samples

presented a cross-over between G' and G" indicating a transition from elastic behaviour to viscoelastic behaviour (Figure 2.23b).

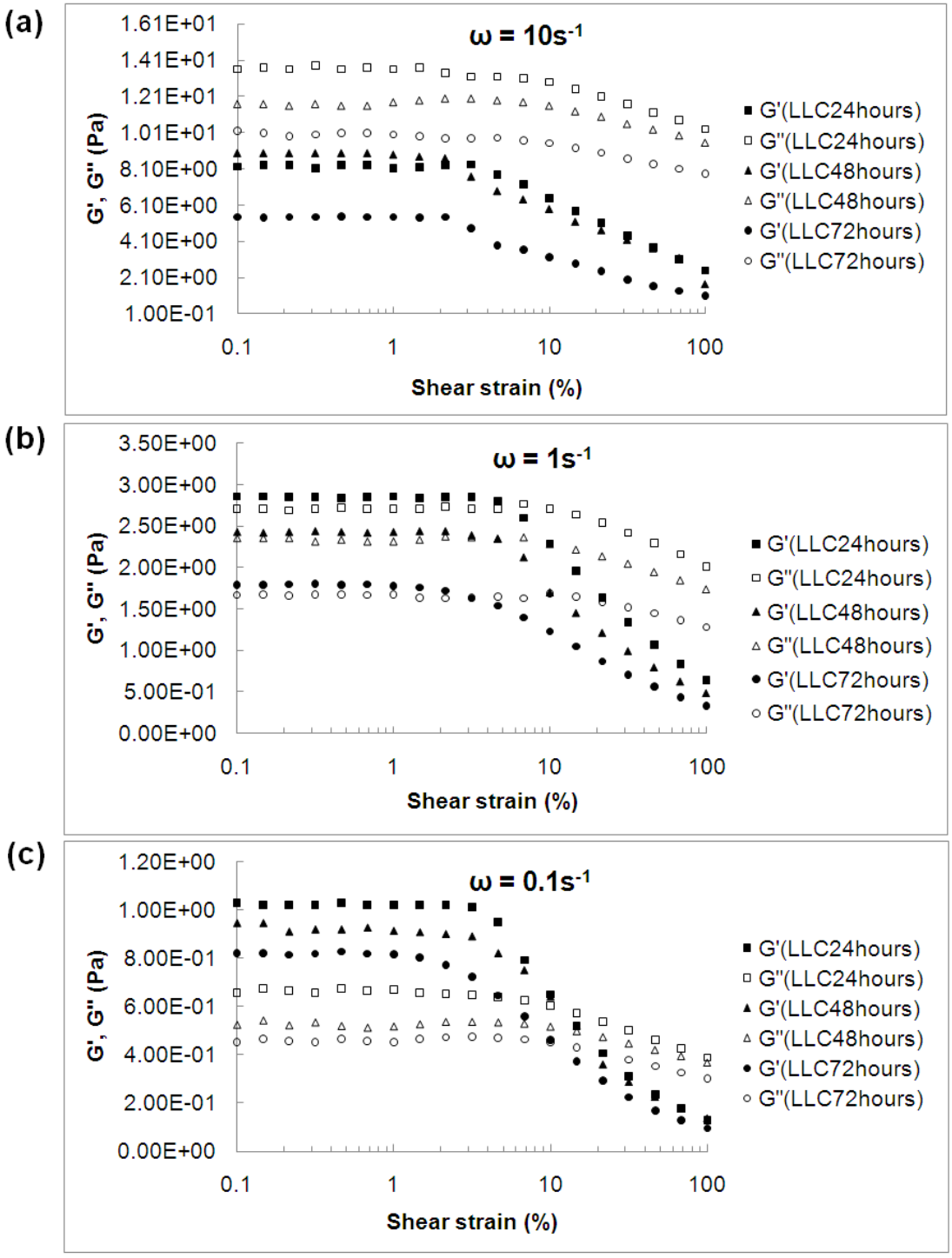

Figure 2.23. Amplitude sweep data showing strain dependent storage modulus (G') and loss modulus (G'') at angular frequencies: (a) ω = 10 s^{-1}, (b) ω = 1 s^{-1}, and (c) ω = 0.1 s^{-1} for LLC24hours, LLC48hours and LLC72hours, respectively.

For ω = 0.1 s^{-1}, G' and G" for both LLC24hours (G' = 1.05 Pa, G" = 0.70Pa), LLC48hours (G' = 0.95 Pa, G" = 0.52 Pa) and LLC72hours (G' = 0.82 Pa, G" = 0.45 Pa) remained constant with G' > G" up to ~10 % strain and decreased gradually after ~10 % strain (Fig. 2C). Similar to the result obtained for ω = 1 s^{-1}, the liquid crystals presented elastic behaviour during the constant phase where G' > G". For all three LLC samples, the difference between G' and G" was greatly increased when the shear rate was decreased to ω = 0.1 s^{-1} indicating an improved elastic behaviour. At approximately 10 % strain at ω = 0.1 s^{-1}, all three LLC samples presented a crossover between G' and G" indicating a transition from elastic behaviour to viscoelastic behaviour (Figure 2.23c).

The results show that at low shear strains (γ < 10 %), both G' and G" remained in plateau where the storage modulus was higher than the loss modulus (G' > G") for the three LLC samples sheared at ω = 0.1 s^{-1} and ω = 1 s^{-1}. However, at high shear strains (γ > 10 %) when ω = 0.1 s^{-1} and ω = 1 s^{-1}, the loss modulus took over the storage modulus (G" > G') of the liquid crystals, which suggests a fluid-like behaviour rather than solid-like behaviour. Therefore, there is a critical shear strain at which transformation from solid-like flow (G' > G") to fluid-like flow (G" > G') occurs. Ramos et al. obtained similar flow behaviour for a cholesteric liquid crystal which showed an upper strain limit of 6 % (Ramos et al., 2002). Overall, the storage modulus (0.3 - 3 Pa) of the three LLC samples is much lower than the storage modulus of the actin filaments of a cell which is approximately ~80 Pa at shear strain of 10 % (Storm et al., 2005). Since modulus reflects the stiffness of a material (Barnes et al., 1989), this suggests that the stresses generated by actin filaments with higher stiffness would deform the liquid crystal surfaces with a lower stiffness.

The gradients of the stress-strain curves (shear modulus) for these LC samples continuously decreased with increasing strain (Figure 2.24a). This result indicates that

the rigidity of the liquid crystals is shear strain dependent. Among the four samples, the shear modulus of LLC72hours is the lowest and this was probably associated with the longest incubation period in a fluidic environment (cell culture media). For CELCP2 and LLC, the shear stress is directly proportional to the shear strain below 10 %, indicating the linear viscoelastic range of the liquid crystal (Figure 2.24b). Within the linear viscoelastic range, these liquid crystals have a constant shear modulus or rigidity. The linear proportionality of shear stress to strain exhibited linear elastic behaviour and can be fitted by Hooke's equation of stress-strain.

When analysing the displacement of the liquid crystals between a stationary platform and a rotation plate, theory of simple shear strain was applied (Whorlow, 1992, Barnes et al., 1989). By applying simple shear to the rotary plates in a rheometer (Figure 2.25), the top layer of the shear plane which is originally parallel to the bottom plane at a thickness of L rotates through an angle, θ and displaced by δL, where $\theta = \tan^{-1} (\delta L / L)$.

This work considered and analysed the example of CELCP2 which was sheared at $\omega = 0.1\ s^{-1}$ and 10 % strain. In this case, 10 % strain was the upper limit of the linear viscoelastic range for the lyotropic liquid crystals in this study. During the experiment, the thickness of the liquid crystals in between the plates was L = 0.5 mm and $\theta = 0.1$ radian (10 % strain), in which the small angle of shear (θ in radian) is equal to the shear strain ($\gamma = \delta L / L$) when the deformation is very small (Whorlow, 1992). Hence, the displacement of δL was calculated by $\delta L = L \tan \theta$. The calculation based on this basic equation gave a displacement of $\delta L \sim 50$ µm. By associating this displacement to the linear viscoelastic curve of CELCP2 (Figure 2.24B), the graph empirically showed that a small stress of 0.128 Pa yielded a 10 % strain or a 50 µm displacement in the liquid crystals. Therefore, the shear modulus of CELCP2 at the linear viscoelastic range was

determined at 128 mPa since the shear modulus is a ratio of shear stress to the shear strain (Kim et al., 2011 , Barnes et al., 1989).

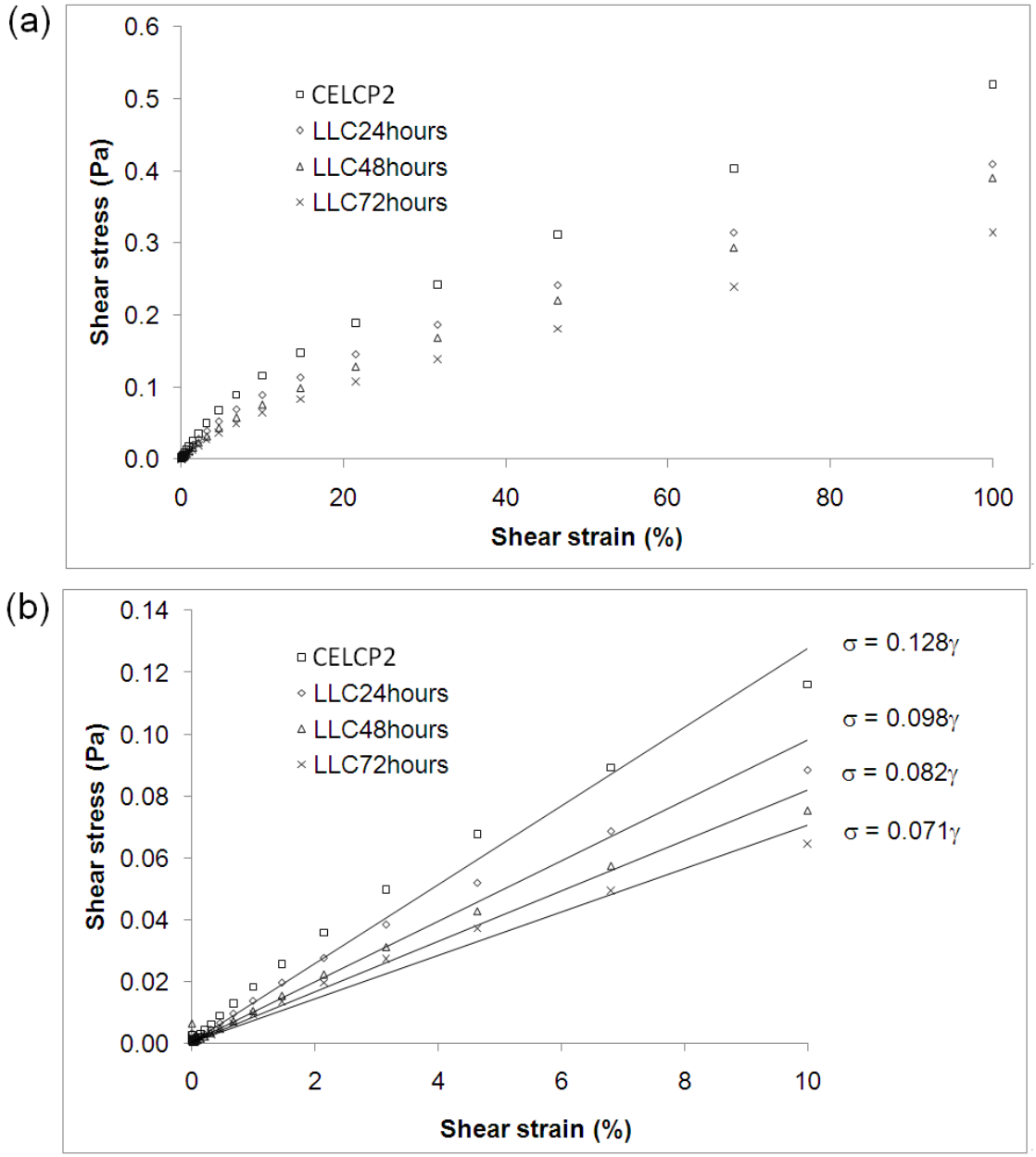

Figure 2.24. Stress-strain curves of CELCP2, LLC24hours, LLC48hours and LLC72hours from 0.1 % up to a strain of (a) 100 % and (b) 10 % at ω = 0.1 s^{-1}. The linear regression lines were used to approximate the linear viscoelastic range of the liquid crystals.

Similarly, the shear moduli for LLC24hours, LLC48hours and LLC72 hours were determined at 98 mPa, 82 mPa and 71 mPa, respectively. These shear moduli are much lower than the shear moduli of PDMS and silicon rubber (MPa range) that were

previously used to sense cell traction forces (Ghannam and Esmail, 1998b, Kim et al., 2011). A previous study showed that silicon rubber with a low stiffness was more sensitive to a wider range of cell forces when compared with silicon rubber with a high stiffness (Burton et al., 1999). Therefore, this is an indication that liquid crystals might have a high sensitivity to low range of applied forces.

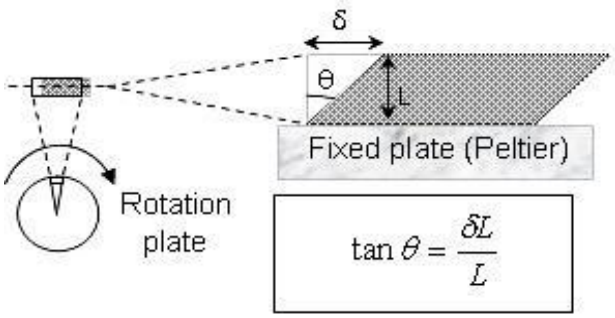

Figure 2.25. Simple shear of the liquid crystals. Left: Top view, Right: Cross-section.

2.3.4 Shear Rate Dependent Shear Modulus of the Lyotropic Liquid Crystals

The frequency sweep result at 5 % strain shows that the shear modulus (G' and G'') and complex viscosity (η*) of a cholesteric and cholesteric based lyotropic liquid crystals is shear rate dependent (Figure 2.26). The shear moduli are normally distributed according to the Shapiro-wilk test which is significant for $p > 0.05$ (Table 2.2).

For CELCP2, LLC24hours, LLC48hours and LLC72hours, the storage modulus increased linearly with increasing shear rate up to 10 s^{-1} but beyond this shear rate, the storage modulus (G') of the four samples decreased sharply (Figure 2.26a). The loss moduli and complex viscosities exponentially increased and decreased with increasing shear rate, respectively. After incubation in the cell culture media for 24 and 48 hours, the storage modulus, loss modulus and complex viscosity of LLC24hours and LLC48hours are very close to those of the CELCP2 over the entire range of shear rate (1

- 100 s^{-1}) (Figure 2.26a). In the frequency sweep data, CELCP2, LLC24hours, LLC48hours and LLC72hours exhibited linear elastic behaviour at a shear rate below 1 s^{-1} where the storage modulus was greater than loss modulus at 5 % strain (Figure 2.26a). The crossovers between the storage modulus and loss modulus at 1 s^{-1} indicate the viscoelastic property of the CELCP2 and LLC (Figure 2.26a). CELCP2 and LLC were characterised by a linear elastic behaviour (G' > G'') at low angular frequencies and viscous behaviour (G'' > G') at high angular frequencies. Ramos at el. (Ramos et al., 2002) and Zapotocky at el. (Zapotocky et al., 1999) observed similar viscoelastic behaviour for a cholesteric liquid crystal impregnated with silica particles and their result attained a crossover at 0.5 s^{-1} for 5 % shear strain.

Table 2.2. Test of normality for storage modulus and loss modulus of the CELCP2 which is significant for p > 0.05. Each sample of CELCP2 was tested 3 times.

	Shapiro-Wilk
Storage modulus	
CELCP2	0.55
LLC24hours	0.579
LLC48 hours	0.189
LLC72 hours	0.609
Loss modulus	
CELCP2	0.475
LLC24hours	0.896
LLC48 hours	0.572
LLC72 hours	0.683

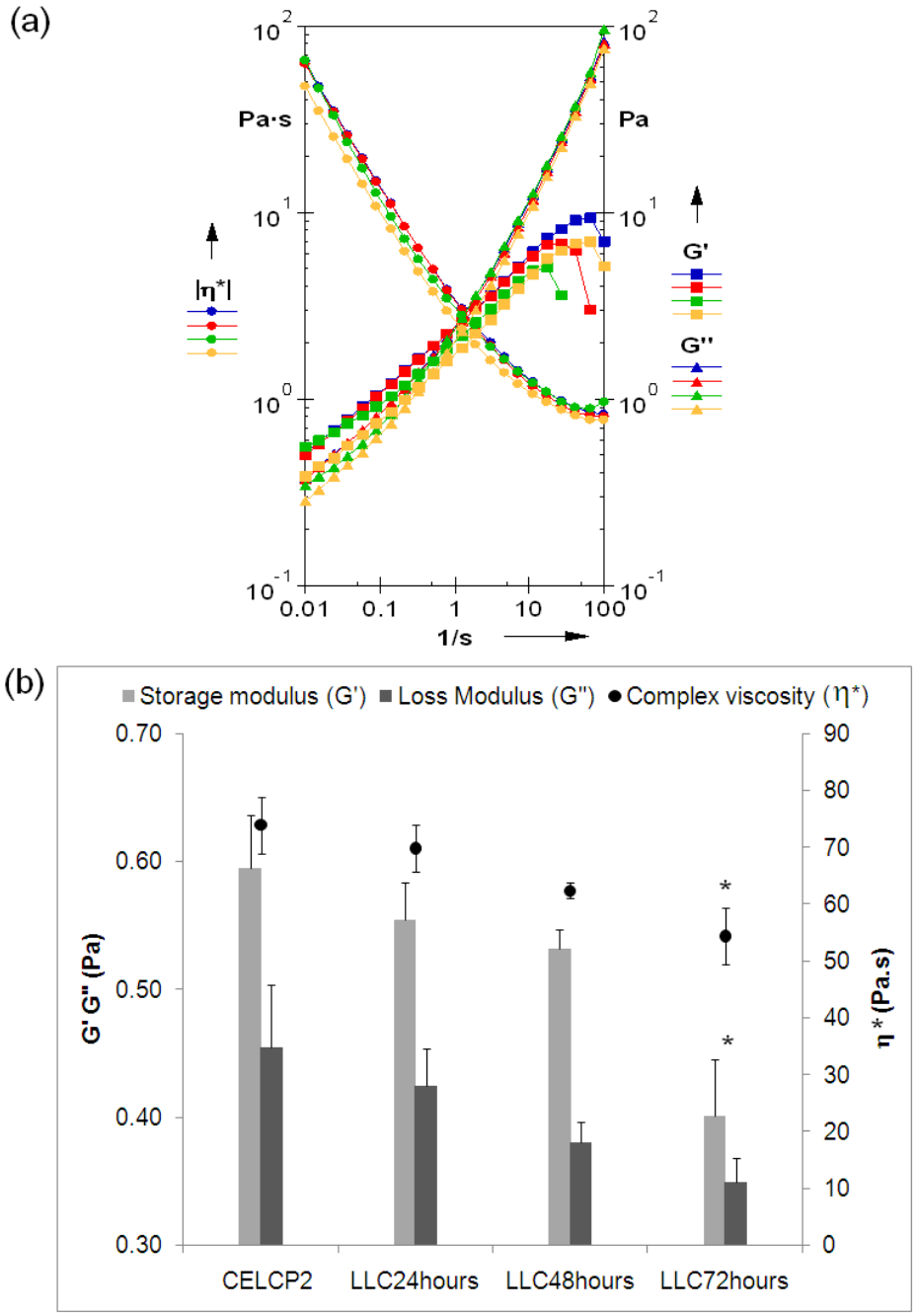

Figure 2.26. The frequency sweep results. (a) Shear rate dependent storage modulus (G', square), loss modulus (G'', triangle) and complex viscosity (η*, circle) of the CELCP2 (Yellow), LLC24hours (Green), LLC48hours (Red) and LLC72hours (Blue) obtained for angular frequencies from 0.01 s^{-1} to 100 s^{-1} at 5 % strain. (b) The bar charges of storage and loss moduli obtained at ω = 0.01 s^{-1}. The scatter plot shows the complex viscosity (η*) of CELCP2, LLC24hours, LLC48hours and LLC72hours. The asterisks (*) indicate that the storage modulus, loss modulus and complex viscosity for LLC72hours are significantly different from the CELCP2 (significant for p < 0.05, Tukey HSD test, N = 3).

The complex viscosity of CLC, LLC24hours, LLC48hours and LLC72hours exponentially decreased with increasing shear rates (0.01 - 100 s^{-1}), indicating pseudo-plastic flow behaviour of a viscoelastic gel (Figure 2.26a). Ramos at el. and Zapotocky at el. observed similar shear rate dependent modulus for their cholesteric liquid crystals (Zapotocky et al., 1999, Ramos et al., 2002).

The viscoelastic behaviour of the cholesteric based lyotropic liquid crystals characterized is contrarily to the polymeric materials such as silicon rubber and PDMS. Previous literature show that hydrogels (Busato et al., 2009), PDMS (Ghannam and Esmail, 1998b, Boutelier et al., 2008) and liquid crystal polymers (Somma and Nobile, 2004) are dominated by viscous behaviour at low shear rates (< 1 s^{-1}) and they exhibit elastic behaviour at high shear rates (> 1 s^{-1}). Comparatively, cholesteryl ester liquid crystals have an advantage of exhibiting linear elastic behavior at low shear rates and seemed to be suitable for use in studying the mechanics of cells.

For the application of lyotropic liquid crystals in monitoring cells traction which occurs at a low speed (a few µm/hour) (Burton and Taylor, 1997), this research was interested in the rheological characteristics of the liquid crystals at a low range of shear rates. At the lowest shear rate of 0.01 s^{-1} (Figure 2.26b), the storage modulus (G') is greater than the loss modulus (G'') for CELCP2 (G' = 0.59 ± 0.04 Pa, G" = 0.45 ± 0.04 Pa), LLC24hours (G' =0.55 ± 0.02 Pa, G" = 0.43 ± 0.03 Pa), LLC48hours (G' =0.53 ± 0.01 Pa, G" = 0.38 ± 0.02 Pa) and LLC72 hours (G' = 0.40 ± 0.04 Pa, G" = 0.316 ± 0.02 Pa) which indicates that the system continued to exhibit elastic behaviour despite a gradual decline of G' and G''.

After 48 hour of incubation, both storage and loss moduli of LLC72hours were significantly different from CELCP2 [p = 0.016 (G'), p = 0.039 (G"), Tukey HSD test, significant for p < 0.05]. However, LLC24hours [p = 0.833 (G'), p=0.885 (G"), Tukey HSD

test] and LLC48hours [p = 0.585 (G'), p = 0.306 (G"), Tukey HSD test] showed no significant differences of viscoelasticity when compared with CELCP2. When the incubation time was prolonged from 48 hours to 72 hours (Figure 2.26b), the viscoelastic behaviour of the lyotropic liquid crystals was significantly affected. The results suggest that probably there is a reduction in the ability of the liquid crystal molecules to store elastic energy.

At the lowest shear rate of 0.01 s^{-1}, the complex viscosity (η^*) for CELCP2, LLC24hours, LLC48hours and LLC72hours were 73.90 ± 4.99 Pa·s, 69.80 ± 4.14 Pa·s, 62.37 ± 1.36 Pa·s and 54.37 ± 4.98 Pa·s, respectively (Figure 2.26b). As shown in Figure 2.26b, the complex viscosity seems to decrease with an increasing incubation time. However, the complex viscosity of LLC72hours was significantly different from CELCP2 (p = 0.027, Tukey HSD test). LLC24hours (p = 0.882, Tukey HSD test) and LLC48hours (p = 0.222, Tukey HSD test) showed no significant differences in complex viscosity when compared with CELCP2. The decrease in complex viscosity which was determined by a rheometer probably indicates a weaken strength of the liquid crystal gel after 72 hours of incubation in an aqueous environment.

LLC72hours was incubated for the longest period of time in the cell culture media displayed a significantly lower G', G'' and η^* when compared with LLC24hours and LLC48hours which were incubated for shorter periods of time in the cell culture media. These results suggest that LLC24hours and LLC48hours presented a higher viscoelasticity compared with LLC72hours. Therefore, the shear modulus and complex viscosity of the lyotropic liquid crystals are the reciprocal of the incubation time in cell culture media. Both temperature and culture media collectively as a function of time might have effects on the viscoelasticity of the lyotropic liquid crystals. However,

isothermal condition at 37 ^{o}C was maintained in the experiments, in which the liquid crystals are thermally stable as characterized by DSC and cross-polarising microscopy.

In a lyotropic lamellar system, the liquid crystal molecules are interlaced by water molecules (Helfrich, 1994) and this probably weakens the cohesion forces between the slabs of lamellar mesophases. When the lyotropic liquid crystals incubated in the culture media for a prolonged period of time, the water infusion continued to increase leading to a decrease in the viscoelasticity of the lyotropic liquid crystals. However, the effects of the water infusion were lower for lyotropic liquid crystals that were incubated below a critical period of 48 hours. In the rheological test, these liquid crystals maintained an elastic behaviour when low shear rates were applied. At low shear rates, the shear forces applied is lower than the cohesion forces of the closely packed molecules in the lyotropic liquid crystals and fluid has little space to lubricate the flow (Mortensen, 2001). Within the elastic regime, these lyotropic liquid crystals retained the ability to restore elastic forces when the shear forces were removed. Above a critical shear rate which exceeds the elastic limit (increase of shear force), the void volume increases and also allows the infusion of the fluid. As a result, the elastic restoring force of the lyotropic layers was destroyed, and the liquid crystals flow-like fluid as indicated by the exponential decrease in the viscosity of the liquid crystals (Figure 2.26a).

2.3.5 Analysis on the Structural Changes of the Liquid Crystal Substrates Cultured with Cells

Having determined the rheology of the liquid crystal which indicates that it might be suitable to be used as a cell traction force transducer, human keratinocyte cell lines were cultured on the liquid crystals at 37 ^{o}C for 24 hours. After culturing HaCaT cells on

the liquid crystals for 24 hours, short and discrete deformation lines (dark field / bright field stratifications) were found radiating out of the periphery of individual and group of cells cultured on the liquid crystal substrates as shown in (Figure 2.27a-d). These deformation lines may be caused by the mass of the cells, electrostatic charges displacing the liquid crystal molecules or by forces generated from the actin cytoskeleton within the cells that were transmitted to the LC surface via focal adhesions. Therefore, the objective of this experiment is to determine the source of the stresses and strain in inducing the stress marks (deformation lines) on the LC surface.

When the liquid crystal substrates were removed from the petri dishes and it was found that the cells were adhering to liquid crystal membranes (Figure 2.27e-f) that might explain the formation of lyotropic layers in relation to Figure 2.19. In order to determine if the deformation lines were induced due to the contraction of cells and how these deformation lines were formed, cytochalasin-B was used to treat a group of cells contracting on the liquid crystal surface. A group of contracted cells with elongated shapes was treated with 30 μM cytochalasin-B over a 60 minutes period on a hot stage maintained at 37 ^{o}C. Before treatment with cytochalasin-B, contracted cells were found indenting LC surface with localised deformation lines growing in oblique directions, and perpendicular to the cell contraction direction as shown in Figure 2.28. After treatment with cytochalasin-B for 30 minutes, the LC deformation lines induced by the cells were very much shortened in an inward direction perpendicular to the cell relaxation direction (Figure 2.28c).

As a result of cytochalasin-B treatment which inhibited the polymerisation of F-actin, the traction forces of cells degenerated with the depolymerisation of actin

filaments, which in turn, reduced the deformation lines in the LC surface (Figure 2.28d).

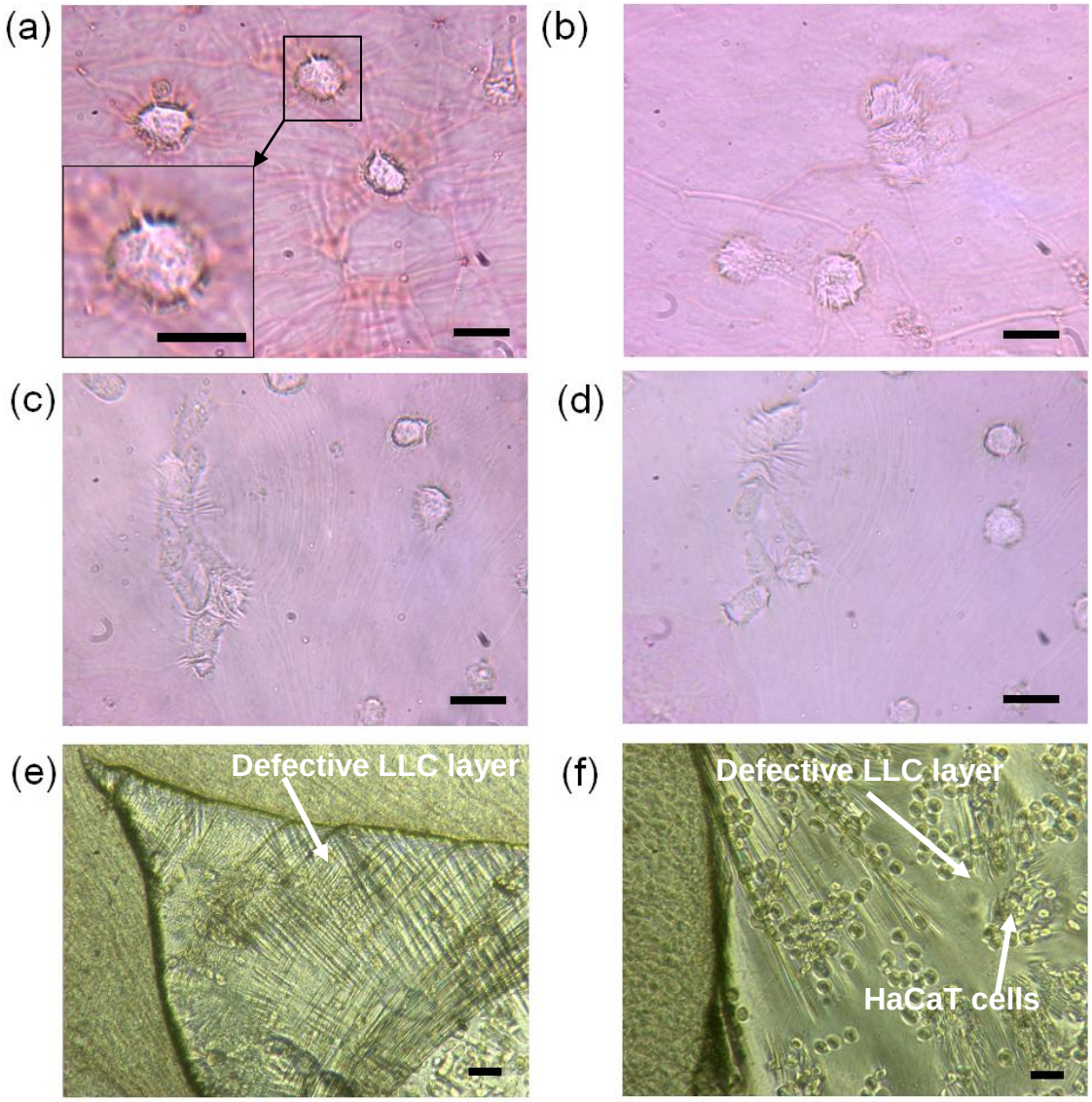

Figure 2.27. (a-d) Phase contrast micrographs of the cells cultured on the liquid crystal substrates, and (e-f) cells adhering to a membrane drifting off the bulk liquid crystals. Enlarge exert of (a) shows the short deformation lines radiating out of the periphery of a cell. (Scale bar: 20 μm)

As shown in Figure 2.28a and c, the relaxation direction is opposed to the contraction direction of the cells as indicate by solid line arrows. The relaxation of HaCaT cells was indicated by an increase in the length of cells (123 μm) compared with the original length of the same group of cells (102 μm).

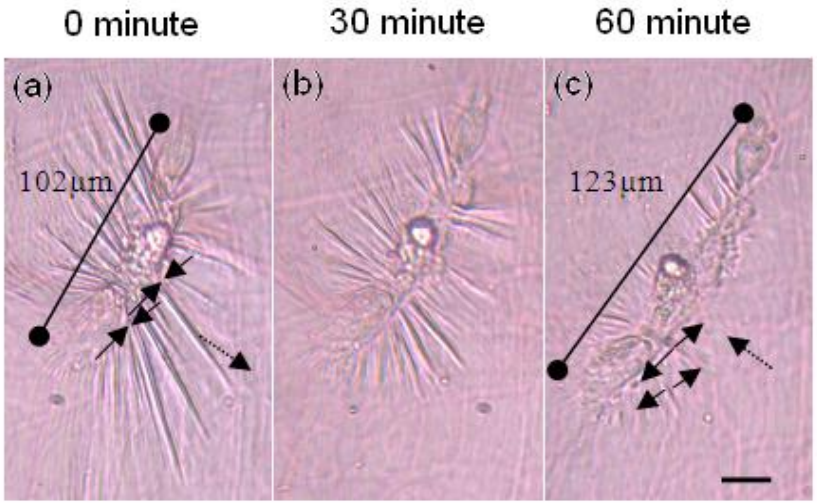

(d)

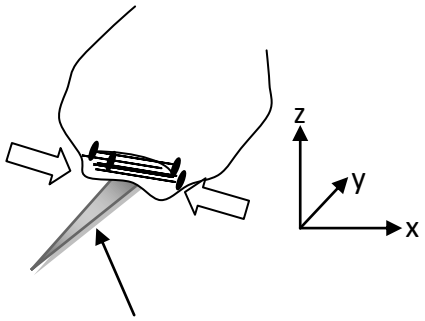

Contraction of circumferential actin filaments mediated by focal adhesions in the LC surface causing a deformation line.

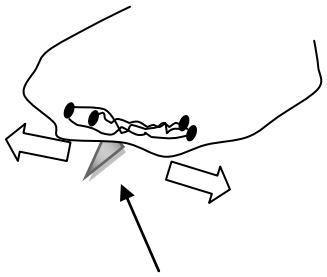

Relaxation of circumferential actin bundles mediated by focal adhesions in the LC surface causing reduced length of a deformation line.

Figure 2.28. HaCaT cells cultured on LC surface in response to 30 µM cytochalasin-B treatment and direction of LC deformation lines shrinkage at (a) 0 minute, (b) 30 minutes, and (c) 60 minutes. Solid line arrows show the direction of the cell contraction and relaxation after treated with cytochalasin-B. Dotted line arrows show the repelling directions of the deformation line. (d) A depiction showing the correlation of the deformation line formed on the liquid crystal film with transverse shear forces induced by the contractions of cell circumferential actin filaments that are anchored at the focal adhesions. Treatment with cytochalasin-B caused F-actin depolymerisation, force degeneration and diminishing deformation lines of the liquid crystal surface. (Scale bar: 25µm)

The induction of the longitudinal deformation line was due to the transverse strain at a finite region on the LC surface (indicated by solid line arrows in Figure 2.28a).

Therefore, the longitudinal deformation lines induced in the LC surfaces is a secondary effect of lateral compression.

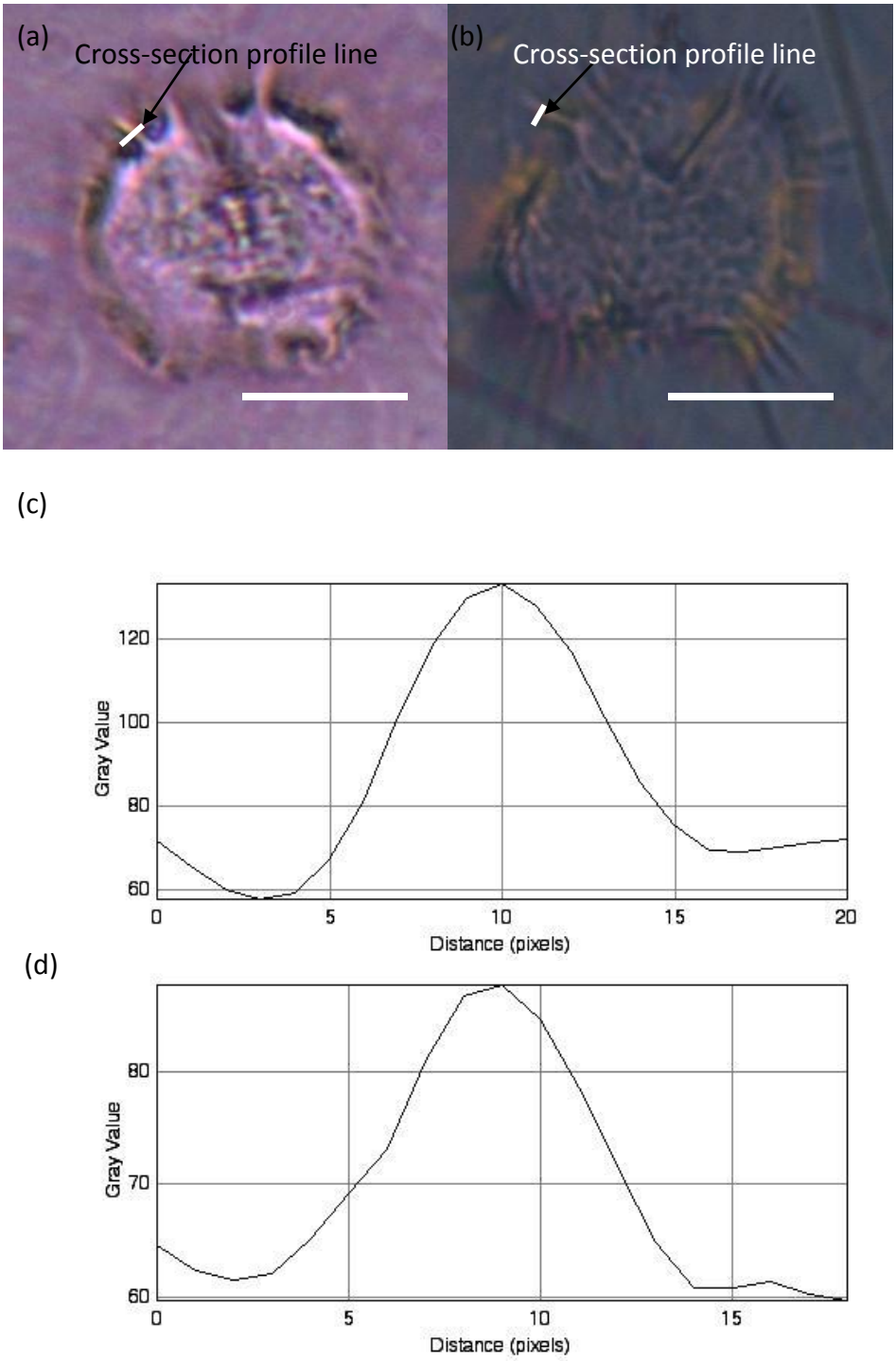

Figure 2.29. (a) Phase contrast and (b) cross-polarising micrographs of deformation lines induced by HaCaT cells in the LC surface. The profile plots (c-d) for the cross-section of a deformation line are as marked in (a) and (b), respectively. (Scale bar: 25 µm)

At a microscopic level, liquid crystals consisted of closely packed molecules that are bound together by cohesion forces (Collings, 2002). Any shear distortion (force) applied transversely (compression) would squeeze the LC molecules upward in a limited space. Further force application would cause the LC molecules to move outward to areas with molecules of a lower packing of density. Upon released of that applied force, the LC molecules would recover to their original position due to their elastic behaviour at low shear rates (as characterised in section 2.3.3).

As a result of the compressions and shears induced by the cells, the LC molecules emerge as bright and dark field stratification of deformation lines as shown in phase contrast (Figure 2.29a) and cross-polarising (Figure 2.29b) micrographs. The contraction profiles obtained from the cross-section of the deformation line seemed to follow a bell-shaped curve in both microscopic images (Figure 2.29c-d) indicating that compression of the LC molecules caused an upward deflection of molecules, which in turn, altered the intensity of reflected light captured via different microscopy techniques.

These traction forces originated from the boundary of the cells are probably related to the contractions of circumferential actin bundles (Omelchenko et al., 2001, Owaribe et al., 1981). Circumferential actin bundles are profound short actin bundles running tangentially along the margins of epithelial cell (Owaribe et al., 1981, Gloushankova et al., 1997, Omelchenko et al., 2001). Their functions are to maintain the discoid shape of the cell by shortening the boundary of the circumference resulting from contractions of the marginal actin fibres (Zhang et al., 2005, Owaribe et al., 1981). Cell traction forces exerted on a substrate via the focal adhesions is originated from the myosin-II contraction activities and the polymerisation of actin bundles (Krendel et al., 1999, Cavey and Lecuit, 2009). Then, these forces transversely shear the liquid

crystal surface under the cell margin resulting in an outward growing deformation lines (Figure 2.28d). The reaction of the liquid crystal surface in forming deformation lines can be explained by Newtons' third law of action and reaction. The stronger the compression, the longer is the deformation line formed.

2.3.6 Viscoelasticity and Viscosity of the Time-Dependent Liquid crystals In-Situ

From the shear modulus measured by a rheometer, the results show that both storage and loss moduli of the liquid crystals gradually decreased with increasing incubation time in the cell culture media. However, the viscoelasticity of the liquid crystals characterised by a rheometer was compared with the behaviour of the liquid crystals in-situ. In-situ characterisation method involved culturing cells on the liquid crystal substrates and treating them with cytochalasin-B and formaldehyde was used to evaluate our rheological measurement results. In a culture with HaCaT cells contracting on the surface of the liquid crystals, cytochalasin-B disrupted the actin filament polymerisation of cells causing degenerated forces applied to the liquid crystals and a reduction of deformation lines (Figure 2.30). However, cells remained attached to the surface of the liquid crystals because of the specific action of cytochalasin-B to the internal cytoskeleton but not to the adhesion proteins that function to attach the cells to a surface. In this study, large groups of cells were intentionally selected to emulate large shear forces on the surface of the liquid crystal substrate and this would enhance any negative effects. Figure 2.30 shows the effects of cytochalasin-B treatment to the cells cultured on the liquid crystal substrate for a period of 24, 48 and 72 hours. For the liquid crystals cultured for 24 and 48 hours, diminishing deformation lines and flat surface recovery were observed after the cells were treated with cytochalasin-B (Figure 2.30, 24 and 48 hours, 0 - 60 minute).

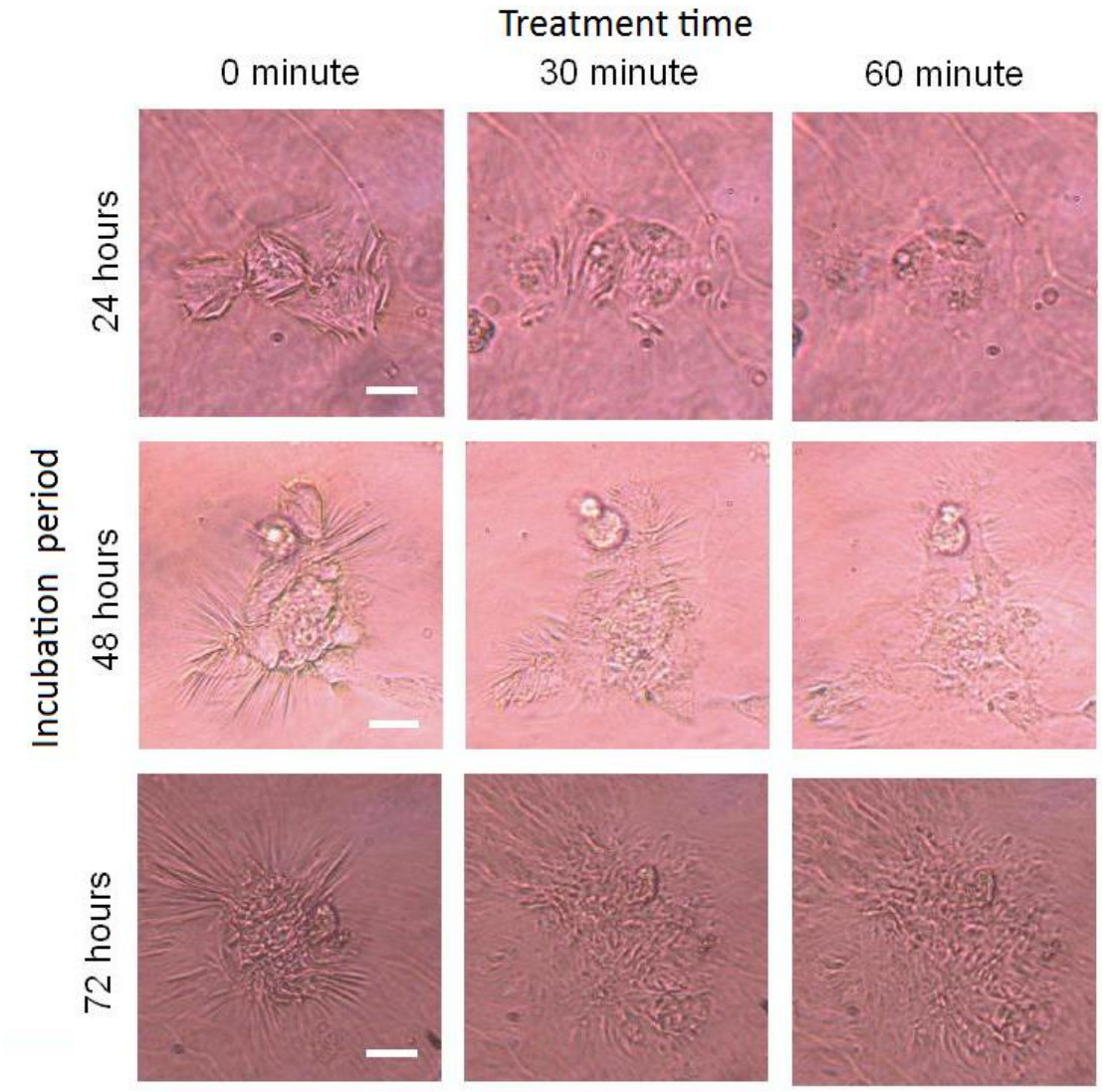

Figure 2.30. Phase contrast micrographs showing the effect of 30 µM cytochalasin B on HaCaT cells cultured over the lyotropic liquid crystals after 24, 48 and 72 hours of incubation taken every 5 minutes over a period of 60 minutes. The time shown is the period of treatment of cells in cytochalasin-B. (Scale bar: 25 µm)

This shows that the liquid crystals were still elastically viable even though they had been immersed in the cell culture media in an isothermal condition for 48 hours. However, a great difference was observed in the behaviour of lyotropic liquid crystals after 72 hours of incubation where elastically unrecoverable deformation lines were formed (Figure 2.30, 72 hours, 0 - 60 minute) due to the viscous response of the lyotropic liquid crystals. The result is consistent with the quantitative result obtained

by frequency sweeps which show a degradation of storage and loss moduli in LLC72hours (Figure 2.26). The surface of the liquid crystals which was once elastic has become less elastic due to the effects of prolonged incubation in a fluidic environment for 72 hours. Similar results were observed for the two repeats of experiments. The in-situ experiment has confirmed the elastic behaviour of the liquid crystals that were incubated in cell culture media within 48 hours and the responses were also consistent with the result characterized by the oscillatory measurements (Figure 2.26).

Creep of the liquid crystals over time was monitored in-situ by imposing a constant stress on the surface of the liquid crystals for a period of 96 hours. The stress of a cell which has induced certain length of deformation line on the surface of the liquid crystals was fixed by applying formaldehyde to the cell. After treating HaCaT cells in formaldehyde for 96 hours, cell shape and size of these cells remained unchanged (Figure 2.31a).

The initial length of deformation lines is a reference to the changes of viscosity in the liquid crystals. To examine if there were any quantitative changes, the measurements of length for same group of deformation lines was taken and marked with arrows as shown in Figure 2.31a. The initial deformation length was determined at 10.25 ± 4.15 µm (mean ± SD) (Figure 2.31a, pre-fixed). After treating cells in formaldehyde for 24, 48, 72 and 96 hours, the lengths of deformations on the liquid crystal surface were determined at 8.72 ± 3.77 µm, 8.71 ± 3.77 µm, 8.67 ± 3.77 µm and 8.23 ± 3.51 µm, respectively. The cells maintained the deformations in the liquid crystal surface well through the 24 - 72 hours treatments in formaldehyde but the deformation lines decreased slightly (creep) after 72 hours of treatment (Figure 2.31b).

(a)

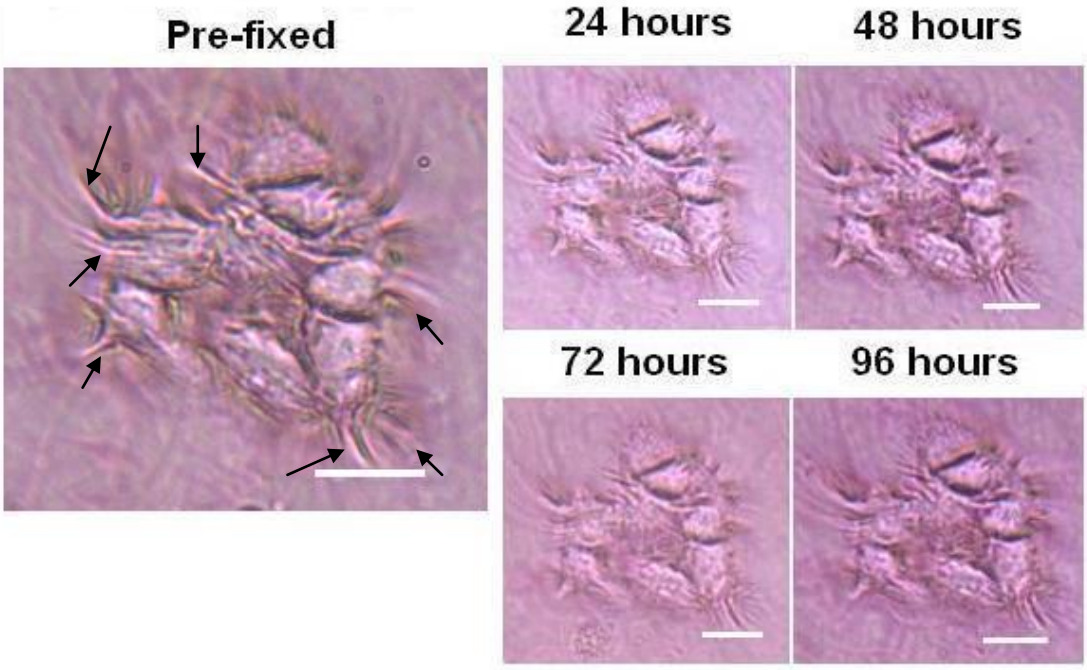

(b)

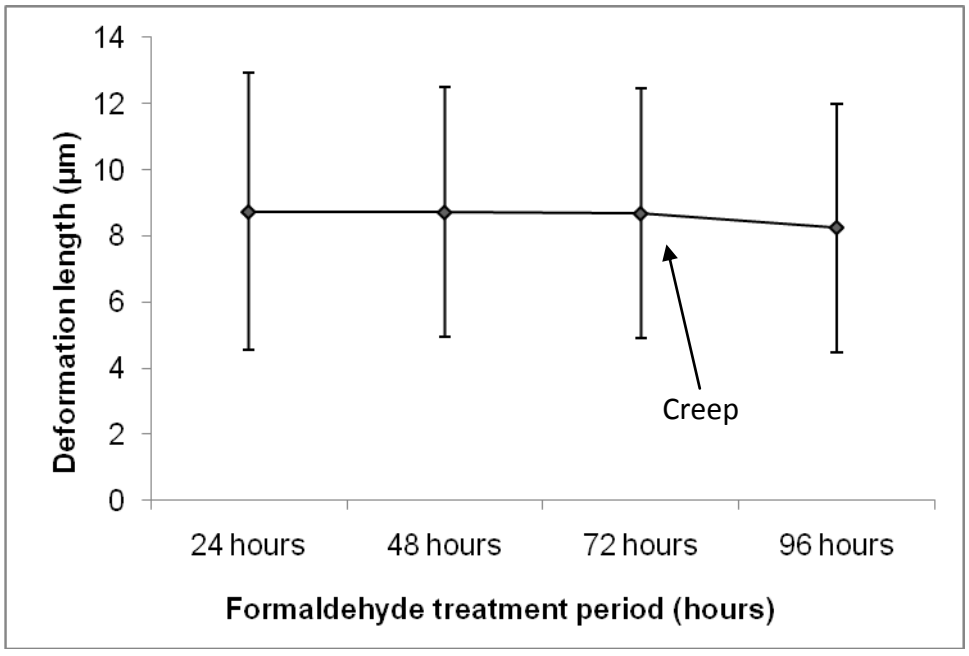

Figure 2.31. (a) Time series images taken every 24 hours up to 96 hours for HaCaT cells treated in 2 % formaldehyde. The arrows in (a) show the deformation lines that were monitored for their changes of length; (b) Length of deformation lines measured (mean ± SD, N = 28, 3 repeats) after cells treated in formaldehyde for 24, 48, 72 and 96 hours. The arrows show the example of deformation lines used for quantification. (Scale bar: 25µm)

However, this reduction in the length of deformations developed in the liquid crystals after 72 hours of cell treatment in formaldehyde was very small and statistically insignificant (N = 28, p = 0.34, Tukey HSD test). It seemed that an immersion in an aqueous surrounding provided a constant hydrodynamic pressure to the surface of the liquid crystals and hence, subjecting the lyotropic liquid crystals in-situ to a very low level of creep. The mean of deformation lengths in the liquid crystal surface calculated were ranging between 5 and 13 um (Figure 2.31b). With reference to the thickness of the liquid crystal substrate (~ 100 μm), these shear strains of 5 - 13 % closely fit the linear viscoelastic range of the liquid crystals (Figure 2.31b).

In comparison with previous cell force measurement techniques that involved the measurement of deformation in the PDMS or silicon rubber (Oliver et al., 1995, Burton and Taylor, 1997, Beningo et al., 2002), the magnitude of the deformations determined was at a range of 10 - 100 μm for single cells (Burton et al., 1999). These large deformation lengths were probably associated with the nonlinear viscous behaviour of the silicon rubber and PDMS at low shear rates (Ghannam and Esmail, 1998b, Boutelier et al., 2008). Due to the non-linear rheological behaviour at low shear rate, these materials tended to deform abruptly under shear stresses, and thus form large deformations.

As reported in previous literature (Stoodley et al., 1999, Barnes et al., 1989), the extent of deformation in a material is dependent on the dynamic viscosity (real part of complex viscosity). The insignificant level of creep found is an indication of the mechanical stability of the viscosity presented by the lyotropic liquid crystal over time. This result seems to be slightly different from the complex viscosity determined using oscillatory test for the lyotropic liquid crystals in which it was found that the complex viscosity was only stable for up to 48 hours in media (Figure 2.31b). This discrepancy

can be explained by the differences in the measurement methods. In the rheological study of lyotropic liquid crystals with a rheometer, this study requires the removal of liquid crystal samples from the culture media in which the integrity of the samples was damaged before the rheological measurements and this probably resulted in an underestimation of the viscosity of the liquid crystal substrate in equilibrium. Therefore, the viscosity of the lyotropic liquid crystals evaluated in-situ was more consistent over time than the complex viscosity over time as measured by a rheometer. By using in-situ techniques for fundamental rheological studies, the structural integrity of the LLC can be retained, and thus this shows more realistic rheological behaviour of the lyotropic liquid crystals.

2.3.7 The Young's Modulus of Liquid Crystals Determined by Using AFM Nano-Indentation

AFM nano-indentation was used to determine the Young's modulus of the surfaces of the LLC substrates after incubated for 24 hours. An example of the force-displacement curve acquired for the liquid crystal substrate using the AFM nano-indenter is as shown in Figure 2.32. During the unloading phase, the total force exerted onto the indenter is a contribution of the laterally derived forces originated from the adherent liquid crystal gel. Hence, the Young's modulus determined is also a function of the lateral elasticity of the liquid crystals. Overall, both loading and unloading curves are non-linear except for the initial portion of the unloading curve (Figure 2.32). This is the portion of unloading curve, in which Young's modulus of the liquid crystals was calculated.

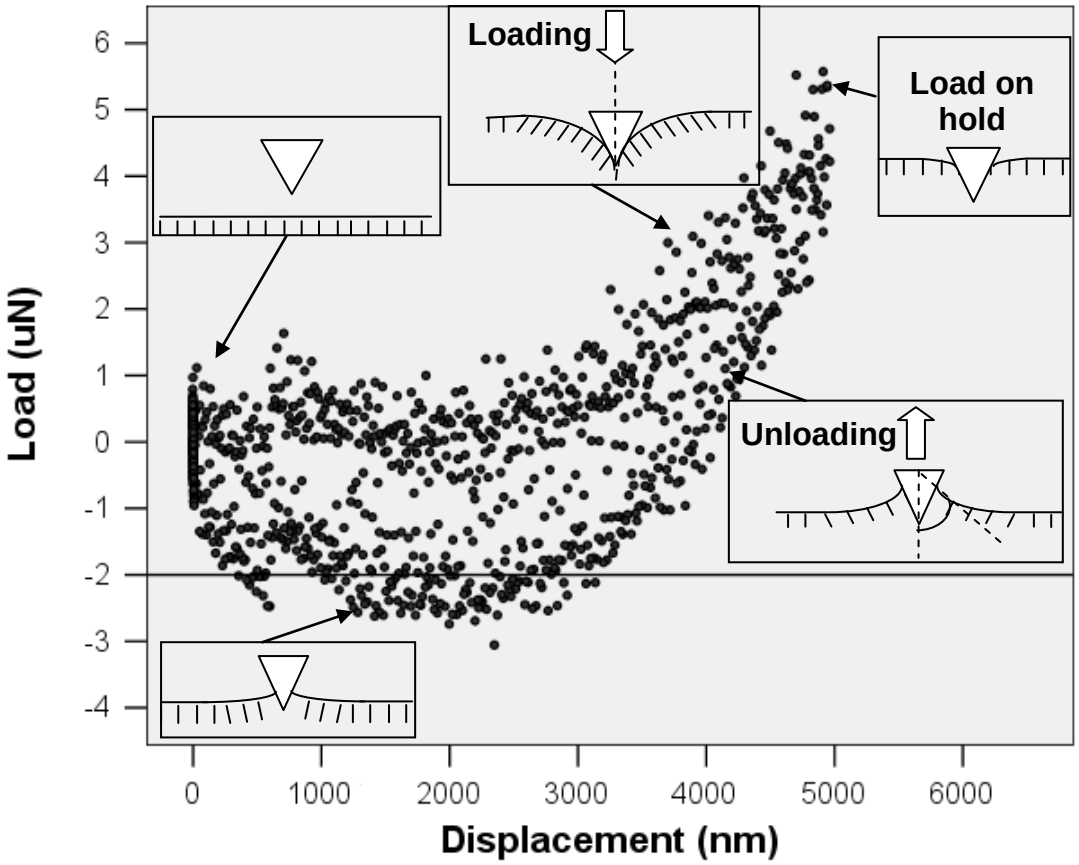

Figure 2.32. A load-displacement curve of the liquid crystals surface and its relations to the loading and unloading of an indenter.

As shown in Figure 2.32, the liquid crystal immersed in the culture media was indented with a peak load of P_{max} = 4.84 µN at a maximum depth of h_{max} = 4910 nm. The final depth after complete unloading, h_f, was determined from the unloading data as 2713 nm. Retraction of the indenter was halted at a depth of h_s = 1068 nm. The power law fitting parameters as determined by the Triboscope software from the unloading data were 1.1 and 1.957 for A and m, respectively, using the least square fitting methods (Oliver and Pharr, 1992). The average stiffness of the liquid crystals calculated from equation (2.1) was 0.0017 ± 0.00067 µN/nm (mean ± SD) and the Young's modulus derived from equation (2.6) was 108 ± 20 kPa (mean ± SD). Out of the three liquid crystal substrates tested at different time, only one substrate has

produced 20 repeatable and measureable results. This probably due to the instability of the AFM system after a break down prior to the last two repeat of the experiments.

2.3.8 The Young's Modulus of the Liquid Crystals Determined by Spherical Indentation

Due to the lack of stability in the AFM nano-indentation system, spherical indentation was used to determine the Young's modulus of the surface of the liquid crystal substrates in the cell culture media. As determined by the spherical indentation, the Young's moduli of the three independent liquid crystal substrates after 24 hours of incubation in cell culture media were determined at 111 ± 17.97 kPa, 108 ± 22.31 kPa and 109 ± 21.33 kPa, respectively. The mean of the Young's modulus (E) was 110 ± 21.33 kPa (N = 60 in three repeats of experiments). 95 % confidence interval for the mean of the Young's modulus was $104.87 < E < 115.18$ kPa. These results show that Young's moduli determined by using spherical indentation for the three liquid crystal samples after incubation for 24 hours at 37 ^{o}C are similar and highly reproducible and comparable to those measured with the AFM nano-indenter.

Figure 2.33a shows the birefringence changes to the surface of the liquid crystals in cross-polarising upon removal of the steel ball indenter from a liquid crystal substrate with a thickness, h of 100 μm. The contact radius, r and vertical displacement, δL for the three samples of liquid crystals (twenty indentation sites per sample) were approximately 26 ± 1.6μm and 1.33 ± 0.16 μm, respectively. At the indentation site, the weight of a steel ball was loaded to the liquid crystal surface, forming a dark circular and concave area. The focal conic texture was formed around the contact circle area (Figure 2.33a, 0 second) in the liquid crystal surface after the surface was deformed by the steel ball in bi-axial direction. This image was taken as

soon as the steel ball was removed. When the steel ball was being unloaded from the surface of the liquid crystal, the displaced liquid crystal molecules rapidly returned to the centre of the contact area. Eventually, the indented area was closed after 15 seconds of recording. The imperfect recovery of the original texture at a little area at the centre was probably due to the removal of the gel, which was stuck to the steel ball during the unloading process.

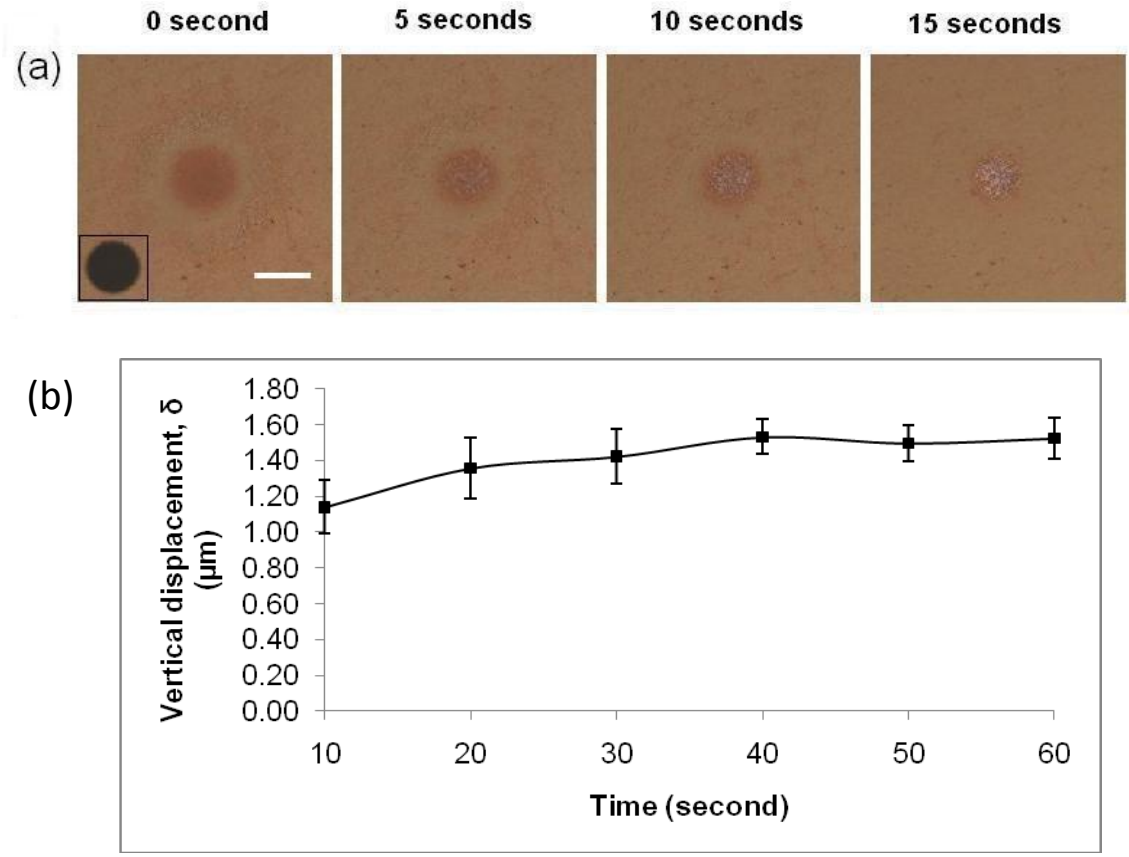

Figure 2.33. (a) Cross-polarised micrographs show the elastic recovery of deformed liquid crystals (0 - 15 seconds) after a steel ball was unloaded. The inset shows the steel ball with a diameter of 500 μm before unloading. (Scale bar: 50μm) (b) A graph of vertical displacement (δ) versus loading time for N = 3 shows the creep deformation of the liquid crystals.

Figure 2.33b shows the vertical displacements (δ) of the liquid crystal surface over time for 60 seconds of measurements. The curve reached a plateau after the steel ball was loaded for 40 seconds. A saturated displacement at 60 seconds was achieved,

which is also the point when the displacement was used to determine the Young's modulus of the liquid crystals. The vertical displacement increased from 1.14 ± 0.15 µm to 1.5 ± 0.1 µm indicates the creep and viscoelastic behavior of the liquid crystals. Although the indentation was loaded vertically, the stress was distributed was over and around the contact circle, and this is clearly shown via the changes of texture at the contact area. The LC molecules at the edges of the contact circle displayed an elastic behaviour which was evidenced by the recovering of the original texture within a short period of time. In the context of the liquid crystal texture in the cross-polarised micrographs, the dark circular area indicates the dispersion of the lyotropic liquid crystals into an isotropic phase when being stressed by the steel ball or it could be due to the compressed layers of lamellar which blocked the penetration of the polarised light, and resulted in dark fields in the optical axis (Figure 2.33a). However, this complex phenomenon is not clear. The results in Figure 2.33 and Figure 2.16 simultaneously indicate that when the liquid crystal molecules are under compression, the characteristics of dark field would be observed in the cross-polarising microscopy which might indicate the dispersion of the liquid crystal molecules.

Table 2.3. Comparison of Young's modulus of cholesteryl ester based lyotropic liquid crystals (after 24 hours of incubation) determined by using AFM based nano-indentation and spherical indentation.

	Young's modulus (kPa)	
	Mean ±SD	Mean ± SD
AFM nano-indentation (N = 20 for a LC sample)	108 ± 19.78	-
Spherical indentation (N = 20 for each of the three LC samples)	111 ± 17.97	110 ± 19.95 for N = 60
	108 ± 22.31	
	109 ± 21.33	

In addition, the result also clearly shows that the surface of the liquid crystals exhibited a viscoelastic behavior at a small axial strain, $\delta/h < 2$ % (δ = 1.33 μm, h = 100 μm) and shear strain of approximately 25 % (r = 25 μm, h = 100 μm). These strains may fall in the linear viscoelastic range of the liquid crystals, which explains the elastic recovery of the indented area as observed in Figure 2.33. The Young's modulus (Table 2.3) of the cholesteric based lyotropic liquid crystals (after 24 hours incubation) by using the AFM nano-indentation and spherical indentation systems were determined at 108 ± 19.78 kPa and 110 ± 19.95 kPa, respectively. Similarly, the measurements of the Young's modulus showed by both techniques were subjected to 20 % of variations.

Despite being indented by different geometries of indenters in AFM nano-indentation and spherical indentation, liquid crystals in both experiments were applied with similar loads (~ 5 μN) and produced similar measurements of Young's modulus. These moduli measured are considerably lower than 300 kPa of the thermotropic cubic phase liquid crystals determined in air (Even et al., 2006). The difference may be due to the hydration effects induced in our experiment. Interestingly, the Young's modulus of LC surface seems to be similar to the elastic modulus of the human skin and epidermis layer measured by using suction (82 ± 60 kPa (mean ± SD)) and tensile (130 kPa) techniques, respectively (Takeo, 2007, Hendriks et al., 2006). Nonetheless, the Young's modulus of the liquid crystals determined in this work is also comparable to the Young's modulus of soft tissues such as the smooth muscle (20 - 150 kPa) (Levental et al., 2007) which is an added advantage in the development of a cell force transducer because this elastic modulus closely resembles the stiffness of the in-vivo system (Levental et al., 2007, Solon et al., 2007), and hence provides a more suitable physical environment for sensing cell traction forces. A material with a much higher or lower

elastic modulus than that of the in-vivo tissue could be perceived as pathological tissue by the cells (Levental et al., 2007, Engler et al., 2004b).

2.3.9 Effects of Incubation Time to the Young's Modulus of the Liquid Crystals

As a result of spherical indentation, the effects of incubation periods in the cell culture media to the cholesteryl ester based lyotropic liquid crystals (LLC) are as shown in Figure 2.34. After 24 hours of incubation, the liquid crystals are still elastically viable when the steel ball was removed from the surface of the LLC. The deformed area was able to close and recover within 15 seconds of recovery time (Figure 2.34a). This elastic behaviour was gradually degraded as the incubation time increased to 72 hours (Figure 2.34).

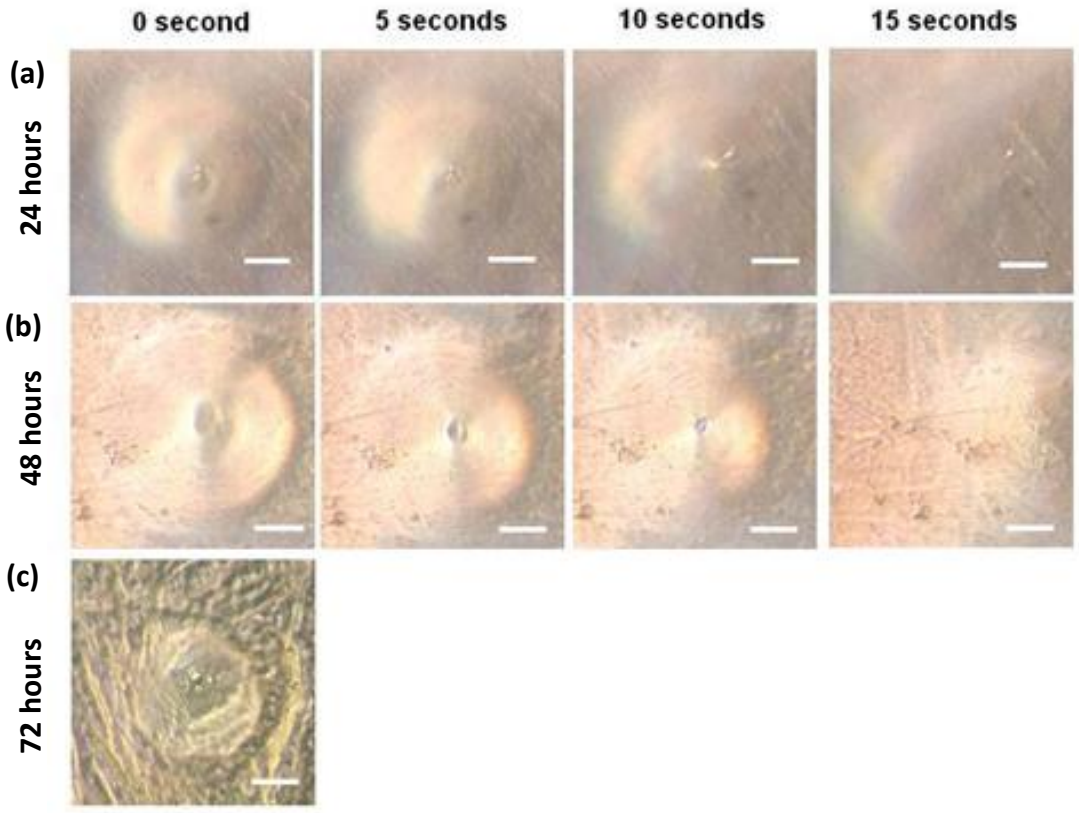

Figure 2.34. Phase contrast micrographs show the behaviors of the lyotropic liquid crystals after a steel ball was unloaded. They were incubated at 37 ^{o}C for (a) 24, (b) 48 and 72 hours, respectively. (Scale bar: 50 μm)

However, the Young's moduli determined for the three LLC samples after 48 hours of incubation were 58 ± 8.26 kPa, 55 ± 6.79 kPa and 51 ± 9.99 kPa, respectively and the mean for Young's modulus of the LLC was 55 ± 9.99 kPa (N = 60, three repeats of experiments). In comparison, the Young's modulus of the LLC incubated for 48 hours decreased to half of the Young's modulus of the LLC incubated for 24 hours (110 ± 19.95 kPa as shown in Table 2.3). Clearly, the viscoelasticity of the liquid crystals had been adversely affected as a function of time and the progressive effects are as shown in Figure 2.34. The LLC sample incubated for 72 hours was no longer elastic and showed a highly viscous behaviour upon removal of the indenter. This result is consistent with the rheological result of the liqud crystals which show that cholesteryl ester liquid crystals reduced their viscoleasticity significantly after 72 hours of exposure to cell culture media. Therefore, acqeous solutions are an imporant factor in determining the integrity of the amphiphillic molecules and clearly, the infusion of water molecules could reduce the binding force amongst the layers of cholesteric liquid crystals as a function of time. The result show a limited period during which lyotropic liquid crystals may be viably used as a cell force transducer. This is consistent with the rheological studies, the best viscoelastic behaviour of the cholesteryl ester based lyotropic liquid crystals found in the spherical indentation studies was also within 48 hours incubation in cell culture media.

2.3.10 Poisson's Ratio of the Liquid Crystals

The Poisson's ratio of the liquid crystals was determined by using a micro-tensile test method. The test system was initially calibrated by using cured polydimethylsiloxane (PDMS) which has a well-established Poisson's ratio (Lacour et al., 2003). Figure 2.35a shows the phase contrast images of the PDMS located in a

small initial space (x_o) of 10 μm between the stationary and movable glass slide after it has been cured for 24 hours. The deformation length of the liquid crystals in longitudinal direction (y) increased gradually and was inversely proportional to the transverse deformation length of the liquid crystals (x). This yielded a Poisson ratio of 0.49 ± 0.0067 (mean ± SD) as determined by using the least square method (Figure 2.35b). This figure seemed to be in good agreement with Poisson ratio of PDMS as reported in (Lacour et al., 2003) which is approximately 0.5 and these measurement results show that the custom-built system developed was reliable and could be used for determining the Poisson's ratio of LC.

Figure 2.36 shows an example of longitudinal strain measurements at different transverse strain (ε_1) for the cholesteryl esters liquid crystals which were captured in the phase contrast microscope. A necking effect was observed at the centre of the liquid crystal slab where the light penetrated through the thinning region. By applying the least-square method, Poisson's ratio of the CELC and LLC (25 ^{o}C) was characterised by a linear regime up to 160 % transverse strain ($\log \varepsilon_1 = 0.2$) and, were both determined at 0.5854 ± 0.0192 (mean ± SD), respectively (Figure 2.37a). At low transverse strain, the longitudinal deformation of LC is linearly dependent on the transverse strain.

This result also shows that Poisson's ratio of LLC did not change much within a short incubation time in cell culture media. As the transverse strain exceeding 160 % ($\log \varepsilon_1 > 0.2$) and increased to 600 % ($\log \varepsilon_1 = 0.8$), both liquid crystals began to show non-linear viscoelastic behaviour and small differences of strains were observed (Figure 2.37b). At a maximum transverse strain of 800 %, the gel reached its ultimate tensile strength and snapped.

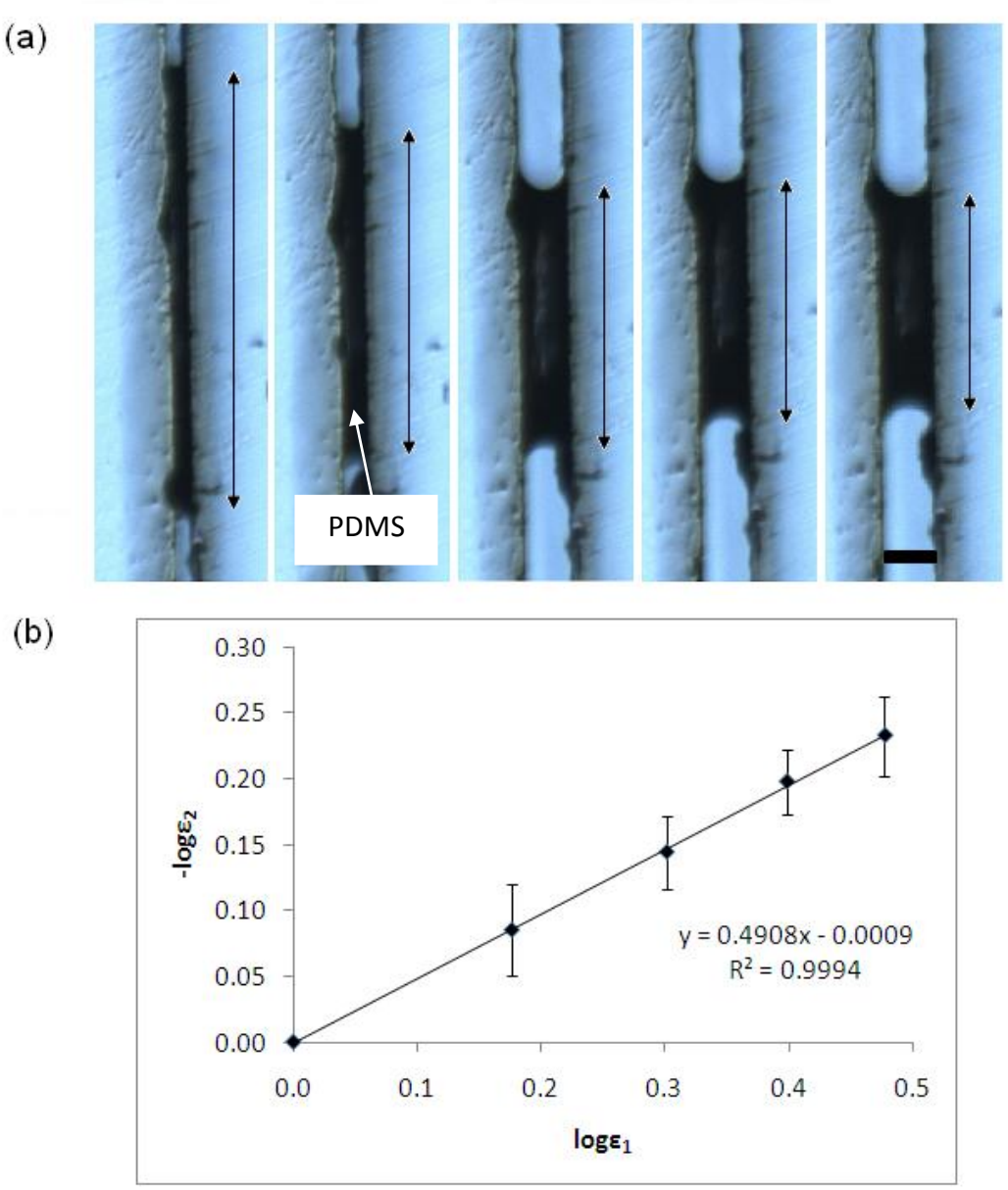

Figure 2.35. (a) Uni-axial deformation of a solid PDMS. The bi-headed arrows show the deformation in longitudinal direction (y) of PDMS at 380 μm, 276 μm, 220 μm, 192 μm and 178 μm that are corresponding to the deformation in transverse direction (x) at 10, 20, 30, 40 and 50 μm, respectively (image from left to right). The first image from the left shows the measurement for x_o and y_o. (Scale bar: 50 μm) (b) Plots of logarithmic longitudinal strain (ε_2) versus transverse strain (ε_1) or the Poisson's ratio of PDMS at room temperature (25 ^oC) in three repeat of experiments (N = 10 per experiment).

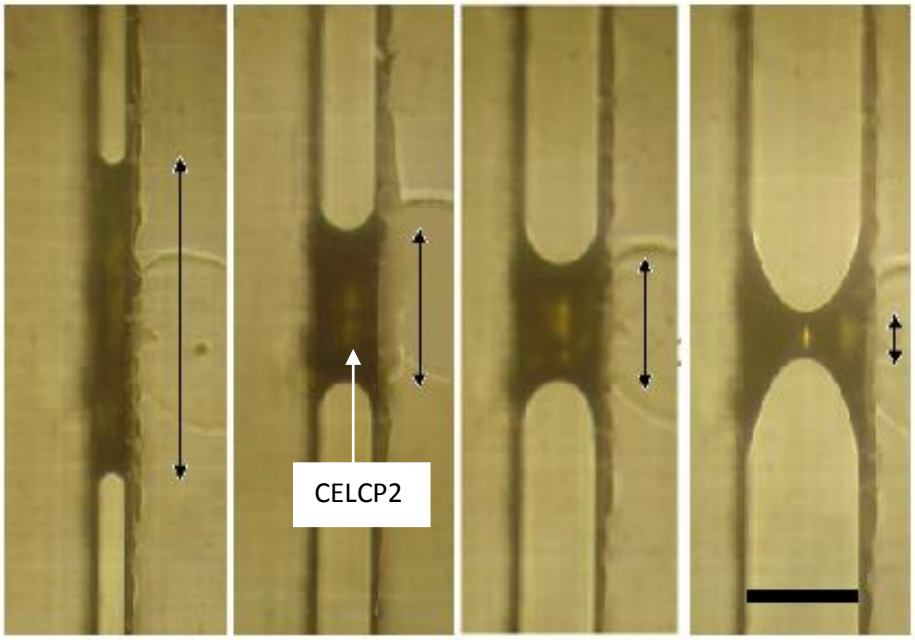

Figure 2.36. Uni-axial deformation of CELC. The bi-headed arrows show deformation in longitudinal direction (y) of LLC at 490 μm, 260 μm, 190 μm and 90 μm that are corresponding to the transverse deformation (x) at 50, 100, 150 and 200 μm, respectively (image from left to right). The first image from the left shows the measurement for x_o and y_o. (Scale bar: 200 μm)

The relationships of the normal pair of strains for LLC determined at 37 ^{o}C for 24, 48 and 72 hours are as shown in Figure 2.38a. Similar to the samples incubated at 25 ^{o}C, the normal pair of strains was linearly proportional to each other up to 160 % of the transverse strain (log ε_1 = 0.2). The LLC was subjected to a wide uni-axial strain (160 % transverse strain). Poisson's ratio of the LLC incubated at 37 ^{o}C for 24, 48 and 72 hours were measured at 0.58 ± 0.0586, 0.58 ± 0.0345, 0.60 ± 0.0254, respectively (Figure 2.38b). Under isothermal condition, the Poisson's ratio of the LLC immersed in cell culture media for first 48 hours showed small differences from the Poisson's ratio of CELCP2 incubated at room temperature (25 ^{o}C). However, the Poisson's ratio of the LLC incubated for 72 hours was higher indicates that the viscoelasticity of the LLC after

72 hours of incubation was reduced. It seems that Poisson's ratio of the LLC is mainly a function of immersion time in culture media.

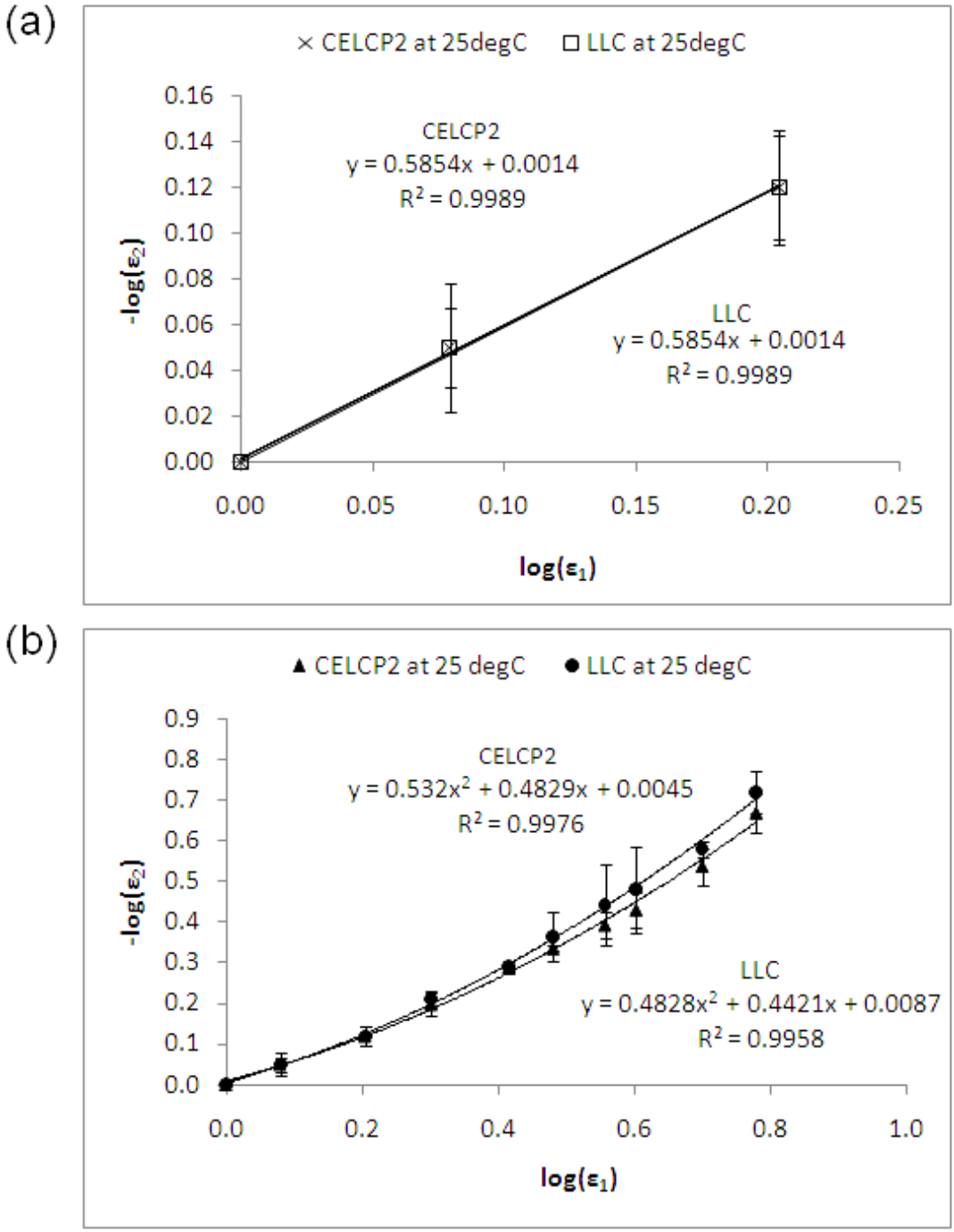

Figure 2.37. Plots of logarithmic longitudinal strain (ε_2) versus transverse strain (ε_1) or the Poisson's ratios for CELC and LLC up to (a) log ε_1 = 0.2 (60 % of strain) and (b) log ε_1 = 0.8 (600 % of strain) determined at 25 ^{o}C. The data are expressed as means ± SD.

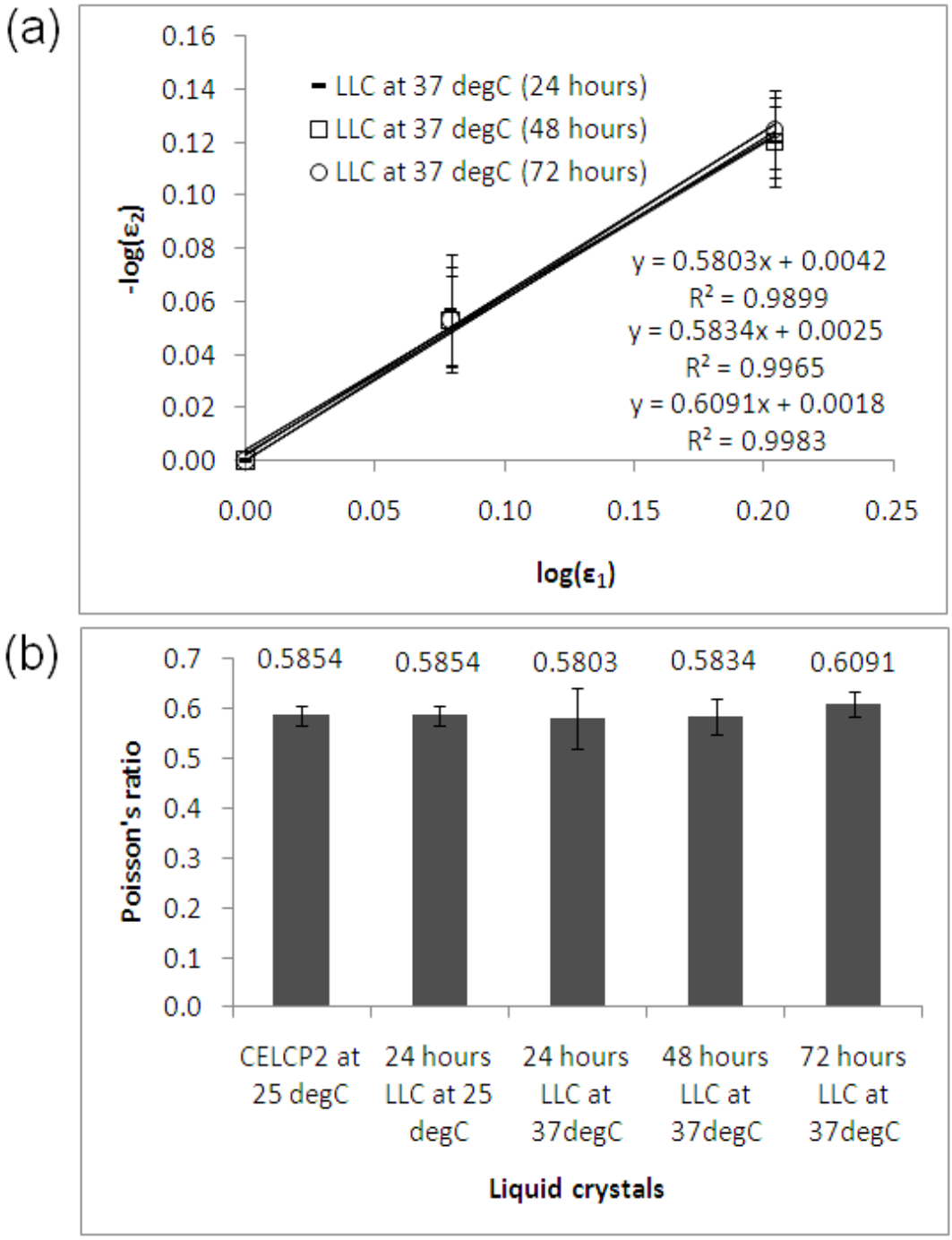

Figure 2.38. (a) Plots of logarithmic longitudinal strain (ε_2) versus transverse strain (ε_1) or CELC and LLC incubated at 37 ^{o}C for 24, 48 and 72 hours. The data are expressed as means ± SD. (b) Comparisons of Poisson's ratio (mean ± SD) for CELC and LLC at room (25 ^{o}C) and incubation temperature (37 ^{o}C).

According to (Smaby et al., 1979, Hilton and Yi, 1998), a higher Poisson's ratio may indicate higher compliance of viscoelastic material and this probably had occurred in the LLC incubated for 72 hours. However, temperature may not be the major factor as indicated by a similar Poisson's ratio of 0.58 for the LC substrates that were incubated at 25 ^{o}C and 37 ^{o}C for the same periods of time (Figure 2.38b). This is supported by a Differential Scanning Calorimetry (DSC) study of LLC which show that cholesteryl ester liquid crystals are thermally stable at room and incubation temperatures.

The result also shows that Poisson's ratio of the liquid crystals is a strain-dependent function. This applies to viscoelastic material regardless whether they are isotropic or anisotropic (Hilton and Yi, 1998). In our study, the Poisson's ratio measured for LLC is slightly greater than normal isotropic material which is greater than 0.5. In previous studies, Poisson's ratio measured for human nucleus pulposus (Cloyd et al., 2007) and polyvinyl alcohol (Lee et al., 2009) was similarly greater than 0.5. This is a typical characteristic of anisotropic material as suggested by (Ting and Chen, 2005). In cholesteric liquid crystals, mesogens of the same director are arranged in layers of helical twist. The cohesion forces binding mesogens of the same layer are different from the forces linking the helical layers. Therefore, in the cholesteric liquid crystals, the strength used for overcoming the molecular binding forces in a plane is different from the strength required to deform molecules lying in another plane or vice versa. Due to the anisotropy, liquid crystals may have more than one Poisson's ratio which depends on the plane and direction of the stress (Norris, 2006a) and it is technically challenging to determine the Poisson's ratio of other plane. A higher Poisson's ratio could suggest weaker layer binding forces between the layers of the liquid crystal and could be attributed to the small increase of water solubility in the

liquid crystal. With the infinitesimal deformation, the Poisson's ratio of the liquid crystals was clearly affected by the immersion time in a fluidic environment. In order to use LLC as a reliable biomaterial over a period of 3 days incubation at 37 ^{o}C, the result suggests a Poisson's ratio of 0.58 for the cholesteryl ester based lyotropic liquid crystals.

2.4 Summary

The cholesteryl ester liquid crystals exhibited physical stability over wide range of temperature (0 – 50 ^{o}C) through differential scanning calorimetry and cross-polarising microscopy. Oscillatory tests and in-situ rheological test were performed to study the viscoelastic behaviour of time-dependent cholesteryl ester liquid crystals after incubating in cell culture media at 37 ^{o}C for 24, 48 and 72 hours. The Young's moduli as determined by AFM nano-indentation and spherical indentation showed good agreement for the modulus of LLC sample incubated for 24 and 48 hours. The Young's modulus of the LLC determined is close to the Young's modulus of the skin epidermis layer studied previously. The LLC may provide a suitable mechanical signal to support adhesion of keratinocytes. The formation of a deformation lines in the liquid crystal surface was due to the bi-axial strains in the liquid crystal induced by cells. Poisson's ratio of the time dependent liquid crystal as measured off-site by micro-tensile stress method yielded a value of 0.58 for LLC incubated at 37 ^{o}C for 48 hours.

CHAPTER 3

BIOPHYSICAL INTERACTIONS OF CELLS AND LIQUID CRYSTALS

3.1 Introduction

In the previous chapter, both cholesteryl ester and TL205 liquid crystals were studied in relation to their physical properties, in order to determine the feasibility of developing liquid crystals into a cell force transducer. This chapter aims to build on that by investigating the biocompatibility and physical interactions between a human keratinocyte cell line (HaCaT) and the cholesteryl ester based lyotropic liquid crystal (LLC). This work will involve examining cell responses to the surface, the interfacial interactions with the liquid crystals, actin cytoskeleton organisations, integrins expression and ECM proteins deposition on the liquid crystals. To study cells responses on the LC, it is important to investigate the adhesion, contraction and morphological characteristic of cells on a soft substrate. In order to achieve this, the nature of the adhesion and contraction of the HaCaT cells on the liquid crystal (LC) coated substrate will be examined by disrupting the actin cytoskeletons using cytochalasin-B and cleaving the integrin proteins on the cells surface using crude trypsin. Cytochalasin B is a solution which specifically inhibits polymerisation of actin filaments (Wikswo and Szabo, 1972, Theodoropoulos et al., 1994), and trypsin is an enzyme used in cell culture to provide proteolytic digestion of cell surface glycoproteins to dissociate single cells from tissue or cell culture substrates (Roberts and Brunt, 1985, Baumann and Doyle, 1979). The cell-surface interactions will be further investigated by using fluorescence staining of F-actin, vinculin, and integrins (α2, α3, α5 and β1) in cells cultured on glass and LC substrates. The deposition of collagen type IV, laminin and fibronectin will also be examined in cells cultured on glass and LC coated substrates using immunoperoxidase and immunofluorescence staining techniques, respectively. Of the various extracellular matrix proteins, collagen type IV, laminin and fibronectin were chosen for this study because they are glycoproteins of the basement membrane

secreted by the keratinocytes that function to provide a stable adhesion and enable cell movement in-vivo and in-vitro (Nguyen et al., 2000, Larjava et al., 1993, Kirfel and Herzog, 2004).

3.2 Material and Methods

3.2.1 The Cell Viability Studies

To verify the cytotoxicity of the synthesised shear sensitive cholesteric and nematic liquid crystals, cell viability on the liquid crystals was investigated. HaCaT cells were grown with three cholesteryl ester liquid crystals of different formulations (CELCP1, CELCP2, CELCP3 as prepared and described in section 2.2.1) and a nematic liquid crystal (TL205) under normal culture condition (37 ^{o}C for 24 hours). In the procedures, 5 µl of each CECLP1-P3 and TL205 were placed into 4 wells of a multi-well cell culture plate (Figure 3.1). After spreading the liquid crystal with a cell scraper (Corning Incorporated) in each well, 1 ml of cell suspension at a density of 3.4 x 10^4 cells/ml and 2 ml of RPMI-1640 media (Sigma Aldrich, UK) were plated in each of the four culture wells containing CELCP1, CELCP2, CELCP3, TL205 and a control (untreated well). After 24 hours of incubation at 37 ^{o}C in an incubator, the media was discarded and trypsin was applied to the cells in the culture. Subsequently, the cells were recollected in a centrifugation tube and spun at 1600 rpm for 5 minutes. Cell pellets were collected and re-suspended in 3 ml of culture media. 0.1 ml of the cell suspensions were treated with 0.1 ml trypan blue (0.4 %) for 3 minutes. The relative proportion of trypan blue stained and unstained cells was then determined with a haemocytometer in a trypan blue exclusion assay. The count was repeated ten times

for each sample in three experiments and the average percentage of viable cells was obtained using the following formula:

Total no of viable cells = A x B x C x 10^4 (3.1)

Total no of dead cells = A x B x D x 10^4 (3.2)

Total cell count = Total no of viable cells + Total dead cell (3.3)

Percentage of viability = (Total viable cells ÷ Total cells) x 100 % (3.4)

where A, B, C and D represent the volume of cells, dilution factor in trypan blue, mean number of unstained cells and mean number of stained (dead cells), respectively. In this case, the volume of cells = 3 ml and dilution factor in trypan blue = 2.

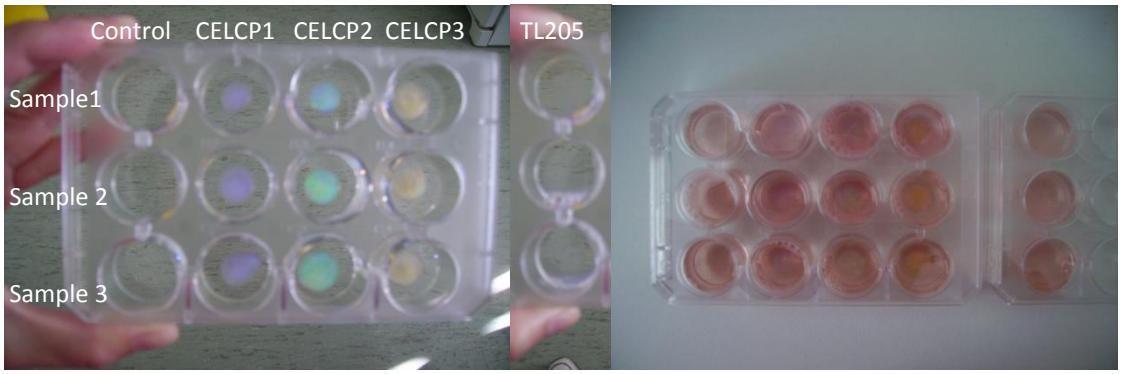

Figure 3.1. Preparation of liquid crystal samples in 15 wells (left, middle). Cell suspensions cultured in the presence of four liquid crystals (CELCP1, CELCP2, CELCP3 and TL205) and controls in 15 well cultures (right).

3.2.2 Treatment with Cytochalasin-B and EDTA-Trypsin

This study aimed at determining if focal adhesions and cell surface integrins are involved in supporting cell adhesion and contraction on the liquid crystal surfaces. The experiment began by coating substrate with a 100 μm thick layer of LC as previously described in section 2.2.3. Subsequently, HaCaT cells were prepared and plated at a density of 500 cells/cm^2 and maintained in RPMI-1640 media as shown in Figure 3.2 (Detail procedures for the preparation of cells were as described in section 2.2.6). After incubation at 37 ^oC for 24 hours, phase contrast and cross-polarising images of the

cells inducing deformation lines were captured. The contraction profiles were measured by taking the cross section of the width of the deformation lines by using profiling tools available in ImageJ.

Then, cell cultures on the LCs were treated with 5 µl of cytochalasin B (30 µM) and individual cells were monitored using a digital camera mounted on a phase contrast microscope. Time lapse phase contrast images of the cells were captured every 5 minutes over an hour. Cytochalasin B (35 mg/ml, Sigma Aldrich, UK) was solubilised in 0.042 % (v/v) ethanol (in distilled water). As a control, 0.042 % (v/v) of ethanol was applied to the cells in identical cell cultures.

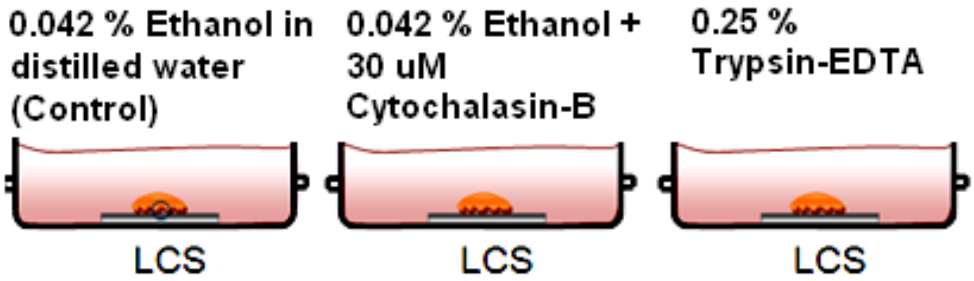

Figure 3.2. A cell relaxation technique implemented by applying Cytochalasin-B and trypsin to cells cultured on liquid crystal substrates (LCS) in petri dishes. Ethanol was used as a control.

Cell surface interactions were also examined in response to treatment with a 0.25 % EDTA-Trypsin solution. In these experiments, HaCaT cells were seeded on LC coated substrates maintained in culture media within petri dishes and cultured for 24 hours. After 24 hours, the cultures were transferred to a hot stage maintained at 37 ^{o}C. The culture media was removed by using a micro-pipette and the cells were treated with 0.25 % EDTA-Trypsin. During trypsinisation, time lapse images were captured via a phase contrast microscope equipped with a digital camera for every 5 minutes over an hour. All of these experiments were performed three times.

3.2.3 Fluorescence Staining of Cytoskeleton, Vinculin and Integrins

The fluorescence staining experiments were conducted to identify the expressions of actin cytoskeleton, vinculin and integrins for cells interacted with the cholesteryl ester liquid crystals. First, liquid crystal substrates were coated with liquid crystals as described in section 2.2.3. Then, HaCaT cell cultures were prepared based on the standard cell culture procedures as described in section 2.2.6. Cells were maintained under two conditions, on plain glass cover slips and on glass cover slips coated with liquid crystals, and both at a density of 1.3 x 10^3 cells/cm^2. After the cells reached sub-confluency, the glass cover slips were removed from the petri dishes and washed twice with Hanks Balanced Salt Solution (HBSS, Sigma Aldrich). Subsequently, the cells were fixed with 1 % formaldehyde in HBSS for 6 minutes, rinsed twice with HBSS and permeabilised with 0.1 % Triton X-100 for 3 minutes. To stain the F-actin after washing, the cells were incubated for 45 minutes with 1 µg/ml of Fluorescence Isothiocyanate (FITC) labeled Phalloidin solution (Sigma Aldrich) in HBSS followed by another three washes. To stain the nuclei, 4'6-diamidino-2-phenylindole-2HCl (DAPI) dihydrochloride solution (0.1 µg/ml in HBSS, Sigma Aldrich, UK) was applied to the cells for 15 minutes.

HaCaT cells on plain cover slips and LC coated cover slips were also immuno-stained for vinculin and integrins expressions. Sub-confluent cells were washed, fixed and permeabilised as described above. In the staining procedure, cells were rinsed and treated with a blocking solution. For vinculin and integrins receptor staining, the cells were bathed with 2 % of bovine serum albumin (BSA, Sigma Aldrich, UK) and 2 % goat serum (Sigma Aldrich, UK), respectively. After blocking, cells were washed three times in HBSS and incubated in 50 µl of primary antibody for 24 hours in a humidity chamber at 5 ^{o}C. The procedures were repeated except that the primary antibody was omitted

but substituted with HBSS for the negative controls. The primary antibodies used to stain vinculin and the integrins (α2, α3, α5 and β1) were anti-human vinculin antibody (1:40 in 1 % BSA), primary mouse monoclonal antibodies raised against CD49b (1:250 in 1 % BSA for α2), CD49c (1:250 in 1 % BSA for α3), CD49e (1:5000 in 1 % BSA for α5) and CD29 (1:2500 in 1 % BSA for β1). All primary antibodies were obtained from Biosciences Incorporated. These experiments were repeated three times. After incubation for 24 hours, the substrates were washed three times with HBSS, blotted and incubated with goat anti-mouse Immunoglobulin (IgG) secondary antibody labeled with Alexor Fluor 488 (5 µg/ml diluted in 1 % BSA, Sigma Aldrich, UK) for one hour. After staining, the substrates were subjected to three five minutes washes in HBSS before mounting onto the glass slides with DAPI dihydrochloride (0.1 µg/ml diluted in HBSS).

3.2.4 Immunoperoxidase Staining of Laminin

Cell surface interactions may affect the proteins secreted by cells (O'Toole, 2001, Kirfel and Herzog, 2004). This work investigated the deposition of endogenous laminin by the HaCaT cells using the immunoperoxidase staining technique. First, LC substrates were prepared as described in section 2.2.3. A sterilised glass cover slip coated with LC and two plain glass coverslips without LC (control and negative control) were placed in three separate petri dishes and seeded with cells at a density of 1.3×10^3 cells/cm^2. After reaching sub-confluency or two days of incubation at 37 ^{o}C, the cells were washed, fixed and blotted. All the reagents used for staining laminin in HaCaT cells were obtained from a laminin immuno-histology kit (IMMH7, Sigma Aldrich, UK). Briefly, two drops of 3 % hydrogen peroxide were applied to the cells plated on control, negative control and the liquid crystal substrate for 5 minutes, followed by

two washes and blotting. Then, the cells were incubated with 2 % BSA for 10 minutes and the excess reagent was discarded. Subsequently, the substrate was incubated with two drops of rabbit anti-laminin primary antibody for 60 minutes. In negative control, the application of the primary antibody was omitted but substituted with an addition of HBSS. After incubation, the cover slips were washed, blotted and treated with two drops of biotin conjugated goat anti-rabbit IgG secondary antibody for 20 minutes. Again, the cells were washed, blotted and treated with peroxidase reagent. After a short incubation of 20 minutes, a mixture of substrate reagents was added to the cover slip for 20 minutes. The mixture contained 4 ml of distilled water, 100 µl of acetate buffer, 5 µl of AEC (3-Amino-9-ethylcarbazole) chromogen and 3 % hydrogen peroxidase. After the final incubation, the cover slips were rinsed in HBSS for 5 minutes and photographed using a phase contrast microscope built-in with a digital camera. These procedures were repeated three times for cells cultured on LC coated substrates, controls and negative controls.

3.2.5 Immunoperoxidase Staining of Collagen Type IV

Cells and liquid crystal substrates were prepared as described in the procedures used in staining the immunoperoxidase staining of laminin. A sterilised glass cover slip with LCs and two glass cover slips without LCs (control and negative control) were placed in three separate petri dishes and each seeded with cells at a density of 1.5 x 10^3 cells/cm^2. After incubation at 37 ^oC for 24 hours, the cells were washed, fixed and blotted. After blotting, the cells were blocked with 2 % BSA for 10 minutes and the cover slips were blotted. Then, the cells on all the cover slips except the negative control were incubated with monoclonal anti-collagen type IV antibody raised in mouse (1 : 400, Sigma Aldrich, UK) for 60 minutes. The cells were then washed, blotted

and followed by treatment in anti-mouse IgG peroxidase conjugate antibody developed in goat (1 : 2000, Sigma Aldrich, UK) for 20 minutes. Then, the cells were washed, blotted and incubated with 2 drops of peroxidase reagent (IMMH7, Sigma Aldrich, UK) for 20 minutes. Subsequently, a mixture of substrate reagents (as prepared in immunoperoxidase staining of laminin in section 3.2.4) was added to the cover slips for 20 minutes and washed with HBSS for 5 minutes. The cover slips were photographed using the procedures as described in section 3.2.4. Similar procedures were repeated three times for cells cultured on LC coated substrates, controls and negative controls. These experiments were repeated three times.

3.2.6 Immunofluorescence Staining of Fibronectin

For the immuno-staining of fibronectin, HaCaT cells were cultured on a plain glass cover slip coated with liquid crystals and two plain glass cover slips (control and negative control) using similar procedures described for the immuno-staining of integrins. After incubation for 37 ^{o}C 24 hours, sub-confluent cells were washed, fixed and permeabilised as described previously. Subsequently, cells were rinsed and blocked with a 2 % goat serum solution. After blocking, cells were washed three times in HBSS and incubated in 50 µl of mouse anti-fibronectin primary antibody (Biosciences Incorporated) for 24 hours in a humidity chamber at 5 ^{o}C. The substrates were washed three times with HBSS, blotted and incubated with goat anti-mouse IgG secondary antibody labeled with Alexor Fluor 488 (5 µg/ml diluted in 1 % BSA) for one hour. After staining, the substrate was subjected to three five minutes washes in HBSS before mounting onto the glass slides with DAPI dihydrochloride (0.1 µg/ml diluted in HBSS). These experiments were repeated three times.

3.2.7 Fluorescence Microscopy

All the immunofluorescence and fluorescence staining were observed using a Nikon Eclipse 80i fluorescence microscopy (Figure 3.3) under dark field (DF) at 40x magnification and images were captured with ACT-2u software. The exposure time of the DF imaging for the blue (nuclei) and green (actin, vinculin, integrins or fibronectin) staining was fixed at 8 seconds and 15 seconds, respectively. Blue and green staining images were digitally merged using ImageJ software. A phase contrast microscope mounted with a digital camera was used to capture the micrographs for all the immunoperoxidase staining at 10x magnification.

Figure 3.3. A Nikon Eclipse 80i immunofluorescence microscope system.

Based on the immuno-staining micrographs of vinculin in three repeats, the cell size in terms of total area covered by each cell, width and length of vinculin stained regions for adherent cells on plain glass cover slips and LC substrates were measured by using the measurement tools available in ImageJ software.

3.2.8 Widefield Surface Plasmon Imaging of Cell-Liquid Crystals Interface

Two round glass substrates with a diameter of 22 mm and coated with a 50 nm thick gold layer were used in this study. These substrates were coated with cholesteryl ester liquid crystals as described in section 2.2.3. Cells at a density of 1.0 x 10^4 cells/cm^2 were plated in the two petri dishes, each containing one gold cover slip

coated with and without liquid crystals (Figure 3.4). Subsequently, the two petri dishes were incubated at 37 ^{o}C for 24 hours. After incubation, the cells were washed in HBSS twice and fixed in 1 % Formaldehyde for 6 minutes. The fixation was followed by a 5 minute wash and dehydration by a series of 5 minute washes in serial dilutions of ethanol in distilled water from 10 % through to 100 %. After dehydration, each gold cover slip was transferred to a widefield surface plasmon resonance (WSPR) microscope to be imaged (Figure 3.5). The WSPR microscope was fitted with a Zeiss Plan Fluar of 1.45 Numerical Aperture (NA) 100x magnification oil immersion objective.

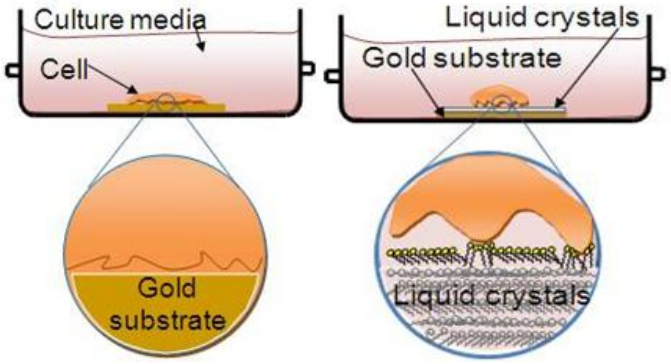

Figure 3.4. Cell culture in the absence (left) and presence (right) of liquid crystals on gold substrate.

In the WSPR system used, an incident p-polarised light from a super bright LED with a light wavelength of 633 nm was used to excite surface plasmons at the gold layer at an excitation angle of 46^{o}. The light wave interacts with the interface medium of different reflective index and generates different levels of reflectivity in the surface plasmon. The reflected light contained information associating with the interfacial interactions, and was captured by a charged coupled device (CCD) camera linked to Scion software. The images acquired were converted into a three dimensional (3D) format using ImageJ. Similar experiments were repeated three times. A detail description of the optical system used can be found in (Jamil et al., 2008).

(a)

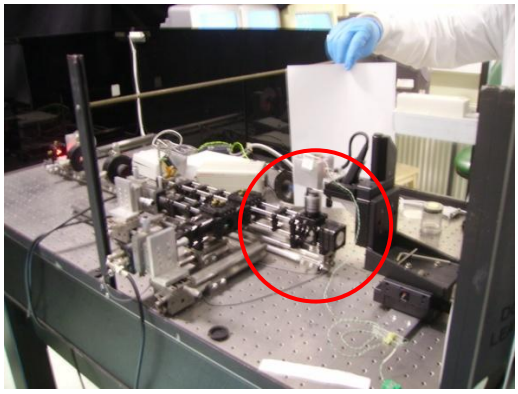

(b)

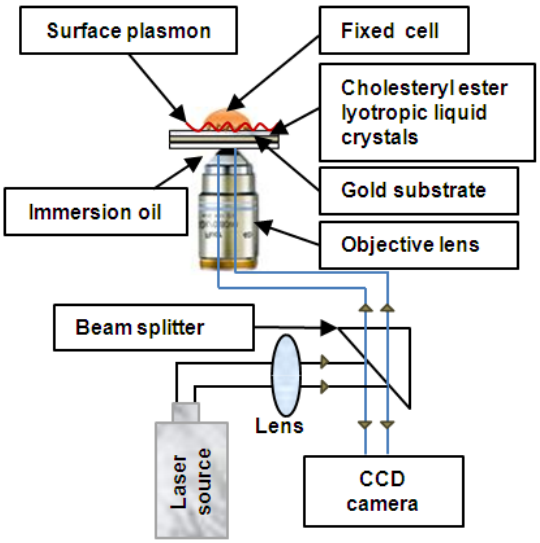

Figure 3.5. (a) A Wide Field Surface Plasmon microscope and (b) the setup for imaging fixed cells. The red circle in the image shows the location of the gold substrate holder and the oil immersion lens in the setup.

3.2.9 Statistical Analysis

Mean percentage of viable cells calculated for the cell viability studies were expressed as means ± standard error (SE). Analysis of variance using one way ANOVA followed by Tukey's HSD test (significant difference for $p < 0.05$) was used to determine the statistical differences between the treatments and controls in the cell viability studies. Cells area, width and the length of the stained vinculin regions were expressed as means ± SE and these were statistically analysed using independent paired t-tests (significant difference for $p < 0.05$). All statistical analysis was performed by using the Statistical Package for Social Sciences (SPSS) software.

3.3 Results and Discussion

3.3.1 Affinity of Liquid Crystals to Cells

Cell viability studies were used to determine the cytotoxicity of the liquid crystals. One sample Kolmogorov-sminov test indicate that the cell viability in CELCP1 ($p = 0.992$), CELCP2 ($p = 0.987$), CELCP3 ($p = 0.948$), and TL205 ($p = 0.985$) were normally distributed ($N = 4$, significant for $p > 0.05$). Figure 3.6 shows the phase contrast micrographs of HaCaT cells cultured on the LC substrates. These results in Figure 3.6 and Figure 3.7 indicate that cholesteric (CELCP1, CELCP2 and CELCP3) and nematic (TL205) liquid crystals were non-toxic to HaCaT cells. After 24 hours in culture, cell viability on all of the liquid crystals tested was 93 % and above, thus the liquid crystals tested were not cytotoxic (Figure 3.7). This view was supported by statistical analyses where no significant differences in HaCaT cell viability was identified for CELCP1 (106 %, $p = 0.993$), CELCP2 (162 %, $p = 0.524$), CELCP3 (107 %, $p = 0.980$) and TL205 ($p= 0.992$) compared with the control (Tukey's HSD test, $P > 0.05$). However, cells survival rate of TL205 (93 %) was slightly less compared to the cholesteric liquid crystals (Figure 3.7). This is most probably due to the dispersion of TL205 in the culture. This finding is contrary to the results reported in (Abbott et al., 2005), in which, cells are more viable in TL205 than cholesteric liquid crystals. However, Abbott et al. did not specify which cholesteric liquid crystal was used in their work. The common finding of this work and that of (Lockwood et al., 2006) was that cells poorly attached to TL205 (Figure 3.6d). This may be due to the low rotational viscosity of TL205, of about 367 mPas (Merck Germany). It is also possibly that the functional groups of TL205 do not support the adhesion of cells. Thus, it seems that TL205 is not

suitable as an interfacing layer for the direct monitoring of cell responses unless pre-coated with an inducer for cell adhesion such as matrigel or ECM proteins.

In comparison, the cholesteryl ester based lyotropic liquid crystals (LLC) enabled cell attachment without treatment with exogenous ECM proteins, a characteristic that may be associated with the cholesteric liquid crystal containing cholesteryl moieties that support cell adhesion (Lada et al., 2002, Small, 1977). This view is supported by a report suggested that cholesterol moieties are positively linked to enhancing the physical properties of cells during cell attachment and proliferation (Hwang et al., 2002). The fact that the cell membrane consists of lyotropic liquid crystals (phospholipid bilayer) distributed with cholesterol moieties may also explain the affinity of the liquid crystals to cells.

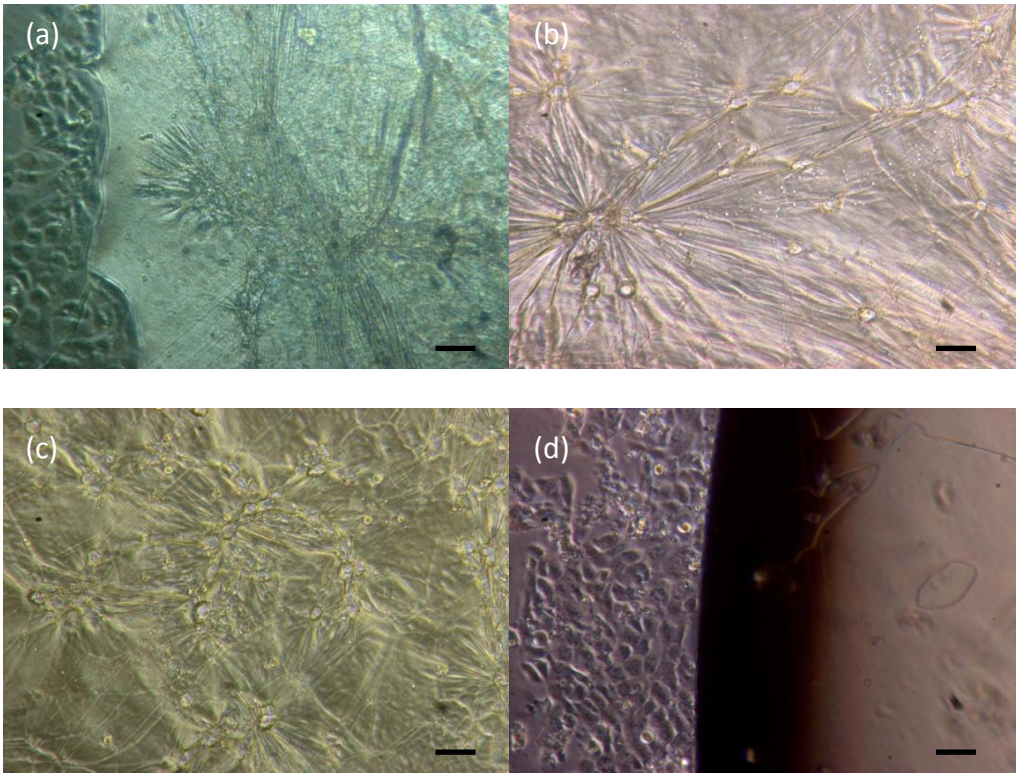

Figure 3.6. HaCaT cells cultured on (a) CELCP1, (b) CELCP2, (c) CELCP3, and (d) TL205 at a cell density of approximately 1200 cells/cm^2. (Scale bar: 25 μm)

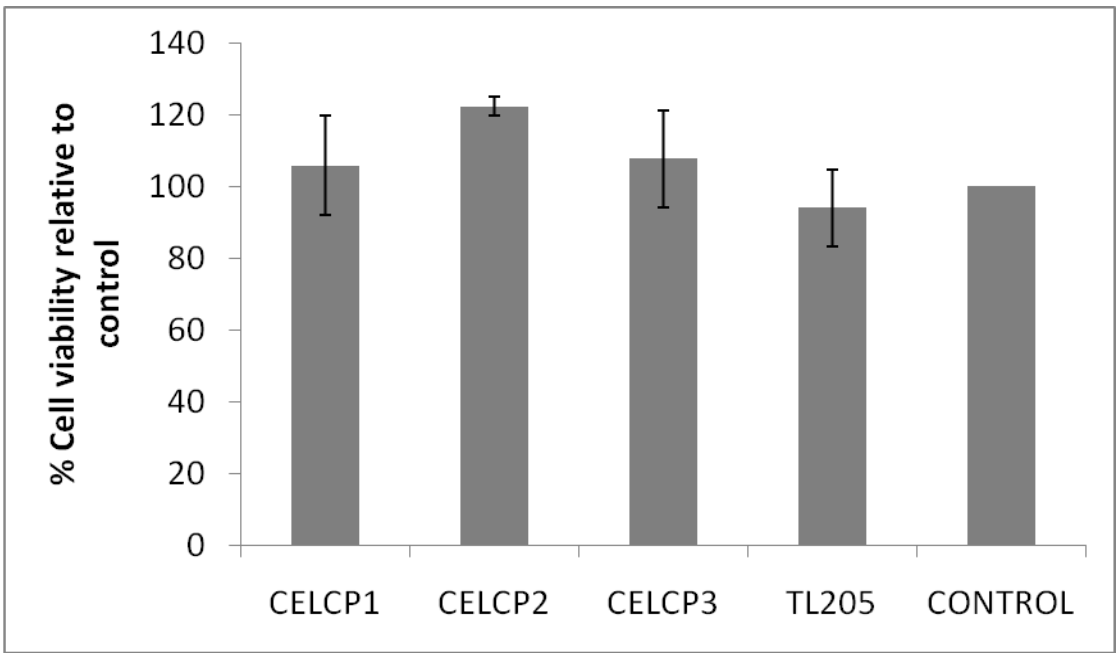

Figure 3.7. Percentage of HaCaT cell viability (mean ± SE) in cholesteric and nematic liquid crystals relative to control.

3.3.2 Effects of Cytochalasin-B, Trypsin and Ethanol to the Cells Adhesion on the Liquid Crystal Substrate

In the experiments of chapter 2, cell relaxation technique involves cytochalasin-B treatment was used to study the characteristic of the LC strain and deformations induced by the cells. This study did not include the investigation on the nature of the cell adhesion and contraction on the liquid crystal substrates. For this study, cytochalasin-B and trypsinisation techniques will be used to treat the cells in order to determine if the generated intracellular forces was transmitted to the LC surfaces via the mediation of cell surface integrins proteins. For the control (ethanol treatment) and two test culture experiments (cytochalasin-B and trypsin treatments), three cells of similar size were chosen. In the phase contrast microscopy, HaCaT cells attached to LC surfaces were not fully spread but ruffles could be observed at the cell periphery before any treatment (Figure 3.8a-c). When ethanol diluted in the distilled water was added to the control (containing culture media and the solvent), no major changes in

cell activity and deformation lines in the liquid crystals were observed over a period of 60 minutes (Figure 3.8a).

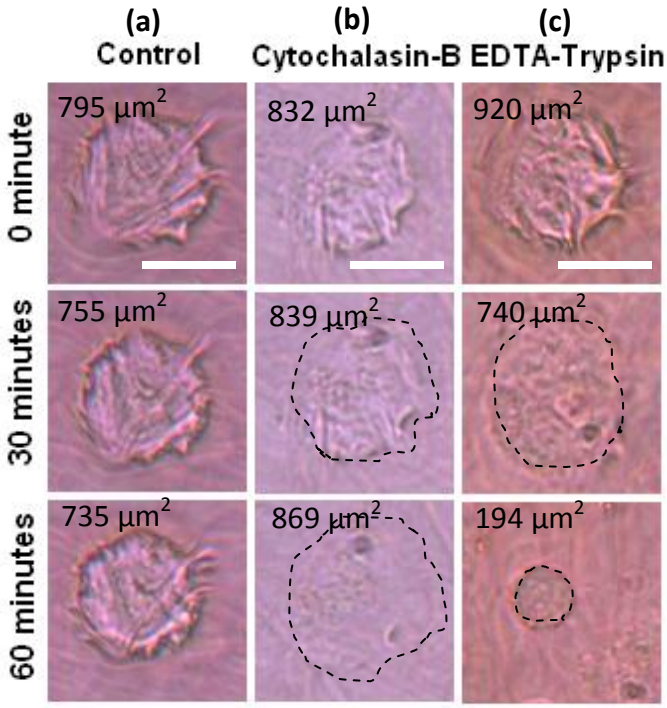

Figure 3.8. Phase contrast micrographs for the treatment effects of (a) 0.0042 % (v/v) ethanol (control), (b) 30 µM cytochalasin B, and (c) 0.25 % trypsin to the cells taken every 5 minutes over a period of 60 minutes. The areas of cell attachment in µm^2 are as outlined in the micrographs. (Scale bar: 25 µm)

Addition of cytochalasin-B to the cultures caused remarkable changes in both cell morphology and the distribution of deformation line in the LC surface when compared with the control (Figure 3.8b). After 15 minutes of cytochalasin–B treatment, HaCaT cells had not changed their morphology but there was a decrease in the length of the deformation lines (Image not shown). After 30 minutes of cytochalasin-B treatment, the cell attachment area seemed to increase from 832 µm^2 to 839 µm^2 and the ruffles on the cell body were greatly reduced (Figure 3.8b, 30 minutes). This indicates a decrease in the intracellular forces. By the end of the 60 minutes treatment, the cells remained attached, but they had acquired a flattened cell morphology and covered an

area of 869 μm^2 (Figure 3.8b, 60 minutes). Over this time, the intense deformation lines in the liquid crystal changed into fine lines (Figure 3.8b).

Experiments involving trypsinisation were used to confirm that the intracellular forces transmitted to the liquid crystals are mediated by focal adhesions and integrins receptors on the cell surface membrane. The trypsinisation effect on HaCaT cells cultured on liquid crystals was very different from previous result where a total loss of liquid crystal deformation line was observed (Figure 3.8c). The initial attachment area of this cell was 920 μm^2. Crude EDTA-Trypsin cleaves the surface receptors that bind cells to the substrate, caused the periphery of the cell edges to detach. In these experiments, this caused a reduction in cell area from 740 μm^2 to 194 μm^2 after 60 minutes of trypsinisation (Figure 3.8c). The decrease in cell area was accompanied by the cells acquiring a more rounded morphology and lifted off the surface of liquid crystals (Figure 3.8c). The detachment of cells from the LC surface allows the elasticity of the cell membrane to pull the cells into a rounded morphology, leading to a decrease in cells size.

The trypsinisation and cytochalasin-B treatment clearly show that that the deformation lines formed in the liquid crystal surface were induced by the tensions generated within the cell. The tensions were exerted by the focal adhesions that are interconnected to the polymerised F-actins. It is these focal adhesions, formed from a complex of vinculin, paxillin or talin molecules coupled to αβ integrin dimers that directly attach cells to the extracellular matrix (ECM) (Geiger and Bershadsky, 2002, Burridge et al., 1997). In bridging focal adhesions to the LC surfaces, ECM proteins may be present in between the cells and the LC surfaces, and this requires further investigations for the presence of ECM proteins.

The result of the cytochalasin B and trypsin treatment also demonstrated that liquid crystal surfaces are sensitive and flexible enough to sense localised stress exerted at a small confined region and this has not been previously reported in any polymer based cell force sensor (Beningo, 2002, Oliver et al., 1995, Munevar et al., 2001). The ability of the liquid crystals to respond to a point source of stress can be explained by the properties of the compactly packed liquid crystal molecules that only dissipate the strain energy in a confined region. In comparison to the silicon rubber technique (Burton et al., 1999), the polymers were observed with chaotic wrinkles when cells exerted stresses on them (Figure 1.12). Some of the deformation lines may not be correlated with the applied stresses due to the propagation of energy to the crossed-linked molecules in the neighbourhood (Oliver et al., 1995, Beningo, 2002, Munevar et al., 2001).

3.3.3 Structure of F-actin and Vinculins

Liquid crystals used in this study did not prevent the cells from differentiating and growing but allowed HaCaT cells to proliferate on the liquid crystals after several days of cultures. On a plain glass cover slip, the cells were readily identifiable (Figure 3.9a). However, on a liquid crystal coated substrate, the liquid crystals partially masked the cells-glass interface (Figure 3.9b). Despite this, it was possible to determine the F-actin and vinculin expressions for cells on the plain glass substrate in comparison with the liquid crystal coated substrate. After reaching sub-confluency, the F-actin and vinculin organisations of keratinocytes cultured on the plain glass substrate and liquid crystal coated substrate displayed distinct differences.

Cells plated on the hard surface of the glass substrate projected linear and striated arrays of actin microfilaments spanning the entire cells body (Figure 3.9c). The

enhanced prominent actin fibres were accompanied by a higher expression of elongated and scattered vinculin stained regions in those cells attached to the glass surface (Figure 3.9c, e). Comparatively, more diffused actin filaments were observed for adherent cells on the LC substrate (Figure 3.9d). This was accompanied by small punctuations of vinculin staining arranged at the periphery of cells membrane (Figure 3.9f).

Kolmogorov-smirnov tests indicate that the length and width of the vinculin stained regions expressed by the HaCaT cells on both substrates were normally distributed (Length of stained vinculin regions: $p = 0.2$ for glass, $p = 0.124$ for LC; width of vinculins: $p = 0.154$ for glass, $p = 0.151$ for LC). The width of vinculin stained regions on the plain glass and LC coated substrates were determined at 0.26 ± 0.01 µm (mean ± SE) and 0.25 ± 0.01 µm (mean ± SE), respectively (Figure 3.10a).

The length of vinculin stained regions for cells cultured on the plain glass and LC coated substrates were determined at 1.4 ± 0.03 µm (mean ± SE) and 1.05 ± 0.02 µm (mean ± SE), respectively (Figure 3.10a). The length of the vinculins stained regions for cells cultured on the plain glass and LC coated substrates differed significantly between treatments ($p = 0$, significant for $p < 0.0001$ $N = 525$) but the width of vinculins stained on both substrate showed no significant difference ($p = 0.383$, significant for $p < 0.0001$ $N = 525$). These results indicate that vinculin tend to elongate than to expand in width when cells were cultured on plain glass substrates. This is consistent with previous reports which demonstrated the development of highly elongated cylindrical assemblies of mature focal adhesions in cells cultured on flat rigid substrates (Goffin et al. 2006, Reveline et al. 2001).

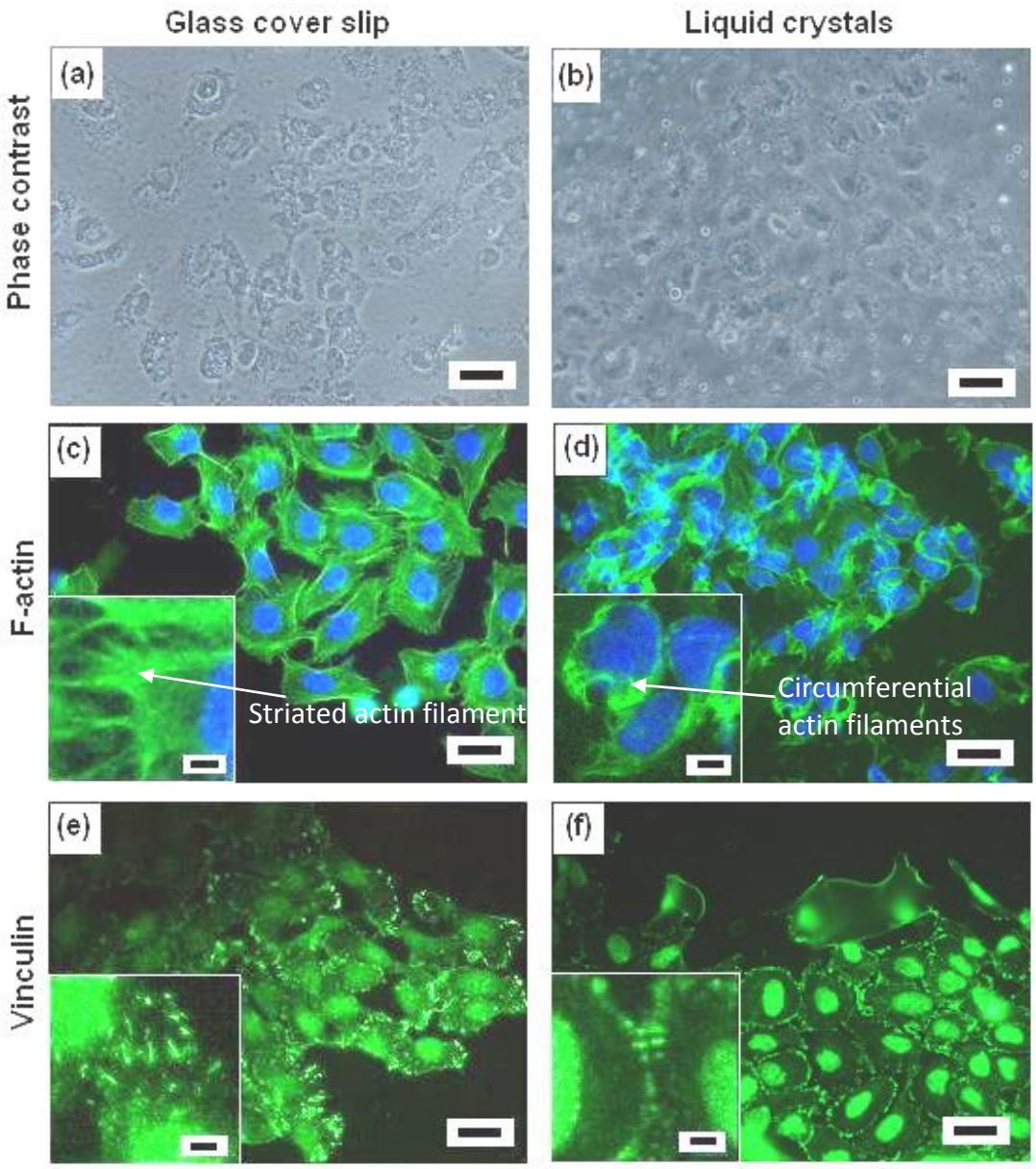

Figure 3.9. Phase contrast micrographs of the interface of HaCaT cells attached to (a) a plain glass and (b) a liquid crystal substrates. Immunofluorescence micrographs of the staining against (c, d) F-actin and (e, f) vinculin, respectively. (Scale bar: 25 µm) (Enlarge exert, scale bar: 1 µm)

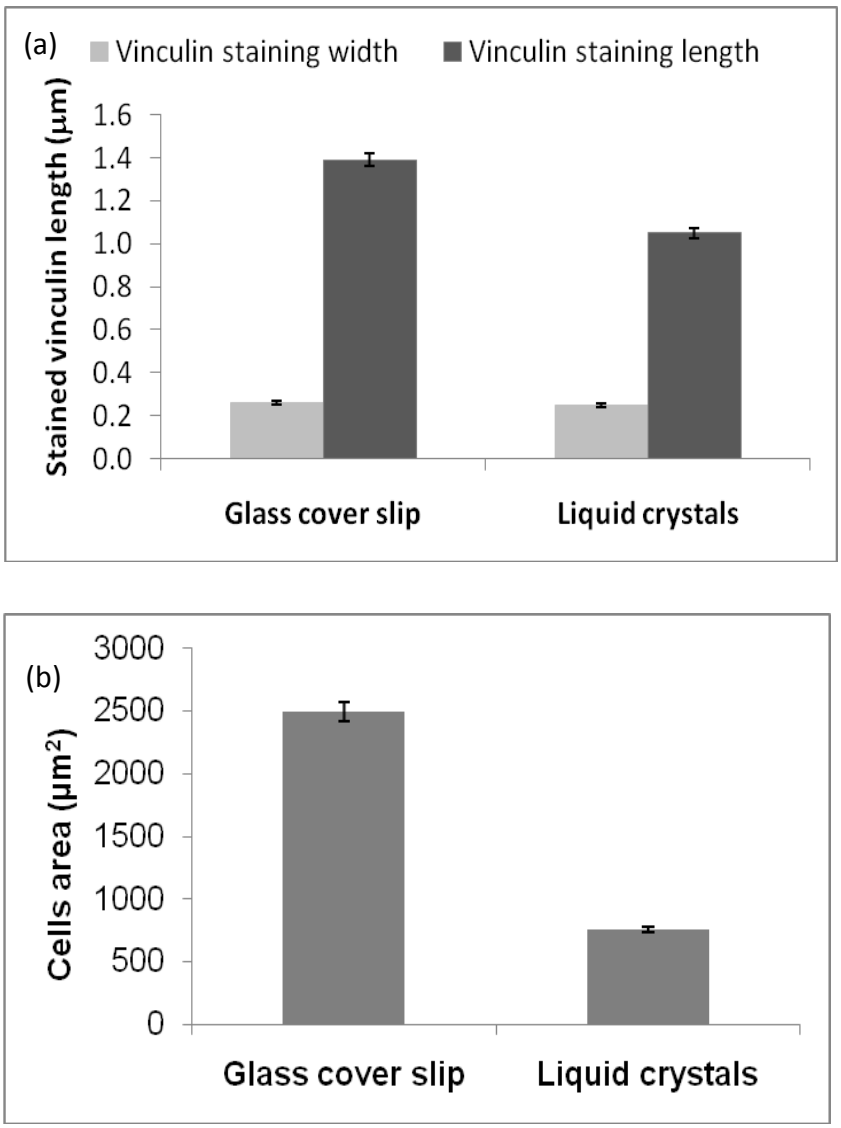

Figure 3.10. A comparison of (a) vinculin width (p = 0.383), length (p = 0), and (b) cell surface area (p = 0) of HaCaT cells attached to plain glass cover slips and liquid crystal substrates. The area of cells, length and width of vinculin are expressed as mean ± standard error which is significant for P < 0.001, N = 258 (cell surface area) and N = 525 (vinculin).

In the context of the area covered by individual cells, one-sample Kolmogorov-smirnov test shows that the cell areas on glass (p = 0.866) and LC substrates (p = 0.532) were normally distributed (significant value for p > 0.05). The cells cultured on the glass covered a significantly greater area (2496 ± 608 µm^2) than cells cultured on the liquid crystal coated substrates (759 ± 169 µm^2, P < 0.001, N = 258) as shown in Figure 3.10. For cells cultured on the LC substrate, the significantly smaller sized vinculin

stained regions or dots of vinculin were diffusely arranged at the edges of the cells membrane especially at the cell-cell interactions. In comparison with the isometric contraction of actin filaments and scattered vinculin staining in cells cultured on the glass substrate, HaCaT cells on the liquid crystals were characterised by diffusely arranged F-actin and well organized vinculin staining regions. These observations indicate that cell attachment and spreading probably have a strong correlation with the stiffness of culture substrate (Yeung et al., 2005, Discher et al., 2005). This result is in agreement with reports which suggest that the size of F-actin and vinculin expressions are proportional to the substrate stiffness (Yeung et al., 2005, Discher et al., 2005). There is evidence that cells have an active mechano-sensing mechanism that monitor the stiffness of a substrate leading to a re-organisation of the cytoskeletons and cell spread area (Yeung et al., 2005, Engler et al., 2004b).

While attaching to a soft substrate, a cell disassembles the focal adhesion proteins via the Rho-GTPase pathways and the disassembly of adhesion proteins, in turn, promotes de-phosphorylation of the actin cytoskeleton driven by Myosin II (Geiger and Bershadsky, 2002, Hotulainen and Lappalainen, 2006, Owaribe et al., 1981). Due to down regulation of the cell focal adhesions and cytoskeletal depolymerisation on the soft liquid crystal substrate, cells may decrease their physical contact with the liquid crystals and take up rounded morphology (Figure 3.9b, d and f). Furthermore, cholesteryl ester based lyotropic liquid crystal has a Young's modulus of ~110 kPa (as determined in Chapter 2) and this closely mimics the elastic modulus of the epidermis layer (Takeo, 2007, Hendriks, 2005). The stiffness of the liquid crystals probably stimulates the cells to behave as those in the in-vivo system. Some studies (Yeung et al., 2005, Discher et al., 2005, Engler et al., 2004b) showed that cells are sensitive to the stiffness of the adhesion substrate.

If cells could adapt their physical structure in response to substrates of different stiffness, then, a cell force transducer developed on a material with a higher or lower elastic modulus than that of the in-vivo system would measure a different range of forces (Discher et al., 2005, Yeung et al., 2005), and such surfaces may even be taken as a pathological condition by the cells (Engler et al., 2004b). Engler et al. suggests that differentiation of cells is best supported by biomaterials that match the stiffness of the in-vitro environment (Engler et al., 2004b) because they would enable the generation of mechanical signals that would promote cell survival. Hence, designing a cell mechano-transducer using biomaterials with elastic moduli closer to that of the tissue would literally provide relevant mechanical signals to the cells. Using a material with a relevant elastic modulus is a point that requires stringent consideration in the development of cell force transducer systems.

3.3.4 Expressions of Integrin α2, α3, α5, β1 and the Associated Extracellular Matrix Proteins

The objective of this experiment is to investigate if the same suites of integrins and ECM proteins are expressed on the liquid crystal substrates when compared with those cells cultured on plain glass substrates. For cells cultured on the liquid crystals, the immuno-stained micrographs of α2, α3, α5 and β1 integrins (Figure 3.11c, f, i, l) seem to be similar to the adherent cells cultured on controls (plain glass substrates) (Figure 3.11b, e, h, k) in comparison with the negative controls (plain glass substrates, treatment without primary antibody) (Figure 3.11a, d, g, j). Similar patchy and diffused appearances of integrins were observed for the cells cultured on control and LC coated substrates (Figure 3.11).

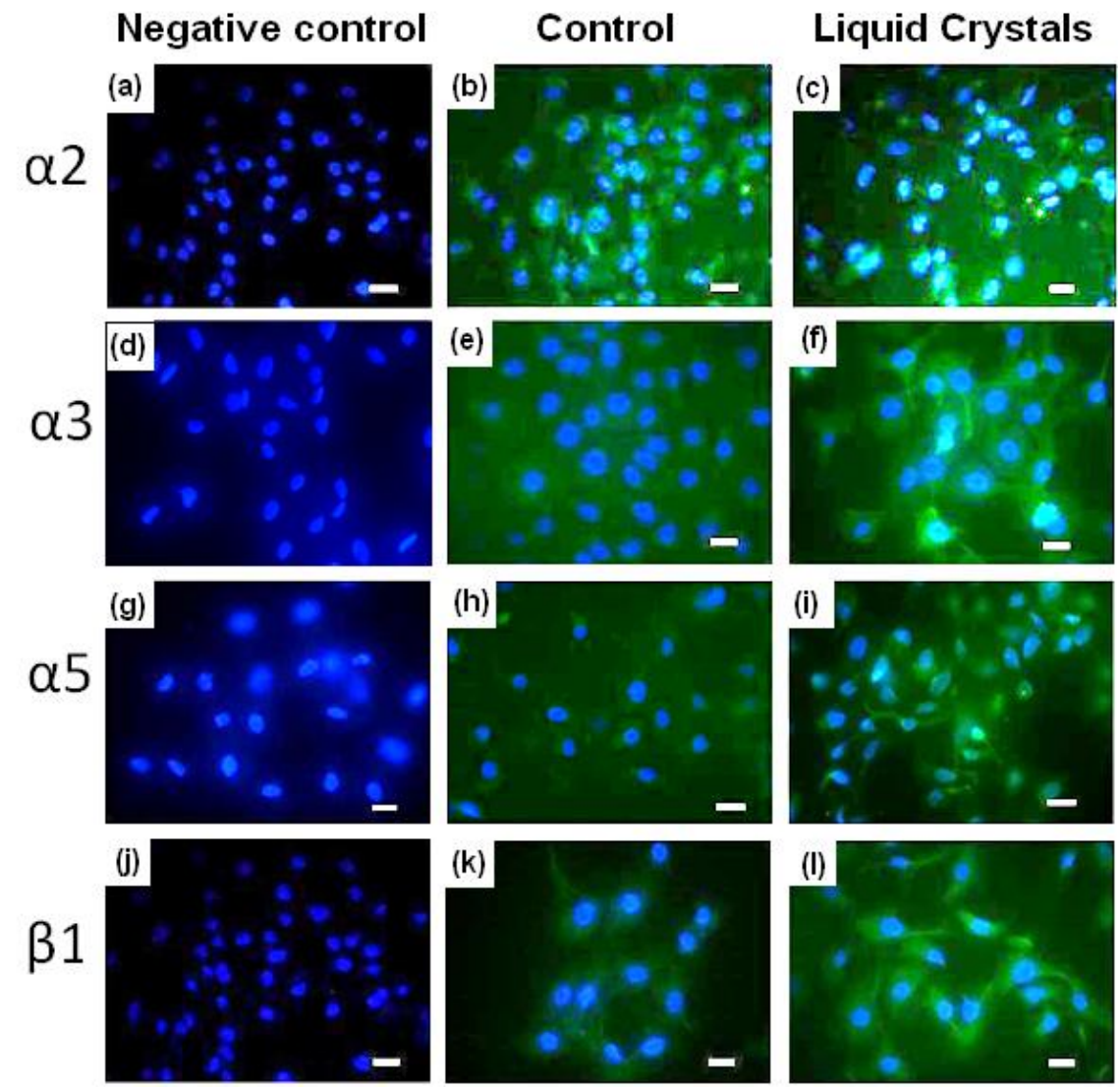

Figure 3.11. Micrographs of immunocytochemical staining against α2, α3, α5 and β1 for (a, d, g, j) negative controls, HaCaT cells cultured on (b, e, h, k) glass cover slips and (c, f, i, l) liquid crystal substrates, respectively. (Scale bar: 25 μm)

α2β1 and α3β1 are integrins used by HaCaT cells to bind to collagen type IV and laminin (Bolognia et al., 2004, O'Toole, 2001, Kainulainen et al., 1998, Kirfel and Herzog, 2004) while α5β1 recognise fibronectin (Kainulainen et al., 1998, Larjava et al., 1993). These three groups of integrins (α2β1, α3β1, α5β1) are found present in cells cultured on control (Figure 3.11b, e, h, k) and LC substrates (Figure 3.11c, f, i, l). Integrins are formed from a heterodimer of α and β subunits. Integrin β1 is usually co-localised with α integrins sub-unit corresponding to the type of ECM proteins present

(O'Toole, 2001, Kirfel and Herzog, 2004, Burridge et al., 1997). The results show that β1 integrin expressions are present in the sub-confluent cells on both glass and liquid crystal substrates, and that could be related to the role of β1 integrin in supporting cell motility during proliferation (Thirkill et al., 2004, Kreidberg, 2000).

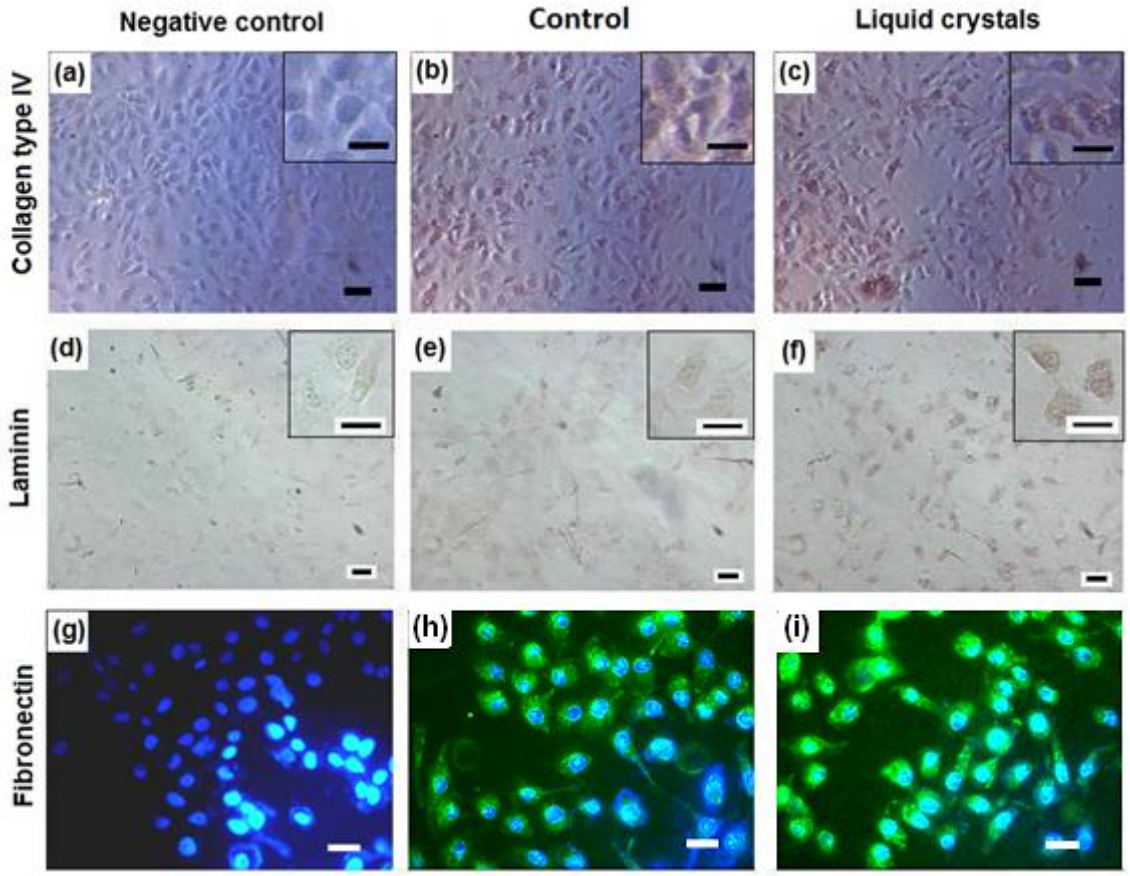

Figure 3.12. Micrographs of immuno-staining against collagen type IV, laminin and fibronectin for HaCaT cells cultured on (a, d, g) negative controls, (b, e, f) controls and (c, f, i) liquid crystal substrates, respectively. (Scale bar: 20 µm). (Enlarged exert, scale bar: 25 µm).

In this work, ECM proteins were not applied to the cultures of cells on the plain glass and LC coated substrates. However, Figure 3.12 and Figure 3.13 show that collagen type IV, laminin and fibronectin proteins are found in the cells cultured on both glass and liquid crystal substrates. This indicates that cells cultured on both substrates secreted collagen type IV, laminin and fibronectin; forming a provisional

basement membrane in an in-vitro culture. This might have enabled HaCaT cells to attach to the LC surface via the naturally produced ECM proteins. This finding is supported by previous literature (Li et al., 2004b, Stanley et al., 1982a, O'Toole, 2001) evidencing keratinocytes secreting their own ECM proteins. Although there might be some slight differences in the staining intensity of integrins and ECM proteins in the immuno-stained micrographs, however, further quantifications on their expressions are beyond the scope of this work.

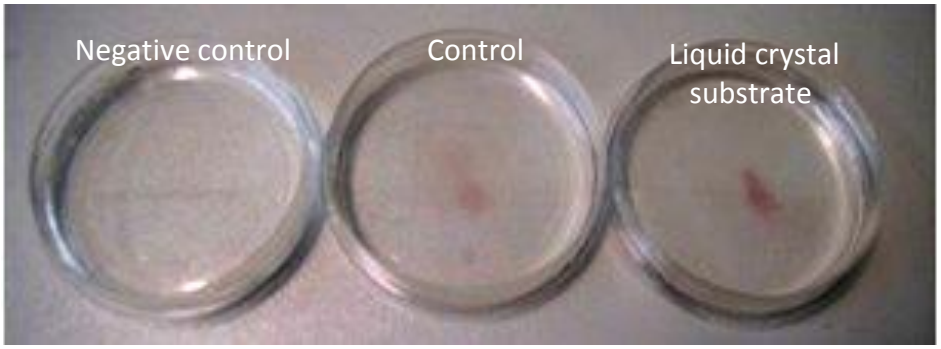

Figure 3.13. Immunoperoxidase staining of laminin for HaCaT cells cultured on a negative control (left), control (middle) and liquid crystal substrate (right).

The deposition of endogenous ECM molecules on the LC surface would require the cells to have an affinity to the substrate. The mixture of cholesteryl ester liquid crystals used is derivatives of cholesterol which consists of cholesteryl perlagonate, cholesteryl chloride and cholesteryl oleyl carbonate (Antczak and Antczak, 2001). These amphiphilic molecules of cholesteryl ester liquid crystals could self-assemble into lyotropic liquid crystals interlaced by multi-layers of water molecules (Fairhurst et al., 1998, Hyde, 2001) as investigated and discussed in Chapter 2. The affinity shown by HaCaT cells to the liquid crystals might be due to the cholesterol moieties of the cholesteryl ester liquid crystals or the hydrophilic head groups directed towards the media as proposed in a model as shown in Figure 3.14. This form a hydrophilic surface

which is probably favourable for the binding of hydrophilic head groups (such as, cholesterol and cholesterol ester molecules) residing over the surface of the bilayer lipid membrane of a cell (Figure 3.14). As suggested in (Collings and Patel, 1997, Fairhurst et al., 1998), hydrophilic molecules in the lyotropic liquid crystals are more likely to attract to other hydrophilic head groups. Furthermore, a cell is prone to attach to hydrophilic surfaces is because hydrophilic surface with high surface energy (interfacial free energy) attracts the adsorption of ECM proteins, which then, lead to the binding of the adhesion receptor protein of the cell membrane to the ligand proteins adsorbed to the surface (Kim et al., 2001, Scholz, 2003, G. et al., 2005, Absolom et al., 1983).

Consequently, the hydrophilic LC surface encourages the cells to secrete their own adhesive proteins onto the LC to facilitate integrins mediated cell adhesion (Figure 3.14). Similarly, Hwang et al, 2002 showed that fibroblasts have an affinity to a lyotropic system consisted of cholesteryl-oligo (l-lactic acid). This is probably due to the cholesterol moieties present in this compound. As previously reported (Simons and Ikonen, 2000, Hwang et al., 2002, Yeagle, 1985), cholesterol is an important component of the lipid membrane of cells which maintains homeostasis, sustains the mechanical durability of cells and improves the permeability of the membrane. The study conducted in this work supports this view by demonstrating that cholesteryl ester based lyotropic liquid crystals can support and maintain the attachment of viable HaCaT cells.

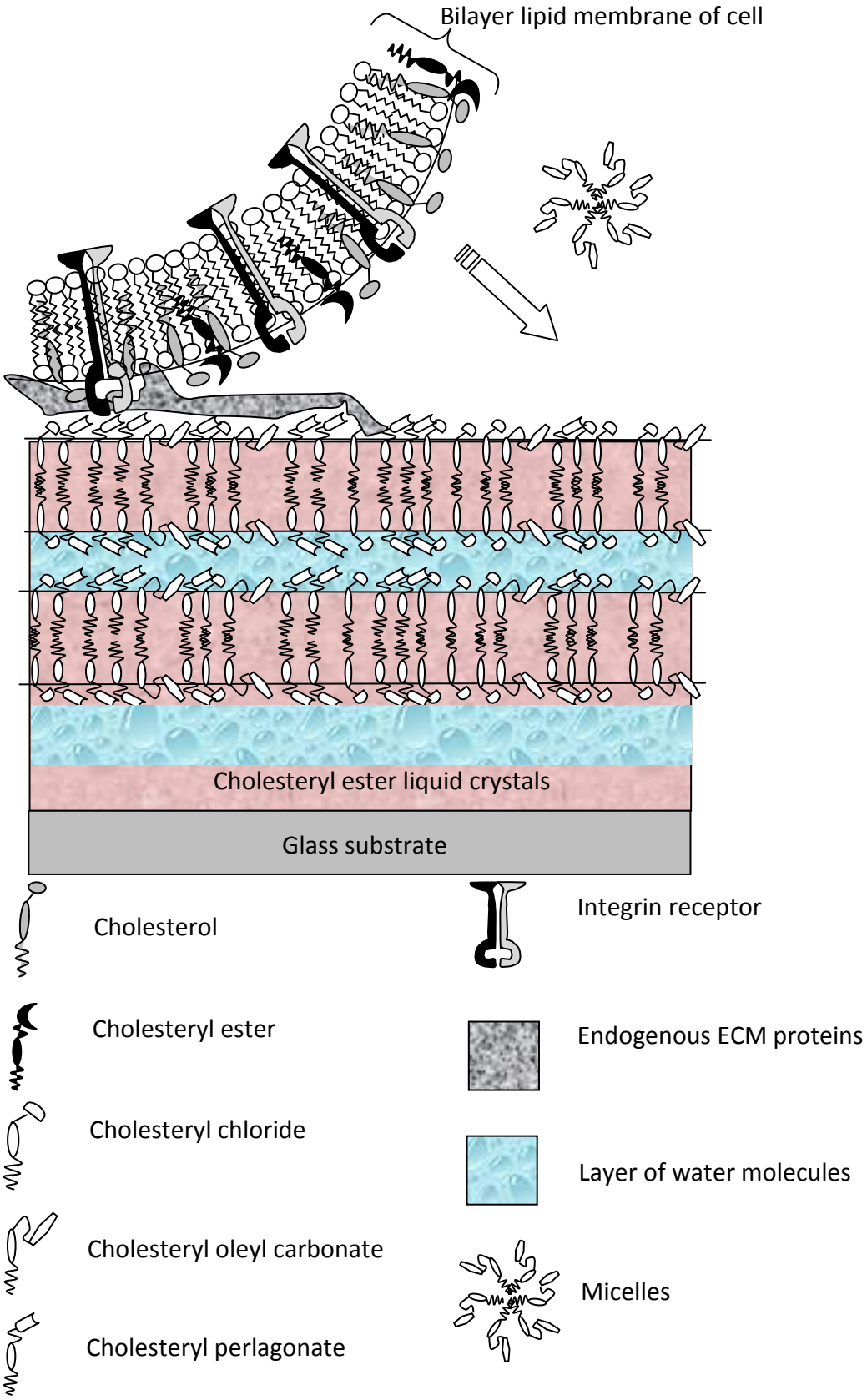
Bilayer lipid membrane of cell
Cholesteryl ester liquid crystals
Glass substrate
Cholesterol
Cholesteryl ester
Cholesteryl chloride
Cholesteryl oleyl carbonate
Cholesteryl perlagonate
Integrin receptor
Endogenous ECM proteins
Layer of water molecules
Micelles

Figure 3.14. A propose model for the interaction of cell membrane and cholesteryl ester based lyotropic liquid crystals.

In order to attach to the liquid crystal substrates, HaCaT cells rely on self-secreted ECM proteins and their adhesions differ greatly from the adhesion of cells to the exogenous ECM proteins coated on PDMS, PAA or silicone rubber which were used as cell traction force sensor. The coating of the ECM proteins on these substrates may be artificially high and this may alter the overall stiffness of the adhesion substrate (Mooney et al., 1995, Provenzano et al., 2009). Furthermore, the use of a specific types of ECM protein as adhesion protein is known to modify the morphology and behaviour of a cell (Kirfel and Herzog, 2004, Decline and Rousselle, 2001). For example, fibronectin has been shown to promote a migratory phenotype of cells resulting in higher expressions of stress fibres (Larjava et al., 1993, Provenzano et al., 2009, Kainulainen et al., 1998). Without pre-treatment with exogenous ECM proteins but relying on endogenous ECM proteins from cells, LC substrates are coupled with naturally synthesised adhesive proteins by the cells to functionalise the attachment of cells.

3.3.5 Interface Patterns of Cell Adhesion

Fluorescence staining was used to show the reorganisation of internal structure in HaCaT cells cultured on the LC coated substrates, while WSPR images qualitatively revealed the interfacial stress as a result of cell restructuring. For the WSPR microscopy, HaCaT cells were broadly spread on the plain gold cover slips. A wide band with irregular distribution of punctuated patterns was formed around the nucleus located at the centre of the cell (middle ring) and this indicates a greater contact area at the cell/glass interface (Figure 3.15a). For a clearer view, a post-processed image for

cells on gold substrate in 3D shows large bands with an irregular hills and valleys type of structure in the spread area (Figure 3.15c). This is in good correlation with the vinculin staining (Figure 3.9e), and the irregular patterns of the wide band (Figure 3.15a) seemed to be related to the stress points of scattered focal adhesions on the plain glass substrate (Jamil et al., 2008).

In comparison, the adherent cells on the liquid crystals were found to be less spread and seemed to be restricted in terms of direct contact with the surfaces. In addition, a lower number of clearly defined narrow concentric rings were seen around the nucleus or periphery of the cell on the LC (Figure 3.15b). The associated 3D image of WSPR image showed a topology of uniform narrow bands around the nucleus and at the edges of the cell membrane (Figure 3.15d).

Consistently, the concentric rings and the regular narrow bands at the cell boundary were associated with the weight of the nucleus and uniform focal adhesion arrangements as indicated in Figure 3.9f, respectively. This suggests that the stress applied by the focal adhesions induced by the actin filaments (qualitatively) was concentrated around the edges of the cells membrane in a regular and narrow contact area. The higher contrast regions as shown in Figure 3.15d are due to the presence of the liquid crystals interfacing with the cells. The result also shows that the attachment strength mediated by the focal adhesion on the liquid crystal substrate was sufficient to prevent cells being removed by rigorous washing during the preparation of the substrates. Nonetheless, this experiment again shows that the physical interaction with the liquid crystals had influenced the morphology of cells. The recognition of the external mechanical signal by the cells may have overtaken the biochemical signal in regulating the cell surface area couplings (Lo et al., 2000).

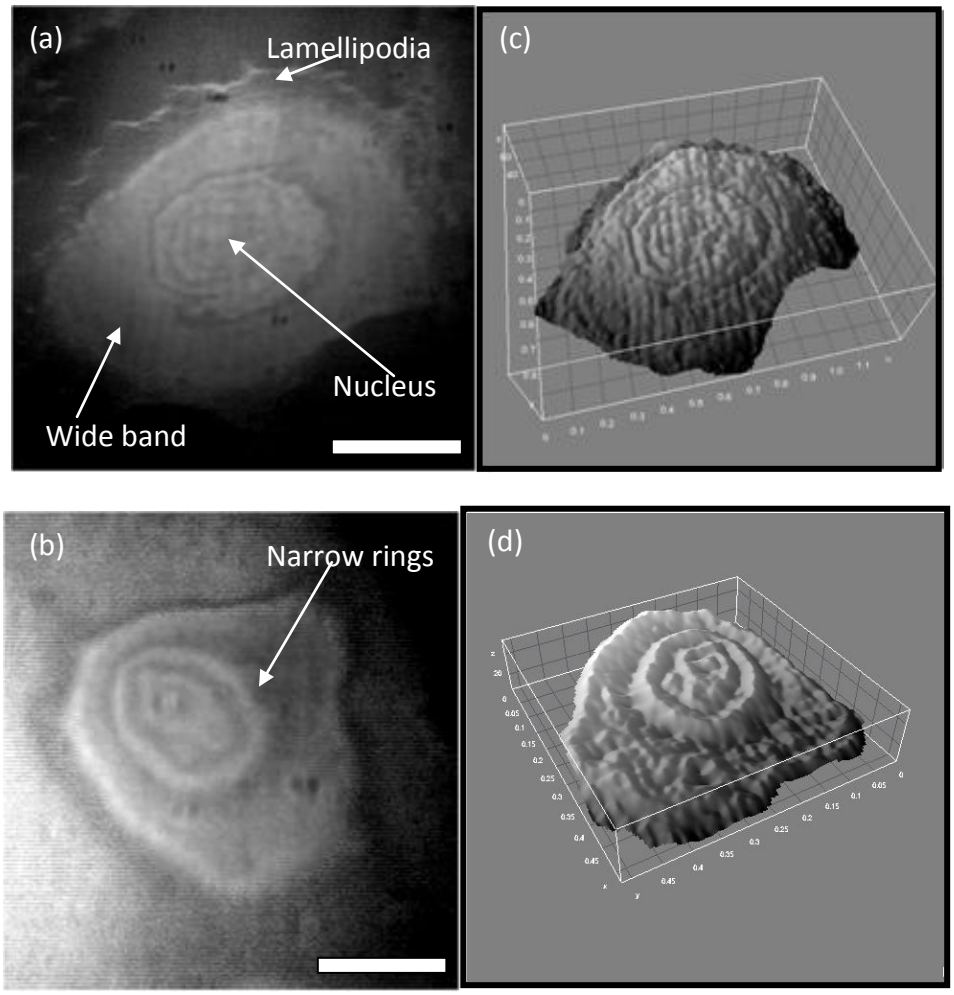

Figure 3.15. WSPR micrographs show the patterns of cells adhesion on the (a) hard cover slip, (b) soft liquid crystals and (c-d) their associated 3D structures displayed in ImageJ software, respectively. (Scale bar: 10 μm)

3.4 Summary

Cholesteryl ester liquid crystals were found to be non-toxic and support viability, adhesion and growth of HaCaT cells in culture. The cell adhesion, contraction and restructuring of the HaCaT cells on the liquid crystals were characterised by using cytochemical techniques. The forces generated within the cells were transmitted to the LC surface as deformation lines in small regions via the focal contacts. The results show that the surface of the liquid crystals was very sensitive to the physical restructuring of cells which was indicated by differences in deformation length and

changes induced by cell treatment with cytochalasin-B and trypsin. Fluorescence staining of actin filament and immunofluorescence staining of vinculin incorporated with WSPR microscopy showed that cell attachment, morphology and cytoskeletal structure are strongly related to the stiffness of liquid crystals. Diffused actin filaments and regular expressions of focal contacts at the periphery of the HaCaT cells were found when they were attaching to the liquid crystal substrates. This work also clearly shows that HaCaT cells cultured on the LC coated substrate deposit endogenous ECM proteins (collagen type IV, fibronectin and laminin) indicating the ability of the HaCaT cells to synthesise a simplified basement membrane on the surface of liquid crystals which has functionalised their adhesions and contractions on the cholesteryl ester based lyotropic liquid crystal substrates.

CHAPTER 4

QUANTIFICATION, MODELLING, MEASUREMENT AND MAPPING OF CELL TRACTION FORCES ON THE LIQUID CRYSTAL BASED CELL TRACTION FORCE TRANSDUCER

4.1 Introduction

Having examined both the physical properties of the cholesteryl ester liquid crystals and determined the nature of cell-LC biophysical interactions, the aim of chapter 4 is to develop a novel approach to quantify the traction forces of the human keratinocytes exerted on the liquid crystal surfaces (a semi solid sub-phase). Quantification for this study was derived from the relative bi-axial strains which are formed as deformation lines in the liquid crystal surface by the cells (as characterized in Chapter 2). In a previous study on a solid sub-phase (Burton and Taylor, 1997), traction forces exerted by a cell on silicon sheets were quantified by multiplying the length of the cell induced wrinkles to the stiffness (nN/μm) of the silicon sheet. The stiffness of the silicon substrate was calibrated by measuring the length of the wrinkles induced by a deflection force (calibrated flexible micro-fibre with load weights) (Burton and Taylor, 1997). However, it is important to restate that, the longitudinal displacement of each LC deformation line formed by cells is a secondary effect. This is due to the trajectory of transverse shear forces acting in pairs, which were induced via the focal adhesions as a result of actin filament contractions. The true relationship between the transverse and longitudinal strains of the deformation lines or wrinkles was established by using the cytochalasin-B treatment technique. Therefore, this work aimed at approaching the derivations of the applied forces required to induce bidirectional strain as related by the Poisson's ratio of the liquid crystals. In order to investigate the profiles of deformations formed in the LC surface that were induced by the focal adhesions, a three dimensional (3D) finite element model incorporating with a linear static analysis was implemented for the interface between liquid crystal-focal adhesions. To this end, a user friendly cell traction force measurement and mapping software (CTFM) was developed. This bespoke software provides tools for

measurement and 3D graphical visualisation of the traction forces exerted by a single keratinocytes in the liquid crystal based cell traction force transducer (LCTFT).

4.2 Material and Methods

4.2.1 Quantification of Cell Traction Force (CTF)

The coating of liquid crystal substrate was prepared as described in section 2.2.3 and HaCaT cells were prepared as previously described in section 2.2.6. Cell suspensions at a cell density of 500 cells/cm^2 were plated in petri dishes containing a LC coated cover slips and incubated at 37 ^{o}C for 24 hours. After incubation, the cells cultured on the liquid crystals were found adhering and contracting, while inducing localised deformation lines in the LC surfaces. The detail mechanism in forming these deformation lines were as discussed in section 2.3.5. Each deformation line formed in the longitudinal direction was induced by a pair of compressive or traction forces originated from two clusters of focal adhesions which sheared the liquid crystal surface at a local region (transverse displacement). The traction is most probably associated with the contraction of the short circumferential actin filaments as investigated in section 3.3.3. The relation of the contractions of the circumferential actin filaments of a cell to the bi-axial strains (a deformation line) induced in the liquid crystals is as depicted in Figure 4.1. For the traction force (F) quantification purpose, the length of a deformation line can be directly measured. However, the transverse displacement (Δx) in the LC surface due to the contractions of the circumferential actin filaments can be determined by relaxing the cell using an actin depolymerisation solution, cytochalasin-B. Cytochalasin-B specifically inhibits actin polymerisation. In this experiment, the adherent cells were treated with 5 µl of 30 µM cytochalasin-B for one hour at 37^{o}C. Cytochalasin-B (35 mg/ml, Sigma Aldrich) was solubilised in 0.042 % (v/v) ethanol (in

distilled water). For the treatments, the petri dish was placed on a heating peltier maintaining at 37 ^{o}C while time lapse images were captured every five minutes for an hour via a phase contrast microscope built-in with a digital camera. This experiment was repeated for each randomly selected cell from ten similar cultures.

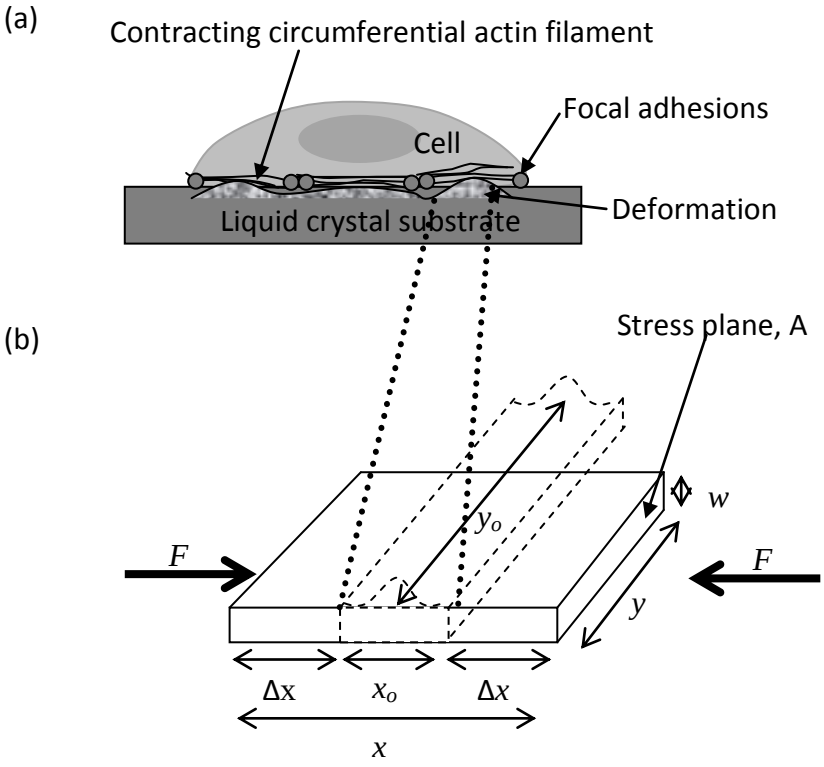

Figure 4.1. (a) Schematic diagram showing lateral view of a cell inducing deformations in the liquid crystal surface due to the contractions of circumferential actin filaments exerting traction force via the focal adhesions. (b) The dimensions of a stress site in LC surface which was loaded (dotted line) and unloaded (solid line) by compressive force (F) applied to the focal adhesion area or stress plane (A).

For each of the phase contrast micrographs containing a cell before and after treatment with cytochalasin-B for a period of 30 minutes, the dimensions of the deformation lines in LC surface (x, y, x_o and y_o) as defined in Figure 4.1b were measured. The bi-axial strains induced in the liquid crystal surface should agree with the Poisson's ratio under small strain theory (Tschoegl et al., 2002, Ren et al., 2008).

The Poisson's ratio, v as

$$\nu = -\frac{Longitudinal\_strain}{Transversse\_strain} = -\frac{\left(\frac{y - y_o}{y_o}\right)}{\left(\frac{x - x_o}{x_o}\right)} \quad (4.1)$$

where x_o and y_o are the initial width and length of deformation line under uni-axial compression (before cytochalasin-B treatment) while x and y are same parameters of the deformation line after released of stresses (after cytochalasin-B treatment). As the actual size of the focal adhesions or contact planes involved was unknown, the length (y) and width (w) of the focal adhesions are assumed to be equivalent to y and 1 µm, respectively. The width at 1 µm is justified by two or three accumulations of focal adhesion (Peterson et al., 2004). These have an average width of approximately 0.5 – 1 µm as approximated from the immuno-stained micrographs of vinculin (See Figure 1.7 Figure 3.9 and Figure 3.10). The transverse displacement (Δx) was obtained by taking half of the difference between the width of a deformation line [$\Delta x=(x-x_0)/2$] before and after a cell treated with cytochalasin-B between 30 minutes (Figure 4.1).

Subsequently, Hooke's equation will be applied to compute the force inducing a deformation line through the stress-strain relationship of the liquid crystals. The equation established by Hooke's theorem in determining the Young's modulus of a linear elastic material through the relationship of stress-strain is as follows:-

$$E = \frac{Stress}{Strain} = \frac{\sigma}{\varepsilon}$$

This equation can be rewritten as,

$$E = \frac{\left(\frac{F}{A}\right)}{\left(\frac{\Delta x}{x}\right)} \quad \text{or}$$

$$F = \frac{EA\Delta x}{x} \tag{4.2}$$

where, E is the Young's modulus, A is the focal contact area (y x 1) μm^2, Δx is the transverse displacement and x is the original length of the deformation line in the LC surface as shown in Figure 4.1b.

4.2.2 Implementation of a 3D Finite Element Model for Focal Adhesion-Liquid Crystal

Having defined physical properties of the liquid crystals, focal contact planes and dimensions of the deformation lines, the next step was to develop a finite element model to simulate the deformation profiles in the liquid crystal surface. The simulation was to correlate with contractions of the short marginal actin fibres for the cell as previously explained. In the developed finite element model, the geometry of a cell was hypothetically placed on the LC substrate. The LC substrate has a height (H_{lc}), length (L_{lc}) and width (W_{lc}) of 30 x 100 x 100 µm, respectively (Figure 4.2a). In the model, a restraint plane was set at the bottom of the liquid crystal substrate. The oval shaped focal adhesion clusters located around the cell was approximated with hollow rectangular shaped structures grafted in the surface of the LC substrate (Figure 4.2a). In order to apply a normal force (F) transversely to the stress plane, a hollow space was set for the focal adhesions assuming that the focal adhesions are embedded in the LC surface (Figure 4.2a). The focal adhesion cluster has a length (L_{fa}) embedded at a thickness (H_{fa}) and width (W_{fa}) of ~ 1 µm with an assumption that a cluster of focal adhesions probably containing two or three accumulations of vinculins (See Figure 1.7) (Peterson et al., 2004). The width or thickness of a focal adhesion was as approximated from the immuno-stained micrographs of vinculins (Figure 3.9-10). Therefore, the area (in μm^2) of a stress plane was obtained by H_{fa} x L_{fa}.

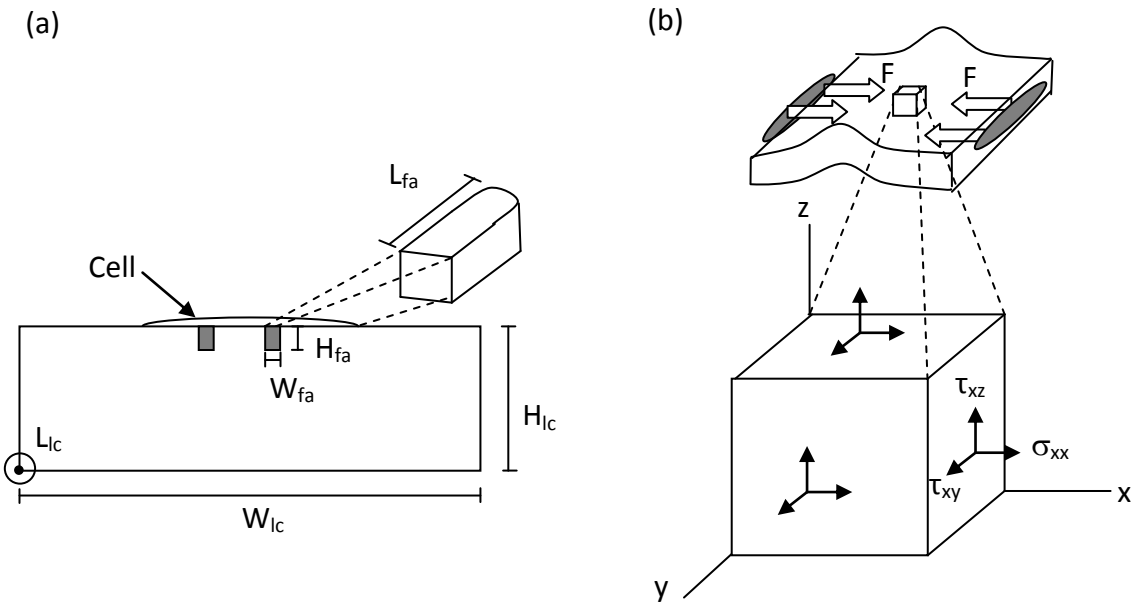

Figure 4.2. (a) Parametrical geometry of the focal adhesion-liquid crystal model. L_{fa}, H_{fa}, W_{fa}, L_{lc}, H_{lc}, and W_{lc} are the length, height and width of the focal adhesion (denoted as fa) and the liquid crystal substrate (denoted as lc), respectively. (b) Schematic diagram of a stress site in the LC surface which is under uni-axial compressive force (F) loaded by two clusters of focal adhesion to the two stress planes. Bottom: the associated tensor diagram in three dimensions. The plane stress, σ_{xx} causes shear stress of τ_{xz} and τ_{xy} in the y and z directions.

Table 4.1. Properties of liquid crystals and dimension of vinculin

Properties of model	Dimensions
LC coating	Thickness = 100 μm, Width x Length = 50 x 50 μm
Young's modulus	110 kPa
Poisson's ratio	μ = 0.5 (maximum limit configured in Cosmosworks)
Dimension of vinculin	H_{fa} = 1 μm, W_{fa} = 0.5 - 1 μm, L_{fa} = 1.3 – 2.8 μm

The physical properties of the liquid crystal substrate and focal adhesions applied in the FE model are as summarised in Table 4.1. In order to establish the constitutive model, a stress tensor diagram (Figure 4.2b) was used to describe the effects of the principal stress in x-plane (σ_{xx}) from the focal adhesions and shear stress to the liquid

crystal slab in the y and z directions (τ_{xy} and τ_{xz}). As a result, the compression stresses applied to the slab cause a deformation of the liquid crystals in y and z directions.

The quantification of the compressive force was always simulated iteratively in the FE modelling software to match the transverse displacement (Δx) obtained from the cell relaxation experiment. This finite element model was meshed into triangular elements before the stresses were computed. Then, the von-Mises stress was computed. It is important to note that Von-mises stress is an indication of the stresses produced without exceeding the yield strength of the material (Donald, 2007). Since the force applied is small and within nano-newton range, it is far below the yield stress, therefore, the criterion for the yield strength (923.7 $nN/\mu m^2$) is satisfied in this model. In this case, yield strength of rubber was assumed for the liquid crystals.

The overall behaviour of the 3D model for the focal adhesion-liquid crystal interface was implemented using Solidworks software. Linear static analysis based on the finite element method available in the Cosmosworks/Solidworks was used to analyse the traction forces applied via the focal contacts. The Cosmosworks software solves the linear elastic problem using Hooke's theorem and the minimum total potential energy method. In the finite element model implemented, force matrix {F} is related to the displacement {U} by $\{F\} = [k]\{U\}$, where [k] is the stiffness matrix (Fagan, 1992).

Young's modulus of 110 kPa (as determined in Chapter 2) and Poisson's ratio of 0.5 were set for the liquid crystal model in Cosmosworks software. Although the Poisson's ratio determined for the lyotropic liquid crystals in Chapter 2 was 0.58, unfortunately, the maximum limit of Poisson's ratio that can be used in the Cosmosworks software is 0.5. Although a Poisson's ratio of 0.5 is below that

determined for the lyotropic liquid crystals, the incompressibility of the liquid crystals induced by the high water content would suggest that a Poisson's ratio of 0.5 is applicable (Dimitriadis et al., 2002).

4.2.3 Development of a Cell Traction Force Measurement and Mapping (CTFM) Software

The bespoke cell force measurement and mapping software (CTFM) was developed by using the MATLAB Integrated Development Environment (IDE). Basically, the computer program functions to map the cell traction force based on the length of deformation line measured by the user in the software interactively. A graphical user interface (GUI) communicates with the user, either to receive instruction from the user or to convey messages to the user. The aim of using a GUI was to increase the speed of use, aid repeatable execution of work and provide attractiveness.

The CTFM software was developed to be as simple to use as possible in order to generate a cell traction force map for further analysis. The design and execution of the program was arranged sequentially and divided into three main steps: The first step involves, importing of an image and performing measurements of the deformation lengths by the user. The second step focuses on enabling the program to calculate the average traction force based on the user inputs and the generation of a visualization system that allows the display of the forces related to each LC deformation line induced by single cells in the phase contrast images. The third step then involved rendering 2D and 3D cell traction force maps into a pseudo color map, which allows representations of the force distributions across the cell. The flow charts for the CTFM are as shown in Figure 4.3-4.4. The full MATLAB codes of the CTFM program are available in Appendix A.

The program initiates by executing a GUI which prompts a user to select an image of file type jpg, tiff or bmp, and reads the image data file to the program as shown in the flow chart (Figure 4.3). The GUI also contains the instructions as a guide for the user to use the software. The size of the image will be determined by the program function, *imread*, and assigned to a Euclidean coordinate system (x, y). A calibration for defining the scale of the image will be performed by the user to define the start and end point on a precluded scale bar in the image by left-clicking the computer mouse. The data of the two points will be stored in an array by *[xr, yr]= ginput*, where r is the number of input. Based on the user input, the program calculates the distance between the two points in a Euclidean vector space using *norm* function in MATLAB which involves with the Pythagoras theorem.

Next, a pop-up window prompts the user to input the length of the scale input through the keyboard. Next, the user will be required to repeat similar steps in order to measure the length of the deformation lines found in the image.

The length of the lines measured by the user will be multiplied by the force-deformation coefficient (determined by the quantification procedures in section 4.2.1) of the LC to yield the value of the traction force correlating to a deformation line. The force value will be stored in an array (z) with a counter of *meas_num,* which update the number of measurements upon completion of a measurement. Once the measurement is completed, the position of the force data point will be stored in (x, y) array and then, similar measurement process can be repeated for another deformation line. To terminate the measurements, the user is required to right-click the mouse anywhere on the image and the program will take over the subsequent processing to generate the 3D traction force map and output data.

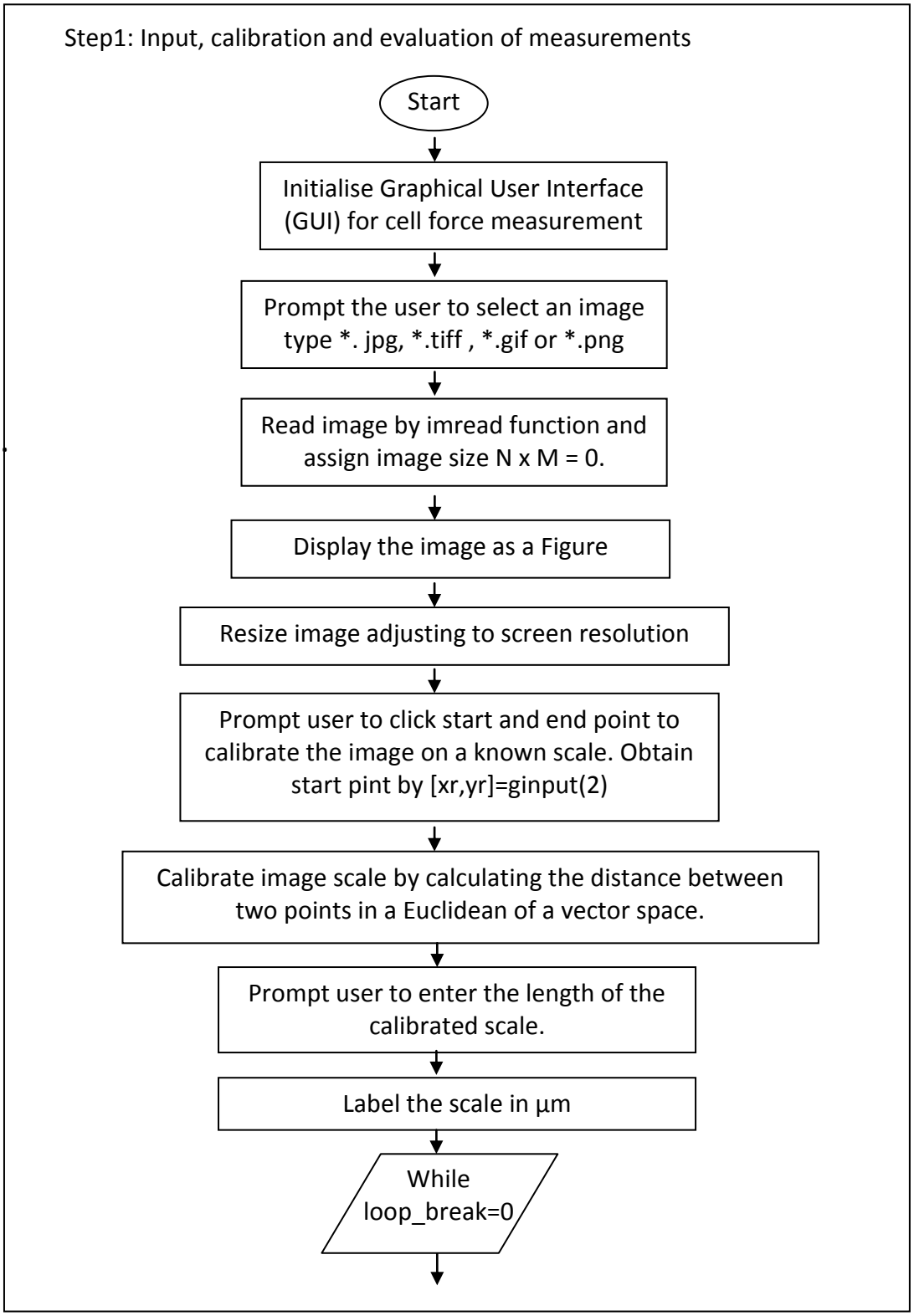

Figure 4.3. Flow chart of the cell traction force measurement algorithm

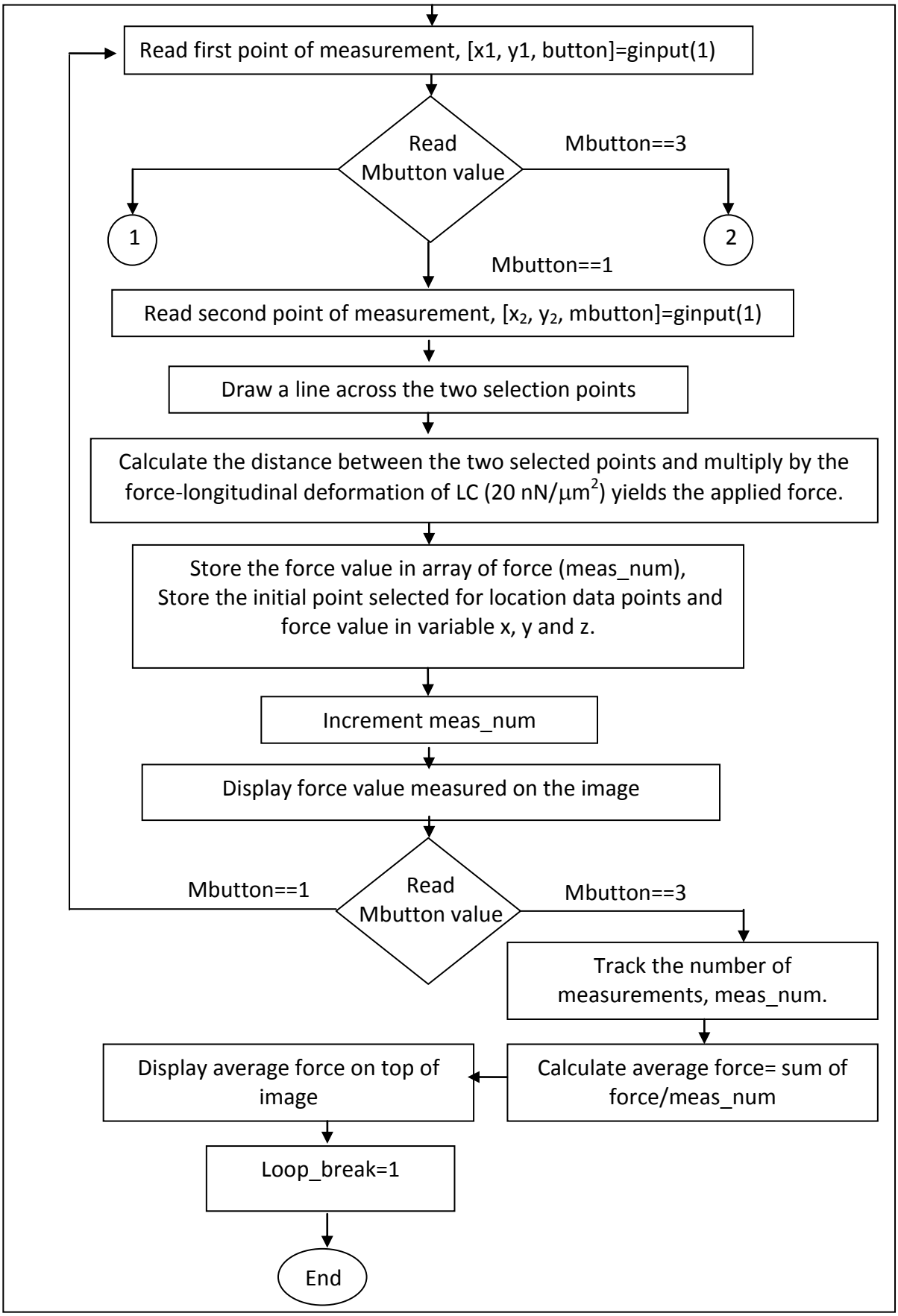

Cont' Figure 4.3. Flow chart of the cell traction force measurement algorithm.

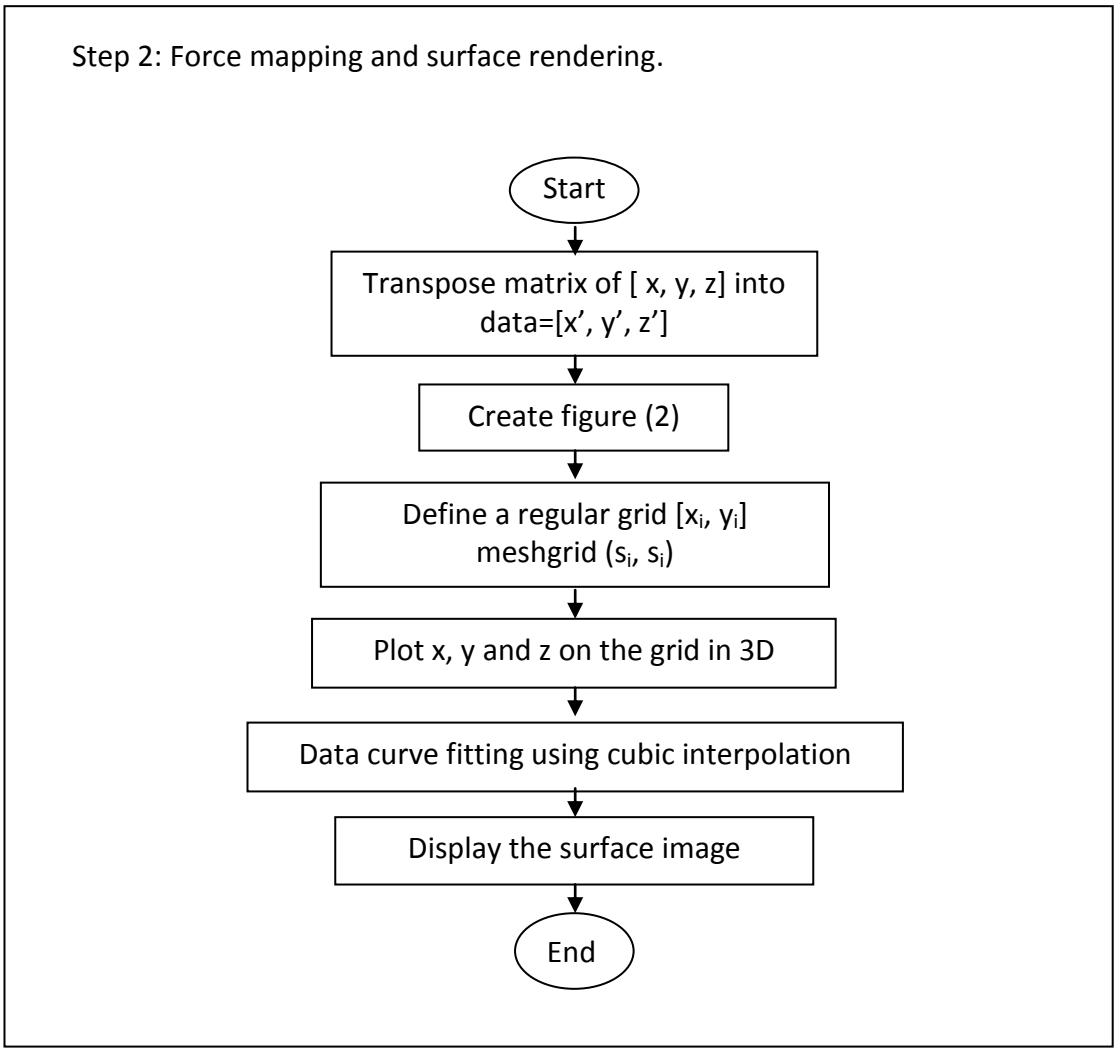

Figure 4.4. Flow chart of the cell traction force mapping and rendering algorithm.

In the process of generating the traction force map, the x, y and z arrays are appended into a matrix and transposed into three data columns (x', y' and z') so that each data in a column can be accessed independently (Figure 4.4). A regular grid will be created using the *meshgrid*, function and the x_i and y_i data are fitted on the grid. These data points can then be interpolated using the *griddata* function included with the linear and cubic interpolation functions. Then, 3D graphical visualisation of the traction force distribution will be rendered by the *surf* function. The graphics produced in the *Figure* window allows rotation of the cell traction force map in 3D, zooming, panning and labeling. The software will be used for analysing the traction forces of quiescent and migrating human keratinocytes.

4.2.4 Determining the Spatial Resolution of CTFM Software

The resolution of the cell force mapping software was calibrated by using an image of a polydimethylsioxane (PDMS) template containing regular line patterns. Two PDMS sheets with regular widths of 3 μm and 5 μm were prepared. These PDMS templates were fabricated by casting and curing an elastometric polymer, Sylgard 184 (Dow Corning, Midland, MI) against a photoresist micro-patterned glass template with line patterns of 3 and 5 μm. The PDMS consists of base elastomer and curing agent that were mixed in a 10:1 (v/v) ratio. After polymerisation on the master template, the flexible PDMS sheets were removed from the master template and phase contrast microscope equipped with ImageJ software was used to capture images for each of the PDMS templates obtained.

In the CTFM software, assumptions of the deformation lines with similar magnitude around a hypothetical cell shape (oval shape) was alternately applied to the edge of the regular line patterns that were placed over the phase contrast images consisting of PDMS line patterns at a regular width of 3 and 5 μm. The procedures used in measuring the deformation lines by using the CTFM software are as described in section 4.2.3.

4.2.5 Statistical Analysis

The mean traction forces calculated for the cells were expressed as means ± standard deviations (SD) and means ± standard errors (SE). Normality of the cell force distribution was tested with one sample Kolmogorov-smirnov test which is significant for $p > 0.05$. N is the number of sample measured. The scatter plot for the Force (F) versus the longitudinal deformation (y_o) was best fitted by using linear regression. Subsequently, the relationship was analysed by using the least-square method to

estimate the standard error of the slope. All statistical analysis was performed by using the Statistical Package for Social Sciences (SPSS) software.

4.3 Results and Discussion

4.3.1 Cell Relaxation and Calculation of Cell Traction Force

Quiescent keratinocytes showed a nearly iso-diametric characteristic on the surface of the LC substrate after 24 hours of cell culture. One of the examples is as shown in Figure 4.5a before treatment with cytochalasin-B. This cell was observed in a contracting state on the surface of the liquid crystals and some short deformations lines were found around the edges of the cell. Based on the ten phase contrast micrographs obtained, each of the ten cells studied had induced an average of 4-5 deformation lines in the LC surface. Due to the stress applied transversely (σ_{xx}) to the contact regions (forces represent by inward arrows in Figure 4.5a, 0 minute), the stress site was sheared in y and z direction by stresses of τ_{xy} and τ_{xz} resulting in a streak of deformation line. In 2D phase contrast images, only strains in x and y plane are visible as seen in Figure 4.5. These bi-axial strains formed in the liquid crystals induced a radial deformation line (Figure 4.5, 0 min) with dimensions as defined in Figure 4.1.

The deformation line formed has a width, x_o by length, y_o. Time lapse phase contrast images of Figure 4.5 show the effects of the cytochalasin-B in relaxing the cells while inducing disappearance of the deformation lines from the LC surface. The time shown in Figure 4.5 is the time of the cell treated with cytochalasin-B. For the cell in Figure 4.5a, the deformation line contained in the rectangular box had a width (x_o) and length (y_o) of 5 μm and 4.6 μm, respectively.

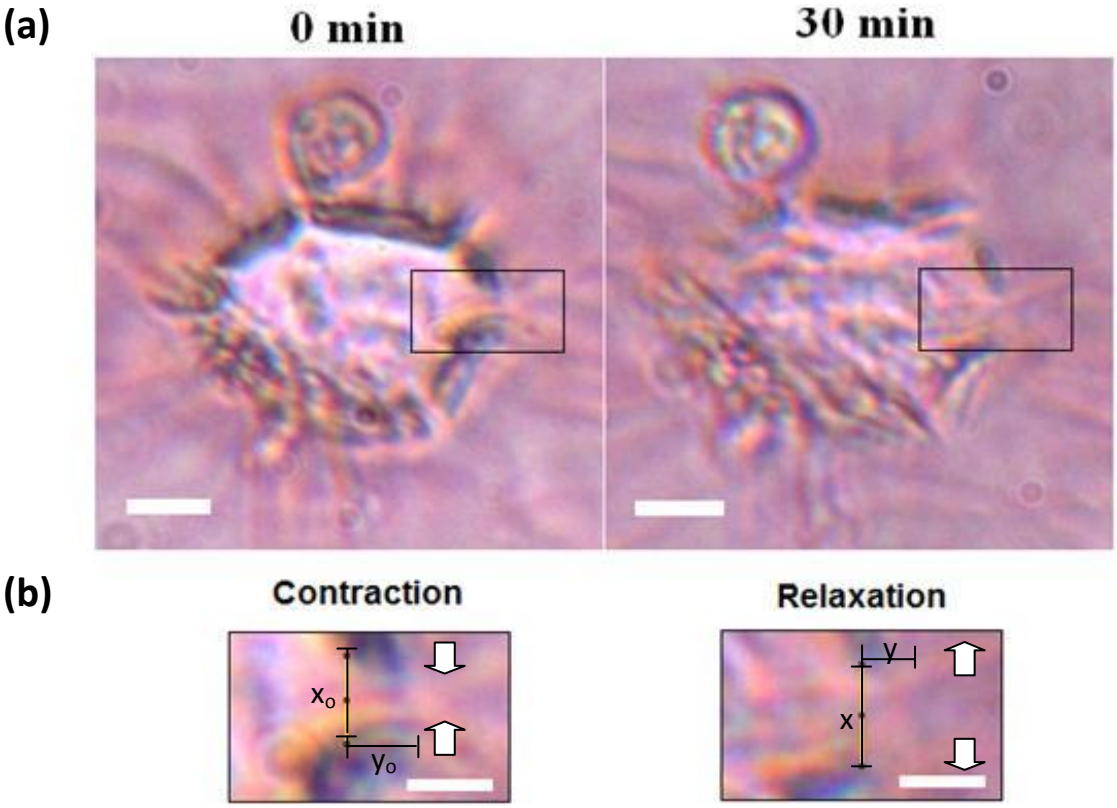

Figure 4.5. (a) The treatment effects of 30 µM cytochalasin-B in phase contrast micrographs taken at 0 and 30 minutes for a cell cultured on the surface of the liquid crystals. (Scale bar: 10 µm) (b) Enlarge exerts for the deformation lines are as shown and labeled in the boxes of (a). The inward and outward arrows show the directions of force application and degeneration, respectively. (Scale bar: 5 µm)

After treating the cell with cytochalasin-B, the actin cytoskeletons depolymerised and the forces applied by the cell were degenerated in two opposing directions that are represented by outward pointing arrows as shown in Figure 4.5b at 30 min. As a result, the width (x) and length (y) of the deformation line increased and decreased to 6 µm and 4.2 µm, respectively. For this example, the traction force required to induce the strains in transverse and longitudinal directions as determined by equation (4.2) was approximately 70 nN.

4.3.2 Determining the Cell Force-Deformation Relationship of the Liquid Crystals

The procedures used in defining and determining the traction forces were repeated for 55 deformation lines from ten cells as explained in section 4.3.1. The relationships among the transverse displacement (Δx), length of longitudinal deformation (y_o) and the traction forces (F) inducing the deformation line in the LC surface were established (Figure 4.6). For the deformation lines induced in the LC surface by non-motile keratinocyte from the ten cultures, the longitudinal length measured at $y_o \leq 8$ μm (thickness of LC substrate = ~100 μm) is probably within the linear viscoelastic range (< 10 % shear strain) of the liquid crystals as characterised in Chapter 2 (see Figure 2.23). The linear relationship of y_o to Δx by a factor of 4.08 shows a strong indication of the liquid crystals having a Poisson's ratio of approximately 0.5 (Figure 4.6a). This is because both parameters y_o and Δx were involved in the calculation of Poisson's ratio and their ratio at about 4 is the determinant for the Poisson's ratio to be around 0.5. Indeed, the lateral shear force (traction force) was found dependent on the longitudinal deformation and transverse deformation which are both related by Poisson's ratio of approximately 0.56 ± 0.06 (mean ± SD). The traction force (F in nN) applied via the stress planes increased proportionally with the transverse displacement (Δx in μm) and length of longitudinal deformation (y_o in μm) induced in the LC surface (Figure 4.6b-c) at 83.65 nN/μm and 20.21 nN/μm, respectively. By using the least square method, the standard error of the linear regression line, $F = 20.21y_o$ was determined at 0.42 nN/μm (SE), in which 20.21 is the coefficient of the force-longitudinal deformation relationship. 95 % confidence interval for the coefficient of the slope was 19.37 < mean of the slope < 21.05 nN/μm.

(a)

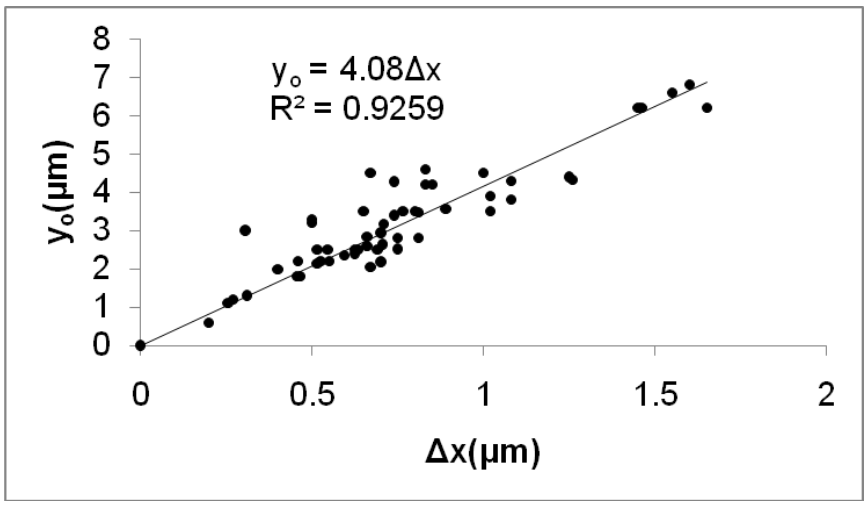

(b)

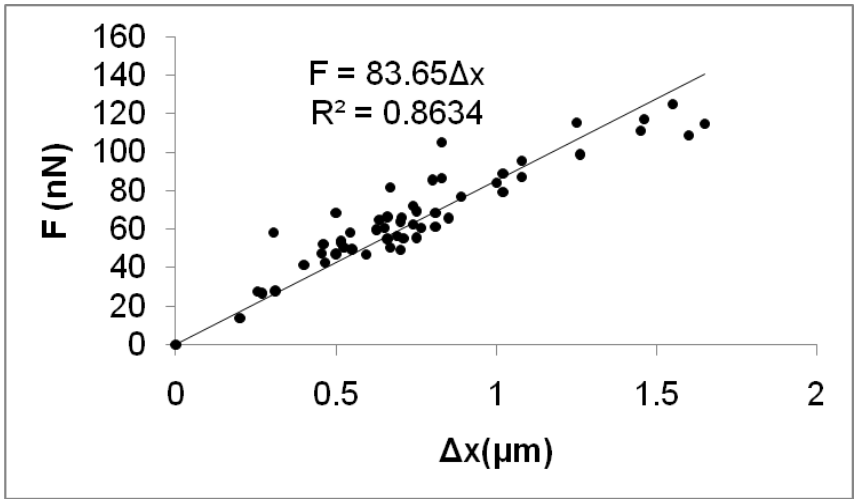

(c)

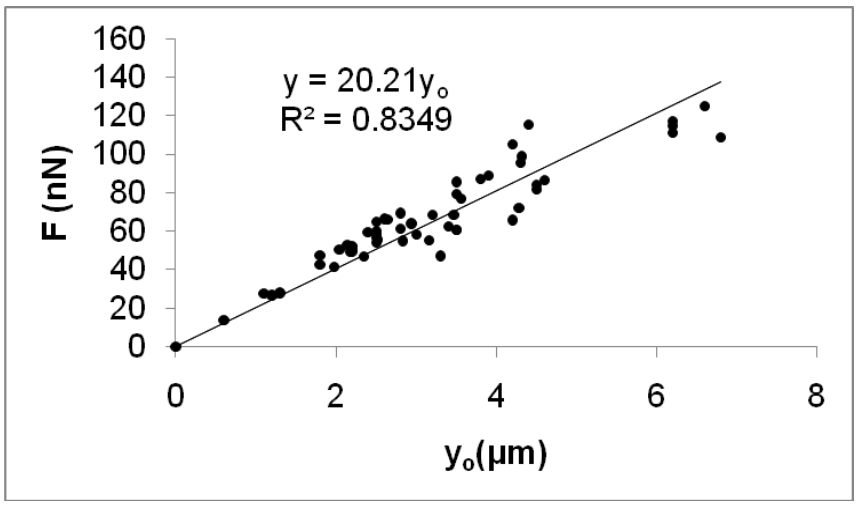

Figure 4.6. (a) The relationship of longitudinal deformation length (y_o) to the transverse displacement. (b) The relationship of traction force (F) to the transverse displacement (Δx). (c) The relationship of traction force (F) to the longitudinal deformation (y_o). The traction force was calculated for ten non-motile keratinocytes (N = 55).

The relationships as shown in Figure 4.6b and c reflect that the liquid crystal deformation line was being displaced in bi-axial directions. This relationship of F-y_o obtained from Figure 4.6c provides an efficient means for rapid estimation of the compressive forces induced by a cell, which is independent of cytochalasin-B treatment if the length of the deformation line is known.

4.3.3 Comparison with Previous Cell Traction Force Measurement Techniques

The traction forces exerted on the liquid crystal surface by non-motile keratinocytes were in a range of 10 nN – 140 nN per stress site (Figure 4.7). Kolmogorov-Smirnov test indicate that the traction forces exerted by keratinocyte cell lines were normally distributed ($p = 0.187$, significant for $p > 0.05$, 55 deformation lines out of 10 cells). The traction forces as measured for the cells were 65 nN ± 25 nN (mean ± SD) and the 95 % confidence interval for the mean traction force was 58.18 < mean of the traction force < 71.66 nN. As the forces measured were subjected to the Young's modulus (108 ± 20 kPa), therefore, the forces should have a variation of approximately 20 % because the Young's modulus measured has a standard deviation of this percentage too (see Table 2.3 in Chapter 2). The traction forces measured by using the liquid crystal based cell force transducer are comparable to the traction forces of MDCK epithelial cells determined in a range of 5 – 35 nN, which was determined by using PDMS micro-pillars technique (Roure et al., 2005). However, the magnitude of the discrete forces expressed via individual focal adhesion of migrating keratinocytes on a micro-patterned PDMS was determined at 6 ± 0.54 nN (mean ± SE) (Mohl et al., 2009), which is lower than the force range determined in this work. This may be due to the discrepancies in the elastic modulus of material used in the force sensor and the differences in the method of measurement. Therefore, it is difficult to

make direct comparisons between the traction forces measured in this work and the work presented by others. A detail comparison of the range of traction forces determined for epithelial cells is as shown in Table 4.2.

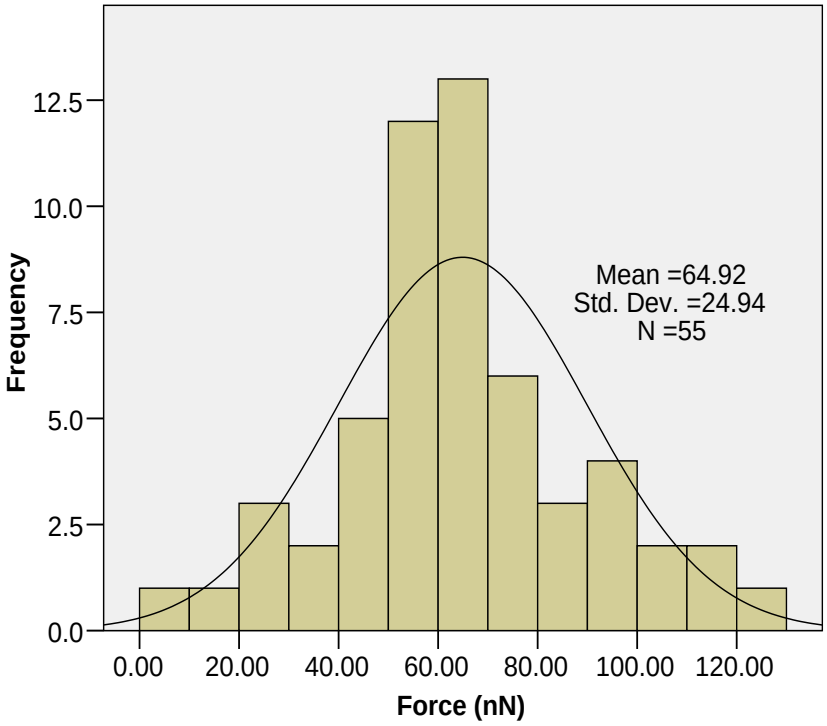

Figure 4.7. Normally distributed traction forces (p = 0.187, significant for p > 0.05) for ten non-motile keratinocytes. N = number of deformation line.

However, by using an AFM cantilever method to probe the posterior of a cell, Sagvolden and co-worker (Sagvolden et al., 1999) showed that cervical carcinoma cell required 100 - 200 nN to dissociate from the cantilever. Similarly, Thoumine et al. showed that epithelial cells require an exposure of 100 nN tangential force to detach from a surface in a centrifugation system (Thoumine et al., 1996). Whereas, a higher range of traction force from 10 nN up to 1200 nN was reported for fibroblast grown on a soft elastic substrate (Burton et al., 1999). For a less motile cell such as the keratinocyte, the forces exerted on a substrate should be expected to be relatively lower than those of the highly motile fibroblast because motility is proportional to the traction forces of cells.

Table 4.2. Comparison of other epithelial cell force measurement techniques

Methods	Cell type	Range of forces	Reference
Liquid crystal based cell force transducer (Young's modulus = ~108 kPa)	Human Keratinocyte cell line (HaCaT)	Range: 10 - 138 nN. 64.92 ± 6.72nN (mean ± 2SE). Force per stress site.	C. F. Soon at. el.
Fluorescence beads labelled-PDMS (Young's modulus = 10 kPa)	Normal human epidermal keratinocytes from neonatal foreskin	10 nN per focal adhesion	Mohl at el., 2009
Micro-patterned cantilever (Young's modulus = 2 MPa)	Epithelial	5 - 35 nN per focal adhesion	OD Roure at el. , 2005
AFM cantilever	Human cervical epithelial	100 - 200 nN	Sagvolden, G at el. 1999
Centrifugation force	Human mammary epithelial cell line, HBL100	100 nN	Thoumine, O at el., 1996

4.3.4 Finite Element Simulations of Focal Adhesion-Liquid Crystal Model

For the cell as seen in Figure 4.5, the simulated displacement and stress distribution for the focal adhesion-liquid crystal model in Solidworks software are as shown in Figure 4.9. A total of 10842 triangular elements at a size of 5.7 μm were used in generating the solid mesh model (Figure 4.8). The von-Mises stresses and displacements applied at five stress sites seem to be dependent on the transverse displacement induced by the cells (Figure 4.9). In addition, the compressive forces applied at the five stress sites are linearly proportional to the transverse displacements applied by the cell in both calculation and finite element simulations (Figure 4.10a). Interestingly, the simulated stresses applied by this cell are similar to each other

although small variations occurred (mean ± SD = 14.93 ± 1.9 nN/µm^2) which might be the characteristic of quiescent cell expressing balancing stresses at the periphery of the cell during equilibrium condition (Figure 4.9 and Figure 4.10b). This result is in good agreement with the iso-diametric characteristic displayed by the cell as shown in Figure 4.5 which may be caused by the regular distribution of actin filaments and lamellipodia at the margin of a non-polarised keratinocyte (Owaribe et al., 1981, Henry et al., 2003, Kirfel and Herzog, 2004).

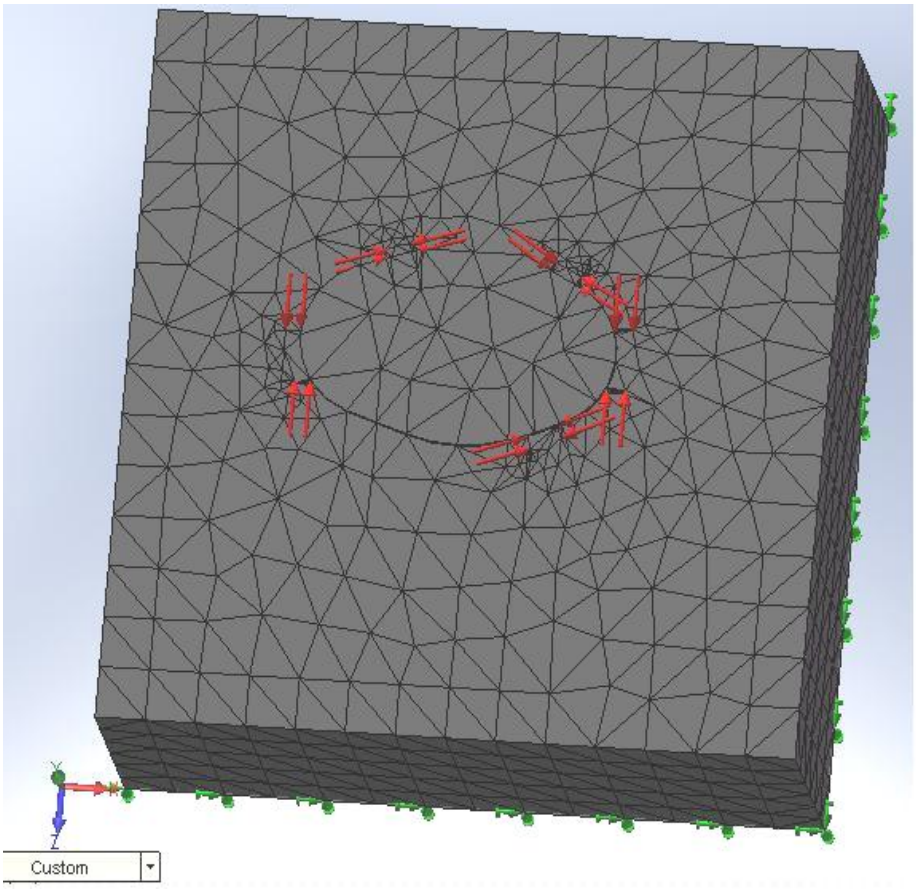

Figure 4.8. A mesh containing 10842 triangular elements at a size of 5.7 µm was used in generating the solid mesh for the focal adhesion-liquid crystal model.

(a)

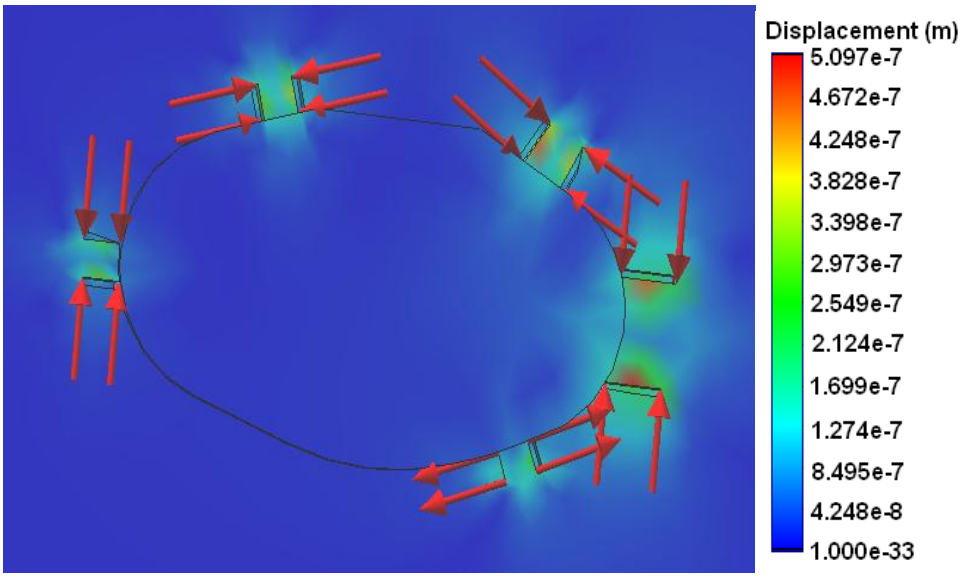

(b)

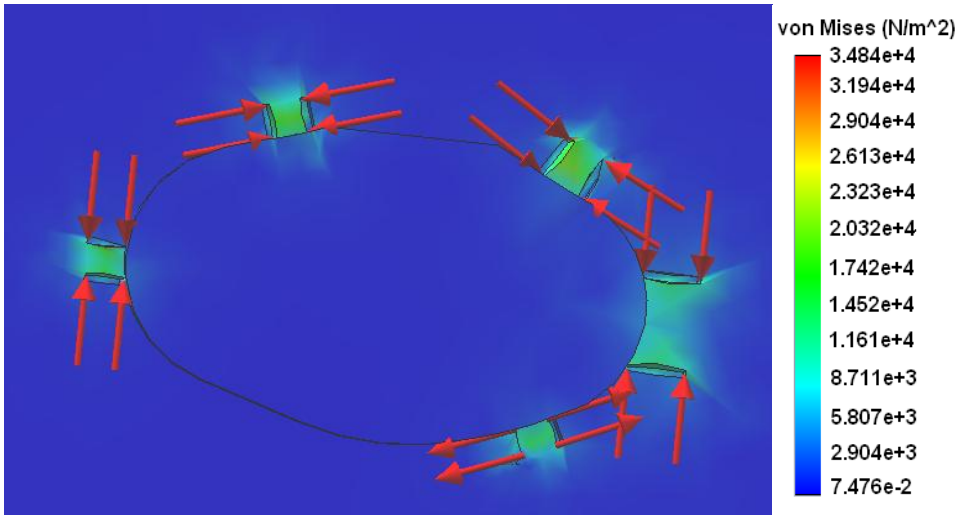

Figure 4.9. (a) Transverse displacement and stress plotted and simulated by Finite Element analysis for the keratinocyte in Figure 4.5.

In simulating the finite element model with the Solidworks software, a Poisson's ratio of 0.5 was used because this is the upper limit configured in the software. In the calculation, Poisson's ratio at 0.58 was used based on the result obtained from micro-tensile experiment. Due to the differences in the Poisson's ratio applied, both calculation and simulation of the forces had a difference of 20 %. In comparison of the results for calculation and simulation, the simulated forces are higher because a lower Poisson's ratio was applied in the model. A material with a lower Poisson's ratio represents a stiffer material. Thus, larger forces are required to deform a stiffer

material (a lower Poisson's ratio) than a softer material (a higher Poisson's ratio) in order to obtain the same displacements in the material. This explains why forces simulated by using FEM model with a Poisson's ratio of 0.5 is higher in comparison to the forces calculated by Hooke's equation with a higher Poisson's ratio of 0.58.

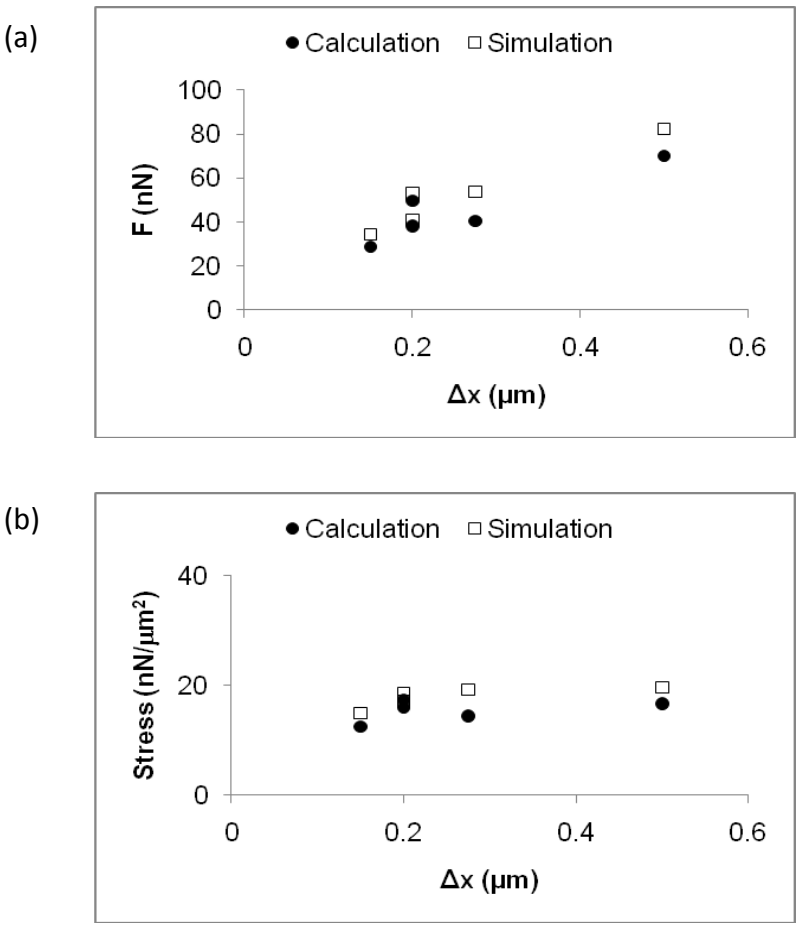

Figure 4.10 The calculation and simulation for the (a) compressive force versus transverse displacement, and (b) stress versus transverse displacement for the cell in Figure 4.5.

For detail investigation on the stress distributions at a stress site, the simulation is as shown in Figure 4.11. Two identical focal adhesion contact areas (4.2 μm^2 as shown in the inset of Figure 4.11) were formed in contact with the liquid crystal surface, and identical compressive forces were applied to each stress plane during the simulation (Figure 4.11). In this example, the applied force per stress plane was

determined at F = 82.36 nN which was induced by a maximum lateral displacement and stress of 0.5 µm (Figure 4.11a). In this model, the maximum stress was determined at 34.84 nN/µm^2 (Figure 4.11b), respectively.

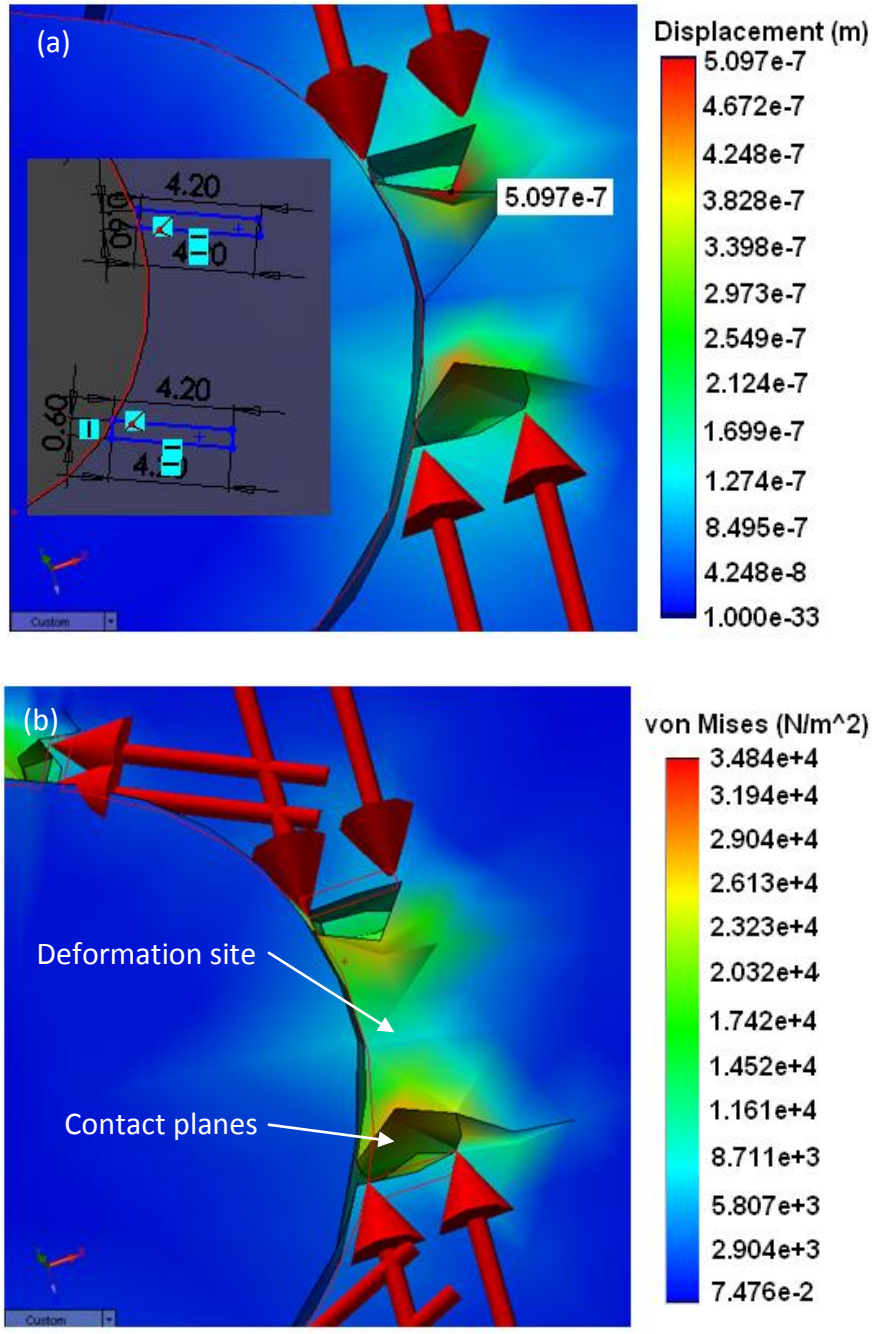

Figure 4.11. (a) A 3-D topography of a deformation with displacements in the liquid crystals induced by the loads via the contact planes. Inset: The dimensions of the focal adhesions used in the finite element model. (b) Von-mises stresses computed for the compressive loads.

For each stress site, the highest expressions of nodal stress and transverse displacement were found exactly at the two stress planes and they quadratically decreased as the distance increased from the stress planes to the centre of the stress site (Figure 4.12).

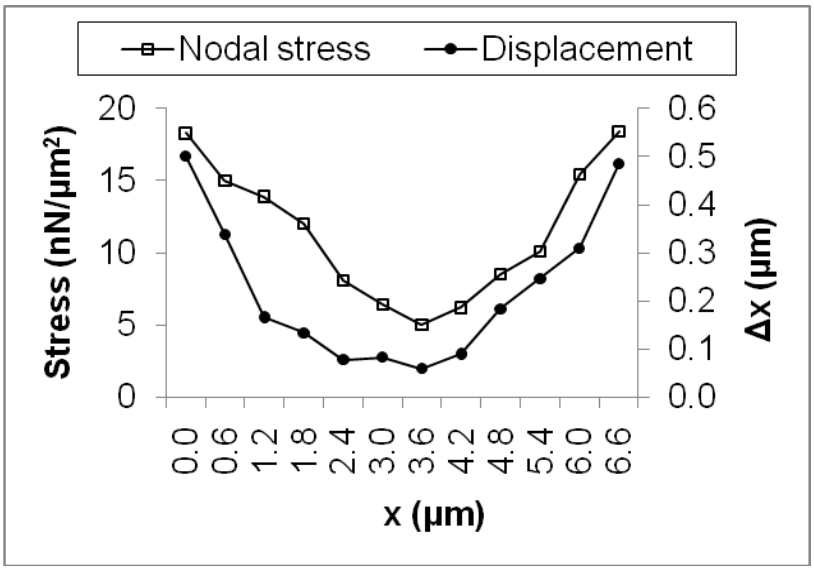

Figure 4.12. The distribution of stresses and transverse displacements across a deformation site.

The responses of the stress and displacement across a deformation site was found to be reciprocal to the contraction profile measured for the deformation line of liquid crystal that were induced by a cell in phase contrast and polarised micrographs (see Figure 2.29 in Chapter 2). Clearly, both results produced by experiment and simulation show that the deformation induced by cells in the liquid crystal surface is characterised by compression and shearing of the underlying material, which is most probably related to the traction forces exerted by the contraction of circumferential actin bundles via the focal contacts. The contraction of the epithelial cell is attributed to the simultaneous shortening of the circumferential actin filaments leading to a decrease in width of the deformation line. The result shows that compression is

appropriately used to describe the mechanics of quiescent HaCaT cells contracting on the liquid crystal surface.

4.3.5 The Cell Traction Force Measurement and Mapping Software

The main GUI of the CTFM software (Figure 4.13) functions by helping the user to load image files into the program for cell force measurement. The imported image must be in a dimension (N x M) which is smaller than the pixel resolution of the computer LCD. On the main interface of the CTFM software, the user will be prompted to select an image from the computer hard disk directory, and then follows a step by step instruction in order to perform the measurements of cell traction forces. In addition, the user has the option not to do anything or to exit the program.

After loading an image of a single cell, the user calibrates the image based on the scale bar available in the image to determine the image dimension or the pixel size of the image. In the image, calibration was performed by selecting the start and end points over the scale bar as shown in Figure 4.14. When the scale bar is measured, a pop-up window will request the user to enter the scale of the image (in µm) as shown in Figure 4.15.

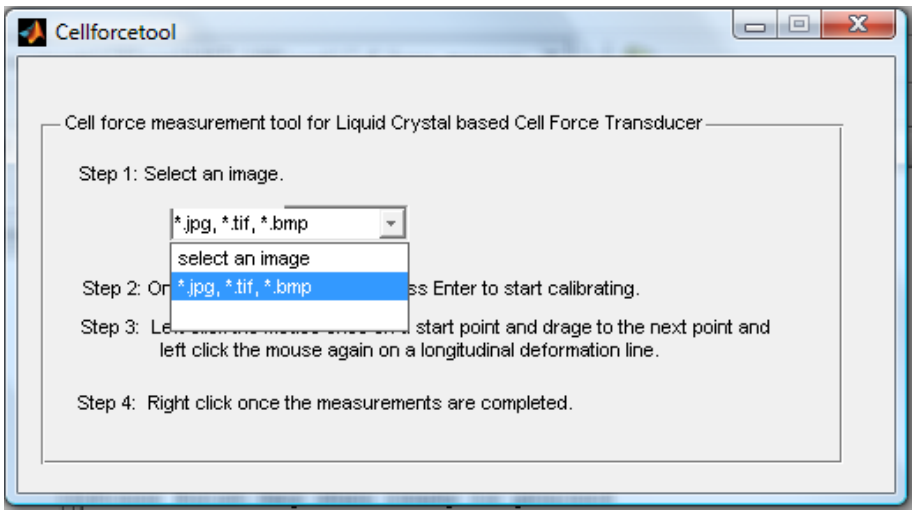

Figure 4.13. The GUI of the cell force measurement and mapping software.

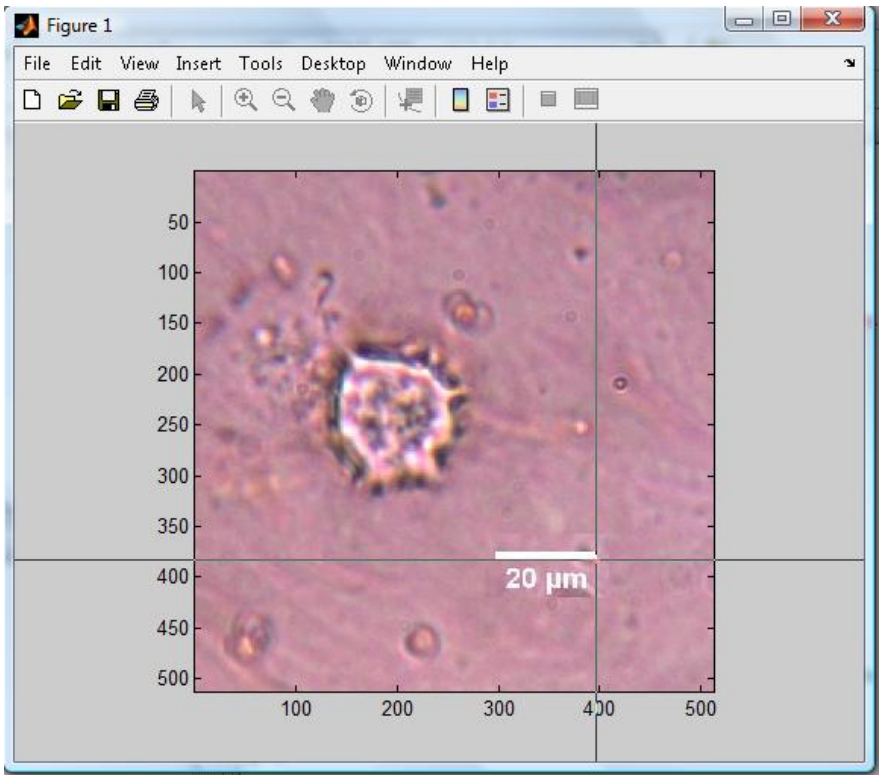

Figure 4.14. Defining the start and end points for calibrating the scale of the image.

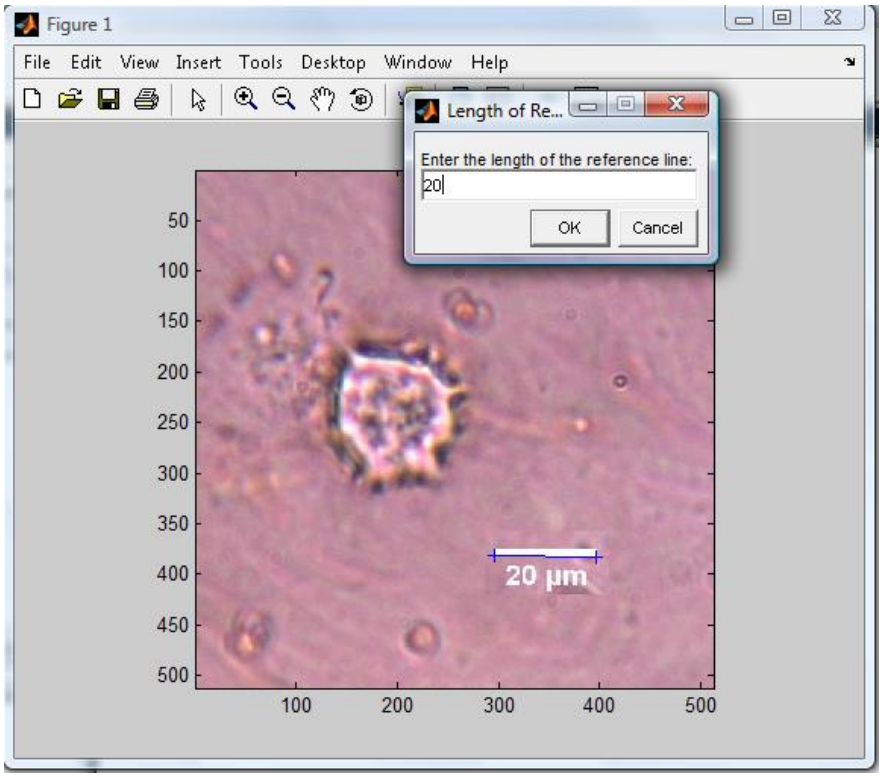

Figure 4.15. Entering the image scale (20 µm) in the pop-up window.

For the calibration of the image scale, the entered value in the pop-up window was used to calculate the ratio of pixels to length of the loaded image. The example in Figure 4.15 has a pixel to length ratio of 100 pixels/μm. Any subsequent measurements of the deformation lengths in pixels were multiplied by this ratio in order to calculate the length in micrometers. Subsequently, the calibrated value will be displayed over the scale bar on the image. Once the value is entered, the user should select the Ok button to proceed with the measurements of deformation length and force.

The measurement of the deformation length in the image is again based on mouse-clicking activation. In the phase contrast image, the user will left-click the mouse to select the start and end points of a deformation line by following the same procedure used in the calibration of the image scale. After selecting the two points by using the mouse, a red line will be plotted across the two points which is over the deformation line (Figure 4.16), and the computed force in nano-Newton (nN) will be indicated above the line. If there is no deformation line found in a particular area of the cell, the user will be required to double-left-click the mouse in order to select the same point, which indicates that no traction force was found for that point (Figure 4.16). In the software, the first few steps are expected to be manually performed by the user. Hence, the measurement accuracy is dependent on the user's ability to identify a deformation line. Once all measurements are completed, the average cell traction force will be computed for force points greater than 0 nN and will be displayed on top of the image (Figure 4.17).

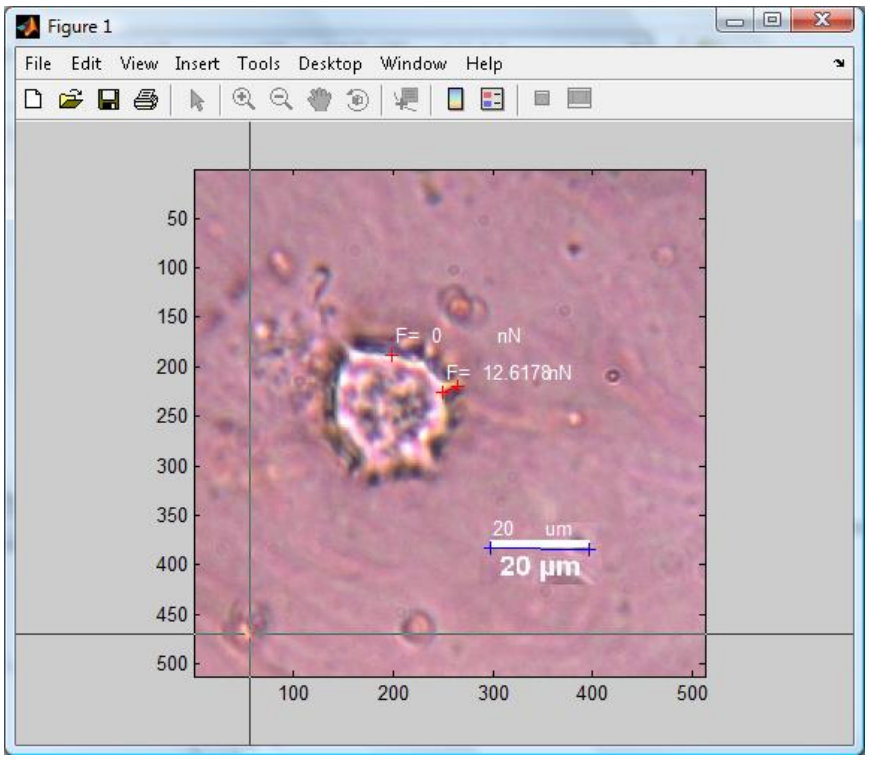

Figure 4.16. Use of mouse to define a deformation line and displays of the calculated force values.

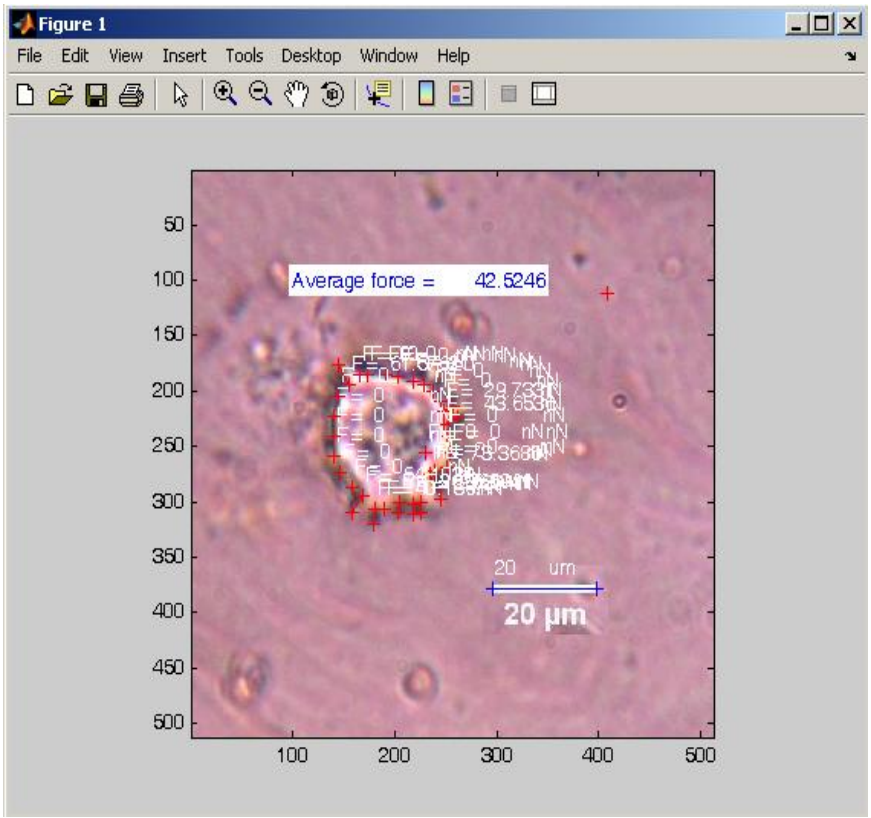

Figure 4.17. The display of traction forces and the average traction force of a cell.

Subsequently, the rest of the computational work will be executed by the program automatically; this generates a graphical visualisation of the force points over a Euclidean coordinate system, and the associated map of traction forces. Figure 4.18 shows the magnitude of the force point (z) projected on a Euclidean coordinate system (x, y). In this example, the pixel size of the image is 256 x 256. From the magnitude of the force point at various positions over the coordinates, data points were fixed on the grid and then fitted by using interpolation fitting functions (such as, linear and cubic curve fitting methods).

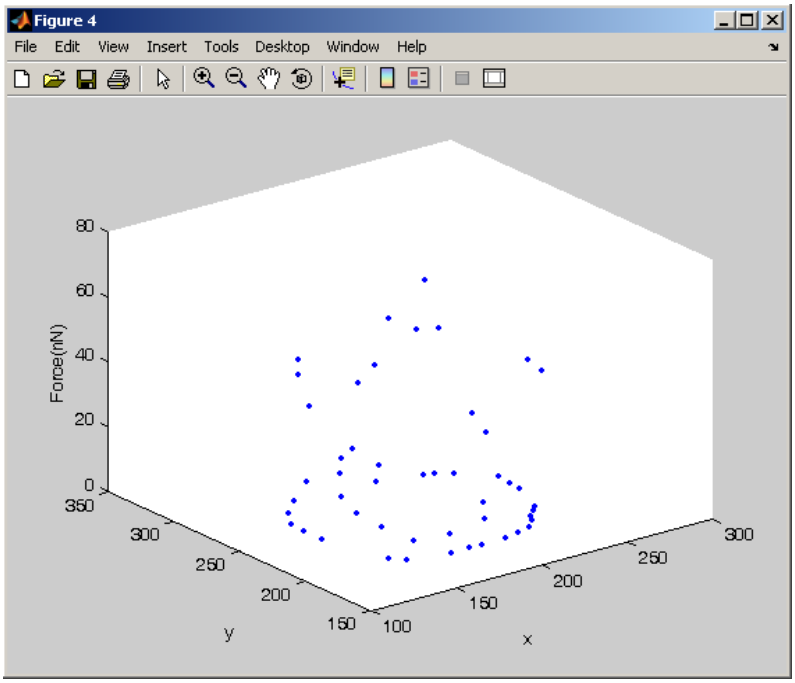

Figure 4.18. A display of the force data points (z) scattering over the x and y Euclidean coordinate system.

The graphical visualisation of the cell traction forces was rendered in pseudo colour in which the colour scale represents the intensity of the force. Gradual changes of blue to red color across the terrain in the map represent the transition of the traction force magnitude from a low level to high level. The colour scale in Figure 4.19a shows the force ranging between 0 to 70 nN, while the scale bar in Figure 4.19b ranges

between -10 to 70 nN. The negative forces found in the result of cubic interpolation are due to the minimum curvature in a curve spline creating an inflection point below 0 nN. This was found to be the flaw of cubic interpolation technique and may provide unrealistic fitting to the minimum force point or over exaggerating the curve data fitting (Wassel, 2009).

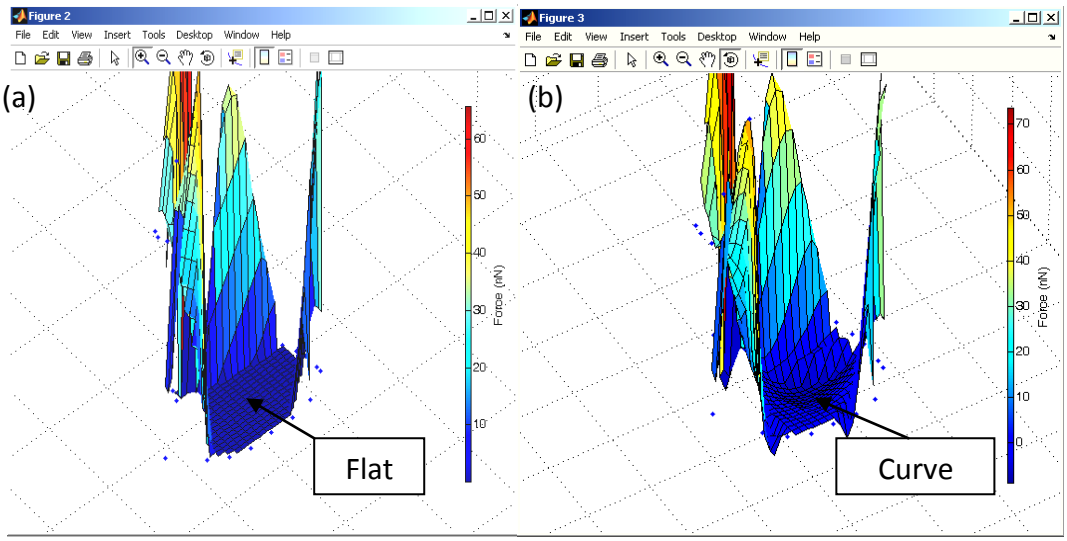

Figure 4.19. The fitting of force data curves by using (a) linear and (b) cubic interpolations.

In the case of cubic interpolation, approximately 10 % of measured forces were overshot at the minimum force curve. Comparatively, linear interpolation is able to terminate the transition from higher force to null force area sharply, and thus it is more suitable to the mapping of cell traction forces (Figure 4.19a).

Although the 3D representation shows that cubic interpolation provides a smoother transition for the force distribution (Figure 4.19b) when compared with the linear interpolation (Figure 4.19a), the differences in the output of the two approaches are indistinguishable in 2D force distribution maps (Figure 4.20). Nonetheless, 2D visualisation is found to be more useful for the analysis of cell force distribution. Both

interpolation methods showed equivalently good isolation of cell traction forces in 2D (Figure 4.20).

(a)

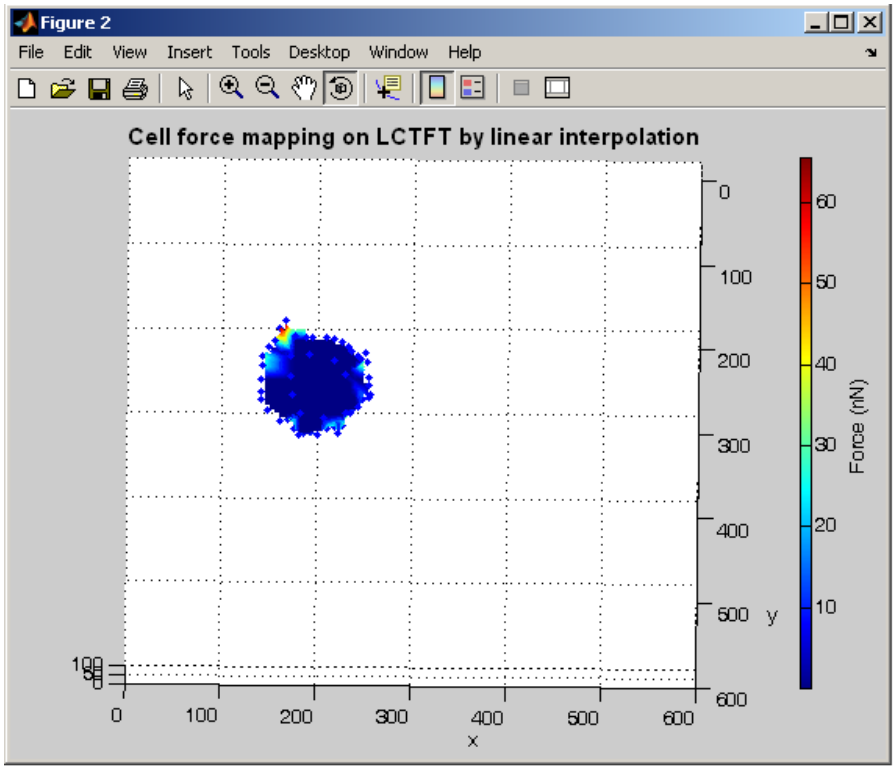

(b)

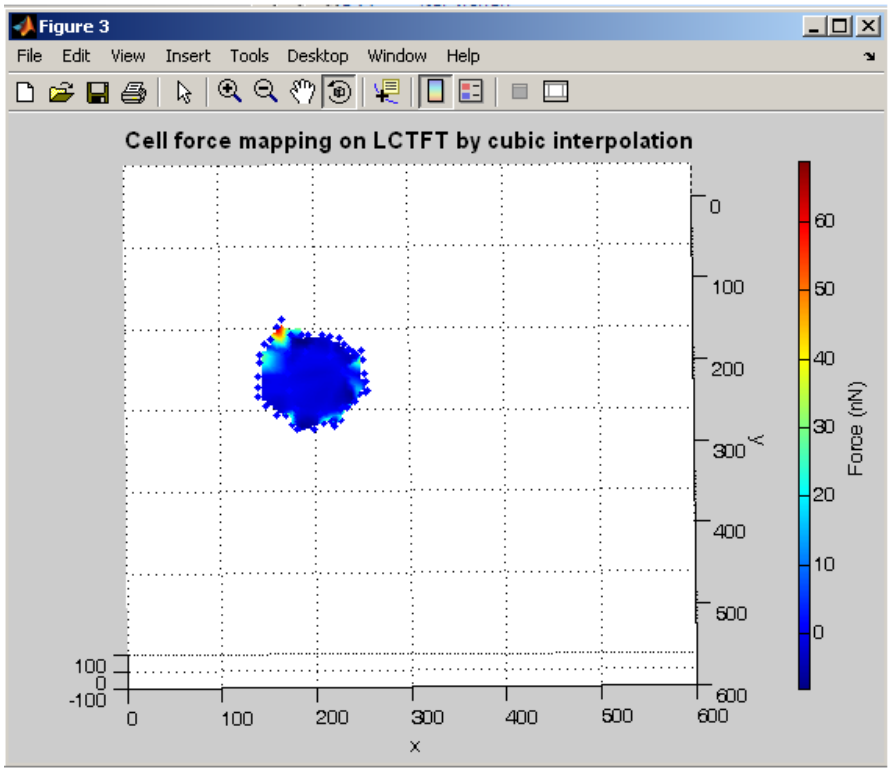

Figure 4.20. 2D cell traction force maps which were fitted with (a) linear and (b) cubic interpolations.

4.3.6 Spatial Resolution of the Cell Force Measurement and Mapping Software

LCTFT is able to resolve a separation of cell traction forces down to 2 µm as shown in Figure 4.21 but the resolution of the cell traction forces for the overall system is dependent on the CTFM software. The hypothetical simulated cell edges and deformation lines on the PDMS line patterns of 3 and 5 µm are as shown in Figure 4.22. The forces interpolated at a distance of 3 µm in the software appeared inseparable and aggregated into clusters of forces (Figure 4.23b). The result from the force simulation indicates that the interpolation function in the software is able to resolve adjacent forces in clear separation within 5 µm to each other (Figure 4.23b). Therefore, the resolving power of the microscope, the liquid crystals and the force mapping software collectively are crucial in determining the spatial resolution of the overall cell traction force mapping system.

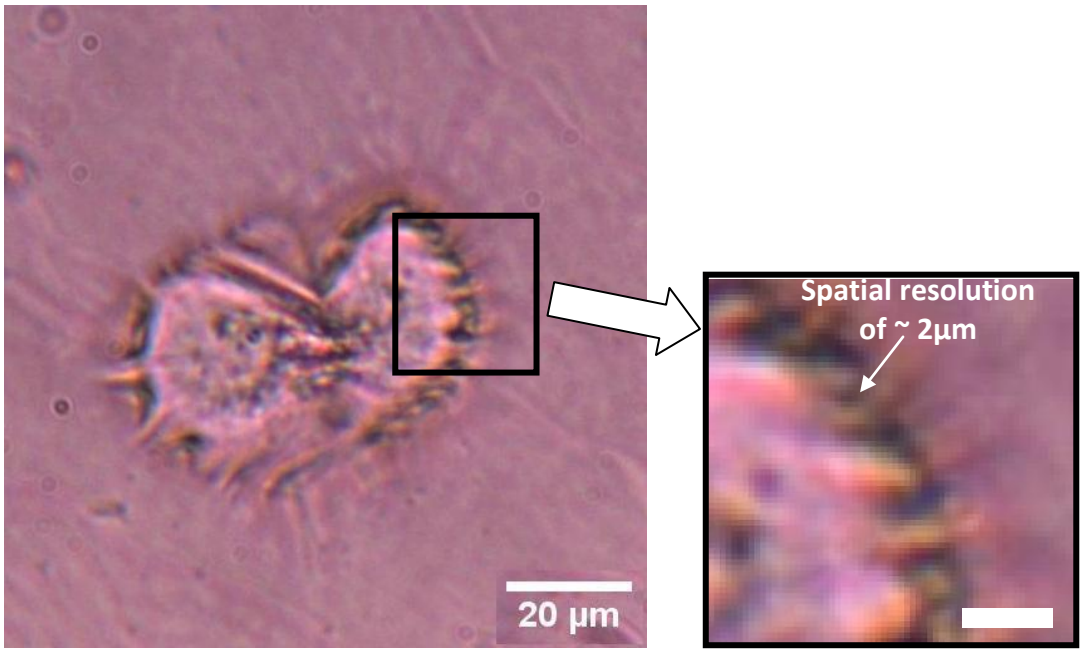

Figure 4.21. Spatial resolution of a liquid crystal based cell traction force transducer. (Enlarged exert, scale bar: 5 µm)

(a)

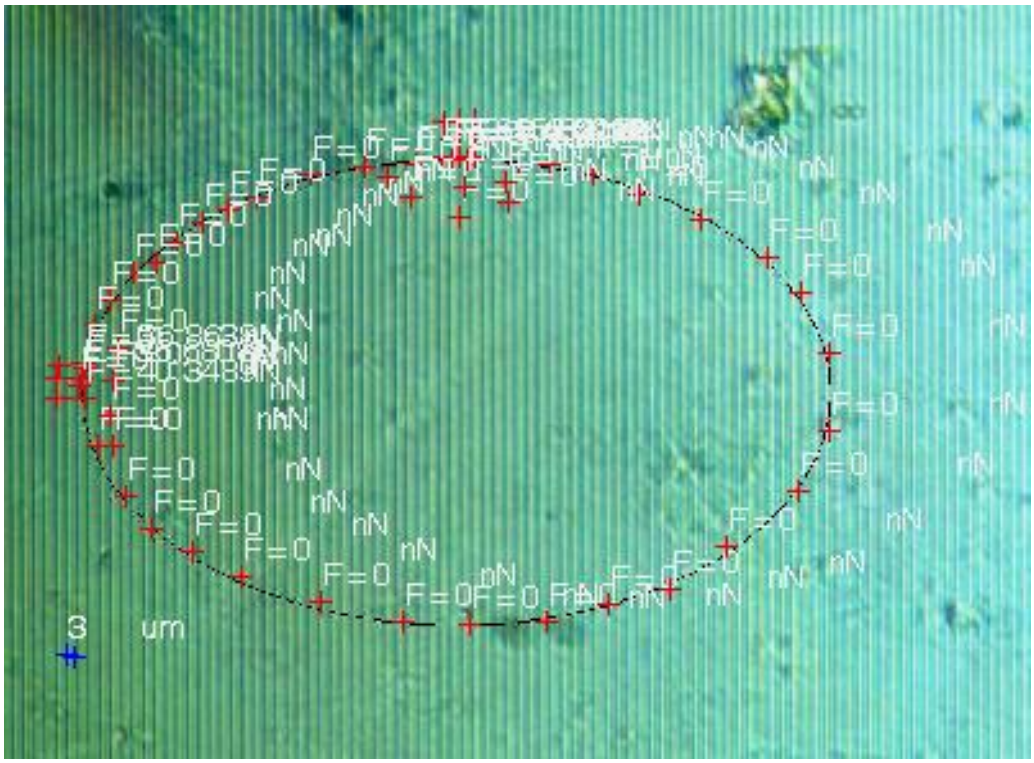

(b)

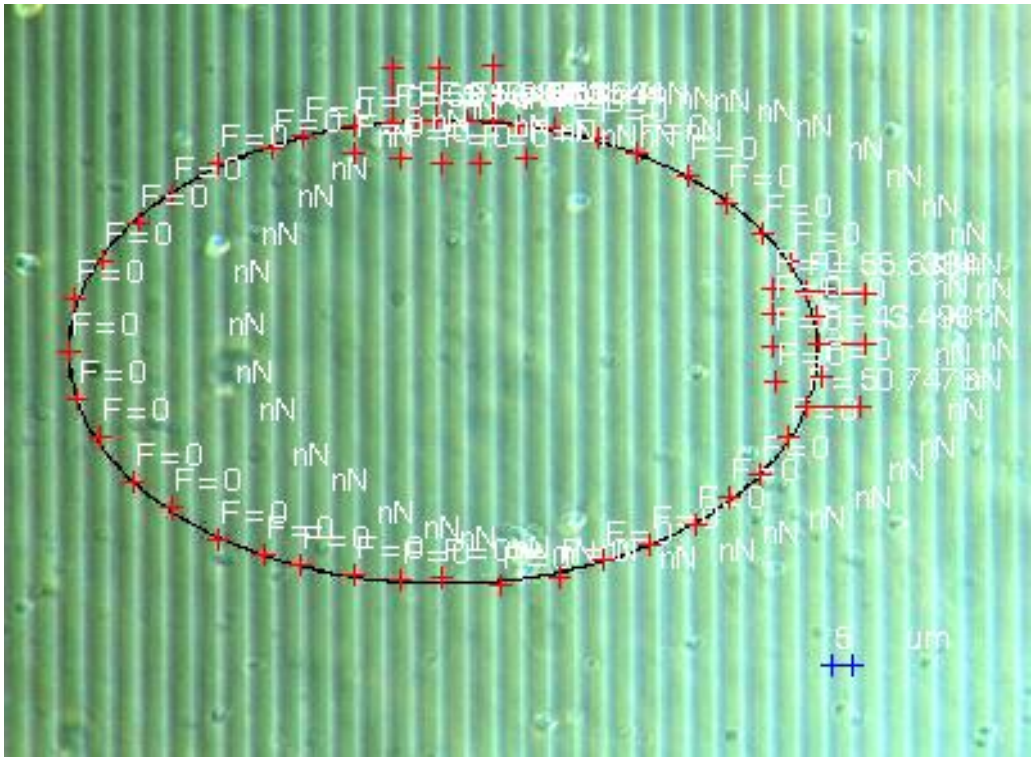

Figure 4.22. Phase contrast micrographs of PDMS calibration gauges consisting of line patterns with an interval of (a) 3 μm and (b) 5 μm.

(a)

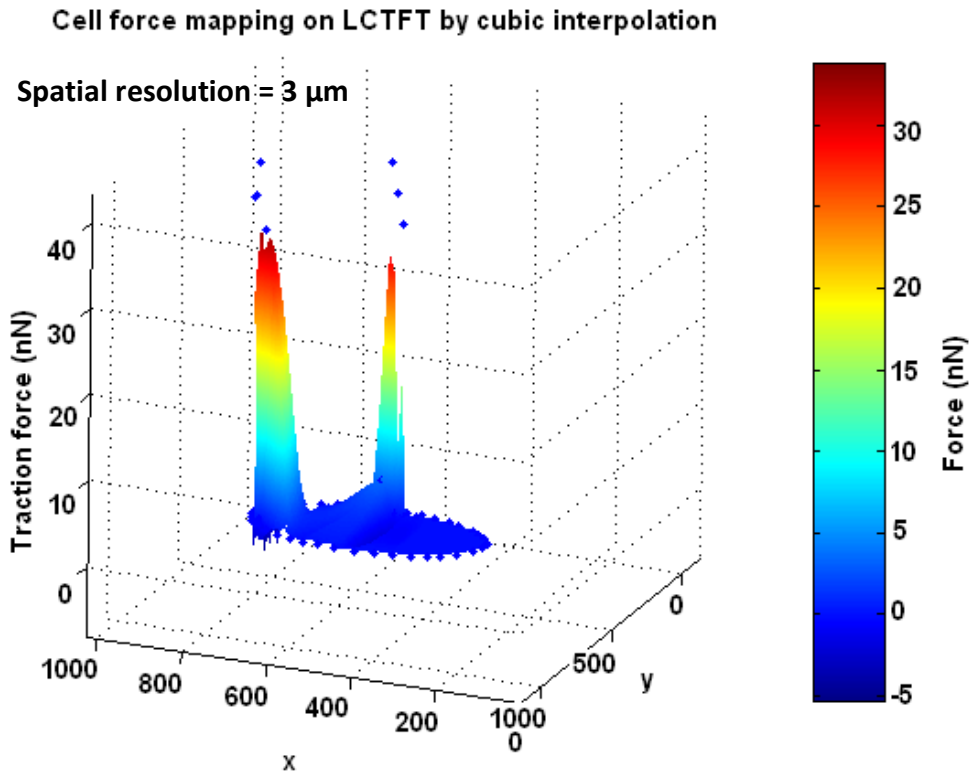

(b)

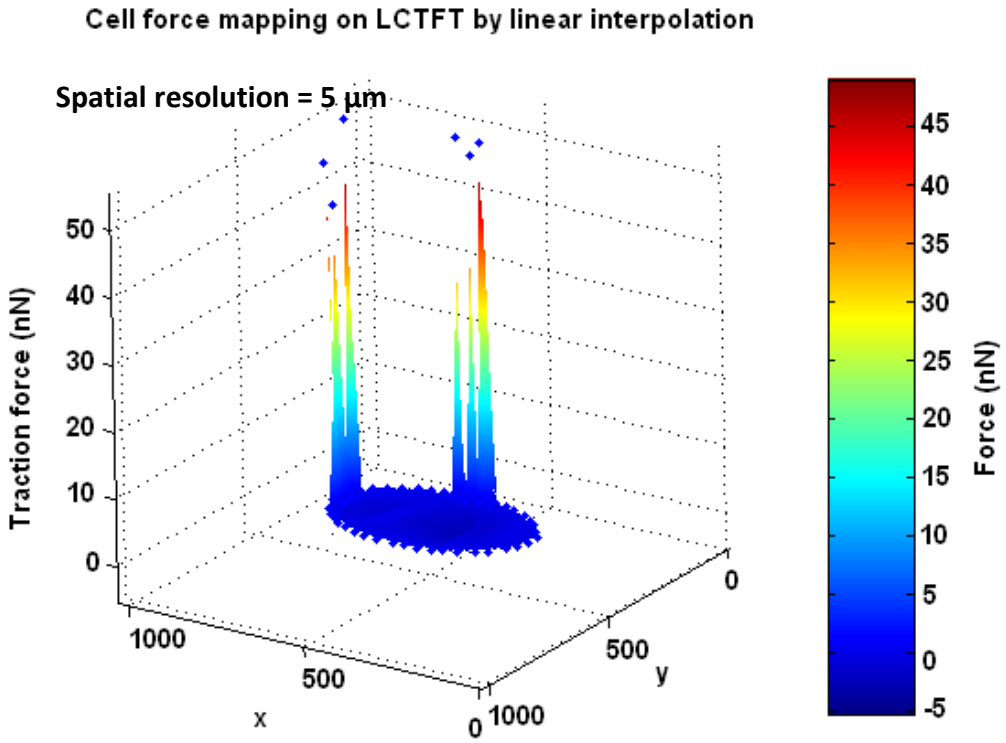

Figure 4.23. The resolution of CTFM software in resolving forces separated by a distance of (a) 3 µm and (b) 5 µm. x and y are the Euclidean coordinates and z is the axis for the traction force in the unit of nano-Newton. The scale bar in pseudo colours represents the magnitude of forces.

4.3.7 Analysis of the Traction Force Distribution of Quiescent Keratinocytes

The study on the distribution of static traction forces for quiescent cells will be essentially used as a reference to compare with the traction force of dynamic cells. Figure 4.24 shows a single HaCaT cell inducing deformation lines in the surface of LCTFT after culturing at 37 ^{o}C for 24 hours and the associated map of cell traction forces. As shown in Figure 2.27, Figure 4.15 and Figure 4.24a, the morphology undertaken by single non-migratory keratinocytes on the LCTFT is generally in a polygonal or rounded shape. Discrete and isolated forces at about 10 – 60 nN were found distributing at the boundary of the cell (Figure 4.24b) and the force distribution was well correlate with the location of the deformation line observed in Figure 4.24a. A peak force of 65 nN was observed at the protrusion edge of the cell marked by an arrow (or red region in the cell traction force map of Figure 4.24b).

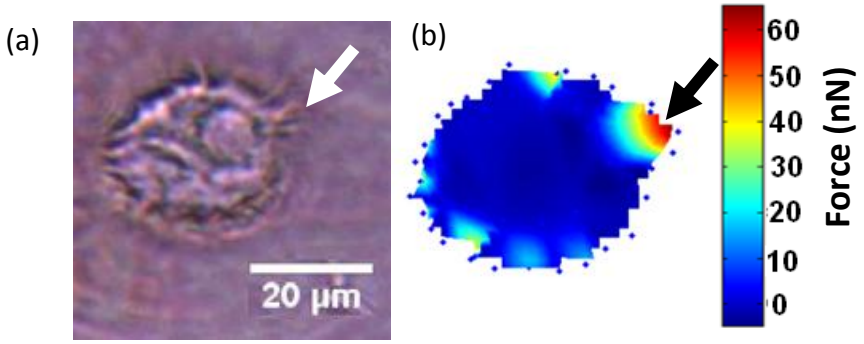

Figure 4.24. (a) A single HaCaT cell contracting on the LC traction force transducer and (b) the force distribution rendered by CTFM system. The arrows indicate the region of protrusion.

For two HaCaT cells located adjacent to one another, it was found that they expressed a similar morphology and active regions were found evenly distributed over a short distance (Figure 4.25a). Under quiescent condition, the mechanical forces of two HaCaT cells as detected by the LCTFT are relatively stable and localised. These

forces are neither expressed at the intersection or centre region of the cells, but limited to a small area at the periphery of the cells.

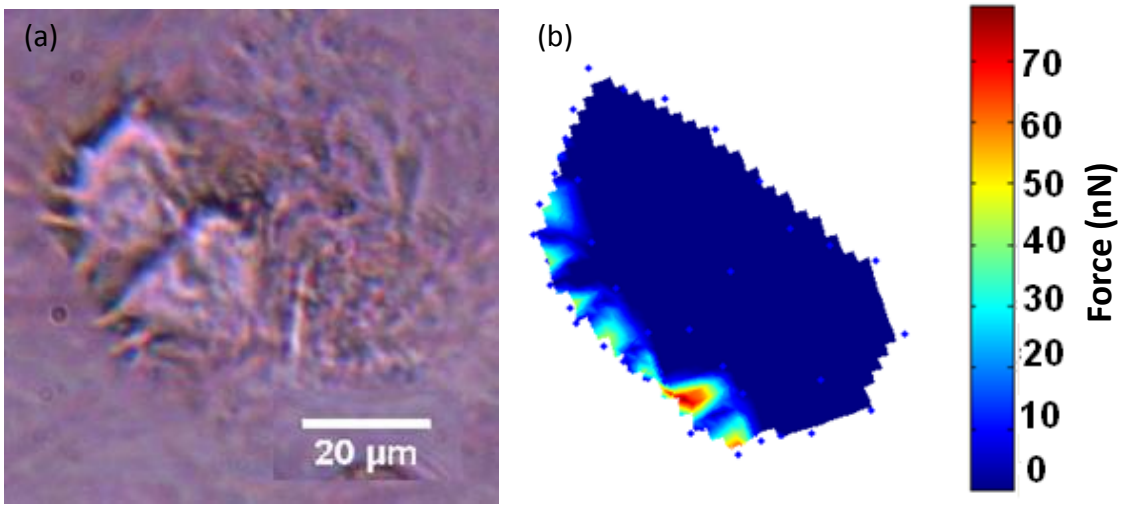

Figure 4.25. (a) Two adjacent HaCaT cells contracting on the LC force transducer, and (b) the force distribution generated by CTFM software.

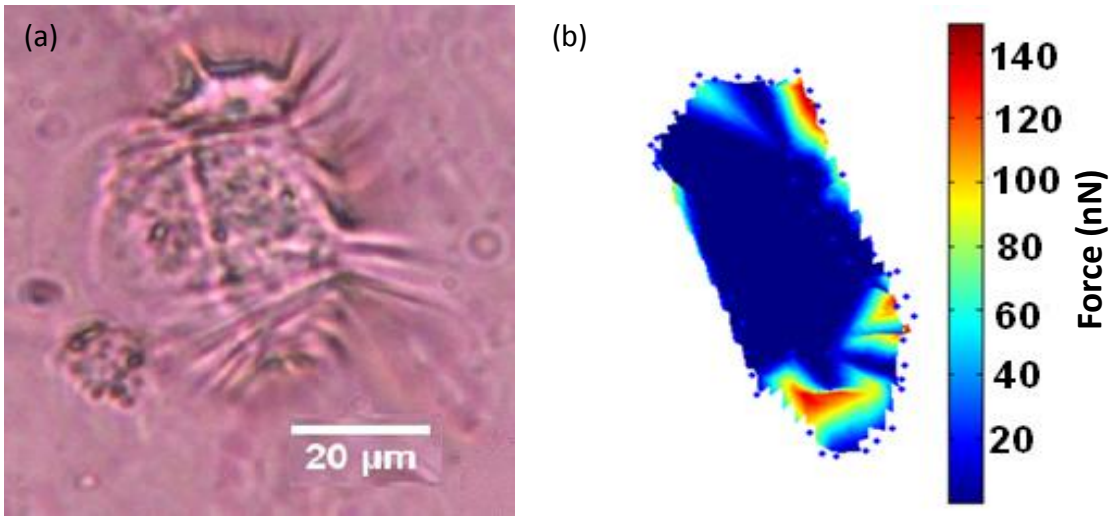

Figure 4.26. (a) A polarised HaCaT contracting on the LC traction force transducer, and (b) the force distribution generated by CTFM software.

For an elongated cell (Figure 4.26a), the expression of force was polarised and was observed to be higher at one end than another (Figure 4.26b). The peak force (140 nN) measured for an elongated cell was greater than the forces expressed by a polygonal shaped cell (60 – 80 nN) as seen in Figure 4.24b and Figure 4.25b. These

results show that the traction force expressed may be closely related to the morphology changes or cytoskeleton restructuring of a cell (Beningo, 2002). Traction forces detected at the periphery of the quiescent HaCaT cells most probably related to the organisation of circumferential actin bundles lining tangentially at the margin of the cell. This profound feature in the keratinocytes is thought to play crucial role during static adhesion and contraction of keratinocytes (Owaribe et al., 1981). The contractile functions of circumferential actin filaments are such as shortening the cell margin length, coordinating with parallel actin bundles in maintaining cells shape (Owaribe et al., 1981), ensuring integrity in relation to other cells in the epithelium sheet, and thus expressing traction stresses at the margin of the keratinocytes (Zhang et al., 2005).

Previous studies (Munevar et al., 2001, Burton et al., 1999, Oliver et al., 1995) focused more on migratory behaviour of cells and rarely investigate the static behaviour of a quiescent cell. Quiescent HaCaT cells do not show prominent characteristic of lamellipodia protrusion (leading and tailing edge) on a soft substrate as compared with fibroblasts (Munevar et al., 2001, Burton et al., 1999). It has been shown that the traction pattern of fibroblasts is different from the traction pattern of fish keratocytes measured on a silicon sheet (Oliver et al., 1995, Jurado et al., 2005). Traction of a fish keratocyte is induced by a compression mechanism at the lateral margins of the cell which shears centripetally (Oliver et al., 1995). In contrast, attachment and contractions of MDCK epithelial cells on the patterned silicon micro-posts tend to detect shear forces in axial direction as shown in Figure 1.15 (Roure et al., 2005). However, very little information is available pertaining to the traction force patterns expressed by epithelial cells (as evidence in Table 4.2).

4.3.8 A Study on the Traction Force Distribution of a Migrating Keratinocyte

The aim of this study is to further investigate the ability of LCTFT in detecting dynamic traction forces generated by a migrating cell. Time lapse phase contrast images of a migrating HaCaT cell and the traction force distributions are as shown in Figure 4.27 while the associated temporal response of the cell traction forces is as given in Figure 4.28. Under the cell, areas of traction in the LCTFT surface were divided into four regions with reference to the regimes of a cell: the leading edge of lamella, the two lateral margins of extension (flanks) and the rear edge of a cell (Figure 4.27a).

During the initial stage of monitoring, the cell was roundish (Figure 4.27a, 0 minute) and showed moderate compressive forces parallel to the rear edge of the cell (80 nN peak) just like those of the quiescent keratinocytes and a small rise of force at the leading edge (55 nN peak) was observed (Figure 4.27b, 0 minute and Figure 4.28). The lateral margins of the cell showed no sign of tractions (Figure 4.27a-c, 0 minute). Only the cell rear showed sign of contraction (Figure 4.27c, 0 minute).

After 5 minutes of monitoring, the leading edge evolving became apparent and was characterised by the projection of lamellipodia (Figure 4.27a-c, 5 minutes). This process was associated with the formation of LC deformation lines which were radiating outward. The deformation lines seem to be caused by the perpendicularly applied traction forces at the leading edge of the cell (Figure 4.27c, 5 minutes). The exerted forces at the leading edge increased dramatically from about 55 nN to 110 nN (Figure 4.27b, 5 minutes). Subsequently, the force expressed in the leading edge decreased slightly to 90 nN and continued decreasing to 80 nN towards the end of the recording (Figure 4.27a-c, 10-15 minutes, Figure 4.28).

During the same period of time (5-15 minutes), retractions were indicated at the rear edge accompanied by release of compressive forces in this region (Figure 4.27a-c,

5-15 minutes). In contrast to the rise of forces at the leading edge, the initial forces at the rear edge decreased from approximately 80 nN down to 10 nN (Figure 4.27a-c, 5 and 15 minutes, and Figure 4.28).

Progressive projections of flanks at both lateral margins of cells occurred concomitantly while the front and the rear of the cell were extending and retracting, respectively, (Figure 4.27a-c, 5-15 minute). In Figure 4.27c (5 minutes), the thick arrows at the front and rear of the cell show the direction of the contraction and relaxation forces, respectively. Strong forces at the right and left flank rose transiently to 160 and 100 nN, respectively, and then gradually decreased to 0 nN. However, towards the end of the recording, both of the flanks remained extended (Figure 4.27a-c, and 15 minutes).

The transverse traction forces (40 - 60 nN) found under the flanks and formed in parallel to the direction of the retraction suggests that the flanks may function to augment the rearward retraction. As the rear edge of the cell was retracting, the force spots formed at the rear edge shifted tangentially along the boundary of the cell towards the leading edge (Figure 4.27a-c, 5 and 10 minutes). The forces seemed to increase gradually and along with the shift of forces to the flanks. At the flanks, the sharp forces seemed to pull the rear region of the cell while the rear edge was retracting forward (Figure 4.27a-c, 5-10 minutes). Due to the protrusion of lamellipodia at the flanks and retraction at the rear edge, both restructured the trailing edge of the cell into a broad curvature (Figure 4.27a-c, 10-15 minutes). As a result, the cells changed from a nearly symmetrical morphology into an asymmetrical morphology. This is a typical characteristic of keratinocytes in the transition from a non-polarised phenotype into a polarised phenotype (Kirfel et al., 2002a).

.

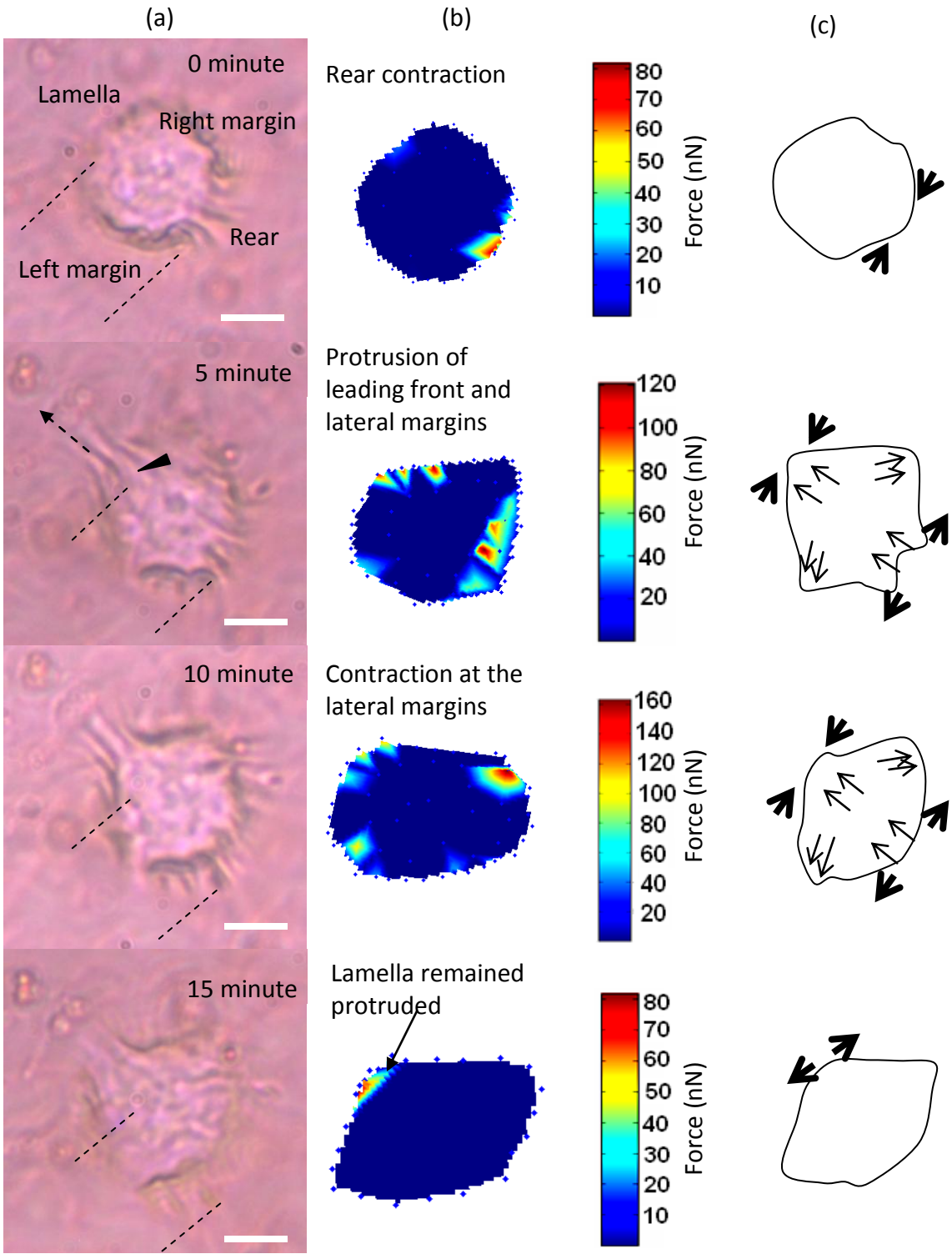

Figure 4.27. Time base tractions of a keratinocyte on a LCTFT displayed in (a) phase contrast micrographs which were taken at 0, 5, 10 and 15 minutes of monitoring. The broken line arrow indicates the direction of movement and the dotted lines are the position of reference for the cell. (b) The associated distribution of traction forces. (c) The directions of forces as shown with thick arrows and the thin arrows represent the direction of the actin bundles flow, respectively. The scale bar in pseudo color represents the magnitude of forces. (Scale bar: 20 µm)

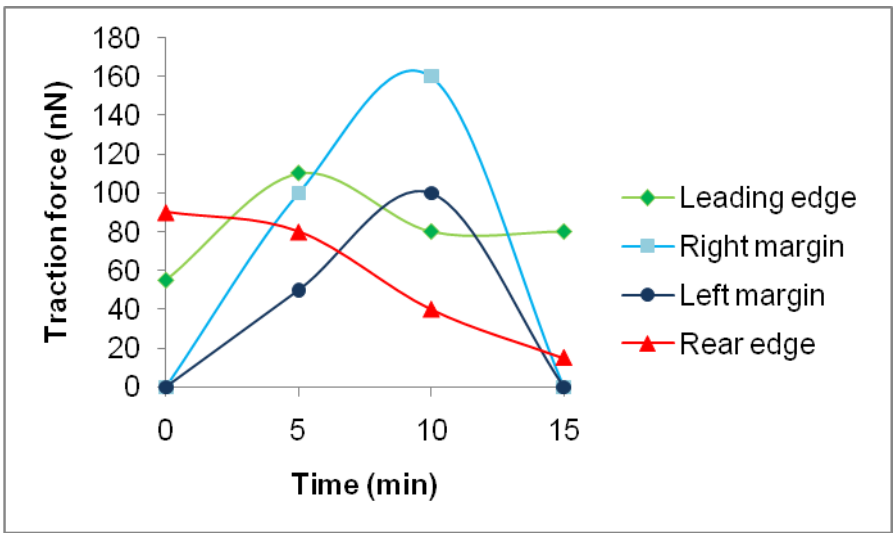

Figure 4.28. Time response curves of the traction force measured at different regions of a single keratinocyte as shown in Figure 4.27.

At the end of the monitoring (15 minutes), the traction forces at the rear edge and both lateral margins were greatly decreased. Some traction forces were still maintained at the protruded lamella (leading front). By referring to the reference position line (Figure 4.27a), the cell has translocated across a distance of 8 µm at a speed of approximately 0.5 µm/min (distance of 8 µm in 15 minutes), which is comparable to the normal migration speed of 0.6 µm/min for keratinocytes as reported in (Kirfel et al., 2002b).

Overall, the lateral margins and leading lamella of the cell were found transmitting the high traction forces in comparison to the rear edge (Figure 4.28). The traction forces induced at the two flanks of the keratinocytes are compressive and seemed to be applied parallel to the lateral margins in forward direction. All through the monitoring of this cell, traction forces were not detected at the posterior or central region of the cell body. The central region of keratinocyte may be weakly adhesive to the substrate, in order that the passive load of the cell body mass could be transported

by the contractile machinery functionalised at the periphery of the keratinocyte. This is in keeping with the findings for fibroblasts reported in (Munevar et al., 2001).

During the transition from a roundish morphology into migratory phenotype, the cell breaks the symmetry of the morphology by initiating rear retraction. This agrees with the common conformity of cells in forming the cell rear first but the reason is not clear (Cramer, 2010). Shortening of the rear edge directed inward is most probably associated with the contraction of the straight radial bundles of actin oriented towards the center region of the cell, resulting in lamellipodia retractions from the cell rear. While these striated bundles of actin are retracting, they are probably accompanied by an expansion of parallel actin bundles at the leading edge. In addition to that, some deformation lines at the leading edge indicating compressive forces applied perpendicular to the lamella was formed and aligned in parallel to the direction of lamella protrusion. The origin of these forces occurred in a small area behind the lamella (marked by an arrowhead in Figure 4.27a at 5 minutes) which is consistent with the localisations of short circumferential actin bundles situated right behind the lamellipodia as reported in (Mohl et al., 2009).

Strong traction forces are found at the edges of the lateral margins most probably associated with the arrangement of the circumferential actin bundles and focal adhesions lining along the boundaries of lateral margins of the keratinocytes (Figure 4.29a-b), which were obtained from the experimental results of Chapter 3. Previous literature shows that migrating keratinocytes have profound circumferential actin bundles but also straight thin and parallel actin bundles in the central region of the cells (Owaribe et al., 1981, Gloushankova et al., 1997).

(a)

(b)

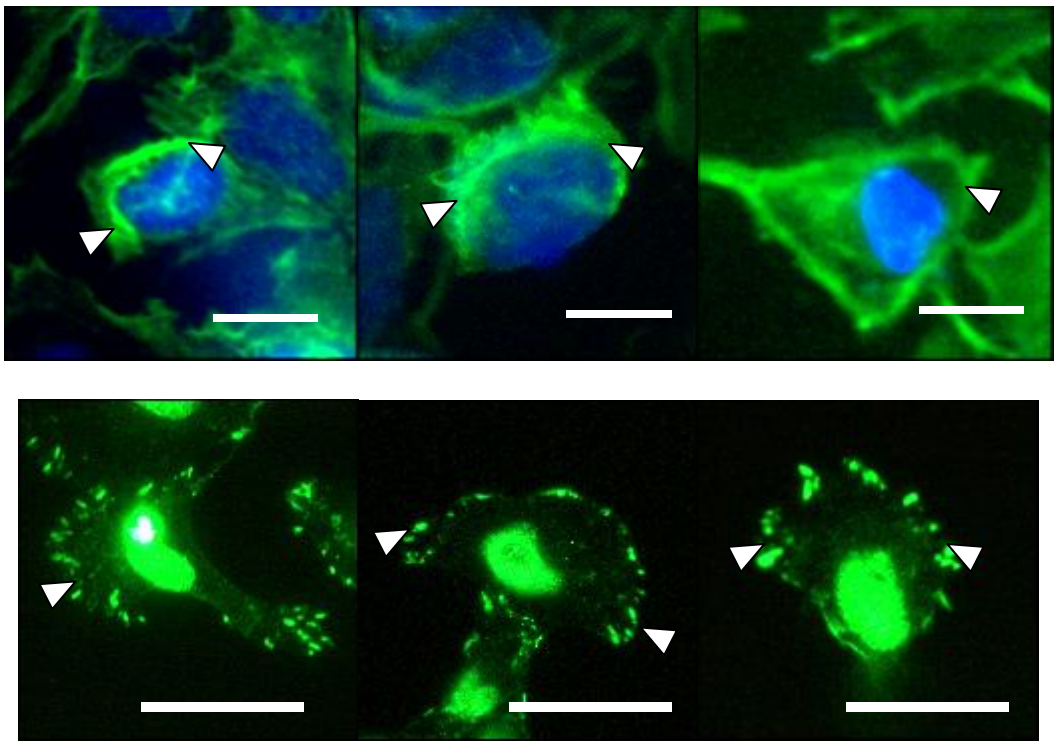

Figure 4.29. (a) Circumferential actin filaments and (b) vinculins located at the lamella of the keratinocytes cultured on LC substrate. The arrow heads indicate the short actin bundles and focal adhesions located at the circumference of the keratinocytes in (a) and (b), respectively. (Scale bar: 25 μm)

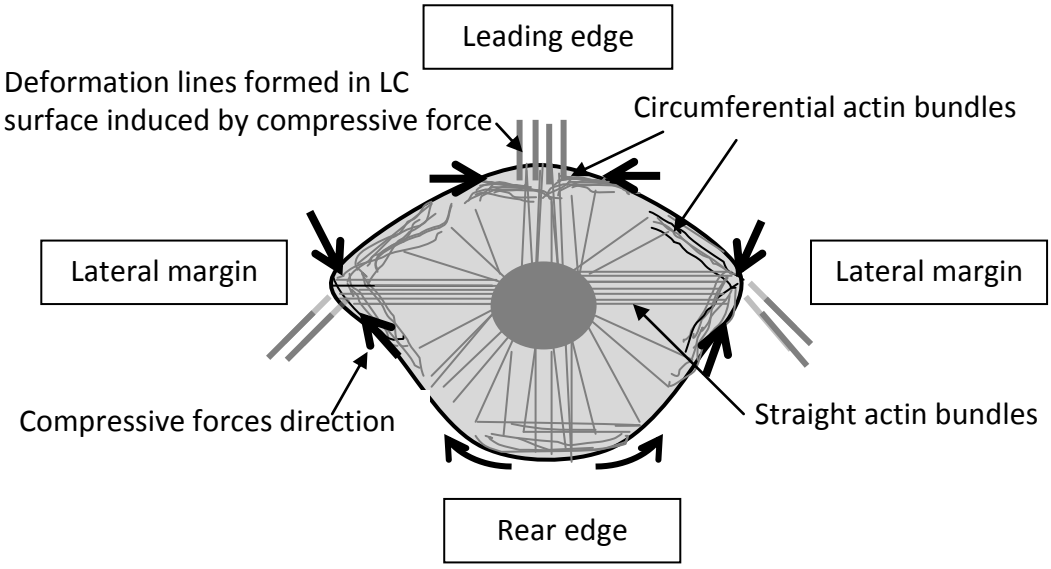

Figure 4.30. A new model proposed for the contraction of circumferential and straight actin bundles of a migrating keratinocyte in relation to the deformation lines form in the liquid crystals.

The circumferential actin bundles mostly consist of short bundles that are contractile (Owaribe et al., 1981, Mohl et al., 2009) and this is consistent with the actin filaments observed in this work (Figure 4.29a).

During the formation of lamella, these circumferential actin bundles disassemble and coincide with the radial expansions of the striated stress fibres from the center of the cell body extending into the lamella (Omelchenko et al., 2001, Gloushankova et al., 1997) which may explain the protrusion of lamella as observed in Figure 4.27. The dynamic re-orientation of actin fibres in relation to the observations of the traction of a migrating keratinocyte obtained in this study can be re-illustrated in a new model as proposed in Figure 4.30.

The contractions of the circumferential actin bundles along the lateral margins of the flanks are postulated to create strong forward forces in pulling the rear of the cell body forward. The straight actin bundles may function to protrude the cell body to form new contact areas. These different organisations of actin cytoskeleton regulate different contractile functions (static contraction, dynamic protrusion and retraction) and may enable the cell to exert variable forces on the LC surfaces in isolated region via the focal adhesions.

In the context of the deformation line formed in the liquid crystal surface, the contractile mechanism of the two types of stress fibre arrangements may be associated with the deformation lines directed oblique (at the lateral margins) and perpendicular (at the leading edge) to the direction of migration. The discontinued circumferential filaments dissected by the radiating actin bundles as suggested in (Owaribe et al., 1981) may contract and form compressive forces inducing the deformation lines in the LC surface that were perpendicular to the protruded leading edge (Figure 4.30).

Similarly, the contractions of the short actin fibres located at the lateral margins could induce deformations lines in the LC surface perpendicular to the lateral margin of the cell. When the movement of the rear side was completed, the activities of contractions at the lateral margins and rear edge of the cell ceased as indicated by the disappearance of deformation lines (Figure 4.27a, 15 minute). However, the deformation lines formed at the leading lamella were persistently oriented forward upon the completion of migration. These results suggest that the migration of this keratinocyte is highly dependent on the contraction at the lateral margins of the cell body in order to move forward.

During the migration of a keratinocyte, new frontal adhesive sites must be formed at the leading edge and this requires the deposition of new ECM proteins (collagen, laminin and fibronectin) by the keratinocytes, which can then be followed by adhesion of cells to the ECM proteins via the integrins (Kirfel et al., 2003, Horwitz and Parsons, 1999). These are the causal events required for anchoring the actin cytoskeleton before the mechanical energy derived from the contractile and relaxation activity of actomyosin can be transmitted to a substrate. The polymerisation of actin cytoskeleton, formation of lamellipodia, re-attachment of lamellipodia on new adhesion sites mediated by focal adhesions and contractions of the myosin-II molecules are a series of coordinated and repetitive activities in migrating a cell (O'Toole, 2001, Horwitz and Parsons, 1999, Kirfel and Herzog, 2004). Reversibly, the adhesion to the ECM proteins must be able to be broken by rapid deployment of integrin receptors and withdrawal of the actin cytoskeletons (Hynes, 2002), and the output of these mechanisms were observed in a HaCaT cell migrating on the LC surface. During the retraction of lamellipodia, the dynamics of movement may involve the de-bundling of actin filaments and the shortening of the dorsal filaments as

suggested in (Pellegrin and Mellor, 2007). This would be associated with disassembling of focal adhesions, thus, de-attaching the lamellipodia from the substrate (Pellegrin and Mellor, 2007, Hotulainen and Lappalainen, 2006) and it is suggested for the retraction phase of the keratinocyte studied in this work.

4.3.9 Comparison with Previous Cell Force Sensors Developed for the Study of Cell Migration

Numerous traction force measurement techniques developed were focused on the study of active traction involving in the locomotion of cells (Roy et al., 1997, Dembo et al., 1996, Munevar et al., 2001, Eastwood et al., 1996, Hinz and Gabbiani, 2003). Previous literature shows that fibroblasts exert a stronger retrograde flow of forces at the lamella than the rearward of the cell body. This is highly correlated with the contractility of the striated parallel actin bundles that are oriented parallel to the direction of migration, in which the traction forces of fibroblasts are directed inward at the leading lamella as the actin filaments contract. These forces were suggested to "tow" the passive cell body forward (Dembo et al., 1996, Munevar et al., 2001).

To date, very limited work has been done to study the migratory pattern of keratinocytes (Kirfel et al., 2003). Mohl at. el. 2009 used the strain of micro beads labeled PDMS to track the traction forces of vinculins in sessile keratinocytes. In their work, large inward directed forces which are perpendicular to the direction of locomotion were found to appear at the rear corners of a migrating keratinocyte. This finding is similar to the early stage of traction forces presented by the migration of keratinocyte studied in this work. The force measured in (Mohl et al., 2009) indicated a very weak retrograde flow of forces (a few nN) at the lamellipodia of the leading edge. In contrast to the work presented by Mohl et al., this work found transverse directed

forces at the leading edge and there were no changes of traction at the leading edge while the rear was retracting. This suggests that the forces at the lamella are unlikely to flow in a retrograde direction (directed inward at the leading edge). However, the traction forces found at the lateral margins of keratinocyte in this work are stronger than the leading edge which is consistent with the findings reported in (Mohl et al., 2009).

The discrepancies in the materials and techniques used may be the main contributing factors to the different findings obtained in this work as compared with previous studies (Mohl et al., 2009, Roure et al., 2005). As revealed in (Burton et al., 1999), silicon rubber with a higher compliance has detected both rearward directed forces at the lamellipodia and forward directed lateral forces at the flanks of a migrating fish keratocyte. In the same work (Burton et al., 1999), similar substrates with a lower compliance were only able to detect the forward directed forces at the lateral margins of the keratocytes. From the same study, it shows that the compliance of a material is a critical factor in determining the sensitivity of cell force transducer developed to detect detail mechanism of a migrating cell (Burton et al., 1999).

4.3.10 Advantages of Liquid Crystal Based Cell Traction Force Transducer

The work by (Harris et al., 1980) pioneered the wrinkle based method for studying the cell traction forces but showed no quantification information and this method was improved by higher compliance silicon rubber (Burton and Taylor, 1997, Burton et al., 1999). However, thinner silicon rubber sheets exhibited problems of generating non-linear and chaotic wrinkles in response to the stresses exerted by fish keratocytes and fibroblasts. As a consequence, the wrinkled based method remained only useful as a qualitative tool in assessing cell traction (Dembo et al., 1996, Addae-

Mensah and Wikswo, 2008). The work presented in this thesis tackled the major issue of the wrinkle based technique that had not previously been solved. This work has advanced the previous techniques by developing a liquid crystal based cell traction force transducer of higher sensitivity for quantifying the traction forces of keratinocytes, in which, the forces were quantified by applying small deformation theory and presented by using computer visualisation software.

The only work which has shown success in rendering the cell traction forces exerted on the PAA gel in computer visualisation was developed by Dembo et al. (Dembo et al., 1996). This involved a statistical approach in which the maximum likelihood was employed to estimate the most probable location and magnitude of the traction energy associated with the displacement of the adjacent markers (fluorescent beads) in a PAA gel. The de-convolution of the estimated displacement of the markers involved complex computational process such as Bayesian probability. This method was not able to precisely determine the location where the cell traction forces were generated (Addae-Mensah and Wikswo, 2008). Furthermore, the acquisition of the strain of the randomly distributed markers is reliant on the PAA gel under null-force condition (reference), in which cytochemical treatment to relax cell is inevitable and resulting in tedious quantification procedures.

By using a similar wrinkled based approach, the LCTFT system uses a direct cell traction force quantification technique which is based on the length of a deformation lines formed in the LC surface, in which the traction force inducing each discrete deformation line can be derived from the force-deformation relationship of the LC substrate. These forces calculated for discrete locations in LC surface were then efficiently translated into a force map by using custom-built CTFM software.

From this study presented in Chapter 4, the advantages of using LCTFT and the CTFM software system were identified as:-

(a) The continuum based LC substrate allows the dispersion of cell contact in arbitrary directions;

(b) LCTFT detects a wide range of traction forces (0 - 200 nN) for polarised and non-polarised cell with a sensitivity down to 10 nN (refer to Table 4.2);

(c) The system allows direct qualitative characterization of the traction forces by using phase contrast microscope;

(d) The liquid crystal substrate can be used to measure traction forces at a spatial resolution of ~2 μm whilst the CTFM software enables a spatial resolution of ~5 μm.

4.4 Summary

Chapter 4 presented a novel means of quantifying the traction forces exerted by keratinocytes on the LCTFT which involved the application of small deformation theory and Hooke's theorem. In the preliminary profiling of the force-displacement relationship for the liquid crystal substrate, this approach used a cell relaxation technique via treatments with cytochalasin-B to determine the cell localised traction forces. The forces quantified for keratinocytes in this work are comparable to forces expressed by other epithelial cells. Nonetheless, the finite element model was used to model the deformation and stress distribution at a stress site in the liquid crystal surface. This model indicates that the highest stresses were exerted at the stress planes and compressive model was suitable to describe the traction of HaCaT cells on a soft substrate. A cell traction force measurement and mapping software was custom-built to render the traction forces in computer visualisation based on the length of

deformation line induced by a cell in the liquid crystal surface. The 2D and 3D maps of cell traction forces rendered in pseudo colour have enabled the study of traction forces for polarised and non-polarised keratinocytes. The overall system has been shown to be useful for analysing time based cell migration.

CHAPTER 5

EVALUATION OF LIQUID CRYSTAL BASED CELL TRACTION FORCE TRANSDUCER

5.1 Introduction

The aim of this chapter is to evaluate the consistency and repeatability of the liquid crystal based cell force transducer (LCTFT) in sensing the contraction responses of human keratinocyte (HaCaT) to treatment with different concentrations of Transforming Growth Factor Beta 1 (TGF-β1) in single application by means of statistical analysis. The contraction responses were measured in terms of traction forces and were quantified by converting the length of the deformation lines induced by single HaCaT cells to traction forces based on the force-displacement relationship of the liquid crystals (LC) established in Chapter 4. In addition, the reliability of the LCTFT will be assessed by the repeatability and consistency of the liquid crystals in sensing the traction forces of cells treated with different concentrations of TGF-β1.

TGF-β1 was chosen as a pharmacological test agent in this study because this cytokine has well established effects to the contraction responses of keratinocytes (Boland et al., 1996, Decline et al., 2003, Li et al., 2004a). An excessive application of TGF-β1 to in-vivo and in-vitro wounds was thought to contribute to several problems, including delayed re-epithelialisation (Garlick and Taichman, 1994), taut-stretched skin, hyperkeratosis and psoriasis (Sellheyer et al., 1993). Delayed reepithelialisation and reduced proliferation due to the introduction of TGF-β1 to the wound are often associated with an increase in migration of keratinocytes and the formation of stress fibres (Zambruno et al., 1995, Boland et al., 1996, Jeong and Kim, 2004, Coffey et al., 1988). Previous studies (Ashcroft et al., 1999, Garlick and Taichman, 1994) show that the stimulatory effects of the exogenous TGF-β1 applied to the in-vitro cultures could be dependent on the dosage and kinetics of administration. Although studies have examined the effect of TGF-β1 on keratinocyte growth and proliferation (Garlick and

Taichman, 1994, Jeong and Kim, 2004), none have so far studied the effects on the contraction at cellular level.

There are very few studies investigated the contraction of keratinocytes (Chakrabarty et al., 2001), yet, the contraction of keratinocytes plays a crucial role in wound healing (Souren et al., 1989, Deneflea et al., 1987, Schafer et al., 1989) and it affects the shrinkage of re-constructed skin graft (Chakrabarty et al., 2001, Harrison et al., 2005). Generally, the contraction of keratinocytes was quantified by measuring the shrinkage area of a collagen sheet seeded with cells over a period of 24 hours (Souren et al., 1989, Dallot et al., 2003, Montesano and Orci, 1988). This technique has been acceptable because of the ease of use and ability to semi-quantifying the stress for a population of cells in the culture, but unfortunately it lacked the sensitivity to probe contractility at the single cell level. Monitoring the intensity of traction forces for single cells in response to different dosage of TGF-β1 may provide more insights into the effects of treatments on the regulation of cellular contractions.

5.2 Material and Methods

5.2.1 Treatment of Cells with Different Concentrations of TGF-β1

The cells and liquid crystal substrates were prepared as described in section 2.2.3 and 2.2.6. Each of the four petri dishes containing a liquid crystal substrate was cultured with HaCaT cells at a density of 1.5 x 10^3 cells/cm^2 and incubated at 37 ^oC for 2 hours initially. After two hour plating onto the liquid crystal coated substrates, the cells containing in the three petri dishes were treated with single dose of 5 ng/ml, 10 ng/ml and 20 ng/ml of TGF-β1 diluted in 8 µl of HBSS, respectively. The last petri dish

was treated with 8 µl of HBSS as a control. Subsequently, the cells in all the four petri dishes were incubated at 37 ^{o}C for the subsequent 22 hours.

The responses of the cells to the liquid crystal substrate after 24 hours of incubation were captured by using a digital camera mounted on a phase contrast microscope which was set at 10x magnification. These experiments were repeated three times. For each treatment with TGF-β1 and controls, images of 100 randomly selected cells were acquired and the length of deformation in the LC surface for each cell was measured by using the measurement tools available in ImageJ software.

5.2.2 Quantifying Contraction Responses of Cells to TGF-β1

The contraction response of HaCaT cells was quantified by determining the average traction forces of single cells in responding to different concentration of TGF-β1. Based on the phase contrast images of cells cultured on the liquid crystal substrate, the length of the deformation lines induced by each cell on the liquid crystal surface were averaged and considered as the average length of deformation lines per cell. The mean traction force for each cell was estimated by this relationship, average traction force = (force-deformation coefficient of the liquid crystals) x (mean length of radial deformation line), where, the force-deformation coefficient of the liquid crystals = 20 nN/µm as determined in Chapter 4. Cells that did not induce traction forces or deformation lines were also included in the analyses. These procedures were repeated three times for cells cultured on the liquid crystal substrate treated with 5 ng/ml, 10 g/ml and 20 ng/ml of TGF-β1 and the control.

5.2.3 Statistical Analysis

The average traction forces quantified were expressed as means ± standard errors (SE). One sample Kolmogorov-smirnov tests were used to test the normality of

the traction forces of the cells per treatment group at a significance level of $p > 0.05$. For non-normally distributed traction forces, non-parametric tests were used to analyse the data. This involved use of the Kruskal-wallis test to investigate the differences in the traction forces of HaCaT cells treated with different TGF-β1 doses. The test was followed by Mann-whitney Post Hoc tests to test the significant difference between treatments. The consistency of the LCTFT in detecting the traction forces of cells in responding to different concentrations of TGF-β1 was tested by Cronbach alpha test (significant at $\alpha > 0.7$).

5.3 Results and Discussion

5.3.1 Differential Traction Forces of Cells Treated with Various Doses of TGF- β1

The enhanced contraction corresponds to the increasing dosage of TGF-β1 was indicated by the proportional increase in the quantity and length of deformation lines in the liquid crystal surface. As observed in Figure 5.1a-b, TGF-β1 as low as 5 ng/ml induces dramatic contraction of HaCaT cells attaching to the liquid crystal surface. The contraction responses are probably an indication of stress fibres formation in which the traction forces were transmitted via the focal adhesions (Burridge and Chrzanowska-Wodnicka, 1996) to the surface of the liquid crystals as deformation lines. The result of this TGF-β1 treatment experiment shows that the maximum length of deformation lines induced by the cells seems to be approximately 30 µm. Therefore, the strain induced by the treated cells could be within the linear viscoelastic range of the liquid crystal substrates as characterized and analysed in Chapter 2 (See Figure 2.24 and discussion in section 2.3.3). In the context of morphology, the cells treated

with TGF-β1 exhibited polyhedron shapes compared with cells in the control, in which cells were mostly remained non-polarised and roundish (Figure 5.1).

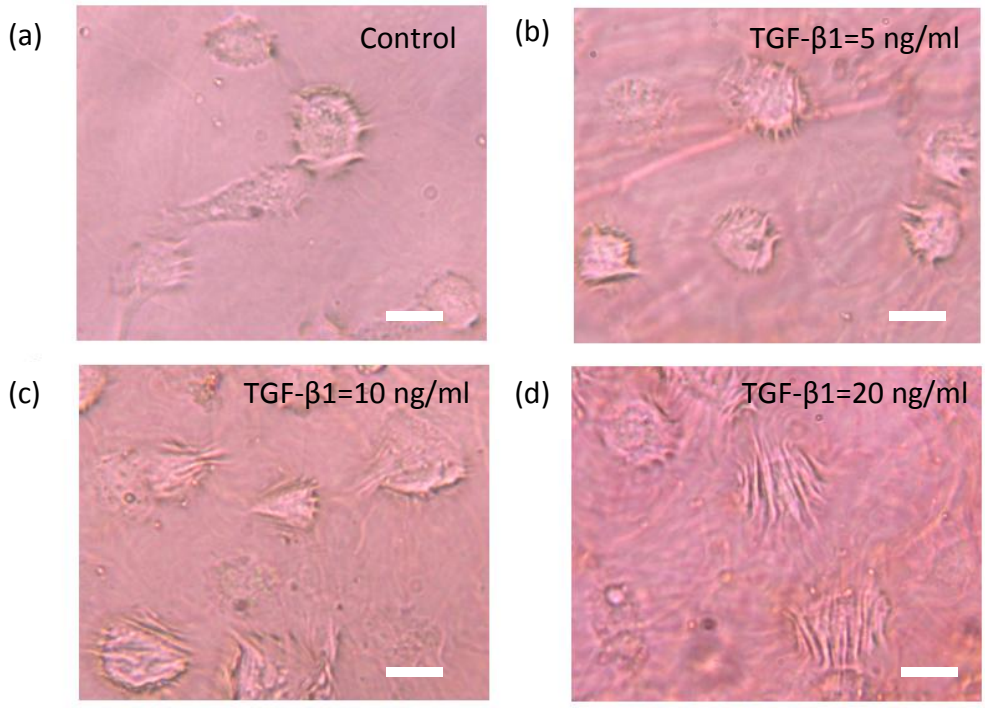

Figure 5.1. Phase contrast micrographs of HaCaT cells contracting on the surface of the liquid crystals in (a) a control and in the treatments with single dose TGF-β1 at (b) 5 ng/ml, (c) 10 ng/ml, and 20 ng/ml at 37 ^{o}C for 24 hours. (Scale bar: 20 μm)

For those cells contracting on the liquid crystal surface, the forces were found distributed at the circumference of the cells in the control but the traction forces were seen elevated to the central region of the cells when 10 ng/ml and 20 ng/ml of TGF-β1 was applied (Figure 5.1c-d). This is probably associated with the elongated stress fibres formed in the HaCaT cells after treated with 10 ng/ml of TGF-β1 (Decline et al., 2003). The phenotype of the keratinocytes induced by TGF-β1 is closely associated with the change of cell morphology and reorganisation of cytoskeleton (Zhang et al., 2003, Boland et al., 1996). As reported previously (Boland et al., 1996, Decline et al., 2003), the effects of treating keratinocytes with TGF-β1 were characterised by a reduction in

cell-cell contact, elongated shape, enlarged morphology and cells adopting a broad extension of lamellipodia similar to those observed in this work (Figure 5.1).

In controls, the cells expressed relatively low average traction forces at 50 ± 3 nN (mean ± SE) (Figure 5.2). These forces expressed in the controls are consistent with the forces quantified for normal culture of HaCaT cells on the liquid crystal substrate as presented in Chapter 4. The treatment of cells with single dose 5 ng/ml, 10 ng/ml and 20 ng/ml of TGF-β1 induced traction forces at 131 ± 6 nN, 205 ± 8 nN and 236 ± 6.5 nN (mean ± SE), respectively. Overall, the addition of TGF-β1 induced a non-linear dose dependent increase for the contraction of HaCaT cells cultured on the liquid crystal substrate, in which the traction forces reached a plateau at approximately 20 ng/ml of treatment (Figure 5.2).

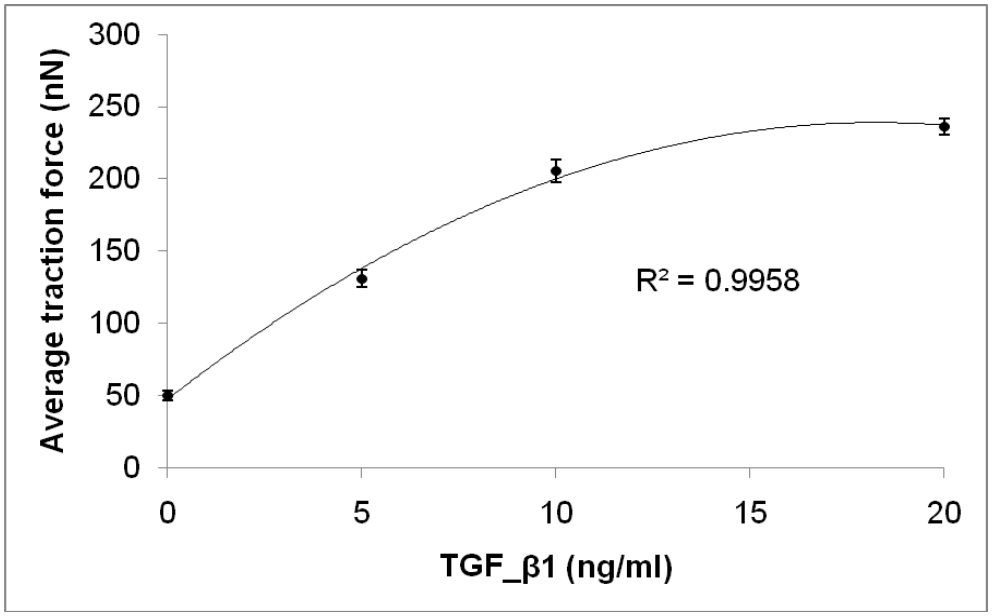

Figure 5.2. Average traction forces (mean ± SE) of HaCaT cells in a control (0 ng/ml) and after treated with of single dose TGF-β1 at 5 ng/ml, 10 ng/ml and 20 ng/ml at 37 ^{o}C for 24 hours in three repeats of experiments (N = 100 cells per experiment).

In the treatment with and without various concentration of TGF-β1, the HaCaT cells showed differential traction forces (from low level of traction forces to very high expression of traction forces) under the same culture conditions (Figure 5.2).

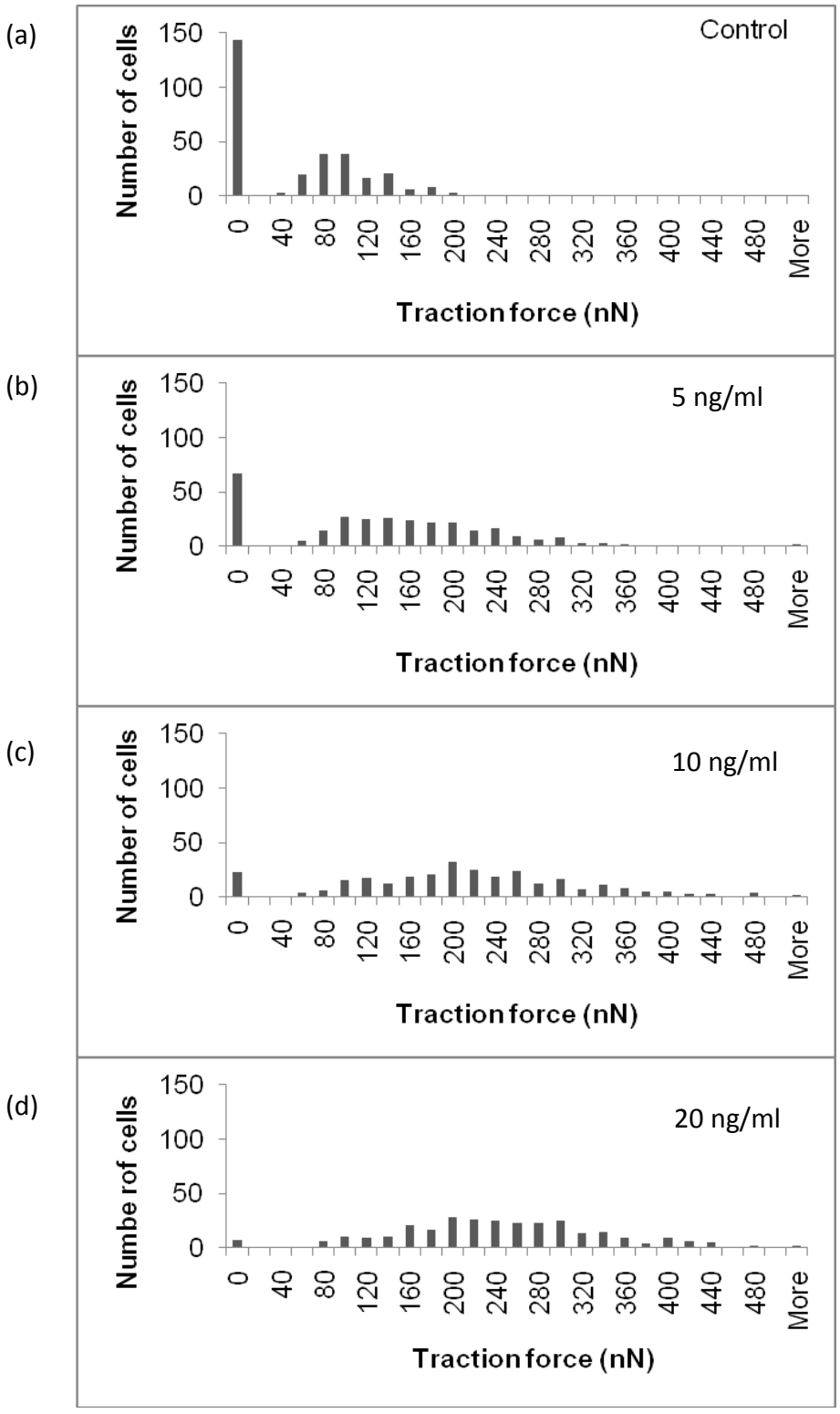

Figure 5.3 The distribution of traction forces for HaCaT cells in the (a) control and after treated with different concentrations of single dose TGF-β1 at (b) 5 ng/ml, (c) 10 ng/ml, and 20 ng/ml for 24 hours at 37 ^{o}C in three repeat of experiments (N = 100 per experiment).

In this aspect, the quantity of cells that responded and did not respond in contractions to the treatment of TGF-β1 was evaluated. In the control, the cells showed traction forces in the range of 40 – 160 nN (Figure 5.3a). After treated with 5 ng/ml of TGF-β1, the traction forces seemed to increase to a higher range of 40 – 360 nN (Figure 5.3b). As the dose of TGF-β1 treatment increases to 10 and 20 ng/ml, the range of traction forces of the cells increased to an even higher range of 40 - 480 nN and 60 – 500 nN, respectively (Figure 5.3c-d). These results show that LCTFT are sensitive to a wide range of traction forces expressed by HaCaT cells treated with difference doses of TGF-β1.

As shown in Figure 5.3, the number of cells that expressed null traction forces seems to decrease as the concentration of TGF-β increased. The percentage of cells responded to different concentrations of TGF-β1 increased non-linearly with the dosage of TGF-β1 (Figure 5.4). In the control (Figure 5.4) approximately 50 % of the cells were found without detectable traces of deformation lines or traction forces in the surface of the liquid crystals. Proportionally, the quantity of cells responding to the treatment increased clearly to 76 %, 91 %, and 96 % when the culture were treated with 5 ng/ml, 10 ng/ml and 20 ng/ml of TGF-β1 in single dose, respectively (Figure 5.3 and Figure 5.4). The curve for the percentage of responses reached a plateau at about 10 – 20 ng/ml of TGF-β1 treatment as seen in Figure 5.4

The contraction of HaCaT cells found is probably associated with the activation of the cell surface receptors (TGFβRII) by molecules of TGFβ and the downstream regulation of the stress fibres formation as reported in (Decline et al., 2003, Boland et al., 1996). Therefore, the contraction responses of HaCaT cells may be indirect responses correlating with the binding of the type II receptor (TGFβRII). This result might indicate that the higher dosage of TGF-β1 (10 ng/ml or 20 ng/ml) has provided

enough growth factor molecules to bind and saturate the cell surface TGFβRII receptors for most of the HaCaT cells in the cultures (91 % and 96 %). Thus, higher cell traction forces observed in the experiment probably reflects more interactions of the receptors with higher dosages of growth factors. At lower dosage of TGF-β1 (5 ng/ml), quantity of the growth factor molecules may be only sufficient to activate a small proportion of TGFβRII receptors over the cell surface which probably led to 16 % more in cell contraction responses when compared with the control as shown in Figure 5.4.

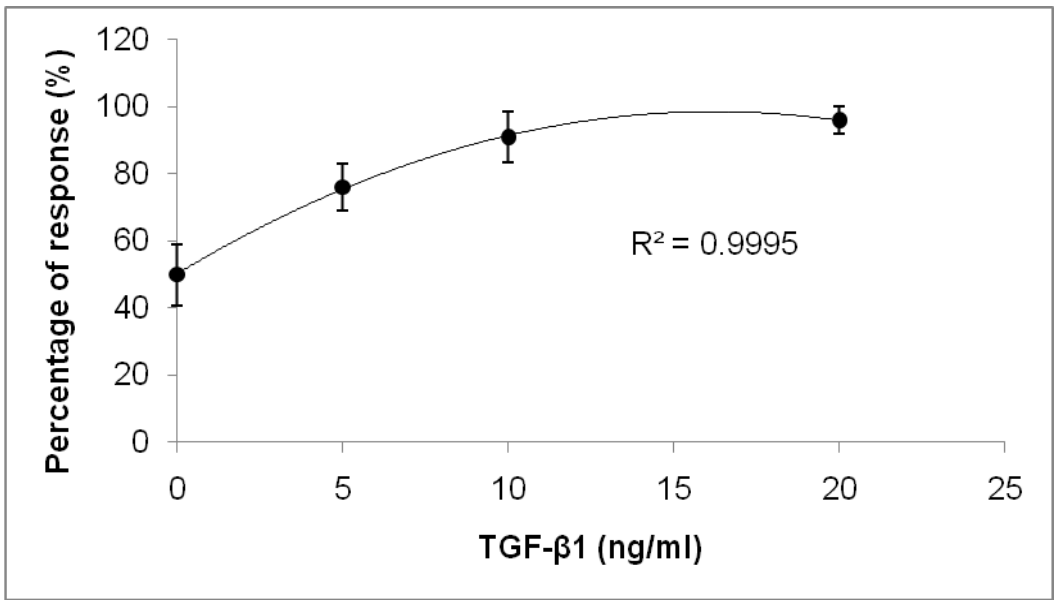

Figure 5.4. Percentage (Mean ± SD) of HaCaT cells responded in contractions to various concentration of single dose exogenous TGF-β1 at 37 ^{o}C in three repeats of experiment (N = 100 cells per experiment).

The results show that the treatment with TGF-β1 has strong effects onto the contraction responses of HaCaT cells (Figure 5.4). At the highest concentration of TGF-β1 at 20 ng/ml, 96 % of the cells were induced to generate traction forces between 60 and 500 nN. These forces were much stronger than the traction forces found in the control cells ranging between 40 - 160 nN. Such a strong contraction response induced by TGF-β1 might support previous observations on over stretched and tightly contracted skin of mice over expressing TGF-β1 (Sellheyer et al., 1993). The increased

contraction responses in HaCaT cells treated with TGF-β1 are probably related to more activation of actin polymerisations and actomyosin activities regulated by the internal cellular pathway of TGFβ (Cross and Mustoe, 2003, Massague and Wotton, 2000). In the cell culture treated with TGF-β1, this cytokine bound to type II receptor (TGFβRII) which then phosphorylates type I receptor (TGFβRI), in which, TGFβRI and TGFβRII are both obligate heteromeric transmembrane receptors (Wrana, 1998). The phosphorylation of TGFβRI leads to a series of down-stream signalling that regulate the target gene, eventually leading to subsequent cellular processes such as cell contraction (Massague and Wotton, 2000, O'kane and Ferguson, 1996).

The contraction responses measured in this work indicate that a minimum threshold of 5 ng/ml of TGF-β1 is enough to trigger remarkable cell contractions in 76 % of the cells (Figure 5.4). This is consistent with the previous reports which had shown that the applications of 5 ng/ml and 10 ng/ml of TGF-β1 can promote a dramatic elevation in the generation of stress fibres and promote the disruption of cell-cell contact within 24 hours of treatment (Bhowmick et al., 2001, Decline et al., 2003). Previous studies also showed that keratinocytes treated with TGF-β1 (10 ng/ml) showed rapid activation of RhoA which in turn induced stress fibres formation (Shen et al., 2001, Bhowmick et al., 2001).

The expressions of the signaling proteins or stress fibres in responding to the treatment with TGF-β1 are usually analysed by using techniques such as western blot analysis and immunofluorescence staining (Decline et al., 2003, Li et al., 2004a). Although western blot analysis can be used to quantify the time base expressions of proteins such as actin and Focal Adhesion Kinase (FAK) associated with the stress fibres and focal adhesions (Decline et al., 2003), the result output of this method is only semi-quantitative and provides no information about the forces generated. In

response to treatment with the different concentrations of TGF-β1, LCTFT measurement system has demonstrated the potential to provide direct quantitative as well as qualitative visualisation of the progressive development of contraction forces for single HaCaT cells. It is highly likely that this method of measuring cell traction forces could easily be applied to study other growth factors and pharmacological agents in wholly different cell types.

5.3.2 Reliability of the Liquid Crystal Based Cell Traction Force Transducer

For HaCaT cells cultured on four similar liquid crystal substrates and treated with 0, 5, 10 and 20 ng/ml of TGF-β1 in isolation, the results (Figure 5.5 and Table 5.1) show that the means and mean ranks of the traction force increased proportionally in relation to different concentrations of TGF-β1. One sample Kolmogorov-sminov test show that the quantity of HaCaT cells responded to the controls ($p = 0$), and treatments with 5 ng/ml ($p = 0$), 10 ng/ml ($p = 0$), and 20 ng/ml ($p = 0$) of TGF-β1 (Figure 5.3) were not normally distributed (significant for $p > 0.05$). Therefore, a non-parametric Kruskal-wallis test was performed to analyse differences in the contraction responses of cells to different treatments of TGF-β1. The rank of the mean traction forces generated by HaCaT cells increased proportionally to the treatment with different concentrations of TGF-β1 (Table 5.1).

For three repeats of experiments, the ranking of cell traction forces shows that the same order of ranks from the lowest to the highest occurs accordingly for the control and treatments with 5 ng/ml, 10 ng/ml and 20 ng/ml of TGF-β1, respectively (Table 5.1). The statistical result in Table 5.1 also shows similar mean ranks for each treatment across the three experiments. For control, the mean ranks of tractions forces for all three experiments were 85.90, 103.46 and 84.30 nN, respectively. For 5

ng/ml of TGF-β1 treatment, the mean ranks of tractions forces for all three repeat of experiments were 205.43, 185.31 and 144.57 nN, respectively. For 10ng/ml TGF-β1 treatment, the mean ranks of tractions forces for all three experiments were 235.87, 243.11, and 263.23 nN, respectively. For 20 ng/ml TGF-β1 treatment, the ranks of tractions forces for all three experiments were 274.81, 270.13, and 309.90 nN, respectively.

Table 5.1. Mean ranks for traction forces of HaCaT cells treated with HBSS (control) and with different doses of TGF-β1 obtained from Kruskal-wallis test. N represents the number of cells.

Ranks

	TGFBeta1	N	Mean Rank
EXP1	Control	100	85.90
	5ng/ml	100	205.43
	10ng/ml	100	235.87
	20ng/ml	100	274.81
	Total	400	
EXP2	Control	100	103.46
	5ng/ml	100	185.31
	10ng/ml	100	243.11
	20ng/ml	100	270.13
	Total	400	
EXP3	Control	100	84.30
	5ng/ml	100	144.57
	10ng/ml	100	263.23
	20ng/ml	100	309.90
	Total	400	

Figure 5.5 shows the traction forces (means ± SE) of HaCaT cells cultured on three isolated liquid crystal substrates (LCS) that were treated with TGF-β1 at 0, 5, 10 and 20 ng/ml, respectively. Post-hoc tests by using Mann-whitney test conducted in between control and 5 ng/ml ($p = 0$), 5 ng/ml and 10 ng/ml ($p = 0$), 10 ng/ml and 20 ng/ml ($p = 0.008$) of TGF-β1 for three repeats of experiments show that there were significant differences (significant for $p < 0.05$) in the traction forces of cells treated without and with TGF-β1 at different concentrations as shown in Figure 5.5. In

addition to these results, Cronbach's alpha test shows that the measurement of traction forces using the LCTFT system appeared to have a reasonable internal consistency for $\alpha = 0.714$ (significant for $\alpha > 0.7$). The results indicate that liquid crystal substrates imposed no effects on the measurements and they are able to consistently reproduce similar measurement results.

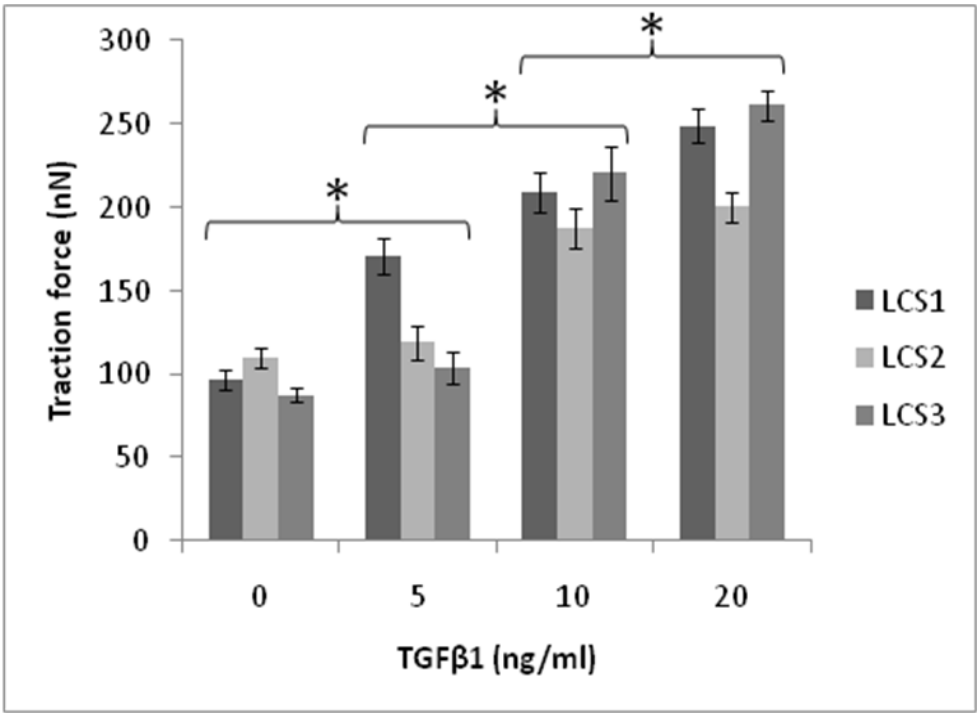

Figure 5.5. Traction forces (means ± SE) of HaCaT cells cultured on three isolated liquid crystal substrates (LCS) that were treated with TGF-β1 at 0, 5, 10 and 20 ng/ml in three repeats of experiment (N = 100 cells per experiment), respectively. Mann-whitney post hoc tests indicate that the treatments between 0 and 5 ng/ml (p = 0), 5 and 10 ng/ml (p = 0), 10 and 20 ng/ml (p = 0.008) are significantly different for p < 0.05. The asterisk * indicates that there is a significant difference in between treatments.

The signaling mechanism associated with the contraction of HaCaT cells induced by TGF-β1 is still under active investigation (Gazel et al., 2006, Alberts and Treisman, 1998, Shen et al., 2001). Although TGF-β1 is a cytokine, overdose of TGF-β1 could lead to skin problems such as hyperkeratosis, tensed skin or even impaired tissue functions

as reported previously (Sellheyer et al., 1993, Coffey et al., 1988). Therefore, in-vitro assays in identifying the cell contraction response in terms of traction forces of cells to different dosages of TGF-β1 is required because the expression of cell traction forces is a manifestation on the intensity of the stress generated within the cells. The LCTFT technique evaluated in this work has demonstrated a consistency and reliability in terms of acquiring repeatable dose responses of HaCaT cells to treatment with different concentrations of TGF-β1. This provides strong evidence that this novel in-vitro single cell based LC assay may have a wider scale of application in the testing of pharmacological agents.

5.4 Summary

This chapter has presented the qualitative and quantitative evaluations of LCTFT system by studying the ability of this assay to differentiate the magnitude of HaCaT cell traction forces in response to different doses of TGF-β1 both. This study shows that the traction forces of cells increased dramatically after treated with TGF-β1 at a threshold higher than 5 ng/ml. This is in good agreement with previous studies examining the effects of TGF-β1 to the formation of stress fibres in keratinocytes. in responding to treatments with different concentrations of TGF-β1, LCTFT has shown considerable reliability and consistency in the measurements of cell traction forces. Nonetheless, LCTFT showed sensitivity to a wide range of traction forces expressed by HaCaT cells. This potentially means that the system may be used to examine traction forces in a range of cells from the poorly contractile to the highly contractile. As such the liquid crystal based LCTFT system may be used to examine the effects of a range of pharmaceutical agents at the single cell level using a range of different cell type.

CHAPTER 6

GENERAL CONCLUSIONS, THESIS CONTRIBUTION AND FUTURE WORK

The end of one journey, the beginning of another…….

6.1 Conclusions

The use of living cells as part of the sensing element in a bio-sensor is gaining growing interest because of the relevant biological responses and high sensitivity to pharmacological agents that directly affect cellular function. These mechano-physiological responses can be directly measured using the displacements induced in soft substrates. The application of these cell-based sensors includes cytochemical sensing, pharmaceutical screening, basic biological research and new drug investigation.

A novel hybridised cell traction force sensing system involving cells and liquid crystals has been successfully developed in this study. In this system, shear sensitive cholesteryl ester liquid crystal that were initially developed for use in liquid crystal displays and in aerodynamic applications, have been used to sense the mechanical forces generated by cells. This study has shown that this liquid crystal is biocompatible, supports cell adhesion and can transduce the mechanical forces exerted by cells into physical displacements or deformation lines in the liquid crystal surface, in which, the length of the cell-induced deformations is related to the magnitude of the forces generated by the cells.

In order to quantify and study the mechanical forces generated by the HaCaT cells and transferred to the liquid crystal substrate, the physical properties of the liquid crystal were profiled by various characterisation techniques. The cholesteryl ester liquid crystals were found to be thermally stable over a wide temperature range (0 – 50 ^{o}C) via differential scanning calorimetry (DSC) and cross-polarising microscopy. The cross-polarising microscopy studies indicated that the cholesteric phase of the cholesteryl ester liquid crystals after incubated in cell culture media at 37 ^{o}C for 24 hours transformed into lyotropic liquid crystals that exhibited a mixture of lamellar,

isotropic and smectic phases. However, these lyotropic systems under defect free conditions were dominated by lyotropic smectic phases due to the self-organisation of the amphiphilic liquid crystal molecules into uniform layers that were interlaced by multi layers of water molecules (see result in Figure 2.19-2.22). The rheological profiling showed that cholesteryl ester based lyotropic liquid crystals (LLC) were characterised by linear viscoelasticity under small shear strain (< 10 %) at low shear rates (< 1 s^{-1}). AFM nano-indentation and spherical indentation measurements both showed similar Young's moduli of 108 ± 19.73 kPa and 110 kPa ± 21.33 kPa (mean ± SD), respectively, for the LLC after incubation in culture media for 24 hours. The Young's modulus was halved for LLC incubated in culture media for 48 hours.

In the cell relaxation experiments, the results show that the formation of deformation lines was due to the bi-axial strains induced by cell tractions in the surface of the liquid crystals. In the context of the time-dependent behaviour, the rheological results indicate that LLC exhibited a reduction in shear and loss moduli after 48 hours in culture media. This was consistent with the qualitative results presented in the in-situ time-dependent rheological studies (see Figure 2.30) and again, supporting the measurements of time-based Young's modulus acquired by spherical indentation (See Figure 2.34). In the cell fixation experiment, the results show that the deformations in the liquid crystal surface did not show significant creep over a four day period which indicate that the viscosity of the liquid crystals in-situ was stable in the cell culture media under constant hydrostatic pressure (see Figure 2.31). Due to the effects of the immersion in cell culture media, the Poisson's ratio of the LLC within 48 hours of incubation in cell culture media was 0.58 as determined by micro-tensile tests. Collectively, the DSC, cross-polarising microscopy, rheology, spherical indentation and micro-tensile experiments showed that the viscoelasticity of the LLC can be affected by

time-dependent factors such as a fluidic environment, incubation period and to minimum extent by incubation temperature. Despite the influences of these time-dependent factors, LLC maintained a linear viscoelasticity at low shear rates (< $1s^{-1}$) and shear strains (< 10 %) and can be stably used if they are incubated in cell culture media at 37 ^{o}C within 48 hours.

LLC seemed to promote cell adhesion and proliferation. Non-motile HaCaT cells were found to induce localised deformation lines around the margin of the cell. The result show that the viscoelastic surface of the liquid crystals is highly sensitive and flexibility to structural or mechanic changes of the adherent cells (see Figure 3.8). The finite response of the liquid crystals to a traction forces at a local region is probably due to the compactly arranged LC molecules in long-range order that only dissipate the energy applied within a finite region, therefore, cell forces induced deformations that were spatially constrained.

The deformation lines around the periphery of the cell might have a relationship with the short circumferential actin filaments arranged tangentially at the margin of the HaCaT cells. Cytochalasin-B and trypsin treatments have confirmed that the deformation lines formed in the liquid crystal surfaces were due to the intracellular forces that were transmitted to the surface via focal adhesions mediated by cell surface integrins. This view was supported by fluorescent staining of the actin filaments that confirmed a diffused arrangement of short actin filaments at the margin of the cell and within the cells (see Figure 3.11d). The Young's modulus of the soft liquid crystals (110 kPa) have induced re-arrangement of the actin cytoskeletons associated with a decrease in cell spreading and changes in cell attachment mediated by a redistribution of focal adhesions. The morphology of cells on the liquid crystal substrate differs greatly from highly spread morphology of cells on hard substrates

such as glass cover slips which has a elastic modulus in GPa range (Figure 3.9c). Previous studies evidenced the effects of substrate stiffness on the cytoskeleton organisation and adhesion of cells (Engler et al., 2004a, Yeung et al., 2005, Engler et al., 2004b). In this work, the liquid crystal substrates had encouraged stable cell adhesions through self-derived ECM proteins (collagen type IV, laminin and fibronectin) and the expression of integrins (α2, α3, α5, and β1). WSPR imaging showed that the stresses exerted by focal adhesions of HaCaT cells on the liquid crystals were uniformly distributed around the periphery of the cells and this was supported by immunostaining studies showing punctuated vinculin and circumferential actin filaments that were expressed at the margins of the cells. Consistent with the structure of actin and spread of vinculin, cells acquired a more rounded morphology when attached to the liquid crystals compared with those grown on hard surfaces of gold substrates in WSPR imaging. Nonetheless, the biocompatibility of the cholesteryl ester liquid crystals strongly supports their suitability as a cell adhesion substrate.

Developing a biosensor which can transduce the traction forces of a single non-motile keratinocyte is challenging because the forces generated by these cells are potentially lower than highly motile cells (Balaban et al., 2006). Thus measuring these forces requires a highly sensitive soft substrate. One of the advantages of using liquid crystal based cell traction force transducer (LCTFT) is the sensitivity of this material to discern the localised cell traction forces and transducing them into clearly separated deformation lines that are linearly correlated with the intensity of the traction forces. Having determined the Young's modulus of the linear viscoelastic liquid crystals and transverse displacements induced by the cell in the liquid crystal surface (obtained by cytochalasin B treatment), the localised traction forces induced by single cells was estimated by using the stress-strain equation ($E = \sigma / \varepsilon$ or $F = E\Delta L / L$) of Hooke's

theorem. In this work, a cell relaxation technique involving cytochalasin-B treatment provided a new means of determining the lateral displacement in the liquid crystal surface which was induced by cells. This longitudinal deformation line was found to be dependent on the lateral shear forces (traction forces) and transverse deformation at a Poisson's ratio of approximately 0.56 ± 0.06 (mean ± SD). After the displacements of the liquid crystals in longitudinal and transverse direction were determined, the traction force was found to be linearly proportional to the displacement induced by cells in both directions. These two relationships of force versus displacement in bi-axial directions (longitudinal and transverse) were determined at 20 nN/μm and 84 nN/μm, respectively. The first derived function of force-longitudinal deformation at 20 nN/μm is useful in estimating the normally distributed traction forces of cell if the length of the linear deformation line formed in the liquid crystal surface is known. The sensitivity of the LCTFT can be inferred from a wide range of traction forces (10 – 140 nN) determined for non-motile keratinocytes. This range of traction forces measured by LCTFT are in good agreement with the traction forces of epithelial cells measured by centrifugal dissociation (Thoumine et al., 1996), AFM cantilever (Sagvolden et al., 1999), micro-patterned cantilever (Roure et al., 2005) and beads labeled PDMS (Mohl et al., 2009) techniques.

Via the relaxation of cells by cytochalasin B treatment and cross section profiling of the deformation line, the cells seemed to impose compressive forces to the local region of the substrate or stress site under the contractions of circumferential actin filaments (see Figure 2.29 and Figure 3.9). The actomyosin contractile activities during the shortening of the actin filaments anchored at the focal adhesions probably created traction forces in opposite directions to the underlying liquid crystal substrate; thus creating a compression effect to a local stress site. This occurrence of compression was

confirmed by using a focal adhesion-liquid crystal finite element model (FEM) in order to study the deformation formed at the stress site. Interestingly, the model showed that the highest stresses were originated from the principal stress planes, and these stresses quadratically decreased towards the centre of a local stress site (Figure 4.11), in which, the stress and deformation profiles indicated a good correlation with the cross section profile of the stratified deformation line measured (Figure 2.29). The simulated traction forces based on the experimental data also showed good agreement with the calculated forces.

A bespoke cell traction force measurements and mapping (CTFM) software was developed to efficiently present the distribution of traction forces for the keratinocytes exerted on the LCTFT (see result in section 4.3.5). Based on the phase contrast images of single HaCaT cells inducing deformation lines, the length of the deformation lines was measured, multiplied by the coefficient of force versus longitudinal deformation (20 nN/μm) of the liquid crystals in the CTFM software. The longitudinal deformation lines were then translated into the proportional traction forces by using the CTFM software. By applying either linear or cubic interpolation fittings to the force data in a Euclidean coordinate system, the user friendly CTFM software generates graphical representations of traction forces for the cell in pseudo colours. A comparison made for the two interpolation methods indicates that a linear interpolation seemed to terminate the traction forces sharply in fitting the force data and it showed a better representation of the localised forces detected by the liquid crystal force transducer. By using calibration images of PDMS measurement gauges and simulation of hypothetical deformation lines over the gauge, the spatial resolution of the CTFM software was determined at 5 μm which is slightly lower than the spatial resolution of the liquid crystal force transducer at about 2 μm. However, the difference in the

resolution of the software and the liquid crystal force transducer did not affect the overall representations of the cell traction forces at a local region.

The CTFM software was proven to show similar and a correlated distribution of traction forces around the periphery of the HaCaT cells for similar length of deformation lines induced under the margin of the cells in the phase contrast images. These traction forces expressed at the periphery of the cells were probably related to the contraction of the short circumferential actin filaments that were mediated via the focal adhesions (see Figure 4.29). In addition to the user-friendliness of the software, another attractive feature of the CTFM software is the versatility to map changes in cell morphologies. Mapping the morphology of cells is really important because morphology reflects the distribution of actin within a cell.

The functionality of coupling the LCTFT and the CTFM software was further examined in the study of keratinocyte migration. Based on the linear elastic behaviour of the liquid crystals, the transducer detected different phases (protrusion, retraction and extension of lateral margins) of cell migration for a keratinocyte at a time interval of 5 minute over a period of 20 minutes (see Figure 4.28). During cell migration, new observations of diminishing deformation lines and appearance of newly formed deformation lines were found at the rear and leading edge of the cell. In this study, the deformation lines formed in the liquid crystal surface that are in perpendicular and oblique directions to the cell margin are probably regulated by the contractile functions of circumferential actin bundle located at the cell margin, while protrusion of the lamellipodia observed might be controlled by the striated parallel stress fibres usually located at the centre region of the HaCaT cells. These results suggest that different regions of the cell may have different functionality in supporting migration of a keratinocyte. In comparison with the traction forces measured for non-motile

keratinocytes, traction forces expressed by a migrating cell are marginally higher with a range of 30 - 160 nN at a migration speed of 0.5 μm/min. These results show that the integrated LCTFT and CTFM system can be used to detect changes in cell generated forces in real time at good spatial resolutions.

Further studies involving the examination of changes in cell forces induced by treatment with TGF-β1, were used to validate the reliability of the LCTFT system. In these studies, it was found that the LCTFT system was able to measure similar mean ranks and means of contraction responses for treatments with different concentrations of TGF-β1. A non-parametric test (Kruskall-wallis) followed by post hoc Mann-whitney tests show that means and mean ranks of the traction forces developed by HaCaT cells after treatment with 0, 5, 10 and 20 ng/m of TGF-β1 increased proportionally with concentrations of TGF-β1, and there were significant differences ($p < 0.05$) in cell traction forces in between the treatments. At a threshold of 5 ng/ml of TGF-β1 treatment, the mean traction forces of the HaCaT cells increased dramatically to 130 nN. This represented an almost two fold increase from the mean traction force of 50 nN expressed by control cells (see Figure 5.2). The alpha coefficient obtained from Cronbach's alpha test for the three repeats of experiment was 0.714, suggesting that traction force measurements result by using LCTFT have demonstrated relatively substantial internal consistency (significant for $\alpha > 0.7$).

6.2 Thesis Contribution

The wrinkle based single cell traction sensing technique based on silicon rubber was developed about three decades ago, but, remains as a qualitative technique because of the chaotic, non-linear and uncorrelated wrinkles of the silicon rubber that were difficult to be quantified (Boutelier et al., 2008, Addae-Mensah and Wikswo,

2008, Beningo, 2002, Ghannam and Esmail, 1998b). Semi-solid liquid crystals were not limited by these problems. Therefore, the main contributions of this thesis are:-

(a) The LCTFT system has advanced and revived previous wrinkle based techniques by showing that the semi-solid LC system can detect localised single cell traction forces generated by poorly contractile cells such as keratinocytes (Balaban et al., 2006) with a high sensitivity and at a high spatial resolution.

(b) The findings obtained from the newly developed LCTFT system have contributed to the understanding of how traction force is involved in driving the mobility of a keratinocyte. Nonetheless, this work has revealed the specific roles played by different facets of the keratinocyte cell body during the translocation of a keratinocyte from the quiescent state on a liquid crystal surface. The combination of LCTFT and CTFM software system is a powerful analytical tool to demonstrate contractility and migration of single keratinocytes, which also has a potential to provide information about the treatments of cells with pharmaceutical drugs in relation to wound healing.

(c) This cell line based traction force measurement assay (LCTFT) can be used for educational purpose to demonstrate single cell contractility which will help to reduce the animal usage in the laboratory.

(d) Nonetheless, LCTFT has demonstrated the feasibility to detect changes of keratinocyte traction forces in response to different concentration of TGF-β1, in which this ability of the LCTFT has not been reported in previous cell traction force measurement technique. Moreover, these responses of cells cultured on the LCTFT correlated well with the observations revealed by the in-vivo physiological response of mice to TGF-β1 (for example, tauted skin of mice was found in response to high dosages of TGF-β1 (Sellheyer K. et al., 1993)).

The merits of using LCTFT technique for cell force sensing are summarised as follows:-

(a) The cholesteryl ester liquid crystal incubated in cell culture media at 37^{o}C within 48 hours are linear viscoelastic and it is suitable to be used to detect cell traction forces.

(b) Cholesteryl ester liquid crystals used in LCTFT showed thermal stability over a wide temperature range (0 - 50 ^{o}C).

(c) Young's modulus of the LCTFT at ~110 kPa is close to the elastic modulus of the skin epidermis determined by using torsion and tensile methods (Takeo, 2007, Hendriks et al., 2006) and this modulus probably provided suitable mechanical signal for the adhesion of keratinocytes cultured on the substrates.

(d) The continuum based LCTFT allows the examination on the contact dispersions of motile and non-motile cells in arbitrary directions, therefore, allowing direct qualitative assessment of the characteristic of cell generated tractions.

(e) Cholesteryl ester based lyotropic liquid crystal is biocompatible and the surface of the liquid crystal was functionalized by the depositions of various endogenous ECM proteins (collagen type-IV, laminin and fibronectin) by the HaCaT cells to form a provisional basement membrane (Kirfel et al., 2002a, Stanley et al., 1982a, O'Toole, 2001).

(f) The LCTFT detects a wide range of traction forces (0 - 200 nN) for polarised and non-polarised cell with a sensitivity down to 10 nN (refer to Table 4.2).

(g) The LCTFT and associated custom-built CTFM software provides a spatial resolution of 2 µm and 5 µm, respectively. Temporal resolution of the LCTFT in detecting traction of a cell was tested at approximately 5 minutes but this is really dependent on the frame rate of a digital camera.

(h) The measurement of traction forces by LCTFT and CTFM can be performed instantly based on a single phase contrast image of a cell adhering on the LCTFT, without the need of a null-force image (PAA gel embedded with fluorescence microbeads) as required in previous developed techniques (Munevar et al., 2001, Oliver et al., 1998a).

6.3 Suggestions for Future Work

This work has mainly focused on characterising and developing the LCTFT system. The potential of this biosensor can be further improved from three aspects: physical property enhancement of the liquid crystals, software development, and further applications in biological studies.

6.3.1 Physical Property Enhancement and Software Development

(a) **Physical strength**: In order to improve the physical strength of the liquid crystals used, colloidal particles can be included to enhance the linear elastic response range of the cholesteric liquid crystals as suggested in (Ramos et al., 2002). This work suggests the use of graphite powder or carbon nano-tubes that are biocompatible and having high strength to weight ratio (Fan et al., 2010), but the impregnation of these particles in the liquid crystals needs to be controlled at defined depths in order to avoid interactions with the cells.

(b) **Video based cell traction force tracking system**: Current version of CTFM software allows frame based analysis of cell migration. Future version of this software may include video tracking facility for displaying the distribution of cell traction forces in pseudo-colours, provided that, a higher frame rate camera system is installed to the phase contrast microscope system. This will provide

more insights into the effects of an induced solution to the mechano-physiological changes of a cell.

6.3.2 Cell Biological Applications

(a) **Other cell types**: The current study of cell traction force did not include highly contractile cells. It would be interesting to compare the traction forces of keratinocyte to Smooth Muscle Cells or Fibroblast.

(b) **Study on the contraction responses of keratinocytes to other cytokines:** Contraction responses of keratinocytes to different doses of TGF-β1 have been established. Similar experiments that include the analysis of cell traction force fields using CTFM software could be performed to study individual or combined dose responses of TGF-β2 and TGF-β3 to the keratinocytes.

(c) **Combine the study of cell traction force and biological structural changes**: Live cell staining agents such as green fluorescence proteins (GFP) against actin and vinculin can be applied in future to study the structural re-organisation of the focal adhesions and actin filaments in correlation with the cell traction forces in real-time which would provide new information about the cell responses during the generation of cell reaction forces.

(d) **Application of actin polymerisation inhibitor at a local region of cell**: Injection of small concentrations of Rac, Rho and Ras inhibitors could locally disrupt the actin cytoskeleton of migrating cells, and therefore disrupt localised or global actin reorganization. This disruption may be monitored by using the LCTFT. Therefore, this would provide novel information about the functions of Rac, Rho and Ras in regulating the traction forces of keratinocytes.

REFERENCES

ABBOTT, N. L., N., L., MURPHY, C. J., CHING, L.-L. & JANG, C.-H. (2005) Engineering interfaces to cells using synthetic liquid crystals. *European Cells and Materials* 10**,** CS1.

ABSOLOM, D., R.,, LAMBERTI, F., V.,, POLICOVA, Z., ZINGG, W., OSS, C., J. VAN, & NEUMANN, A. W. (1983) Surface Thermodynamics of Bacterial Adhesion. *Applied and Environmental Microbiology,* 46**,** 90-97.

ADDAE-MENSAH, K. & WIKSWO, J. (2008) Measurement techniques for cellular biomechanics in vitro. *Experimental Biology and Medicine (Maywood),* 233**,** 792-809.

AHEARNE, M., YANG, Y., EL HAJ, A. J., THEN, K. Y. & LIU, K.-K. (2005) Characterizing the viscoelastic properties of thin hydrogel-based constructs for tissue engineering applications. *Journal of The Royal Society of Interface,* 2**,** 455-463.

AKIHO, H., BLENNERHASSETT, P., YIKANG, D. & COLLINS, S. M. (2002) Role of IL-4, IL-13, and STAT6 in inflammation-induced hypercontractility of murine smooth muscle cells. *American journal of physiology,* 45**,** G226-G232.

ALBERTS, A. S. & TREISMAN, R. (1998) Activation of RhoA and SAPK/JNK signalling pathways by the RhoA-specific exchange factor mNET1. *The EMBO Journal,* 17**,** 4075–4085.

ALBERTS, B., JOHNSON, A., LEWIS, J., RAFF, M., ROBERTS, K. & WALTER, P. (2002) *Molecular Biology of the Cell*, Garland Science.

ALCANTARA, M. R. & FERNADES JR., E. G. (2002) Twenty years of research on cholesteric lyotropic liquid crystals at the chemistry institute of the University of Sao Paulo. *Brazillian Journal of Physics,* 32**,** 509-515.

ANTCZAK, S. & ANTCZAK, G. (2001) *Cosmetics unmasked*, Thorsons, HarperCollins.

ASHCROFT, G. S., YANG, X., GLICK, A. B., WEINSTEIN, M., LETTERIO, J. L., MIZEL, D. E., ANZANO, M., GREEWELL-WILD, T., WAHI, S. M., DENG, C. & ROBERTS, A. B. (1999) Mice lacking Smad3 show accelerated wound healing and an impaired local inflammatory response. *Nature Cell Biology,* 1**,** 260-266.

ASHER, S. A. & PERSHAN, P. S. (1979) Alignment and defect structures in oriented phosphatidylcholine multilayers. *Biophysical Journal* 27**,** 393-421.

AUMAILLEY, M., NURCOMBEG, V., EDGAR, D., PAULSSON, M. & TIMPL, R. (1987) The cellular Interactions of laminin fragments. *The Journal of Biological Chemistry,* 262**,** 11532-11538.

BALABAN, N., SCHWARZ, U., RIVELINE, D., GOICHBERG, P., TZUR, G., SABANAY, I., MAHALU D, S. S., BERSHADSKY, A., ADDADI, L. & GEIGER, B. (2001) Force and focal adhesion assembly: a close relationship studied using elastic micropatterned substrates. *Nature Cell Biology,* 3.

BALABAN, N. Q., SCHWARZ, U. S. & GEIGER, B. (2006) Measurement of cellular contractile forces using patterned elastomer. IN CELIS, J. E. (Ed.) *Cell biology: a laboratory handbook, Volume 1.* Elsevier.

BAO, G. & SURESH, S. (2003) Cell and molecular mechanics of biological materials. *Nature Materials,* 2**,** 715-725.

BAREL, A., COURAGE, W. & CLARYS, P. (1995) Suction method for measurement of skin mechanical properties: the cutometer. IN SERUP, J. A. J., G.B.E. (Ed.) *Handbook of Non-Invasive Methods and the skin. .* Boca Raton, CRC Press.

BARNES, H. A., HUTTON, J. F. & WALTERS, K. (1989) *An introduction to rheology,* Amsterdam, Elsevier.

BARTKOVA, J., GRØN, B., DABELSTEEN, E. & BARTEK, J. (2003) Cell-cycle regulatory proteins in human wound healing. *Archives of Oral Biology,* 48**,** 125—132.

BASAPPA, G., SUNEEL, KUMARAN, V., NOTT, P. R., RAMASWAMY, S., NAIK, V. M. & ROUT, D. (1999) Structure and rheology of the defect-gel states of pure and particle-dispersed lyotropic lamellar phases. *The European Physical Journal B,* 12**,** 269-276.

BAUMANN, H. & DOYLE, D. (1979) Effect of trypsin on the cell surface proteins of hepatoma tissue culture cells. *The Journal of Biological Chemistry,* 254**,** 3935-3946.

BECK, K., HUNTER, I. & ENGEL, J. (1990) Structure and function of laminin: anatomy of a multidomain glycoprotein. *The FASEB journal,* 4**,** 148-160.

BECKER, W., HETTICH, B. S. & HOENICKE, P. (2001) Toxicological and ecotoxicological investigations of liquid crystals and disposal of LCDs IN KGAA, M. (Ed. *Liquid Crystals Division and Institute of Toxicology 64271.* Darmstadt, Germany.

BEHRENDS, J. C. & FERTIG, N. (2007) Neuromethods. IN WALZ, W. (Ed.) *Patch clamp analysis.* 2nd ed.

BENINGO, K., LO, C. & WANG, Y. (2002) Flexible polyacrylamide substrata for the analysis of mechanical interactions at cell-substratum adhesions. *Methods Cell Biol.,* 69**,** 325-339.

BENINGO, K. A. (2002) Flexible substrata for the detection of cellular traction forces. *Trends in Cell Biology,* 12**,** 79-84.

BENNETT, M. R., M & PETTIGREW, A. G. (1974) The formation of synapses in striated muscle during development. *Journal of Physiology,* 241**,** 515-545.

BERGHAUSEN, J., ZIPFEL, J., DIAT, O., NARAYANAN, T. & RICHTERING, W. (2000) Lamellar phases under shear : variation of the layer orientation across the couette gap. *Phys. Chem. Chem. Phys,* 2**,** 2623-3626.

BERSHADSKY, A., BALABAN, N. & GEIGER, B. (2003) Adhesion-dependent cell mechanosensitivity. *Annu Rev Cell Dev Biol.,* 19**,** 677-695.

BETZ. W. J. & SAKMANN, B. (1971) "Disjunction" of frog neuromuscular synapses by treatment with proteolytic enzymes. *Nature New Biology,* 232**,** 94-95.

BHOWMICK, N. A., GHIASSI, M., BAKIN, A., AAKRE, M., LUNDQUIST, C. A., ENGEL, M. E., ARTEGA, C. L. & MOSES, H. L. (2001) Transforming growth factor-β1 mediates epithelial to mesenchymal transdifferentiation through a RhoA-dependent mechanism. *Molecular Biology of the Cell,* 12**,** 27-36.

BIRCHALL, L. S., ULIJN, R. V. & WEBB, S. J. (2008) A combined SPS-LCD sensor for screening protease specificity. *Chemistry Communication,* 25**,** 2861-2863.

BITAR, K. N. & MAKHLOUF, G. M. (1985) Measurements of function in isolated single smooth muscle cells. *Am J Physiol Gastrointest Liver Physiol* 250**,** G357-360.

BOLAND , S., BOISVIUX-ULRICH, E., HOUCINE, O., BAEZA-SWUIBAN, A., POUCHELET, M., SCHOEVAERT, D. & MARANO, F. (1996) TGFβ1 promotes actin cytoskeleton reorganization and migratory phenotype in epithelial tracheal cells in primary culture. *Journal of cell Science,* 109**,** 2207-2219.

BOLOGNIA, J. L., JORIZZO, J. L. & RAPINI, R. P. (2004) *Dermatology,* Spain, Mosby.

BORON, W. F. & BOULPAEP, E. L. (2004) *Medical Physiology: A Cellular And Molecular Approach*, Elsevier/Saunders.

BOUTELIER, D., SCHRANK, C. & CRUDEN, A. (2008) Power-law viscous materials for analogue experiments: New data on the rheology of highly-filled silicone polymers. *Journal of Structural Geology* 30 341-353.

BOYD, R. H. (1993) *The science of polymer molecules: an introduction concerning the synthesis, structure and properties of the individual molecules that constitute polymeric materials. ,* Cambridge, Camb. U. P.

BRAKE, J. M., DASCHNER, M. K., LUK, Y.-Y. & ABBOTT, N. L. (2003) Biomolecular interactions at phospholipid-decorated surfaces of liquid crystals. *Science,* 302**,** 2094-2097.

BRITLAND, S., PERRIDGE, C., DENYER, M., MORGAN, H., CURTIS, A. & WILKINSON, C. (1996) Morphogenetic guidance cues can interact synergistically and hierarchically in steering nerve cell growth. *Experimental Biology Online,* 1**,** 1-15.

BUCK, C. A. & HORWITZ, A. F. (1987) Cell surface receptors for extracellular matrix molecules. *Annual Review of Cell Biology,* 3**,** 179-205.

BURRIDGE, K., CHRZANOWSKA-WODENICKA, M. & ZHONG, C. (1997) Focal adhesion assembly. *Trends in Cell Biology,* 7**,** 342-347.

BURRIDGE, K. & CHRZANOWSKA-WODNICKA, M. (1996) Focal adhesions, contractility and signaling. *Annual Review of Cell and Developmental Biology,* 12 463-519

BURRIDGE, K., FATH, K., KELLY, T., NUCKOLLS, G. & TURNER, C. (1986) Focal adhesions: transmembrane junctions between the extracellular matrix and the cytoskeleton. *Annual Review of Cell Biology,* 4**,** 487-525.

BURTON, K., PARK, J. H. & TAYLOR, D. L. (1999) Keratocytes generate traction forces in two phases. *Molecular Biology of the Cell,* 10**,** 3745-3769.

BURTON, K. & TAYLOR, D. L. (1997) Traction forces of cytokinesis measured with optically modified substrata. *Nature,* 385**,** 450-454.

BUSATO, A. P., RIECHER, F., DOMINGUES, R. & SILVEIRA, J. L. M. (2009) Rheological properties of thermally xyloglucan gel from the seeds of Hymenaea courbaril. *Materials Science and Engineering C,* 29**,** 410-414.

CAMPBELL, B. H., CLARK, W. W. & WANG, J. H.-C. (2003) A multi-station culture force monitor system to study cellular contractility *Biomechanics,* 36**,** 137-140.

CAVEY, M. & LECUIT, T. (2009) Molecular bases of cell–cell junctions stability and dynamics. *Cold Spring Harbor Perspective of Biology,* 1**,** 1-18.

CHAKRABARTY, K., HEATON, M., DALLEY, A., DAWSON, R., FREEDLANDER, E., KHAW, P. & MAC NEIL, S. (2001) Keratinocyte-driven contraction of reconstructed human skin. *Wound Repair Regeneration,* 9**,** 95-106.

CHANDRASEKHAR, S. (1992) Liquid Crystals. *Cambridge University Press, Second Edition***,** 1, 12.

CHENG, L.-L., LUK, Y.-Y., CHRISTOPHER, J. M., A. ISRAEL, B. & ABBOTT, N. L. (2005) Compatibility of lyotropic liquid crystals with virus and mammalian cells that support the replication of virus. *Biomaterials* 26**,** 7173-7182.

CHOI, M. C., PFOH, T., WEN, Z., LI, M. Y., KIM, W., ISRAELACHVILLI, J. N. & SAFINYA, C. R. (2004) Ordered patterns of liquid crystal toroidal defects by microchannel confinement. *Proceedings of the National Academy Sciences of the United States of America,* 101**,** 17340-17344.

CLEARY, E. G. & GIBSON, M. A. (1983) Elastin-associated microfibrils and microfibrillar proteins. *International Review of Connective Tissue Research,* 10**,** 97-209.

CLOYD, J. M., MALHOTRA, N. R., WENG, L., CHEN, W., MAUCK, R. L. & ELLIOTT, D. M. (2007) Material properties in unconfined compression of human nucleus pulposus, injectable hyaluronic acid-based hydrogels and tissue engineering scaffolds. *European Spine Journal,* 16**,** 1892-1898.

COFFEY, R. J., BASCOM, C. C., SIPES, N. J., GRAVES-DEAL, R., WEISSMAN, B. E. & MOSES, H. (1988) Selective inhibition of growth-related gene expression in murine keratinocytes by transforming growth factor β. *Molecular and Cellular Biology,* 8**,** 3088-3093.

COHEN, L. B. & SALZEBERG, B. M. (1978) *Optical measurement of membrane potential,* Berliln-Heidelberg, Springer.
COLLINGS, P. J. (2002) *Liquid crystals: nature's delicate phase of matter*, Princeton University Press.
COLLINGS, P. J. & PATEL, J. S. (1997) *Handbook of Liquid Crystal Research*, Oxford University Press, Oxford.
CRAMER, L. P. (2010) Forming the cell rear first: breaking cell symmetry to trigger directed cell migration. *Nature Cell Biology,* 12**,** 628-632.
CRANEFIELD, P. & HOFFMAN, B. (1958) Electrophysiology of single cardiac cells. *Physiological Reviews,* 38**,** 41-76.
CROSS, K. J. & MUSTOE, T. A. (2003) Growth factors in wound healing. *Surgical Clinics of North America,* 83**,** 531-545.
CURTIS, A. S. G. (2004) Small is beautiful but smaller is the aim: review of a life of research. *European Cells and Materials,* 8**,** 27-36.
DALLOT, E., POUCHELETB, M., GOUHIERB, N., CABROLC, D., FERRÉA, F. & BREUILLER-FOUCHÉ, M. (2003) Contraction of cultured human uterine smooth muscle cells after stimulation with endothelin-1 *Biology of Reproduction,* 68**,** 937-942.
DECLINE, F., OKAMOTO, O., MALLEIN-GERIN, F., HELBERT, B., BERANUD, J., RIGAL, D. & ROUSSELLE, P. (2003) Keratinocyte motility induced by TGF-beta1 is accompanied by dramatic changes in cellular interactions with laminin 5. *Cell motility and the cytoskeleton,* 54**,** 64-80.
DECLINE, F. & ROUSSELLE, P. (2001) Keratinocyte migration requires alpha2beta1 integrin mediated interaction with the laminin 5 gamma 2 chain. *Journal of Cell Science,* 114**,** 811-823.
DELVOYE, P., WILIQUET, P., LEVÊQUE, J., NUSGENS, B. & LAPIÈRE, C. (1991) Measurement of mechanical forces generated by skin fibroblasts embedded in a three-dimensional collagen gel. *Investigative Dermotology,* 97**,** 898-902.
DEMBO, M., OLIVER, T., ISHIHARA, A. & JACOBSON, K. (1996) Imaging the traction stresses exerted by locomoting cells with the elastic subtratum method. *Biophysical Journal,* 70**,** 2008-2022.
DENEFLEA, J.-P., LECHAIREA, J.-P. & ZHUA, Q.-L. (1987) Cultured epidermis influences the fibril organization of purified type I collagen gels *Tissue and Cell,* 19**,** 469-478.
DEUGNIER, M.-A., TEULIÈRE, J., FARALDO, M. M., THIERY, J. P. & GLUKHOVA, M. (2002) The importance of being a myoepithelial cell. *Breast Cancer Research* 4.
DIERKING, I. (2003) *Textures of Liquid Crystals*, Wiley-VCH.
DIMITRIADIS, E. K., HORKAY, F., MARESCA, J., KACHAR, B. & CHADWICK, R. S. (2002) Determination of Elastic Moduli of Thin Layers of Soft Material Using the Atomic Force Microscope. *Biophysical Journal,* 82**,** 2798-2810.
DIRIDOLLOU, S., PATAT, F., GENS, F., VAILLANT, L., BLACK, D., LAGARDE, J., GALL, Y. & BERSON, M. (2000) In vivo model of the mechanical properties of the human skin under suction. *Skin Research and Technology,* 6**,** 214-221.
DISCHER, D. E., JANMEY, P. & WANG, Y.-L. (2005) Tissue cells feel and respond to the stiffness of their substrate. *Science,* 310**,** 1139-1143.
DOERNER, M. F. & NIX, W. D. (1986) A method for interpreting the data from depth-sensing indentation instruments. *Journal of Material Research,* 1**,** 601-609.
DOLE, M. (1941) *The glass electrode : methods, applications and theory*, Wiley.
DONALD, B. J. M. (2007) *Practical stress analysis with finite elements,* Dublin, Glasnevin publishing.

DUNMUR, D. A., FUKUDA, A. & LUCKHURST, G. R. (2001) *Physical Properties of Liquid Crystals: Nematic,* London, UK. The Institution of Engineering and Technology.

DZAMBA, B. J., BOLTON, M. & DESIMONE, D. W. (2001) The integrin family of cell adhesion molecules. IN BERKERLY, M. (Ed.) *Cell adhesion.* Oxford, Oxford University Press.

EASTWOOD, M., PORTER, R., KHAN, U., MCGROUTHER, G. & BROWN, R. (1996) Quantitative analysis of collagen gel contractile forces generated by dermal fibroblasts and the relationship to cell morphology. *Cellular Physiology,* 166**,** 33-42.

ENGLER, A., BACAKOVA, L., NEWMAN , C., HATEGAN, A., GRIFFIN, M. & DISCHER, D. (2004a) Substrate compliance versus ligand density in cell on gel responses. *Biophysical Journal,* 86**,** 617-628.

ENGLER, A. J., GRIFFIN, M. A., SEN, S., BÖNNEMANN, C. G., SWEENEY, H. L. & DISCHER, D. E. (2004b) Myotubes differentiate optimally on substrates with tissue-like stiffness pathological implications for soft or stiff microenvironments. *The Journal of Cell Biology,* 166**,** 877-887.

EVEN, C., M. IMP´EROR-CLER & PIERANSKI., P. (2006) Exploring the facets of "soft crystals" using an atomic force microscope. *The European Physical Journal E,* 20**,** 89-98.

FAGAN, M. J. (1992) *Finite element analysis: theory and practice,* Singapore, Longman.

FAIRHURST, C. E., FULLER, S., GRAY, J., HOLMES, M. C. & TIDDY, G. J. T. (1998) *Lyotropic Surfactant Liquid Crystals,* Weinheim, Wiley-VCH.

FAN, H., WANG, L., ZHAO, K., LI, N., SHI, Z., GE, Z. & JIN, Z. (2010) Fabrication, mechanical properties, and biocompatibility of graphene-reinforced chitosan composites, *Biomacromolecules,* 11**,** 2345-51.

FANG, J., MA, W., JONATHAN, V. S. & R., S. (2003) Imaging biological cells using liquid crystals. *Langmuir,* 19**,** 2865-2869.

FARQUHAR, M. G. & PALADE, G. E. (1963) Junctional complex in various epithelia. *Journal of Cell Biology,* 17**,** 375-412.

FASTIER, F. N. & REID, C. S. W. (1949) "Constant flow" organ-bath technique. *British Journal of Pharmacology,* 4**,** 109-110.

FEINGOLD, K. R. (2007) The importance of lipids in cutaneous function. *Journal of Lipid Research,* 48**,** 2529-2530.

FERGASON, J. L., GOLDBERG, N. N. & JONES, C. H. (1965) Detection of liquid crystal gases. *Technical Report No. RADC-TR-64-569.* New York, Rome Air Development Center.

FERRY, J. D. (1948) Viscoelastic properties of polymer solutions. *Journal of Research of the National Bureau of Standards,* 41**,** 53-61.

FRANK, F. C. (1958) Liquid crystals: on the theory of liquid crystals. *Discuss Faraday Society***,** 19-28.

FREYMAN, T. M., YANNAS, I. V., YOKOO, R. & GIBSON, L. J. (2001) Fibroblast contraction of a collagen-GAG matrix. *Biomaterials,* 22**,** 2883-2891.

FROMHERZ, P. (2003) Semiconductor chips with ion channels, nerve cells and brain. *Physica E,* 16**,** 24-34.

FURUSE, M., FUJITA, K., HIIRAGI, T., FUJIMOTO, K. & TSUKITA, S. (1998) Claudin-1 and -2: novel integral membrane proteins localizing at tight junctions with no sequence similarity to occludin. *Journal of Cell Biology,* 141**,** 1539-1540.

GAILIT, J., WELCH, M. P. & CLARK, R. A. F. (1994) TGF-β1 stimulates expression of keratinocyte integrins during re-epithelialization of cutaneous wounds. *The Journal of Investigative Dermatology,* 103**,** 221-227.

GANTER, B., TUGENDREICH, S., CPEARSON, E. I., AYANOGLU, E., BAUMHUETER, S. & BRADY, L. (2005) Development of a large-scale chemogenomics database to improve drug candidate selection and to understand mechanisms of chemical toxicity and action *Journal of Biotechnology,* 119**,** 219-244

GANZ, A., LAMBERT, M., SAEZ, A., SILBERZAN, P., BUGUIN, A., MÈGE, R. & LADOUX, B. (2006) Traction forces exerted through N-cadherin contacts. *Biology of the cell* 98**,** 721-730.

GARLICK, J. A. & TAICHMAN, L. B. (1994) Effect of TGF-β1 on re-epithelialization of human keratinocytes in vitro: an organotypic model. *The Journal of Investigative Dermatology,* 103**,** 554-559.

GAWKRODGER, D. (2003) *Dermatology: an illustrated color text,* Edinburg, Churchill livingstone.

GAZEL, A., BANNO, T., WALSH, R. & BLUMENBERG, M. (2006) Inhibition of JNK Promotes Differentiation of Epidermal Keratinocytes. *The Journal of Biological Chemistry,* 281**,** 20530-20541.

GEIGER, B. & BERSHADSKY, A. (2001) Assembly and mechanosensory function of focal contacts *Current Opinion in Cell Biology,* 13**,** 584-592.

GEIGER, B. & BERSHADSKY, A. (2002) Exploring the neighborhood: adhesion-coupled cell mechanosensors. *Cell Press Journal,* 110**,** 139-142.

GEIGER, B., BERSHADSKY, A., PANKOV, R. & YAMADA, K. M. (2001) Transmembrane extracellular matrix-cytoskeleton crosstalk. *Nature Reviews Molecular Cell Biology,* 2**,** 793-805.

GEIGER, B. & GINSBER, D. (1991) The cytoplasmic domain of adherens-type junctions. *Cell Motility and the Cytoskeleton,* 20**,** 1-6.

GENNES, P. G. (1974) The Physics of Liquid Crystals. *The International Series of Monographs on Physics, Clarendon Press, Oxford***,** 6.

GHANNAM, M. T. & ESMAIL, M. N. (1998a) Rheological properties of aqueous polyacrylamide solutions. *Journal of Applied Polymer Science,* 69**,** 1587-1597.

GHANNAM, M. T. & ESMAIL, M. N. (1998b) Rheological Properties of Poly(dimethylsiloxane). *Indian Engineering Chemistry Research* 37**,** 1335-1340.

GLOUSHANKOVA, N. A., ALIEVA, N. A., KRENDEL, M. F., BONDER, E. M., FEDER, H. H., VASILIEV, J. M. & GELFAND, I. M. (1997) Cell-cell contact changes the dynamics of lamellar activity in nontransformed epitheliocytes but not in their ra-transformed descendants. *Proceedings of the National Academy Sciences of the United States of America,* 94**,** 879-883.

GOFFIN, J. M., PITTET, P., CSUCS, G., J LUSSI, O. W., MEISTER, J.-J. & HINZ, B. (2006) Focal adhesion size controls tension-dependent recruitment of smooth muscle actin to stress fibers *The Journal of Cell Biology,* 172**,** 259-268.

GOTTE, L. & SERAFINI-FRACASSINI, A. (1963) Electron microscope observations on the structure of elastin. 3**,** 247-251

GRAY, S., TITZE, I., ALIPOUR, F. & HAMMOND, T. (2000) Biomechanical and histologic observations of vocal fold fibrous proteins. *The Annal Otology, Rhinology, Laryngology* 109**,** 77-85.

GREEN, K. & JONES, J. (1996) Desmosomes and hemidesmosomes: structure and function of molecular components. *The FASEB Journal,* 10**,** 871-881.

GRIFFTHS, J. S. (1988) Preparation of pressure sensitive liquid crystals. Available: www.chymist.com/Liquid%20Crystals.pdf [Accessed 15 March 2011].

GROSS, G. G., ROCHA-MIRANDA, C. E. & BENDER, D. B. (1972) Visual properties of neurons in inferotemporal cortex of the macaque. *Journal of Neurophysiology,* 35**,** 96-111.

GROSS, G. W., RIESKE, E., KREUTZBERG, G. W. & MEYER, A. (1977) A new fixed-array multi-microelectrode system designed for long-term monitoring of extracellular single unit neuronal activity in vitro *Neuroscience Letters,* 6**,** 101-105.

GUMBINER, B. M. (1996) Cell Adhesion:The Molecular Basis of Tissue Architecture and Morphogenesis. *Cell* 84**,** 345-357.

GUPTA, V. K., SKAIFE, J. J., DUBROVSKY, T. B. & ABBOTT, N. L. (1998) Optical amplification of ligand-receptor binding using liquid crystals. *Science,* 279**,** 2077-2080.

HALL, A. (1998) Rho GTPases and the actin cytoskeleton. *Science* 279**,** 509-514.

HALL, A. (2005) Rho GTPases and the control of cell behaviour. *Biochemical Society Transactions,* 33**,** 891-895.

HARA, Y., KUBOTA, M. & SZURSZEWSKI, J. H. (1986) Electrophysiology of smooth muscle of the small intestine of some mammals. *Journal of Physiology,* 372**,** 501-520.

HARLEY, B. A., FREYMAN, T. M., WONG, M. Q. & GIBSON, L. J. (2007) A New Technique for Calculating Individual Dermal Fibroblast Contractile Forces Generated within Collagen-GAG Scaffolds. *Biophysical Journal,* 93**,** 2911-2922.

HARRIS, A., WILD, P. & STOPAK, D. (1980) Silicone rubber substrata: a new wrinkle in the study of cell locomotion *Science,* 208**,** 177-179.

HARRISON, C. A., HEATON, M. J., LAYTON, C. M. & MAC NEIL, S. (2005) Use of an in vitro model of tissue-engineered human skin to study keratinocyte attachment and migration in the process of reepithelialization. *Wound Repair and Regeneration,* 14**,** 203-209.

HAY, E. D. (1981) Extracellular matrix. *The Journal of Cell Biology,* 91**,** 205s-233s.

HEIDA, Y., IWAI, K., MORITA, T. & NAKANISHI, Y. (1996) Mouse embryonic submandibular gland epithelium loses its tissue integrity during early branching morphogenesis. *Developmental Dynamics* 207**,** S86-403.

HEINO, J. (2007) The collagen family members as cell adhesion proteins. *Bioessays,* 29**,** 1001-1010.

HELFRICH, W. (1994) Lyotropic lamellar phases. *Journal of Physics: Condensed Matter,* 6**,** A79-A92.

HENDRIKS, F. M. (2005) *Mechanical behaviour of human epidermal and dermal layers invivo,* Eindhoven, Technische Universiteit Eindhoven.

HENDRIKS, F. M., BROKKEN, D., OOMENS, C. W. J., BADER, D. L. & BAAIJENS, F. P. T. (2006) The relative contributions of different skin layers to the machanical behavior of human skin in vivo using suction experiment. *Medical Engineering & Physics,* 28**,** 259-266.

HENRY, G., LI, W., GARNER, W. & WOODLEY, D. T. (2003) Migration of human keratinocytes in plasma and serum and wound re-epithelialisation *Lancet* 361**,** 574-576.

HILLNER, E. & STEFANOU, S. (2004) Making a valve in PDMS. *Experimental BioPhysics Mini Symposium.* PosLab (C368), Solid State Physics, LTH, Lund.

HILTON, H. H. & YI, S. (1998) The significance of (an) isotropic viscoelastic poisson ratio stress and time dependencies. *International Journal of Solids and Structures,* 35**,** 3081-3095.

HINZ, B. & GABBIANI, G. (2003) Mechanisms of force generation and transmission by myofibroblasts. *Current Opinion in Biotechnology,* 14**,** 538-546.

HODGKIN, A. L. (1937) Evidence for electrical transmission in nerve. Part I. *Journal of Physiology,* 90**,** 183-210.

HODGKIN, A. L. & KEYNES, R. D. (1955) Active transport of cations in giant axons from Sepia and Loligo. *Journal of Physiology,* 128**,** 28-60.

HOOK, M., KJELLEN, L., JOHANSSON, S. & ROBINSON, J. (1984) Cell-surface glycosaminoglycans. *Annual Review of Biochemistry,* 53**,** 847-869.

HORWITZ, A. R. & PARSONS, J. T. (1999) Cell migration-movin' on. *Science,* 286**,** 1102-1103.

HOTULAINEN, P. & LAPPALAINEN, P. (2006) Stress fibers are generated by two distinct actin assembly mechanisms in motile cells. *Journal of Cell Biology,* 173**,** 383-394.

HWANG, J. J., IYER, S. N., LI, L.-S., CLAUSSEN, R., HARRINGTON, D. A. & I., S. (2002) Self-assembling biomaterials: Liquid crystal phases of cholesteryl oligo(l-lactic acid) and their interactions with cells *Proceedings of National Academy of United States,* 99**,** 9662-9667.

HYDE, S. (2001) Identification of lyotropic liquid crystalline mesophase. IN HOLMBERG, K. (Ed.) *Handbook of applied surface and colloid chemistry.* New York, John Wiley & Sons, ltd.

HYNES, R. O. (2002) Integrins: bidirectional, allosteris signaling machines. *Cell,* 110**,** 673-687.

HYNES, R. O. & YAMADA, K. M. (1982) Fibronectins: multifunctional modular glycoproteins. *The Journal of Cell Biology* 95**,** 369-377.

IM, S. H. & HUANG, R. (2005) Evolution of wrinkles in elastic-viscoelastic bilayer thin films. *Journal of Applied Mechanics,* 722**,** 955-961.

JACOBSON-KRAM, D. & MILLS, G. (2008) Leveraging exploratory investigational new drug studies to accelerate drug development. *Clinical Cancer Research,* 14**,** 3670-3674.

JAMIL, M. M. A., DENYER, M. C. T., YOUSEFFI, M., BRITLAND, S. T., LIU, S., SEE, C. W., SOMEKH, M. G. & ZHANG, J. (2008) Imaging of the cell surface interface using objective coupled widefield surface plasmon microscopy. *Journal of Structural Biology,* 164**,** 75-80.

JEONG, H.-W. & KIM, I.-S. (2004) TGF-β1 enhances βig-h3-mediated keratinocyte cell migration through the α3β1 integrin and PI3K *Journal of Cellular Biochemistry,* 92**,** 770-780.

JURADO, C., HASERICK, J. R. & LEE, J. (2005) Slipping or gripping? Fluorescent speckle Microscopy in fish keratocytes reveals two different mechanisms for generating a retrograde flow of actin. *Molecular Biology of the Cell,* 16**,** 507-518.

KAINULAINEN, T., HÄKKINEN, L., HAMIDI, S., LARJAVA, K., KALLIOINEN, M., PELTONEN, J., SALO, T., LARJAVA, H. & OIKARINEN, A. (1998) Laminin-5 expression is independent of the injury and the microenvironment during reepithelialization of wounds. *The Journal of Histochemistry and Cytochemistry,* 46**,** 353-360.

KANG, H.-W. & MURAMATSU, H. (2008) Monitoring of cultured cell activity by the quartz crystal and the micro CCD camera under chemical stressors. *Biosensors and Bioelectronics,* 24**,** 1318-1323.

KARAMICHOS, D., BROWN, R. A. & MUDERA, V. (2006) Complex dependence of substrate stiffness and serum concentration on cell-force generation. *Biomedical Materials Research Part A,* 78A**,** 407-415.

KIM, J. P., ZHANG, K., KRAMER, R., SCHALL, T. & WOODLEY, D. (1992) Integrin receptors and RGD sequences in human keratinocyte migration: unique anti-migratory function of alpha 3 beta 1 epiligrin receptor. *Journal of Investigative Dermatology,* 98**,** 764-770.

KIM, K.-H., CHO, J.-S., CHOI, D.-J. & KOH, S.-K. (2001) Hydrophilic group formation and cell culturing on polysytrene petri-dish modified by ion-assisted reaction. *Nuclear Instruments & Methods in Physics Research B,* 175-177**,** 542-547.

KIM, T. K., KIM, J. K. & JEONG, O. C. (2011) Measurement of nonlinear mechanical properties of PDMS elastomer. *Journal of Microeletronic Engineering***,** [In Press].

KIRFEL, G., BORM, B., RIGORT, A. & HERZOG, V. (2002) The secretory amyloid precursor protein is a motogen for human epidermal keratinocytes. *European Journal of Cell Biology* 81**,** 664-676.

KIRFEL, G. & HERZOG, H. (2004) Migration of epidermal keratinocytes: mechanisms, regulation, and biological significance. *Protoplasma,* 223**,** 67-78.

KIRFEL, G., RIGORT, A., BORM, B., SCHULTE, C. & HERZOG, V. (2003) Structural and compositional analysis of the keratinocyte migration track. *Cell Motility and the Cytoskeleton* 55**,** 1-13.

KLEIN, E. J. & MARGOZZI, A. (1969) Exploratory investigation on the measurement of skin friction by means of liquid crystals. *NASA Technical Memorandum,* X-1774**,** 1-11.

KOVACS, G. T. (2003) Electronic sensors with living cellular components. *Proceedings of The IEEE,* 91**,** 915-929.

KRAFT, R. & PATT, S. (2006) *An introduction to molecular biotechnology : molecular fundmentals, methods and applications in modern biotechnology* Heidelberg, Wiley-VCH.

KREIDBERG, J. A. (2000) Functions of α3β1 integrin. *Current Opinion in Cell Biology,* 12**,** 548-553

KRENDEL, M., GLOUSHANKOVA, N. A., BONDER, E. M., FEDER, H. H., VASILIEV, J. M. & GELFAND, I. M. (1999) Myosin-dependent contractile activity of the actin cytoskeleton modulates the spatial organization of cell- cell contacts in cultured epitheliocytes. *Proceedings of National Academy of United States,* 96 9666-9670.

KUBALL, H.-G., TRK, O., KIESEWALTER, I. & DORR, E. (2000) A Non-Traceless Molecular Pseudotensor for a Description of the HTP *Molecular Crystals and Liquid Crystals,* 352**,** 195 – 204.

LACOUR, S. P., WAGNER, S., HUANG, Z. & SUO, Z. (2003) Stretchable gold conductors on elastomeric substrates. *Appl. Phys. Lett.,* 82**,** 2404-2406.

LADA, A. T., WILLINGHAM, M. C. & CLAIR, R. W. S. (2002) Triglyceride depletion in THP-1 cells alters cholesteryl ester physical state and cholesterol efflux. *Journal of lipid research,* 43**,** 618-628.

LAMPEA, P. D. & LAUB, A. F. (2004) The effects of connexin phosphorylation on gap junctional communication. *International Journal of Biochemistry and Cell Biology,* 36**,** 1171-1186.

LANGANGER, G., MOEREMANS, M., DANEELS, G., SOBIESZEK, A., BRABANDER, M. D. & MEY, J. D. (1986) The molecular organization of myosin in stress fibers of cultured cells. *The Journal of Cell Biology,* 102**,** 200-209.

LARJAVA, H., SALO, T., HAAPASALMI, K., KRAMER, R. H. & HEINOLL, J. (1993) Expression of integrins and basement membrane components by wound keratinocytes. *Journla of Clinical Investigation,* 92**,** 1425-1435.

LAURIE, G. W., LEBLOND, C. O. & MARTIN, G. R. (1982) Localization of Type IV Collagen, Laminin, Heparan SulfateProteoglycan, and Fibronectin to the Basal Basement *The Journal of Cell Biology,* 95**,** 340-344.

LAZARIDES, E. & WEBER, K. (1974) Actin antibody: The specific visualization of actin filaments in non-muscle cells. *Proceedings of National Academy of United States,* 71**,** 2268-2272.

LEE, S. Y., PEREIRA, B., P., YUSOF, N., SELVARATNAM, L., YU, Z., AABBAS, A. & KAMARULT. (2009) Unconfined compression properties of a porous poly(vinyl alcohol)–chitosan-based hydrogel after hydration. *Acta Biomaterialia,* 5**,** 1919-1925.

LEHNERT, D., WEHRLE-HALLER, B., DAVID, C., WEILAND, U., BALLESTREM, C., IMHOF, B. & BASTMEYER, M. (2003) Cell behaviour on micropatterned substrata: limits of extracellular matrix geometry for spreading and adhesion. *Journal of Cell Science,* 117**,** 41-52.

LEONG, A. S. & GILHAM, P. N. (1989) The effects of progressive Formaldehyde fixation on the preservation of tissue antigens. *Pathology,* 21**,** 266-268.

LEVENTAL, I., GEORGESA, P. C. & JANMEY, P. A. (2007) Soft biological materials and their impact on cell function. *Soft Matter,* 3**,** 299-306.

LI, A. G., WANG, D., FENG, X.-H. & WANG, X.-J. (2004a) Latent TGF-beta 1 overexpression in keratinocytes results in severe psoriasis-like skin disorder. *The EMBO Journal,* 23**,** 1770-1781.

LI, W., HENRY, G., FAN, J., BANDYOPADHYAY, B., PANG, K., GARNER, W., CHEN, M. & WOODLEY, D. (2004b) Signals that initiate, augment, and provide directionality for human keratinocyte motility. *The Journal of Investigative Dermatology,* 123**,** 622-633.

LI, Z., SONG, J., MANTINI, G., LU, M.-Y., FANG, H., FALCONI, C., CHEN, L.-J. & WANG, Z. L. (2009) Quantifying the traction torce of a single cell by aligned silicon nanowire array. *Nano Letters,* 9**,** 3575–3580.

LILLIE, J. H., MACCALLUM, D. K. & JEPSEN, A. (1988) Growth of stratified squamous epithelium on reconstituted extracellular matrices: long-term culture. *The Journal of Investigative Dermatology,* 90.

LIN, C.-C., YANG, F. & LEE, S. (2008) Surface wrinkling of an elastic film: effect of residual surface stress. *Langmuir,* 24**,** 13627-13631.

LIN, I.-K., OU, K.-S., LIAO, Y.-M., LIU, Y., CHEN, K.-S. & ZHANG, X. (2009) Viscoelastic characterization and modeling of polymer transducers for biological applications. *Journal of Microelectromechanical Systems,* 18**,** 1087-1099.

LO, C.-M., WANG, H.-B., DEMBO, M. & WANG, Y.-L. (2000) Cell movement is guided by the rigidity of the substrate. *Biophysical Journal* 79 144-152.

LOCKWOOD, N., MOHR, J. C., JI, L., MURPHY, C. J., PALECEK, S. P., PABLO, J. J. D. & ABBOTT, N. L. (2006) Thermotropic liquid crystals as substrates for imaging the reorganization of matrigel by human embryonic stem cells. *Advanced Functional Materials,* 16**,** 618-624.

LOEW, L. W. (1996) Potentiometric dyes: imaging electrical activity of cell membranes. *Pure and Applied Chemistry,* 68**,** 1405-1409.

LUK, Y.-Y., YANG, K.-L., CADWELL, K. & ABBOTT, N. L. (2004) Deciphering the interactions between liquid crystals and chemically functionalized surfaces: role of hydrogen bonding on orientations of liquid crystals. *Surface Science,* 570**,** 43-56.

MA, X., CHENG , Z., KONG, H., WANG, Y., UNRUH, H., STEPHENS, N. L. & LAVIOLETTE, M. (2002) Changes in biophysical and biochemical properties of single bronchial smooth muscle cells from asthmatic subjects. *American Journal of Physiology Lung Cell,* 283**,** 1181-1189.

MACKAY, D. J. G. & HALL, A. (1998) Rho GTPases. *The Journal of Biological Chemistry,* 273**,** 20685–20688.

MARX, K. A., ZHOU, T., MONTRONE, A., DONNA MCINTOSH & BRAUNHUT, S. J. (2005) Quartz crystal microbalance biosensor study of endothelial cells and their extracellular matrix following cell removal: Evidence for transient cellular stress and viscoelastic changes during detachment and the elastic behavior of the pure matrix. *Analytical Biochemistry* 343**,** 23-34.

MASSAGUE, J. & WOTTON, D. (2000) Transcriptional control by the TGF beta/SMAD signaling system. *The EMBO Journal,* 19**,** 1745-1754.

MATTHEWS, B. D., OVERBY, D. R., MANNIX, R. & INGBER, D. E. (2006) Cellular adaptation to mechanical stress: role of integrins, Rho, cytoskeletal tension and mechanosensitive ion channels. *Journal of Cell Science,* 119**,** 508-518.

MILLER, R. J. & GLEESON, H. F. (1993) The influence of pretransitional phenomena on blue phase range *Liquid Crystals,* 14**,** 2001 - 2011

MOHL, C., KIRCHGEBNER, N., SCHAFER, C., KUPPER, K., BORN, S., DIEZ, G., GOLDMANN, W. H., MERKEL, R. & HOFFMAN, B. (2009) Becoming stable and strong: the interplay between vinculin exchange dynamics and adhesion strength during adhesion site maturation. *Cell Motility and the Cytoskeleton,* 66**,** 350-364.

MONTESANO, R. & ORCI, L. (1988) Transforming growth factor f3 stimulates collagen-matrix contraction by fibroblasts: Implications for wound healing. *Proceedings of National Academy of United States,* 85**,** 4894-4897.

MOONEY, D. J., LANGER, R. & INGBER, D. E. (1995) Cytoskeletal filament assembly and the control of cell spreading and function by extracellular matrix. *Journal of Cell Science,* 108**,** 2311-2320.

MORTENSEN, K. (2001) Structural studies of lamellar surfactant systems under shear. *Current Opinion in Colloid & Interface Science,* 6**,** 140-145.

MOUMMI, C. & WOODFORD, M. (1992) A computerised system for measuring cell length of single isolated smooth muscle cells. *Drug development research,* 25**,** 325-329.

MUNEVAR, S., WANG, Y.-L. & DEMBO, M. (2001) Traction force microscopy of migrating normal and H-ras transformed 3T3 Fibroblasts. *Biophysical Journal,* 80**,** 1744-1757.

MUNOZ, J. & ALFARO, M. C. (2000) Rheological and phase behavior of amphiphilic lipids. *Grasas y Aceites,* 51**,** 6-25.

MUTHUSWAMY, J., OKANDAN, M., GILLETTI, A., BAKER, M. S. & JAIN, T. (2005) An array of microactuated microelectrodes for monitoring single-neuronal activity in rodents. *IEEE Transactions on Biomedical Engineering,* 52**,** 1470-1477.

NGUYEN, B. P., RYAN, M. C., GIL, S. G. & CARTER, W. G. (2000) Deposition of laminin 5 in epidermal wounds regulates integrin signaling and adhesion. *Current Opinion in Cell Biology* 12**,** 554-562

NORRIS, A. N. (2006a) Extreme values of poisson's ratio and other engineering moduli in anisotropic materials. *Journal of Mechanics of Materials and Structures,* 1**,** 793-812.

O'KANE, S. & FERGUSON, M. W. J. (1996) Transforming growth factor βs and wound healing. *International Journal of Biochemistry & Cell Biology,* 29**,** 63-78.

O'TOOLE, E. A. (2001) Extracellular matrix and keratinocyte migration. *Clinical and Experimental Dermatology,* 26**,** 525-530.

OBAID, A. L., LOWE, L., M., WUSKELL, J. P. & SALZBERG, B. M. (2004) Novel naphthylstyrl-pyridinium potentiometric dyes offer advantages for neural network analysis. ;:. *Journal of Neuroscience Methods,* 134**,** 179-190.

OFFENHAUSSER, A., SPROSSLER, C., MATSUZAWA, M. & KNOLL, W. (1997) Field-Effect transistor array for monitoring electrical activity from mammalian neurons in culture. *Biosensors & Bioelectronics* 12**,** 819-826.

OLIVER, T., DEMBO, M. & JACOBSON, K. (1995) Traction forces in locomoting cells. *Cell Motility and the Cytoskeleton* 31**,** 225-240.

OLIVER, T., JACOBSON, K. & DEMBO, M. (1998) Design and use of substrata to measure traction forces exerted by cultured cells. *Methods in Enzymology,* 298**,** 497-521.

OLIVER, W. C. & PHARR, G. M. (1992) An improved technique for determining hardness and elastic modulus using load and displacement sensing indentation experiments. *Journal of Materials Research,* 7**,** 1564-1583.

OMELCHENKO, T., FETISOVA, E., IVANOVA, O., BONDER, E. M., FEDER, H., VASILIEV, J. M. & GELFAND, I. M. (2001) Contact interactions between epitheliocytes and fibroblasts: Formation of heterotypic cadherin-containing adhesion sites is accompanied by local cytoskeletal reorganization *Proceedings of the National Academy of Sciences* 98**,** 8632–8637.

OWARIBE, K., KODAMA, R. & EGUCHI, G. (1981) Demonstration of contractility of circumferential actin bundles and its morphogenetic significance in pigmented epithelium in vitro and in vivo. *The Journal of Cell Biology,* 90 507-514.

PALJARVI, L., GARCIA, J. H. & KALIMO, H. (1979) The efficiency of aldehyde fixation for electron microscopy: stabilization of rat brain tissue to withstand osmotic stress. *Histochemical Journal,* 11**,** 267-276.

PARK, T. H. & SHULER, M. L. (2003) Integration of Cell Culture and Microfabrication Technology. *Biotechnol. Prog. ,* 19**,** 243-253.

PATHAK, A., DESHPANDE, V. S., MCMEEKING, R. M. & EVANS, A. G. (2008) The simulation of stress fibre and focal adhesion development in cells on patterned substrates. *Journal of Royal Society Interface,* 5**,** 507-524.

PAX, M., RIEGER, J., EIBL, R., THIELEMANN, C. & JOHANNSMANN, D. (2005) Measurements of fast fluctuations of viscoelastic properties with the quartz crystal microbalance. *Analyst,* 130**,** 1474-1477.

PELHAM, R. J. & WANG, Y.-L. (1997) Cell locomotion and focal adhesions are regulated by substrate flexibility. *Proceedings of the National Academy Sciences of the United States of America,* 94**,** 13661-13665.

PELLEGRIN, S. & MELLOR, H. (2007) Actin stress fibres. *Journal of Cells Science,* 120**,** 3491-3499.

PETERSON, L. J., RAJFUR, Z., MADDOX, A. S., FREEL, C. D., CHEN, Y., EDLUND, M., OTEY, C. & BURRIDGE, K. (2004) Simultaneous stretching and contraction of stress fibers in vivo. *Molecular Biology of the Cell,* 15**,** 3497-3508.

PHARR, G. M. (1998) Measurement of mechanical properties by ultra low load indentation. *Materials Science and Engineering A,* 253**,** 151-159.

PORCAR, L., WARR, G. G., HAMILTON, W. A. & BUTLER, P. D. (2005) Shear-Induced Collapse in a Lyotropic Lamellar Phase. *Physical Review Letters,* 95**,** 078302(1-4).

PÖSCHL, E., SCHLÖTZER-SCHREHARDT, U., BRACHVOGEL, B., SAITO, K., NINOMIYA, Y., I & MAYER, U. (2004) Collagen IV is essential for basement membrane stability but dispensable for initiation of its assembly during early development. *Development,* 131**,** 1619-1628.

PRIESTLEY, E. B., WOJTOWICZ, P. J. & SHENG, P. (1974) Introduction to Liquid Crystals. *Plenum Press, New York and London***,** 3.

PROVENZANO, P. P., INMAN, D. R., ELICEIRI, K. W. & KEELY, P. J. (2009) Matrix density-induced mechanoregulation of breast cell phenotype, signaling and gene expression through a FAK/ERK linkage. *Oncogene,* 28**,** 4326-4343.

PRUNIÉRAS, M., RÉGNIER, M., FOUGÈRE, S. & WOODLEY, D. (1983) Keratinocytes synthesize basal-lamina proteins in culture. *Journal of Investigative Dermatology,* 81**,** 74s-81s.

RABATIC, B. M., PRALLE, M. U., TEW, G. N. & STUPP, S. I. (2003) Nanostructured Semiconductors templated by cholesteryl-oligo(ethylene oxide) amphiphiles. *Chemistry Materials,* 15**,** 1249-1255.

RAMOS, L., ZAPOTOCKY, M., LUBENSKY, T. C. & WEITZ, D. A. (2002) Rheology of defect networks in cholesteric liquid crystals. *Physical Review E,* 66**,** 1-10.

REDA, D. C. & MURATORE, J. J. (1994) Measurement of Surface Shear Stress Vectors Using Liquid Crystal Coatings. *AIAA Journal* 32**,** 1576-1582.

REN, W., MCMULLAN, P. J. & GRIFFIN, A. C. (2008) Poisson's ratio of monodomain liquid crystalline elastomers. *Macromolecular Chemistry and Physics,* 209**,** 1896-1899.

REST, M. V. D. & GARRONE, R. (1991) Collagen family of proteins. *The Faseb Journal,* 5**,** 2814-2823.

RICH, A. & CRICK, H. C. (1955) The structure of collagen. *Nature,* 4489**,** 915-916.

RIVELINEA, D., ZAMIR, E., BALABAN, N. Q., SCHWARZ, U. S., ISHIZAKI, T., NARUMIYA, S., KAM, Z., GEIGER, B. & BERSHADSKY, A. D. (2001) Focal Contacts as Mechanosensors: Externally Applied Local Mechanical Force Induces Growth of Focal Contacts by an mDia1-dependent and ROCK-independent Mechanism. *The Journal of Cell Biology,* 153**,** 1175-1185.

ROBERTS, G. P. & BRUNT, J. (1985) Identification of an epidermal cell-adhesion glycoprotein. *Biochemistry Journal* 232**,** 67-70.

ROCCHAD, A. & BARRODON, Y. (2009) *Essential of stem cell biology,* Canada, Academic Press.

ROHR, S. (2004) Role of gap junctions in the propagation of the cardiac action potential. *Cardiovascular Research,* 62**,** 30-322.

ROSENBLOOM, J., ABRAMS, W. R. & MECHAM, R. (1993) Extracellular matrix 4: the elastic fiber. *The FASEB Journal,* 7**,** 1208-1218.

ROURE, O. D., SAEZ, A., BUGUIN, A., ROBERT H, A., CHAVRIER, P., SIBERZAN, P. & BENOIT, L. (2005) Force mapping in epithelial cell migration. *Proceedings of the National Academy Sciences of the United States of America,* 102**,** 2390-2395.

ROY, P., PETROLL, W. M., CAVANAGH, H. D., CHUONGC. J. & JESTERJ. V. (1997) An in VitroForce Measurement Assay to Study the Early Mechanical Interaction between Corneal Fibroblasts and Collagen Matrix. *Experimental Cell Research,* 232**,** 106-117.

SAEZ, A., GHIBAUDO, M., BUGUIN, A., SILBERZAN, P. & LADOUX, B. (2007) Rigidity-driven growth and migration of epithelial cells on microstructured anisotropic substrates. Proceedings of National Academy of Sciences of USA.

SAGVOLDEN, G., GIAEVER, I., PETTERSEN, E., O., & FEDER, J. (1999) Cell adhesion force microscopy. *Proceedings of National Academy of United States,* 96**,** 471-476.

SCHAFER, I., SHAPIRO, A., KOVACH, M., LANG, C. & FRATIANNE, R. (1989) The interaction of human papillary and reticular fibroblasts and human keratinocytes in the contraction of three-dimensional floating collagen lattices. *Experimental Cell Research,* 183**,** 112-125.

SCHNEEBERGER, E. E. & LYNCH, R. D. (1992) Structure, function, and regulation of cellular tight junctions. *American Journal of Physiology Lung Cellular Molecular Physiology* 262**,** L647-L661.

SCHOLZ, W. K. (2003) Cell adhesion and growth on coated or modified glass or plastic surfaces. *nunc.* Nalge Nunc International.

SCHWARTZ, M. A. & DESIMONE, D. W. (2008) Cell adhesion receptors in mechanotransduction. *Current Opinion in Cell Biology* 20**,** 551-556.

SELLHEYER, K., BICKENBACK, J. R., ROTHNAGEL, J. A., BUNDMAN, D., LONGLEY, M. A., KRIEG, T., ROCHE, N. S., ROBERTS, A. B. & ROOP, D. R. (1993) Inhibition of skin development by overexpression of transforming growth factor β1 in the epidermis of transgenic mice. *Proceedings of National Academy of United States,* 90**,** 5237-5241.

SHEN, X., LI, J., HU, P. P.-C., WADDELL, D., ZHANG, J. & WANG, X.-F. (2001) The activity of Guanine Exchange Factor NET is essential for Transforming Growth Factor-beta-mediated stress fiber formation. *The Journal of Biological Chemistry,* 276**,** 15362-15368.

SHOHAM, S., CONNOR, D. H. O. & SEGEV, R. (2006) How silent is the brain: is there a "dark matter" problem in neuroscience? *J Comparative Physiology A* 192**,** 777-784.

SILVER, F. H., SIPERKO, L. M. & SEEHRA, G. P. (2003) Mechanobiology of force transduction in dermal tissue. *Skin Research and Technology,* 9**,** 3-23.

SIMONS, K. & IKONEN, E. (2000) How cells handle cholesterol. *Science,* 290**,** 1721-1726.

SINGER, A. J., RICHARD, A. F. & CLARK, A. F. (1999) Cutaneous wound healing. *The New England Journal of Medicine***,** 738-746.

SMABY, J. M., BUAMANN, W. J. & BORCKMAN, H. L. (1979) Lipid structure and the behavior of cholesteryl esters in monolayer and bulk phases. *Journal of lipid research,* 20**,** 789-795.

SMALL, D. M. (1977) Liquid crystals in living and dying systems. *Journal of Colloid and Interface Science,* 58**,** 581-602.

SMALL, J. V., STRADAL, T., VIGNAL, E. & ROTTNER, K. (2002) The lamellipodium: where motility begins. *TRENDS in Cell Biology* 12**,** 112-120.

SOLON, J., LEVENTAL, I., SENGUPTA, K., GEORGES, P. C. & JANMEY, P. A. (2007) Fibroblast adaptation and stiffness matching to soft elastic substrates. *Biophysical Journal* 93**,** 4453-4461.

SOMMA, E. & NOBILE, M. R. (2004) The linear viscoelastic behavior of a series of molecular weights of the thermotropic main-chain liquid crystal plymers HBA/HNA 73/27. *Journal of Rheology,* 48**,** 1407-1423.

SOUREN, J. E., PONEC, M. & VAN WIJIK, A. (1989) Contraction of collagen by human fibroblasts and keratinocytes. *In Vitro Cellular & Developmental Biology,* 25**,** 1039-1045.

STANLEY, J., HAWLEY-NELSON, P., YAAH, M., MARTIN, G. R. & KATZ, S. (1982a) Laminin and bullous pemphigoid antigen are distinct basement membrane proteins synthesized by epidermal cells. *The Journal of Investigative Dermatology,* 78**,** 456-459.

STANLEY, J. R., WOODLEY, D. T., KATZ, S. I. & MARTIN, G. R. (1982b) Structure and function of basement membrane. *Journal of Investigative Dermatology,* 79**,** 69s-72s.

STANNARIUS, R., KÖHLER, R., RÖSSLE, M. & ZENTEL, R. (2004) Study of smectic elastomer films under uniaxial stress. *Liquid Crystals,* 31**,** 895 - 906

STASIEKA, J., STASIEKA, A., JEWARTOWSKIA, M. & COLLINS, M. W. (2006) Liquid crystal thermography and true-colour digital image processing. *Optics and Laser Technology,* 38**,** 243-256.

STENGER, D. A., GROSS, G. W., KEEFER, E. W., SHAFFER, K. M., ANDREADIS, J. D., MA WU & PANCRAZIO, J. J. (2001) Detection of physiologically active compounds using cell-based biosensors. *Trends in Biotechnology,* 19**,** 304-309.

STOODLEY, P., LEWANDOWSKI, Z., BOYLE, J. D. & LAPPIN-SCOTT, H. M. (1999) Structural deformation of bacterial biofilms caused by short-term fluctuations in fluid shear: an in situ investigation of biofilm rheology. *Biotechnology and Bioengineering,* 65**,** 83-92.

STORM, C., PASTORE, J. J., MACKINTOSH, F. C., LUBENSKY, T. C. & JANMEY, P. A. (2005) Nonlinear elasticity in biological gels. *Letters to Nature,* 435**,** 191-194.

STOURNARAS, C., STIAKAKI, E., KOUKOURITAKI, S. B., THEODORPOLOUS, P. A., KALMANI, M., FOSTINIS, Y. & AGRAVANIS, A. (1996) Altered actin polymerization dyanamics in various malignant cell types: evidence for differential sensitivity to cytochalasin B. *Biochemical and Pharmacology,* 52**,** 1339-1346.

TAKEO, M. (2007) Skin biomechanics from microscopic viewpoint: mechanical properties and their measurement of horny layer, living epidermis, and dermis. *Fagrance Journal,* 35**,** 36-40.

TAKIGAWA, T., MORINO, Y., URAYAMA, K. & MASUDA, T. (1996) Poisson's Ratio of Polyacrylamide (PAAm) Gels. *Polymer Gels and Networks,* 4**,** 1-5.

TAN, J. L., RAVID, S. & SPUDICH, J. A. (1992) Control of nonmuscle myosins by phosphorylation. *Annual Review of Biochemistry* 6**,** 721-759.

TAN, J. L., TIEN, J., PIRONE, D. M., GRAY, D. S., BHADRIRAJU, K. & CHEN, C. S. (2003) Cells lying on a bed of microneedles: An approach to isolate mechanical force. *Proceedings of the National Academy Sciences of the United States of America,* 100**,** 1484-1489.

THEODOROPOULOS, P. A., GRAVANIS, A., TSAPARA, A., MARGIORIS, A. N., PAPADOGIORGAKI, E., GALANOPOULOS, V. & STOURNARAS, C. (1994) Cytochalasin B may shorten actin filaments by a mechanism independent of barbed end capping. *Biochemical Pharmacology* 47**,** 1875-1881.

THIRKILL, T. L., HENDREN, S. R., SOGHOMONIANS, A., MARIANO, N. F., BARAKAT, A. I. & DOUGLAS, G. C. (2004) Regulation of trophoblast beta1-integrin expression by contact with endothelial cells *Journal of Cell Communication and Signaling,* 2**,** 4.

THOMAS, C. A., SPRINGER, P. A., LOEB, G. E., BERWALD-NETTER, Y. & OKUN, L. M. (1972) A miniature microelectrode array to monitor the bioelectric activity of cultured cells. *Experimental Cell Research,* 74**,** 61-66.

THOMAS, R. C. (1972) Electrogenic sodium pump in nerve and muscle cells. *Physiological Reviews,* 52**,** 563-594.

THORSLUND, S. (2006) Digital Comprehensive Summaries of Uppsala Dissertations. *Faculty of Science and Technology.* Uppsala University, Uppsala, Sweden.

THOUMINE, O., OTT, A. & LOUVARD, D. (1996) Critical centrifugal forces induce adhesion rupture or structural reorganization in cultured cells. *Cell Motility and the Cytoskeleton* 33**,** 276-287.

TING, T. C. T. & CHEN, T. (2005) Poisson's ratio for anisotropic elastic materials can have no bounds. *Journal of mechanical applied maths,* 58**,** 73-82.

TSCHOEGL, N. W., KNAUSS, W. G. & IGOR, E. (2002) Poisson's ratio in linear viscoelasticity-a critical review. *Journal of Mechanics of time-dependent materials,* 6**,** 3-51.

TURKESEN, K., AUBIN, J. E., SODEK, J. & KALNINS, V. I. (1985) Localization of laminin, type IV collagen, fibronectin, and heparan sulfate proteoglycan in chick retinal pigment epithelium basement membrane during embryonic development. *The Journal of Histochemistry and Cytochemistry,* 33**,** 665-671.

URAYAMA, K., TAKIGAWA, T. & MASUDA, T. (1993) Poisson's Ratio of Poly(vinyl alcohol) Gels. *Macromolecules,* 26**,** 3092-3096.

VASIOUKHIN, V., BAUER, C., YIN, M. & FUCHS, E. (2000) Directed actin polymerization Is the driving force for epithelial cell–cell adhesion. *Cell,* 100**,** 209-219.

WAGGNONER, A. S. (1979) Dye indicators of membrane potential. *Annual Review of Biophysical Bioengineering,* 8**,** 47-68.

WARD, I. M. & SWEENEY, J. (2004) *An introduction to the mechanical properties of solid polymers* Chicheste, Wiley.

WASSEL, P. (2009) A general purpose Greens function-based interpolator. *Computers and Geosciences,* 35**,** 1247-1254.

WHORLOW, R. W. (1992) *Rheological techniques*, Chichester, Ellis Horwood, New York.

WIKSWO, M. A. & SZABO, G. (1972) Effects of cytochalasin B on mammalian melanocytes and keratinocytes. *The Journal of Investigative Dermatology,* 59**,** 163-168.

WOLBURG, H., NEUHAUS, J., KNIESEL, U., KRAUß, B., SCHMID, E.-M., ÖCALAN, M., FARRELL, C. & RISAU, W. (1994) Modulation of tight junction structure in blood-brain barrier endothelial cells: Effects of tissue culture, second messengers and cocultured astrocytes. *Journal of Cell Science,* 107**,** 1347-1357.

WOLTMAN, S. J., JAY, G. D. & CRAWFORD, G. P. (2007) Liquid-crystal materials find a new order in biomedical applications. *Nature Materials* 6**,** 929-938.

WONG, J. (1999) Tissue Engineering-tractional forces of cells. *Science and Medicine,* 6**,** 6-7.

WOOLVERTON, C. J., GUSTELY, E., LI, L. & LAVRENTOVICH, O. D. (2005) Liquid crystal effects on bacterial viability. *Liquid Crystals,* 32**,** 417-423.

WRANA, J. L. (1998) TGF- Receptors and Signaling Mechanisms. *Mineral and Electrolyte Metabolism,* 24**,** 2-3.

YANG, D. K., WEST, J. L., CHIEN, L. C. & DOANE, J. W. (1994) Control of reflectivity and bistability in displays using cholesteric liquid crystals. *Journal of Applied Physics,* 76**,** 1381-1333.

YEAGLE, P. L. (1985) Cholesterol and the cell membrane *Biochimica et Biophysica Acta* 822**,** 267-287.

YEUNG, T., GEORGES, P. C., FLANAGAN, L. A., MARG, B., ORTIZ, M., FUNAKI, M., ZAHIR, N., MING, W., WEAVER, V. & JANMEY, P. A. (2005) Effects of substrate stiffness on cell morphology, cytoskeletal structure, and adhesion. *Cell Motility and the Cytoskeleton,* 60**,** 24-34.

YU, C., CUI, H. F., YE, J. S., CHONG, S. C., LIM, T. M., SHEU, F. S. & HUI, F. S. (2006) Electrochemical biochip for drug screening at cellular level. *Journal of Physics: Conference Series,* 34**,** 198-203.

ZAMBRUNO, G., MARCHISIO, P. C., MARCONI, A., VASCHIERI, C., MELCHIORI, A., GIANNETTI, A. & LUCALL, M. D. (1995) Transforming Growth Factor-β1 modulates beta1 and beta 5 integrin receptors and induces the de novo expression of the alpha αvbeta6 heterodimer in normal human keratinocytes: implications for wound healing. *The Journal of Cell Biology,* 129**,** 853-865.

ZAPOTOCKY, M., RAMOS, L., POULIN, P., LUBENSKY, T. C. & WEITZ, D. A. (1999) Particle-stabilized defect gel in cholesteric liquid crystals *Science,* 283**,** 209-212.

ZHANG, J., BETSON, M., ERASMUS, J., ZEIKOS, K., BAILLY, M., CRAMER, L. P. & BRAGA, V. M. M. (2005) Actin at cell-cell junctions is composed of two dynamic and functional populations. *Journal of Cell Science,* 118**,** 5549-5562.

ZHANG, L., WANG, W., HAYASHI, Y., JESTER, J. V., BIRK, D. E., GAO, M., LIU, C.-Y., KAO, W. W.-Y., KARIN, M. & XIA, Y. (2003) A role for MEK kinase 1 in TGF-Beta/activin-induced epithelium movement and embryonic eyelid closure. *The EMBO Journal,* 22**,** 4443-4454.

ZHAO, G., SCHWARTZ, Z., WIELAND, M., RUPP, F., GEIS-GERSTORFER, J. (2005) High surface energy enhances cell response to titanium substrate microstructure. *Journal of Biomedical Materials Research Part A,* 74A**,** 49-58.

ZHAO, Y., MAHAJAN, N., LU, R. & FANG, J. (2005) Liquid-crystal imaging of molecular-tilt ordering in self-assembled lipid tubules. *Proceedings of the National Academy Sciences of the United States of America,* 102**,** 7438-7442.

ZIPFEL, J., BERGHAUSEN, J., LINDNER, P. & RICHTERING, W. (1999) Influence of shear on lyotropic lamellar phases with different membrane defects. *J. Phys. Chem. B,* 103**,** 2841-2849.

APPENDIX A

MATLAB CODES FOR THE CELL TRACTION FORCE MEASUREMENT AND MAPPING (CTFM) SOFTWARE

```
function varargout = Cellforcetool(varargin)
%CELLFORCETOOL M-file for GUI Cellforcetool.fig
%Version 17 September 2010
%Developed by Chin Fhong, Soon (2010)
%Estimate the traction force of HaCaT cells from image by point-click
%An image with a known calibration length is needed for image scale
%calibration.
%The calibration can be done if the image scale is pre-fixed over the
%image.
%For example: 10x- set ImageJ scale to 2 pixels/um
%                  20x- set ImageJ scale to 5 pixels/um
%The length measurement codes was adapted from Matt Allen, Fall 2007
%available in http://www.matlabcentral.com

% Begin initialization code
gui_Singleton = 1;
gui_State = struct('gui_Name',       mfilename, ...
                   'gui_Singleton',  gui_Singleton, ...
                   'gui_OpeningFcn', @Cellforcetool_OpeningFcn, ...
                   'gui_OutputFcn',  @Cellforcetool_OutputFcn, ...
                   'gui_LayoutFcn',  [] , ...
                   'gui_Callback',   []);
if nargin && ischar(varargin{1})
   gui_State.gui_Callback = str2func(varargin{1});
end

if nargout
   [varargout{1:nargout}] = gui_mainfcn(gui_State, varargin);
else
   gui_mainfcn(gui_State, varargin);
end
% End initialization code - DO NOT EDIT

% --- Executes just before Cellforcetool is made visible.
function Cellforcetool_OpeningFcn(hObject, eventdata, handles, varargin)
% This function has no output args, see OutputFcn.
% hObject    handle to figure
% eventdata  reserved - to be defined in a future version of MATLAB
% handles    structure with handles and user data (see GUIDATA)
% varargin   command line arguments to Cellforcetool (see VARARGIN)

% Choose default command line output for Cellforcetool
handles.output = hObject;

% Update handles structure
guidata(hObject, handles);

% UIWAIT makes Cellforcetool wait for user response (see UIRESUME)
% uiwait(handles.figure1);


% --- Outputs from this function are returned to the command line.
function varargout = Cellforcetool_OutputFcn(hObject, eventdata, handles)
% varargout  cell array for returning output args (see VARARGOUT);
% hObject    handle to figure
% eventdata  reserved - to be defined in a future version of MATLAB
% handles    structure with handles and user data (see GUIDATA)

% Get default command line output from handles structure
```

```
varargout{1} = handles.output;

% --- Executes on selection change in listImageformat.
function listImageformat_Callback(hObject, eventdata, handles)
% hObject    handle to listImageformat (see GCBO)
% eventdata  reserved - to be defined in a future version of MATLAB
% handles    structure with handles and user data (see GUIDATA)

% Hints: contents = get(hObject,'String') returns listImageformat contents as cell array
%        contents{get(hObject,'Value')} returns selected item from listImageformat

% --- Executes during object creation, after setting all properties.
function listImageformat_CreateFcn(hObject, eventdata, handles)
% hObject    handle to listImageformat (see GCBO)
% eventdata  reserved - to be defined in a future version of MATLAB
% handles    empty - handles not created until after all CreateFcns called

% Hint: listbox controls usually have a white background on Windows.
%       See ISPC and COMPUTER.
if ispc
   set(hObject,'BackgroundColor','white');
else
   set(hObject,'BackgroundColor',get(0,'defaultUicontrolBackgroundColor'));
end

% --- Executes on selection change in popupImage.
function popupImage_Callback(hObject, eventdata, handles)
% hObject    handle to popupImage (see GCBO)
% eventdata  reserved - to be defined in a future version of MATLAB
% handles    structure with handles and user data (see GUIDATA)

% Hints: contents = get(hObject,'String') returns popupImage contents as cell array
%        contents{get(hObject,'Value')} returns selected item from popupImage

switch get(handles.popupImage,'Value')
   case 1
     %Do nothing

   case 2
     [filename,pathname] = uigetfile({'*.jpg;*.tif;*.png;*.gif','All Image Files';...
       '*.*','All Files' })
     im_data = imread([pathname,filename]);
          figure; image(im_data)
      M = size(im_data,1);
      N = size(im_data,2);
      data(M,N)=0;
input('Press Enter key when ready to proceed');

axis image % make sure image is not distorted before starting

[xr,yr] = ginput(2);
line(xr,yr,'Marker','+','Color','b');
l_ref_img = norm([xr(1),yr(1)]-[xr(2),yr(2)]);

%Calibration with known lenght of line
% Prompt for length of this line:
   prompt = {'Enter the length of the reference line:'};
   dlg_title = 'Length of Ref. Line';
   num_lines = 1;
```

```
   def = {'1'};
   answer = inputdlg(prompt,dlg_title,num_lines,def);
   lscale = str2num(answer{1})/l_ref_img;

   % Displace labels slightly
   text(xr(1)+3,yr(1)-20,num2str(l_ref_img*lscale),'Color','w');
   text(xr(1)+55,yr(1)-20, 'um', 'Color','w');

% Zoom out if Right mouse button is depressed.  If the middle button is
% depressed, zoom in again.
loop_break = 0; meas_num = 1; SumForce = 0; i=0; num=0; xnum=0;
while loop_break == 0;
   [x1,y1,mbutton] = ginput(1);
   line(x1,y1,'Marker','+','Color','r');
   % right click the mouse to end the meausurement when mbutton==3
   if mbutton == 3;
      xnum=num; % Tracking the number of measurements
         AverageForce=SumForce/xnum;
         text(100,100,'Average force =           nN','BackgroundColor','w','Color','b');
         text(280,100,num2str(AverageForce),'BackgroundColor','w','Color','b');

      loop_break = 1;
      % This signifies that the user is done
   elseif mbutton == 1;
      % Get second point and measure
      [x2,y2,mbutton] = ginput(1);

      if mbutton == 3;
        loop_break = 1; break; end

      %Draw a line across the two selection points
      line([x1,x2],[y1,y2],'Marker','+','Color','r');

      % Multiply the length with the Force factor to calculate the force
      % F=15.07yo
      force(meas_num) = norm([x1,y1]-[x2,y2])*lscale*15.07;
      if force(meas_num)> 0
         num=num+1; % update the number of force>0
      end
      Force=force(meas_num);
       x(meas_num)=round(x1); % round up the coordinate value
       y(meas_num)=round(y1);
       z(meas_num)=Force;

       %for 2nd set data storage
        a(meas_num)=round(x2);
        b(meas_num)=round(y2);

      if mbutton~=3;
       z(meas_num)=Force;
      end

      SumForce=SumForce+Force;

      % Increment of counter for the next input
      meas_num = meas_num +1;

      %Display the current input
      text(x1+4,y1-20, 'F=          nN', 'Color','w');
```

```
            text(x1+40,y1-20,num2str(force(meas_num-1)),'Color','w');
            end
        end

            x=x';
            y=y';
            z=z';
            data=[x y z];
            x = data(:,1);
            y = data(:,2);
            z = data(:,3);
        % ti = 0:10:512;

         %%%%%%%%%%%%%%%%%%%%%%%%%%%%%%%%%%%%%%%%%%%%%%%%%%%%%%%%%%%%%%%%
        %Plot vector of the longitudinal deformation or vector force
        %
        %figure (5)
        %a0=[x]';
        %a1=[y]';
        %a2=[a];
        %a3=[b];
           %for j=1:meas_num-1,
             % x0=a0(j);
             % x1=a1(j);
             % y0=a2(j);
             % y1=a3(j);
              %% plot([x0;y0],[x1;y1],'Marker','>','MarkerSize',4);
              %%  line([x0;y0],[x1;y1],'Marker','','Color','b','MarkerSize',6);
             % arrow([x0;x1],[y0;y1],'Length', 10);
              %hold on
              %%grid on
              % xlabel('x')
              % ylabel('y')
           %end

%%%%%%%%%%%%%%%%%%%%%%%%%%%%%%%%%%%%%%%%%%%%%%%%%%%%%%%%%%%%%%%%
            figure(2)
             xi=0:50:M;
            yi=0:50:N;
        % First define a regular grid.Set up a MxN grid
            ti=linspace(M,0,100);
        % x and y will both be 512x512. xi contains the x-coords of each point
        % on this new grid, and yi contains the y-coords.
            [xi,yi] = meshgrid(ti,ti);
  %%%%%%%%%%%%%%%%%%%%%%%%%%%%%%%%%%%%%%%%%%%%%%%%%%%%%%%%%%%%%%%%
        %Plot linear interpolation
        % now interpolate - find z values at each of these grid points
            ZI = griddata(x, y, z, xi, yi, 'linear');
        % Display this as a surface
            %surf(xi, yi, ZI) % use only when the grid lines are required
            surf(xi, yi, ZI,'EdgeColor','none','FaceColor','interp','FaceLighting','phong');
            hold on
            %contour3(xi, yi, ZI)

            hold on % this prevents clearing the graphics window
            %alpha(0.8);
            colormap(jet(256));
            colorbar;
        % plot the original data x, y and z obtained from user selection
```

```
        plot3(x,y,z,'.'), hold on
        line(x,y,z,'marker','.','markersize',4,'linestyle','none');
       title ('Cell force mapping on liquid crystal transducer by linear interpolation');
        xlabel('x');
        ylabel('y');
        c=colorbar;
        ylabel(c,'Force (nN)')

 %%%%%%%%%%%%%%%%%%%%%%%%%%%%%%%%%%%%%
      %Plot cubic interpolation
        % now interpolate - find z values at each of these grid points
        figure(3)
         ZI = griddata(x, y, z, xi, yi, 'cubic');
      % Display this as a surface
         %surf(xi, yi, ZI) % use only when the grid lines are required
         surf(xi, yi, ZI,'EdgeColor','none','FaceColor','interp','FaceLighting','phong');
         hold on % this prevents clearing the graphics window

         %alpha(0.8);
         colormap(jet(256));
         colorbar;
      % plot the original data x, y and z obtained from user selection
        plot3(x,y,z,'.'), hold on
        line(x,y,z,'marker','.','markersize',6,'linestyle','none');
       title ('Cell force mapping on liquid crystal transducer by cubic interpolation');
        xlabel('x');
        ylabel('y');
        c=colorbar;
        ylabel(c,'Force (nN)')

%%%%%%%%%%%%%%%%%%%%%%%%%%%%%%%%%%%%%
      %Plot data points only
        figure(4)
        plot3(x,y,z,'.');
         xlabel('x');
        ylabel('y');
        zlabel('Force(nN)')
       otherwise
      end
       % --- Executes during object creation, after setting all properties.
      function popupImage_CreateFcn(hObject, eventdata, handles)
      % hObject    handle to popupImage (see GCBO)
      % eventdata  reserved - to be defined in a future version of MATLAB
      % handles    empty - handles not created until after all CreateFcns called

      % Hint: popupmenu controls usually have a white background on Windows.
      %       See ISPC and COMPUTER.
      if ispc
        set(hObject,'BackgroundColor','white');
      else
        set(hObject,'BackgroundColor',get(0,'defaultUicontrolBackgroundColor'));
      end
```